DISSERTATION

EXPANDING THE TOOLBOX FOR HIV-1 PROTEASE INHIBITOR RESISTANCE ASSESSMENT AND DRUG DISCOVERY TARGETING PROTEASE PRECURSOR AUTOPROCESSING

Submitted by

Ryan Jeep

Department of Biochemistry and Molecular Biology

In partial fulfillment of the requirements

For the Degree of Doctor of Philosophy

Colorado State University

Fort Collins, Colorado

Summer 2025

Doctoral Committee:

Advisor: Chaoping Chen

Tim Stasevich
Grant Schauer
Sandra Quackenbush

ABSTRACT

EXPANDING THE TOOLBOX FOR HIV-1 PROTEASE INHIBITOR RESISTANCE ASSESSMENT AND DRUG DISCOVERY TARGETING PROTEASE PRECURSOR AUTOPROCESSING

HIV-1 protease (PR) is initially synthesized as part of the Gag-Pol polyprotein precursor. Regulated protease precursor autoprocessing liberates the mature PR, which is required for viral infectivity. Thus, mature PR is the primary target of nine FDA-approved protease inhibitors (PIs). Numerous resistance-associated mutations (RAMs) within and beyond the PR gene have been identified which undermine the efficacy and prognosis of combination antiretroviral therapy (cART). The precise relationship between PR genotype, phenotype, and clinical treatment outcome is still not fully understood, and thus resistance to HIV-1 protease inhibitors (PI) remains a persistent challenge.

Using a variety of mammalian cell-based assays, including a newly developed infectivity assay capable of detecting single infectious units, we investigated a PR double mutant, V77I/V82T, identified in a patient resistant to indinavir (IDV). These assays revealed notable variations in PI susceptibility, implicating the context-dependent catalytic flexibility of HIV-1 mature PR and its precursors in resistance development. Our infectivity assay accurately replicated the clinically observed IDV resistance mediated by the V77I/V82T mutant and delineated the roles of individual mutations, demonstrating that while V82T confers resistance to IDV, it also increases sensitivity to darunavir (DRV). These findings add to the mounting evidence that precursor PRs are less sensitive to PI than mature PRs and define our lab's infectivity assay as a powerful tool for sensitive evaluation of drug effectiveness and resistance.

We also evaluated PI response of a panel of prototypical multi-PI-resistant mutants. Our comparative analyses demonstrated that our infectivity assay performed comparably to the conventional PhenoSense® assay in assessing drug resistance. Our results confirmed that the tested mutants exhibited diverse and distinct response profiles to darunavir (DRV), lopinavir (LPV), atazanavir (ATV), and saquinavir (SQV). Notably, our analysis revealed that high levels of resistance to LPV and ATV develop more easily than resistance to DRV and SQV suggesting that different RAM combinations result in distinct resistance profiles in these strains (see Chapter 3). Our infectivity assay provided improved resolution on PI susceptibility by correlating drug responses with PI concentrations and thus may aid in optimizing treatment regimens for people living with HIV experiencing drug resistance.

To explore alternative therapeutic strategies, we developed a cell-based high-throughput screening (HTS) platform targeting precursor autoprocessing and screened approximately 320,000 small molecules and 2,000 natural product extracts (NPEs). We identified 27 small molecules and 20 NPEs that partially suppress precursor autoprocessing. A highly sensitive infectivity assay confirmed that several small molecules inhibited viral infectivity in a dose-dependent manner, with EC_{50} values in the low micromolar range. Notably, small molecule C7 exhibited comparable potency against both wild-type and drug-resistant HIV strains, suggesting a novel mechanism of action. Two crude NPEs showed dose-dependent inhibitory activity in live virus and preliminary fractionation of the crude extracts partially separated inhibitory from non-inhibitory compounds. This study provides proof of concept for an innovative drug discovery approach targeting HIV-1 PR autoprocessing as a potential strategy to combat drug resistance.

ACKNOWLEDGEMENTS

First and foremost, I would like to thank my PhD advisor, Dr. Chaoping Chen. She has been invaluable in my development as a researcher and scientist. She has been in my corner from day one, and I greatly appreciate all of her help, wisdom, and support throughout my time as a graduate student. The cliché holds true: I would absolutely not be where I am in my scientific career without her. I would also like to thank Dr. Liangqun Huang, who is a technical wizard in the lab and has taught me numerous techniques and protocols. I think of her as part of the foundation of the Chen lab and I am grateful for all of her help, guidance, and perspective. To the numerous undergraduate students, graduate students, REU students, and research scientists I’ve had the pleasure of working with throughout the years: it was a pleasure to work with and learn from each of you. I want to specifically thank James Boehlke, Luke Bennett, Megan Gish, Kade Orstad, Stanton Ashman, EJ King, Natalie Cortez, Kira Boyce, Troy Sensano, and Bailey Howe. You have all been an absolute pleasure to work with and have made significant contribution to the work presented in this thesis. To Scott Burlingham, Leah Dixon, Ryan Coops, Projit Mukherjee, Sam Klink, Alex Alon, Riyasa Shrestha, and Colby Williams: it was my pleasure to work with each of you, and you all have contributed in one way or another to my growth as a scientist.

I would also like to thank my committee members, Dr. Tim Stasevich and Dr. Grant Schauer, for your support, input, and guidance over the years. I’ve greatly enjoyed my interactions with you both, as they are always both entertaining and fruitful. To my third committee member, Dr. Sandra Quackenbush, you have been a foundational committee member since the beginning. You have supported me through it all, and I cannot express how grateful I am to have your unwavering support throughout my PhD journey. Your belief in me has impacted me deeply and increased my confidence as a researcher, scientist, and person, and for that I cannot thank you enough. I also want to thank Dr. Tom Santangelo and Dr. Santiago DiPietro for your impact on me in the early years of my graduate school journey. Your insights have helped me grow immensely as a scientist and person, and for that I will always be thankful. I would like to specifically thank department chair Dr. Laurie Stargell and graduate chair Dr. Jake DeLuca for your continued support throughout my graduate career. You both have supported and advocated for me throughout my graduate study, for which I am very thankful. To CMB director Dr. Carol Wilusz: you have also supported me greatly and advocated for me in numerous ways. I am forever indebted for your help, guidance, and belief. To CMB program manager Mercedes Cooper: you truly keep the wheels on the bus. You are an absolutely stellar, kind, thoughtful person, and I am forever grateful for all of your help. To the rest of CMB, thank you for welcoming me with open arms.

My friends and family have been anchors for me for the past six years. I want to thank my parents. You both have been nothing but supportive, no matter what graduate school has thrown at me. You have watched me take every step of life, and I am honored for you to see me take this step as well. My sister, brother-in-law, niece, and nephew have been sources of comfort, fun, and comedy throughout my time living in Fort Collins, and I’ve loved every second of it. You have truly made Fort Collins seem like home. I also want to thank my friends for the game nights, pickleball sessions, tennis matches, basketball-watch parties, trips, and fun times in general. Many of you share the graduate school life, and I am grateful that I’ve found a supportive, fun, caring group of people to make life better.

Lastly, I want to thank my partner, Erica. We’ve shared our adult lives together, and you are and will always be my best friend. We’ve supported each other and grown together through thick and thin. Despite all the challenges we’ve faced, we’ve faced them together.

TABLE OF CONTENTS

CHAPTER 1:

INTRODUCTION

1.1 Background and Pathogenesis of Human Immunodeficiency Virus (HIV)

Human Immunodeficiency Virus (HIV) belongs to the *Retroviridae* family in the *Lentivirus* genus and is the causative pathogen of acquired immunodeficiency syndrome (AIDS). Retroviruses are enveloped viruses that carry two copies of single-stranded, positive-sense RNA and are known to infect a wide array of animals as well as humans. Retroviruses are generally divided into two classes: simple retroviruses or complex retroviruses. Simple retroviruses include three coding domains: *gag*, *pol*, and *env*, which collectively encode the basic viral proteins required for viral replication. Complex retroviruses also carry genetic information that encodes various accessory viral proteins in addition to the *gag*, *pol*, and *env* genes. Retroviruses, both simple and complex, derived the “retro” prefix due to their unique replication strategy, wherein viral RNA is reverse transcribed into proviral DNA that is then integrated into the host chromosome. Within the *Retroviridae* family, there are seven genera: Alpha-retrovirus, Beta-retrovirus, Gamma-retrovirus, Delta-retrovirus, Epsilon-retrovirus, Lentivirus, and Spumavirus [1].

Lentiviruses are a group of viruses known for the slow progression of the diseases they cause. Key members include human immunodeficiency virus (HIV), simian immunodeficiency virus (SIV), feline immunodeficiency virus (FIV), bovine immunodeficiency virus (BIV), equine infectious anemia virus (EIAV), and Visna-maedi virus. SIV is an extensively studied lentivirus, that infects CD4+ T-lymphocytes in primates. Separate cross-species transmission events from SIV-infected primates to humans are believed to have given rise to two types of HIV, HIV-1 and HIV-2 [2]. Several lineages are present within both HIV type 1 and type 2; HIV-1 includes groups M, N, O, and P, while HIV-2 includes groups A-H. HIV-1 groups M and N are thought to have been transmitted to humans directly from an SIV strain carried by central chimpanzees (*Pan troglodytes troglodytes*), while groups O and P likely came from SIV-positive western lowland gorillas (*Gorilla gorilla gorilla*) [2-4]. HIV-2 originated after human transfer from SIV-infected sooty mangabey monkeys (*Cercocebus atys*) [3]. However, HIV-2 infection is marked by reduced transmissibility and is much less likely to progress into AIDS compared to HIV-1; HIV-1 accounts for roughly 95% of all HIV infections worldwide [5].

HIV-1 infects CD4+ T-lymphocytes in humans. Based on cellular tropism, HIV-1 strains are generally categorized into three groups: 1) macrophage-tropic (M-tropic); 2) T-cell line tropic (T-tropic); 3) dual-tropic [6]. Besides CD4 serving as the primary receptor, either C-C chemokine receptor type 5 (CCR5) or C-X-C chemokine receptor type 4 (CXCR-4) coreceptor is required for infection. M-tropic strains require the CCR5 coreceptor for infection, while T-tropic strains require the CXCR4 coreceptor; dual-tropic strains use either coreceptor for infection [6]. There are three stages of HIV-1 infection defined by the NIH: acute infection, chronic infection, and AIDS. Viral replication is high during the acute stage and is usually associated with flu-like symptoms, although some HIV-positive patients may only experience mild symptoms. Acute HIV-1 infection leads to death of CD4+ T-cells, thus gradually depleting these cells and weakening the host immune system as the infection spreads. During the chronic stage of infection, also classified as clinical latency, viral replication continues but at a much lower level. Treatment with anti-retroviral therapy (ART) controls viral progression from the chronic stage of infection, as sustained viral suppression via ART delays the onset of the final stage of infection. AIDS is defined by a drastically weakened immune system, therefore increasing the likelihood of infection with opportunistic pathogens.

The HIV-1 RNA genome is roughly 9,700 nucleotides and contains nine open reading frames (ORFs) which collectively express 15 viral proteins (Figure 1.1) [7]. Three ORFs, *gag*, *pol*, and

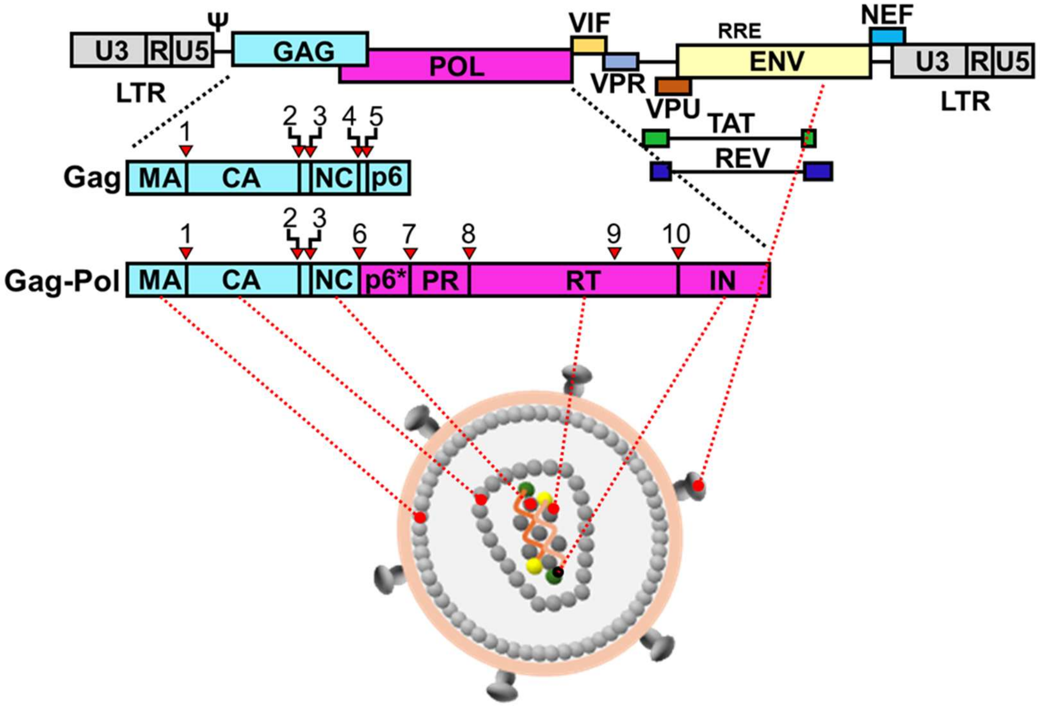

Figure 1.1. HIV-1 genome and virus particle. HIV-1 genome (top), polyproteins (middle), and mature, infectious viral particle cartoons (bottom). Numbers (1-10) indicate protease cleavage sites. Red dashed lines/dots indicate location of mature viral proteins in mature viral particle.

env, encode the structural viral proteins in addition to three viral enzymes required for viral replication. The *env* gene encodes the Env glycoprotein present on the surface of virus particles which is responsible for receptor and coreceptor binding and subsequent particle fusion. The *gag* and *pol* genes each encode multiple proteins in tandem and are thus known as polyproteins. The Gag polyprotein contains four viral proteins: matrix (MA), capsid (CA), nucleocapsid (NC), and p6, plus two spacer peptides (sp1 and sp2) [7]. The viral enzymes encoded by the *pol* gene, protease (PR), reverse transcriptase (RT), and integrase (IN), are responsible for proteolytic cleavage of Gag and Gag-Pol, reverse transcription of viral RNA into cDNA, and integration of cDNA into the host chromosome as the proviral genome, respectively. The remaining six ORFs in the HIV-1 genome encode six regulatory viral proteins. The *tat* and *rev* genes encode indispensable regulatory proteins Tat and Rev, respectively, while the *nef*, *vif*, *vpr*, and *vpu* genes encode the accessory proteins Nef, Vif, Vpr, and Vpu [7]. Gag, Gag-Pol, Env, Tat, and Rev are all indispensable for viral replication and infectivity, as all play critical roles in the viral lifecycle. Nef, Vif, Vpr, and Vpu are considered “dispensable” for viral replication, however these proteins are necessary for productive, pathogenic infection in humans.

1.2 The HIV-1 Lifecycle

The HIV-1 lifecycle can be divided into seven distinct stages: 1) binding, 2) fusion, 3) reverse transcription, 4) integration, 5) transcription and translation, 6) assembly, and 7) budding and maturation. The maturation phase is mainly facilitated by the mature PR (Figure 1.1), which catalyzes the cleavage of Gag and Gag-Pol that results in a drastic rearrangement of the inner particle landscape required for infectivity. The mature, infectious HIV-1 virus particle is roughly 150-200 nm in diameter and consists of the capsid core encased in a lipid envelope bilayer derived from the host cell membrane. The mature capsid core consists of roughly 250 CA (24 kDa) hexamers and exactly 12 CA pentamers that form a hollow, fullerene cone geometry [8, 9].

The capsid core houses the reverse transcription complex (RTC), which includes the viral genomic RNA in complex with nucleocapsid (NC), the viral reverse transcriptase, cellular Lys3 tRNA, and the viral integrase. Trimeric Env glycoproteins, embedded in the viral membrane, mediate viral fusion with a target cell. The Env trimer is composed of three heterodimers formed by interaction between two Env subunits, gp41 and gp120.

Substantial conformational changes in gp41 and gp120 upon CD4 receptor and CCR5/CXCR-4 coreceptor binding facilitate membrane fusion. Initial interaction between the CD4 receptor and the V1V2 (variable region 1, variable region 2) region of gp120 facilitates the transition from the "closed" conformation to the "open" conformation, which displaces the V1V2 loops, exposes the V3 loop (variable region 3), and induces conformational change in gp41 [10, 11]. The exposed V3 loop in gp120 interacts with the N-terminal domain of the co-receptor by mimicking native chemokine ligands [12, 13]. Co-receptor interaction with gp120 induces the formation of an exposed coiled-coil domain, called the fusion peptide, at the N-terminus of gp41 which inserts into the target cell membrane to form a pre-hairpin intermediate [14, 15]. Fusion of the viral and target cell membrane ensues, mediated by large gp41 conformational shift in which the separated N- and C-termini fold together into a six-helix bundle, called a hairpin, which packs their hydrophobic termini together and fuses the membranes in the process [16-18]. Upon membrane fusion the capsid core is released into the cytoplasm. It is believed that the capsid cores remain largely intact during transport to the host cell nucleus by attaching to the microtubule motor protein dynein [19-22]. During translocation, the capsid core shields the RTC from cellular immune factors and facilitates initiation of reverse transcription [23-26].

The viral RT (Figure 1.1) catalyzes reverse transcription, wherein viral RNA is reverse transcribed into proviral DNA within the RTC. RT is active as a heterodimer composed of one 66kDa species which includes the C-terminal RNase H domain and a 51kDa species from which the RNase H domain is removed by the PR during particle maturation via site 9 cleavage (Figure 1.1) [27-29]. The heterodimer adopts an overall conformation like a human right hand, wherein the RNA-DNA or DNA-DNA duplex sits in the palm and interacts with the thumb and fingers; the polymerase active site is in the palm domain, while the RNase H active site is spatially separated and lies near the thumb domain [30, 31]. Nucleic acid duplex substrates bind the palm region with the 3' hydroxyl group (3' OH) positioned in the priming site (P site), while incoming deoxynucleotides (dNTPs) bind in the nucleotide site (N site) immediately adjacent to the P site [31]. Together, iterative conformational changes in the thumb and fingers position incoming dNTPs, form the phosphodiester bond, and translocate the substrate to position the newly formed 3' OH group in the active site [32].

Initiation of reverse transcription requires both a template and a primer. The primer for reverse transcription is a Lys3 tRNA, which is incorporated into immature viral particles during virus assembly and binds approximately 180 nucleotides from the 5' end of the genomic RNA at the primer binding site (PBS) (Figure 1.2). Primer binding relies on the nucleocapsid (NC) protein which aids in the partial unfolding of the tRNA primer required for complete primer binding [33, 34]. RT binds the RNA:primer duplex to initiate minus strand synthesis, during which the RNase H domain of RT degrades the RNA template after cDNA synthesis by the polymerase domain [27]. Upon complete extension of the minus strand from the PBS to the 5' end, minus-strand transfer occurs which involves the complimentary binding of the newly synthesized cDNA minus strand with the 3' end of the genomic RNA through the repeat sequences (R, Figure 1.2) present at both the 5' and 3' ends of the genomic RNA; this process is largely dependent on various activities of the viral nucleocapsid (NC) protein [36-38]. The 3' end of the minus strand serves as the new primer for reverse transcription to extend the minus strand and complete minus strand synthesis, which corresponds with RNase H-mediated degradation of the positive strand.

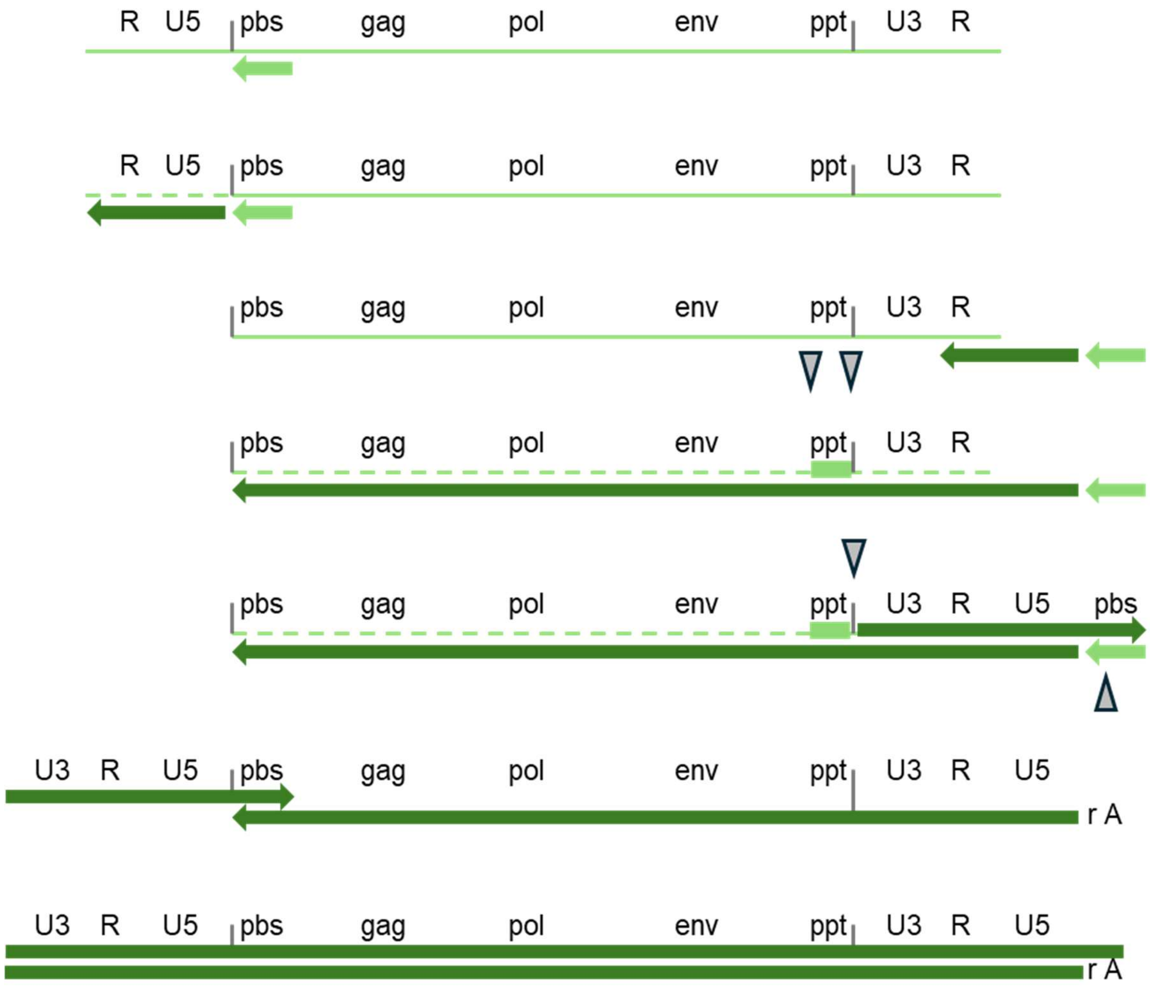

Figure 1.2. Steps in reverse transcription. Light green = RNA; dark green = DNA; dashed lines = RNase H-mediated RNA degradation; triangles indicate locations of specific RNase H cleavage; pbs = primer binding site; ppt = polypurine tract. The location of the gag, pol, and env genes are indicated. Adapted from [35]

The genomic RNA contains a sequence near the 3’ end directly upstream of the U3 sequence called the polypurine tract (PPT), an A-G rich region which is resistant to RNase H degradation; the 3’ end of the PPT left after RNase H degradation of the remaining plus strand therefore serves as the initial primer for plus strand synthesis. RT binds the PPT/minus strand duplex and extends the 3’ end of the PPT after which the RNase H domain selectively cleaves between the PPT primer and extended cDNA sequence [39]. Following selective cleavage, RT extends the 12-mer DNA primer on the plus strand to completion (Figure 1.2). Upon removal of the initial tRNA primer by RNase H, plus-strand transfer occurs in which complimentary PBS sequences on the 3’ ends of each respective strand base-pair with each other (Figure 1.2). Synthesis of the double stranded proviral DNA molecule is completed upon successful elongation of the plus and minus strand by RT, using each of the 3’ ends as primers and the opposite strands as templates. Upon arrival at the nucleus, the capsid core enters the nucleus through the nuclear pore complex and rapidly uncoats near sites of integration upon the completion of reverse transcription [40-43]. Many factors are thought to be involved in shuttling the capsid core through the nuclear pore complex, including cleavage and polyadenylation specificity factor 6 (CPSF6), various nucleoporin proteins (Nup153 and Nup358), and cyclophilin A (CypA) [44-47], however this is an active area under intensive investigation.

After completion of reverse transcription and uncoating, the double stranded proviral DNA is integrated into the host chromosome by IN, which is present within the capsid core and part of RTC. Proteolytic processing of Gag-Pol in the viral particle liberates the mature 32 kDa IN, composed of three distinct domains: the N-terminal domain, the C-terminal domain, and the catalytic core domain (CCD) which contains the active site and bridges the N- and C-terminal domains [48]. HIV-1 IN forms active tetramers, however various studies suggest that HIV-1 IN may also form active octamers [49, 50]. The oligomerized IN, known as the intasome, is the active enzymatic species required for integration [51, 52]. The intasome binds each end of the proviral DNA in two of the four available IN active sites; this complex is known as the pre-integration complex (PIC).

HIV-1 preferentially integrates in transcriptionally active, gene-dense regions of the host genome and also seems to favor integration within gene bodies [53]. The host cleavage and polyadenylation specificity factor 6 (CPSF6) and lens epithelium-derived growth factor (LEDGF) largely drive integration targeting to transcriptionally active genomic regions via interaction with CA and IN, respectively [54-60]. Several other cellular factors in addition to CPSF6 and LEDGF are important for integration targeting via interaction with the viral CA, including nucleoporin (NUP) 153, Nup358, and cyclophilin A (CypA) [61, 62]. Various studies indicate a similar role for Nup153, Nup358, and CypA in integration targeting compared to CPSF6: each protein is involved in integration targeting to gene-dense regions of chromatin with less impact on integration site selection within gene bodies [61, 63, 64]. In addition to the observed integration site preference for sequences within genes in highly active regions of chromatin, integration also appears to occur mainly at the nuclear periphery and preferentially within nuclear speckles, *i.e.* regions of the nucleus rich in pre-mRNA splicing factors [65-68]. A preference for integration in DNA wrapped around nucleosomes has also been demonstrated, as intasome binding favors bent DNA versus linear DNA [69, 70]. Taken together, HIV-1 preferentially integrates into nucleosomal DNA within gene-bodies in gene-rich, transcriptionally active regions of the genome near the nuclear periphery.

The intasome catalyzes two major biochemical reactions: first, the intasome processes each of the 3’ ends of the proviral DNA; second, the intasome catalyzes the strand transfer reaction, wherein the proviral DNA sequence is incorporated into the host cell chromosome. The first reaction removes a dinucleotide pair at each 3’ DNA end to generate a 5’-CA-3’-OH sequence at both ends [71, 72]. Upon DNA end processing, the intasome binds the chromosomal DNA to form the target capture complex (TCC) [73]. The strand transfer reaction, otherwise known as the transesterification reaction, involves nucleophilic attack of the phosphate backbone of host DNA by each 3’ OH [73, 74]. Due to the geometry of the active sites of IN protomers within the intasome, 3’ end joining with host DNA generates a five base-pair gap between each 5’ end of viral DNA and each 3’ end of host DNA [75]. After joining the viral DNA with host DNA, the intasome remains associated with host DNA in a complex called the strand transfer complex (STC). Degradation of the STC, mediated by ubiquitination and proteosome degradation, is required for access and subsequent repair of the 5 base-pair gaps left after integration; both processes are mediated by cellular factors [73, 76-78]. After degradation of the STC, the DNA gaps on each end of the proviral DNA sequence are repaired and ligated by host machinery [79-82].

In general, it is believed that proviral DNA transcription follows integration. Hundreds of transcription factors have been implicated in regulation of provirus transcription and many different pathways have been identified that upregulate, downregulate, or silence viral transcription; transcription is also intimately influenced by the cell cycle, stress response, chromatin structure, and a plethora of cell-signaling pathways. Viral transcription can be segmented into three separate phases: the basal phase, the host phase, and the viral phase [83]. Each phase is defined by the relative level of transcription. In the basal phase, the level of viral transcription is nearly undetectable. The host and viral phases are categorized by either low or high levels of transcription, respectively, wherein the “switch” from host to viral phase is associated with an exponential upregulation of transcription [83]. The 5’ region of the provirus contains many sequence motifs and transcription factor binding sites that regulate the transition between transcriptional phases and contains the major splice donor site (D1) for the first exon that is included in all viral transcripts [84]. The 5’ long terminal repeat (5’ LTR) contains the U3, R, and U5 sequences, followed by a downstream 5’ untranslated region (5’ UTR), then the *gag*

ORF. The U3 region contains the modulatory region, followed by the enhancer region, followed by the core promoter which contains the transcription start site (TSS) at the U3/R junction. The sequence that spans from the TSS through U5 is called the leader region, which ends at the junction between U5 and the 5' UTR [83]. 25 base-pairs upstream of the TSS is the TATA box, required for correct assembly of transcriptional machinery; overlapping with the TSS is the Initiator element, required for proper transcription initiation; and immediately downstream the TSS is a sequence that encodes the *trans*-activation response (TAR) RNA, which is important for transcription elongation. Additionally, two nucleosomes are incorporated in the 5' LTR at precise positions after integration [85, 86]. The upstream nucleosome (Nuc-0) is present at the 5' end of the modulatory region in U3, while the downstream nucleosome (Nuc-1) is present just downstream of the TSS in the leader region and is implicated in the transition from transcription initiation to elongation [87, 88].

Of the many factors associated with transcriptional repression, two major factors dictate the repressive transcriptional landscape in the basal phase: leader-binding protein 1 (LBP-1) binds the TATA box in the core promoter, and a homodimeric nuclear factor kappa-light-chain-enhancer of activated B cells (NF-κB) binds in the enhancer region to facilitate positioning of Nuc-1 downstream of the TSS to curb transcription initiation and elongation [86, 89, 90]. Transition from basal to host phase begins with the recruitment of TATA-binding protein (TBP) to the TATA box, which subsequently recruits RNA polymerase II (Pol II) and various general transcription factors (TFIIA, TFIIB, TFIIF, TFIIE, TFIIH) that associate with Pol II to form the pre-initiation complex [91, 92]. The large, 28-subunit Mediator complex, which serves as a global "mediator" for transcriptional regulation, is also recruited to the transcription start site via high affinity for the unphosphorylated C-terminal domain of Pol II and plays an indispensable role in promoting viral transcription [93-95]. Transcription initiation and promoter escape is facilitated by phosphorylation of the 5th and 7th serine residues in the Pol II C-terminal domain by transcription factor TFIIH [96, 97]. Nuc-1, positioned downstream of the TSS, is destabilized during transcription initiation via acetylation by histone acetyltransferases [98, 99]. Following initiation and promoter escape, Pol II pauses ~20-50 nucleotides downstream of the transcription start site (TSS) which is largely established by the host factors DRB sensitivity inducing factor (DSIF) and negative elongation factor (NELF) [100, 101].

Recruitment of the positive transcription elongation factor b (P-TEFb) complex relieves Pol II pausing by phosphorylation of both the Pol II C-terminal tail and DSIF, which promotes transcriptional elongation during the host phase of viral transcription [102]. The R region in LTR contains the necessary signals for transcription termination and polyadenylation: the polyadenylation hairpin signal, the cleavage site, and a G/U rich downstream element [103]. The transition from the host to viral phase of transcription, which is associated with a drastic increase in viral transcript production, is largely due to interaction between cis-regulatory elements encoded in the 5’ LTR and the viral protein Tat (trans-activator), a 15 kDa protein encoded by the *tat* gene initially produced from transcripts synthesized in the host phase [104-107]. Tat positively regulates viral transcription by binding the trans-activation response (TAR) RNA in the 5’ LTR, which recruits the P-TEFb complex along with other constitutive and inducible transcription factors that promote a significant upregulation in viral transcription [83]. The TAR sequence lies immediately downstream of the TSS, and the nascent TAR RNA forms a complex stem-loop structure after transcription. In the host phase, low levels of viral transcription occur to produce early transcripts. Tat is one of three early gene-products of these viral transcripts; Tat is translocated back to the host nucleus after translation where it binds the TAR RNA stem-loop, recruits transcription factors, and transitions the transcriptional regime from the host phase to the viral phase. Thus, the Tat-TAR interaction acts as a positive feedback loop to promote high levels of viral transcription.

Tat, along with the viral Rev and Nef proteins, are translated from fully spliced mRNA molecules; all other viral proteins are translated from either full length (unspliced) mRNA or from incompletely spliced mRNA. The majority of RNAs transcribed from the integrated provirus remain unspliced [84]. Four splice donor sites (D1-D4) and seven splice acceptor sites (A1-A7) used in combination with each other collectively produce the remaining incompletely and completely spliced RNA molecules. *Tat*, *rev*, and *nef* mRNAs undergo two splicing events, the first of which uses the D1 donor site with a respective acceptor site (depending on the gene) and the second of which uses the D4 donor and A7 acceptor sites [84]. The 20 kDa Rev protein (regulator of expression of virion proteins), the *rev* gene product, facilitates nuclear export of unspliced and incompletely spliced HIV-1 RNA species from the nucleus to the cytoplasm for translation via mechanisms that bypass endogenous regulatory pathways that normally prevent export of incompletely spliced RNA [108-110]. Nef (negative factor), the 30kDa *nef* gene product that is also an early gene product translated from completely spliced viral RNA, increases pathogenesis of infection via downregulation of CD4 as well as major histocompatibility complex 1 (MHC-1) proteins on the cell surface but is not required for replication [111-115]. The Gag and Gag-Pol polyproteins are translated from unspliced, full-length viral mRNA molecules.

The *vif*, *vpr*, *vpu*, and *env* genes are all translated from singly spliced mRNA molecules which use the D1 donor splice site and an acceptor site that includes the respective exon. Briefly, Vif (virion infectivity factor) is a 23 kDa protein that has broad effects on multiple cellular pathways with two well-characterized functions. Vif facilitates the degradation of a host restriction factor, apolipoprotein B mRNA editing enzyme, catalytic polypeptide-like 3G (APOBEC3G), which deaminates cytosine bases in the newly transcribed HIV cDNA and thus increases error rates causing subsequent mutagenesis which disrupts the viral lifecycle [116-118]. Vif has also been shown to induce G2 cell cycle arrest by targeting several phosphatases involved in cell-cycle regulation for degradation [119, 120]. The 14kDa Vpr (viral protein R) interacts with the C-terminal p6 domain of Gag and is thus incorporated into viral particles; Vpr interacts with cellular tRNAs, mediates G2 cell cycle arrest, and targets various cellular restriction factors for degradation via interaction with E3 ubiquitin ligases [121-124].

The sequence between D4 and A7 contains the 350 nucleotide Rev response element (RRE) within the *env* coding region, which is included in all partially spliced or unspliced viral RNAs; the viral Rev protein binds the RRE, oligomerizes, and shuttles the incompletely spliced and unspliced RNAs to the cytoplasm for translation [125]. Taken together, upon proviral integration, low levels of host-mediated transcription produce early viral RNA transcripts. These fully spliced transcripts (encoding *tat*, *rev*, and *nef* genes) are translated into viral proteins, after which both Tat and Rev are imported back to the nucleus. Tat facilitates significant upregulation in viral transcription, while Rev exports incompletely spliced viral RNAs to the cytoplasm for translation. After viral RNA export to the host cytoplasm, either via endogenous or Rev-dependent pathways, the RNA is translated with host translation machinery. All viral proteins are collectively translated from a pool of over 50 viral RNA splice variants, though the usage of each splice variant for translation remains to be determined [126, 127].

Of particular importance to the production of infectious viral particles is the translation of the Gag and Gag-Pol polyproteins from full-length, unspliced viral RNA. Both Gag and Gag-Pol share the same N-terminus; Gag-Pol translation is the result of a regulated -1 ribosomal frameshift near the end of the Gag ORF which is responsible for a conserved Gag:Gag-Pol ratio of 20:1 [128-131]. Frameshifting is facilitated by a “slippery” heptameric sequence of RNA and an RNA stem-loop structure downstream of the slippery sequence [132]. Perturbation of the tightly regulated Gag:Gag-Pol ratio by either overexpression of Gag-Pol or mutation of the slippery sequence that facilitates Gag-Pol translation led to premature PR activity that caused similar defects in viral particle budding and infectivity [133-135]. The dynamics of HIV-1 frameshifting remain to be fully characterized, however it has been shown that subsets of frameshifting RNAs may localize in “frameshifting factories” and that frameshifting likely occurs in bursts [136]. Ongoing work in our lab also aims to investigate frameshifting dynamics (see Chapter 6). Env is translated in the infected cell by ER-associated ribosomes to produce the Env gp160 precursor protein which undergoes glycosylation and forms trimers in the ER [137]. The gp160 trimeric precursors are further glycosylated in the Golgi apparatus, and undergo furin-mediated cleavage to produce the gp41 and gp120 [137-141]. The intact trimers are delivered to the plasma membrane after processing in the Golgi for subsequent incorporation into viral particles [138, 139, 142].

The Gag polyprotein precursor contains matrix (MA), capsid (CA), nucleocapsid (NC), and p6, along with short sp1 and sp2 peptides between CA/NC and NC/p6, respectively. The translational frameshift site is immediately after NC in the *gag* ORF, and thus Gag-Pol contains MA, CA, and NC, in addition to the *pol* gene products p6*, PR, RT, RNase H, and IN. Assembling virus particles package all necessary components required for infectivity, which include both Gag and Gag-Pol, along with two copies of full-length genomic RNA, cellular Lys3 tRNA required for RT priming, the viral Env protein, and Vpr, although Vpr is not required for infectivity [143]. Virus assembly and budding are largely driven by domains within the Gag polyprotein. The MA domain at the N-terminus enhances Gag multimerization and promotes incorporation of Env into viral particles [144-149]. The MA also helps anchor Gag in the inner plasma membrane leaflet via a hydrophobic N-terminal myristoyl post-translational modification [150, 151]. It has been shown that Gag preferentially anchors to regions of the inner plasma membrane rich in sphingomyelin, phosphatidyl serine, phosphatidyl ethanol, and cholesterol, otherwise known as lipid rafts [152, 153]. The CA domain of Gag is also implicated in Gag localization to the plasma membrane via formation of hexameric bundles composed of six CA domains from separate Gag polyproteins, the formation of which involves cellular inositol hexakisphosphate (IP6) as a cofactor [154-158].

NC contains two zinc-finger motifs that bind viral RNA dimers; the NC domain embedded in Gag binds viral RNA for incorporation into viral particles, and the mature 7 kDa NC after proteolytic processing remains associated with viral RNA inside the viral capsid core to protect the RNA and aid in reverse transcription [159-163]. A large portion of the 5' UTR has been implicated in RNA dimerization and packaging, though two 5' UTR sequences are indispensable. Full-length viral RNA dimerization is initiated at the dimer initiation site (DIS) in the 5' UTR that forms a "kissing-loop" structure that mediates dimerization [143]; a downstream packaging signal (Ψ) is then recognized and bound by the Gag-associated NC for packing into virions [164]. NC has also been shown to interact with cellular tRNAs that are incorporated into the virus particle and used for priming of reverse transcription [165-168].

Together, Gag and Gag-Pol localize at the cell membrane in oligomeric complexes, the formation of which are mediated by MA oligomerization, CA-CA interaction and NC:RNA binding. Once localized at the plasma membrane, these oligomeric complexes interact with adjacent oligomers to form the immature Gag lattice, which is largely driven by lateral interactions between the CA-sp1 regions of neighboring Gag molecules and non-sequence specific interaction between NC and viral RNA. Finally, upon formation of the immature Gag lattice at the cell membrane, the C-terminal p6 domain of Gag, otherwise known as the late domain (L-domain), recruits host ESCRT proteins TSG101 and ALIX which initiate ESCRT-mediated viral budding and membrane fission to release immature viral particles [169-172]. The L-domain also binds Vpr and shuttles it into viral particles via direct interaction with p6 [173-175]. Notably, the viral protein Vpu has been implicated in the budding process as it has been shown to facilitate degradation of a host restriction factor, Tetherin, via ubiquitination and proteosome-mediated degradation [176-178]. Tetherin anchors both its N- and C-termini in the plasma membrane of host cells and inhibits viral particle release by tethering budded viral particles to the host cell and to each other [176, 179].

1.3 Viral Particle Maturation and HIV-1 Protease Autoprocessing

The newly released viral particles are immature and non-infectious as Gag and Gag-Pol are still in polyprotein form. Although the detailed mechanism remains unknown, the budding event triggers a highly regulated process called PR autoprocessing [131, 135, 180], in which the PR domain still embedded in Gag-Pol catalyzes autoproteolysis at its own N- and C- termini to liberate the mature PR [143, 181-187]. The free, mature PR is proficient at processing 10 distinct cleavage sites within Gag and Gag-Pol. Using purified mature PR *in vitro*, these sites are processed at rates that vary up to 400-fold [188, 189]. Proteolytic processing results in a drastic rearrangement of the inner viral particle landscape that coincides with a gain of particle infectivity [190]. Because of the indispensable role for viral infectivity, the mature PR is a proven target for the development of antiretroviral (ARV) drugs. There are nine FDA-approved PR inhibitors (PIs) available for clinical use, all of which are non-cleavable substrate analogs that bind the active site with high affinity [191-196].

Although it is well-accepted that PR precursor autoprocessing must be suppressed during Gag and Gag-Pol assembly and then activated upon virion release, the underlying molecular mechanisms responsible for this temporospatial regulation remain largely elusive. Early work showed that premature protease activation (i.e., protease activation before Gag and Gag-Pol assemble into immature virions) in the cytoplasm of transfected cells drastically impaired viral production and subsequent infectivity, indicating that PR precursors must remain inactive until the late stages of viral assembly or the early stages of viral budding [197, 198]. Based on the mature PR structure, it is thought that precursor dimerization is essential for the formation of the active site and is driven by the local concentration of Gag-Pol polyprotein, which increases as Gag and Gag-Pol assemble into viral particles.

In the Gag-Pol polyprotein form, the upstream p6* peptide plays a negative role in precursor autoprocessing by preventing dimerization of the PR domain, as studies using a PR attached to its native N-terminal p6* peptide showed a roughly 100-fold decrease in dimerization kinetics [199-201]. In contrast, the downstream RT is believed to facilitate PR dimerization and activation of precursor autoprocessing as mature RT exist as stable dimers. Recently, it has been shown that some RT inhibitors that induce RT dimerization also lead to activation of proteolytic activity, likely due to the transient formation of PR active sites upon RT dimerization [202-204]. More recently, various studies have shown that HIV PR activity in the cytoplasm of infected cells activates an inflammasome sensor, caspase recruitment domain-containing protein-8 (CARD8), which induces cell death via pyroptosis [205-207]. It has also been shown that treatment of infected cells with non-nucleoside reverse transcriptase inhibitors prematurely activates the PR, likely through inducing RT-mediated dimerization of Gag-Pol in the cytoplasm, which leads to increased CARD8 cleavage by PR [208].

Very recent data using a combination of flow cytometry and FRET has shown that proteolytic activity is detectable within the host cell immediately preceding immature particle budding and becomes highly active within the first few minutes after particle budding [190, 209]. Mutations in the C-terminal p6 region of Gag that delay viral particle budding via disruption of p6-ESCRT interaction have been shown cause premature PR activation [210], however mutations in the matrix (MA) at the N-terminus of Gag/Gag-Pol that disrupt membrane localization and targeting do not prematurely activate the PR [211]. These data together suggest that autoprocessing initiation is likely driven by the local increase in Gag-Pol concentration during assembly and budding that encourages dimerization. The timing of activation must be tightly regulated to ensure that PR is inactive during translation and assembly to avoid major defects in particle budding and infectivity.

Given that a single viral particle contains, on average, 1,500 copies of Gag and 80 copies of Gag-Pol, ~8,000 proteolytic reactions are required for complete particle maturation. The order and rate of Gag and Gag-Pol processing by mature PR is challenging to measure in live virus particles, however many studies using *in vitro* transcription/translation systems have established a relative order of processing. Recombinant mature PR added in *trans* to Gag precursors processes the SP1/NC site first, followed by the MA/CA and SP2/p6 sites, and concludes with processing the CA/SP1 and NC/SP2 sites [188]. When mature PR is added in *trans* to Gag-Pol precursors with mutations inactivating the embedded PR, the SP1/NC site is also processed first, followed by processing at the MA/CA and RH/IN sites followed closely by processing at the RT/RH site. The sites closest to the PR gene, namely NC/p6*, p6*/PR, and PR/RT are collectively processed at the slowest rate with the PR/RT site being the last [212, 213]. Mutations that alter the time of processing or the order in which these sites are cleaved, or that produce incorrect cleavage at individual sites, cause the release of aberrant virions that are significantly less infectious [214-220].

The structure and kinetics of mature PR have been extensively investigated. The mature PR is a 22 kDa aspartyl protease homodimer composed of two identical 99 amino acid subunits, each of which contributes one of the two catalytic aspartic acid residues at position 25 (Figure 1.3) [187]. Two regions at the structural interface regulate mature PR dimerization: the active site and the termini [221]. The first and last four amino acids (the N-terminal and C-terminal amino acids) from each monomer contribute an estimated 75% of the total dimerization energy via the formation of four antiparallel B-sheets that interlock and stabilize the dimer [222, 223]. Studies

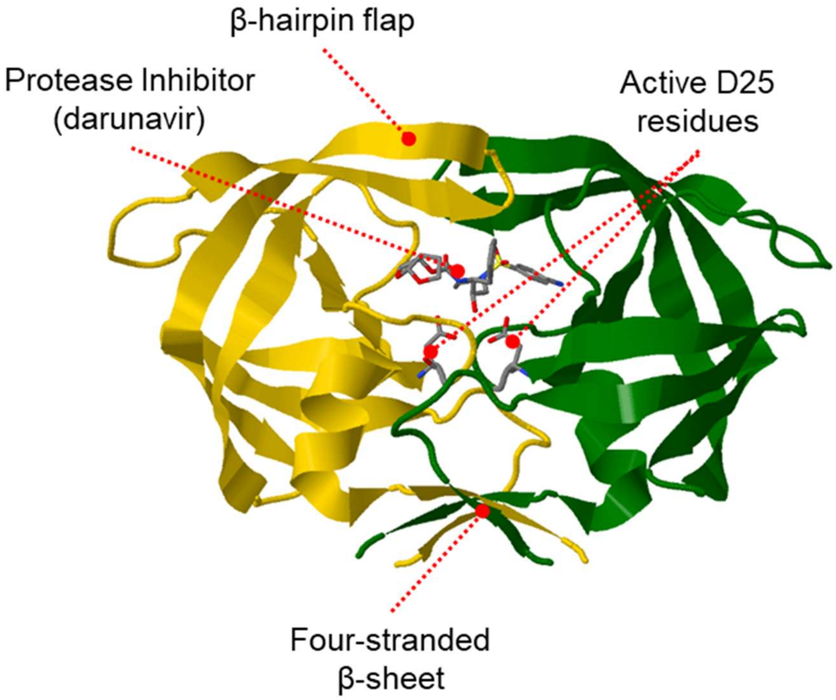

Figure 1.3. Mature PR structure. The two protomers are shown in gold and green.

aiming to investigate the monomeric PR have shown that mutation of residues T26, D29, and R87, all of which are located in the active site interface, results in the formation of stable monomers, indicating the contribution of these residues to stabilize dimer formation [202, 203].

The active site of the mature PR contains two conserved catalytic triads (D25-T26-G27; “fireman’s grip”) contributed by each monomer which facilitate hydrolysis of the substrate via coordination of a nucleophilic water molecule by the two aspartic acid residues at position 25 that attacks the scissile bond of the substrate [224]. Each monomer also contributes two flexible B-hairpin domains (Figure 1.3) that shift between an “open” conformation to allow substrate docking in the active site and a “closed” conformation to stabilize substrate binding in the active site for cleavage [225, 226]. There is no consensus cleavage sequence recognized by the mature PR, as each of the 10 cleavage sites in Gag-Pol are unique in their sequence. However, the mature PR appears to prefer residues N, L, F, Y, or M at the P1 position and slightly favors P but also recognizes L, F, Y, M, or A at the P1’ position [187]. The PR has also been shown to recognize and cleave at least 120 cellular protein targets *in vitro,* highlighting the low sequence-specificity requirements for PR processing [227]. Thus, it has recently been hypothesized that the mature PR recognizes and cleaves substrates based on the shape of the substrate and whether the substrate fits within the three-dimensional “substrate envelope,” a conformation adopted by the mature PR active site [228-230].

In distinct contrast to mature PR, investigations on precursor autoprocessing have been scarce and the underlying regulation mechanisms therefore remain largely undefined. Although it is well accepted that virion maturation catalyzed by mature PR must be temporospatially coupled with protease autoprocessing, it is technically challenging to study these thousands of reactions at a single-virus level or in synchronized fashion to provide sufficient resolution in time and space. Many fundamental questions are only partially addressed by using a combination of model systems. The following summarizes the background information and major findings related to HIV-1 protease precursor regulation, which laid the foundation for this dissertation.

1.4 Definition and expression of PR precursors

Of the two cleavage events necessary to liberate the mature PR, the N-terminal cleavage between p6*/PR corresponds with mature PR-like activity when assessed using recombinant, truncated Gag-Pol fragments containing PR with its native N- and C-terminal extensions [200, 212, 231]. Also, blocking the cleavage site between p6* and PR results in the production of non-infectious particles with defective Gag processing due to the lack of mature PR [232, 233]. In contrast, blocking the C-terminal cleavage site between PR and RT results in detection of a PR-RT fusion enzyme in the released viral particles, which has minor impact (~20-fold) on viral infectivity [234], suggesting that C-terminal fusions are generally well tolerated.

These findings define p6*-PR as a functional miniprecursor [200, 203, 235-238] and identify the cleavage between p6*-PR as a critical step for releasing mature PR, which is required for viral infectivity. Therefore, PR precursor species prior to the removal of p6* are generally considered as precursors. Although these precursors have intrinsic proteolytic activity to varying extents, they are insufficient to mediate particle maturation required for infectivity. Previous studies, using *in vitro* transcription coupled with translation systems to measure the rate and order of Gag-Pol cleavage catalyzed by the embedded PR, indicate that the SP1/NC site appears to be processed first followed by NC/p6* [239-241]. Additional processing by the embedded PR was not observed in this system; however, mutation of the first amino acid in the PR gene (P1A) resulted in processing of the p6*/PR, RT/RH, and RH/IN sites by the embedded PR, indicating that the WT PR in Gag-Pol may be structurally constrained during initial processing events and thus limited to processing at only a few sites [239, 240]. Regardless of the potential structural restraint on the embedded PR, the initial cleavage events at the SP1/NC and NC/p6* are thought to occur via an intramolecular mechanism, wherein the transient PR active site formed by two Gag-Pol polyproteins processes the respective sites in *cis* [241].

To study precursor autoprocessing in mammalian cells, we developed a cell-based assay using fusion precursors with the NL4-3 derived p6*-PR miniprecursor sandwiched between various fusion tags [187, 242-248]. Efficient autoprocessing is measured by the disappearance of the full-length precursor and the appearance of processed products in cell lysates, which are detected via Western blot with tag-specific antibodies. The full-length p6*-PR fusion precursor contains two native cleavage sites: the distal (D) site in the N-terminal region of p6* and the proximal (P) site between p6* and PR. Our previous work demonstrates that these two cleavage sites are processed independently [244, 245], which allows us to specifically study autoprocessing at each site as well as both the p6*-PR fragments and mature PRs released from autoprocessing at each respective site. Processing at the P site releases mature PRs that typically undergo rapid self-degradation and are therefore undetectable. The p6*-PR fragments released from processing at the D site may either undergo an additional autoprocessing reaction to release mature PR or directly undergo self-degradation, however discerning which pathway predominates was not feasible in this system. Regardless, mature PR self-degradation can be suppressed in a dose-dependent manner by PI treatment while p6*-PR fragments also accumulate in the presence of PI [242, 244].

Using this precursor autoprocessing system, we demonstrate that fusion precursor autoprocessing at both the P and D site is much less sensitive to PI than the mature PR, a phenomenon that has also been observed both *in vitro* and in *E. coli* [242, 244, 245, 248-251]. We previously reported estimated IC_{50} values for inhibition of precursor autoprocessing at the D and P sites at ~7500 nM and ~1500 nM DRV, respectively, whereas the estimated IC_{50} value for inhibition of mature PR self-degradation was ~10 nM DRV and the half-maximal detection intensity of the p6*-PR fragment was achieved at ~60 nM DRV [244]. We also expressed the mature PR or p6*-PR by placing the coding sequence downstream of the P2A peptide derived from porcine teschovirus-1[252] to bypass autoprocessing. A side-by-side comparison of PR vs. p6*-PR made by P2A-mediated ribosomal skipping also illustrated differences in PI response. This data together suggests that precursor PRs and mature PRs are distinct in their enzymatic and catalytic properties. This observation therefore highlights the necessity for inhibitor development targeting precursor PRs, as precursor PRs are much less sensitive to PI treatment than the mature PR.

1.5 Precursor catalysis and outcome are flexible and subject to regulation

Recent work from our lab has shown that, in addition to the observed differences in enzymatic properties between precursor and mature PR, the activity and biochemical properties of both precursor and mature PR are also highly context dependent. A 2018 study from our lab established that the propensity for mature PR self-degradation after autocatalytic release from fusion precursors in mammalian cells is dependent upon the upstream fusion tag present in the precursor. Fusion precursors that contain either an N-terminal GST or partially truncated maltose binding protein (MBP) tag that lacks the endogenous N-terminal signal peptide (sigP), commonly used for protein expression in *E. coli* to increase solubility [253, 254], release mature PRs that undergo rapid self-degradation in the absence of PI [242, 244, 245]. However, precursors that contained an MBP tag that included its endogenous N-terminal sigP, responsible for signaling MBP trafficking to the periplasm in *E. coli*, released mature PRs that did not undergo self-degradation and were readily detectable in the absence of PI. This phenotype was conserved when the sigP was added to the N-terminus of GST-containing precursors or when added to the N-terminus of p6*-PR without a bulky fusion tag [245].

Fusion precursors that contain an N-terminal sigP readily undergo precursor autoprocessing [245] and readily process inactive mini-precursor substrates in mammalian cells, discounting any obvious defect in PR activity to explain the large decrease in self-degradation propensity. In the same study our lab showed that virus-associated mature PR does not undergo self-degradation, as the mature PR is detectable in cell-free virus particles via Western blot using a PR-specific antibody. Interestingly, the H69D mutation completely abolishes autoprocessing in both sigP-containing fusion precursors [245] and in virus-like particles [243], yet autoprocessing products are readily detectable in fusion precursors that lack the signal peptide [242, 244]. Confocal microscopy showed that signal peptide-containing fusion precursors were enriched at vesicle-like structures, indicating that the unique phenotype of the mature PRs released from these precursors may be mediated by membranous regions in the cytoplasm [245]; however, further study is needed to provide additional insight into the exact subcellular environment to which the signal peptide drives precursor localization. Nonetheless, these studies indicate that the enzymatic and catalytic properties of the mature PR are flexible and regulated by sequences beyond the PR. Additionally, the similarity in phenotypic traits between virus-associated PRs and sigP-associated PRs highlights the feasibility for use of sigP-containing fusion precursors in mechanistic studies, drug resistance, and drug discovery.

1.6 Rationale for high-throughput screening (HTS) targeting precursor PR

The precursor PR is an exciting target for inhibitor development due to the aforementioned differences in PI sensitivity and context-dependence. No structures of precursor PRs exist and as such efforts to develop precursor protease inhibitors, referred to as autoprocessing inhibitors herein, requires the development of functional assay platforms for high-throughput screening (HTS) efforts. Because of the observed context-dependent effect of N-terminal fusion tags on fusion precursor autoprocessing, specifically the signal peptide derived from the N-terminus of maltose binding protein, our lab developed a platform to screen for novel autoprocessing inhibitors using an assay context that best represents the viral environment. A 2019 paper from our lab established proof-of-concept for autoprocessing inhibitor screening using an amplified luminescent proximity homogeneous assay ELISA (AlphaLISA)-based platform, which measures the autoprocessing efficiency of signal peptide-containing fusion precursors in response to compound treatment. The pilot study screened ~23,000 compounds for autoprocessing inhibition, but was unable to identify a positive hit compound [248]. Encouragingly, this study established AlphaLISA as an extremely sensitive platform for autoprocessing inhibitor screening capable of detecting GST/Flag pairs in the low picomolar range in cell lysate [248, 255].

1.7 Addressing the correlation gap between genotype and phenotype in drug resistance assessment

Random mutations occur frequently in the HIV-1 lifecycle, in large part due to errors during reverse transcription and a lack of subsequent proofreading mechanisms [256]. Mutations that confer resistance to PIs, or resistance-associated mutations (RAMs), are the result of random mutational insertions during replication that decrease PI binding affinity while simultaneously supporting sufficient proteolytic activity to enhance replication and fitness [257]. RAMs can be loosely categorized into two groups: primary and secondary mutations [258, 259]. Primary mutations involve mutations at residues directly involved in substrate binding or those present in the active site (residues 25-32, 47-53, and 80-84), while secondary mutations occur in regions removed from the active site and often compensate for decreased proteolytic activity caused by primary mutations [260]. Both genotypic and phenotypic approaches are currently in use to investigate PI resistance. Genotypic approaches, wherein patient-derived strains are isolated and sequenced to identify mutations associated with resistance, are advantageous to detect

RAMs present at levels below the detection limit of phenotypic tests and also to detect mutations that do not cause resistance themselves but are associated with the acquirement of additional RAMs [261]. The accuracy of genotypic analysis is inherently limited by both the number and specific combination of RAMs present in the PR gene due to the increasingly complex effect of RAMs as they accumulate. Phenotypic investigation directly assess PI response of specific mutations and therefore is not limited by the number or combination of RAMs present in a given mutant. However, many phenotypic assays are limited in resolution and display poor correlation to cART prognosis. For example, our lab previously investigated the resistance profile of a PR double mutant with mutations at V77 and V82, originally isolated from a patient experiencing clinical indinavir (IDV) resistance [262]. A very subtle decrease in sensitivity to indinavir (IDV) was observed in the mutant versus WT as measured by fusion precursor autoprocessing efficiency, however the small difference does not recapitulate the clinical resistance phenotype [244]. Additionally, the currently available PhenoSense® assay, which measures PI resistance in live virus, lacks the sensitivity to reliably detect resistance conferred by single point mutations. We therefore hypothesized, because mature PRs liberated from signal peptide-containing fusion precursors harbor phenotypes consistent with viral particle-associated PRs, that these fusion precursors may offer a more complete, reproducible assay context for drug resistance assessment with enhanced reproducibility and faithful recapitulation of clinically observed resistance phenotypes.

1.8 Thesis outline

Chapter 2 of this thesis investigates the context-dependent nature of the autoprocessing reaction as it relates to drug resistance assessment using a PR double mutant, V77I/V82T, as a model. This double mutant was derived from a patient experiencing resistance to ARV regimen containing indinavir, an HIV-1 PI, but was unable to reproduce the drug resistance phenotype by other in vitro assessment assays. To address this technical gap, we developed a highly sensitive infectivity assay to measure the complex relationship among drug concentration, viral load, and infectivity in both WT virus and V77I/V82T-containing virus. This assay also enabled precise mapping of the contribution of individual mutations to the development of drug resistance. Chapter 3 of this thesis continues to validate our novel infectivity assay for drug resistance assessment by analyzing a panel of 13 multi-PI resistant mutant virus strains isolated from patients. Comparison of our results to previously reported PhenoSense® data confirmed improved sensitivity of our assay and offered additional insights into precision medicine for managing drug resistance. Chapter 4 summarizes our recent HTS campaign against 320,000 small-molecule compounds, subsequent characterizations of positive hit compounds, and initial structure-activity relationship analysis using our infectivity assay. Chapter 5 describes another HTS of natural-product-extracts (NPEs) and subsequent characterization of positive NPEs once again utilizing our infectivity assay.

CHAPTER 2:

CATALYTIC FLEXIBILITY OF HIV-1 MATURE PROTEASE AND ITS PRECURSORS REVEALED BY VARIATIONS IN PROTEASE INHIBITOR SUSCEPTIBILITY ACROSS DIVERSE CELL-BASED ASSAYS

2.1 Introduction

Human immunodeficiency virus (HIV) protease (PR) is a virally encoded enzyme initially synthesized as part of the Gag-Pol polyprotein precursor in infected cells. It is flanked by reverse transcriptase (RT) at its C-terminus and the p6* peptide, also known as the transframe region (TFR), at its N-terminus. The TFR overlaps with the p6 domain in the Gag reading frame [235, 263-265]. The Gag-Pol polyprotein co-assembles with Gag and the viral RNA genome to form viral particles, which bud from the host cell with the aid of the host's ESCRT machinery [143, 266, 267]. Following viral budding, the Gag-Pol precursor undergoes a tightly regulated process of protease autoprocessing, liberating the free mature PR [187, 219, 239, 241]. Mature PR functions as a homodimer with a catalytic site formed at the dimer interface and a dissociation constant (K_d) of less than 5 nM [200, 236, 265, 268, 269]. It cleaves at least ten sites within the Gag and Gag-Pol polyproteins, which exhibit low sequence homology [213, 270, 271]. Proteolysis of these sites induces significant morphological changes, resulting in a gain of viral infectivity [133, 143, 198, 213-216, 218, 239, 272-274]. Due to its essential role in viral infectivity, mature PR is a validated target for antiretroviral drug development. Currently, ten FDA-approved protease inhibitors (PIs) are available, all non-cleavable substrate analogs, bind the catalytic site of mature PR with high affinity [187, 259, 275-279]. Combination antiretroviral therapy (cART), which targets multiple viral components essential for HIV replication, has been highly effective in controlling viral replication. However, the emergence of drug-resistant strains compromises its overall efficacy [259, 280-285].

HIV drug resistance (DR) primarily arises from mutations in target proteins, such as PR, that reduce inhibitor binding affinity while maintaining enzymatic activity for natural substrates. Many primary mutations impair inhibitor binding but often reduce substrate affinity, impacting viral fitness. Therefore, compensatory secondary mutations outside the active site are needed to restore catalytic activity [286-288]. Extensive sequencing of target genes from patients with DR has identified numerous resistance-associated mutations (RAMs), implicating diverse mechanisms in DR development. For example, PI RAMs have been associated with over half of the 99 amino acids in HIV-1 mature PR [257, 289]. Moreover, not all mutations contribute equally to DR. Genotypic analyses of RAMs have been inconsistent in predicting cART efficacy, highlighting the need for more reliable methods to assess DR and guide regimen selection. Studies of PR precursor autoprocessing remain limited. Previous reports from our group and others have shown that PR precursors, such as p6*-PR model mini-precursor, exhibit distinct enzymatic properties compared to mature PRs, including increased resistance to PI inhibition [238, 241, 244, 247, 249, 290]. These precursors are also flexible in catalysis, modulated by alterations within or beyond the coding region, resulting in mature PRs with distinct properties, such as self-degradation prone *vs.* resistant [245, 246, 248]. RAMs outside drug target genes have been implicated in DR [246, 262, 272, 291-293], suggesting additional layers of complexity. Thus, more sensitive and reliable tools are needed to assess DR and optimize salvage cART regimen.

In this study, we characterized a PR double mutant (V77I/V82T) to elucidate its impact on DR using various assays. This mutant, identified in a patient with IDV resistance, showed varying susceptibilities to IDV across these assays, consistent with previous reports [262, 294-296]. While V82T is a well-established primary mutation associated with resistance to tipranavir [297] and IDV [298], it is generally considered insufficient alone to confer resistance, as not all patients harboring this mutation experience resistance to IDV-based cART. V77I is typically regarded as a polymorphic variation; however, our previous work demonstrated its intricate interplay with residue 93 in regulating precursor autoprocessing catalysis [247]. Here, we show that this double mutation displays different resistance profiles, highlighting the complex catalytic flexibility of both mature PR and its precursors depending on the assay context. Using a newly established infectivity assay, we successfully replicated the reported IDV resistance associated with this double mutation under laboratory conditions, underscoring the multifaceted determinants of DR outcomes. Furthermore, we delineated the individual contributions of these point mutations in modulating PI susceptibility, providing valuable insights into the underlying DR mechanisms.

2.2 Materials and Methods

DNA mutagenesis

All plasmids used in this report were constructed using standard PCR-mediated mutagenesis and cloning procedures, as previously described [238, 242-245, 248]. The H2B reporter proviral construct was engineered from a pNL4-3 reporter expressing human placental alkaline phosphatase in the place of Nef (a kind gift from Dr. Ned R. Landau) [299]. In brief, an H2B-mRFP coding sequence inserted in-frame right after the third codon of Nef, followed by a stop codon upstream of the unique XhoI site in the Nef sequence. Consequently, no expression of Nef is anticipated and only H2B-mRFP is expressed upon productive infection. Additionally, the PciI-to-PciI fragment (1.4 kb) covering the entire Vpu and the N-terminal half of Env in the parental NL4-3 was deleted and replaced with an 8-nt linker containing a BssHII site. This modification ensures that neither Vpu nor functional Env is produced by this reporter. Each construct was verified by sequencing analysis and is available upon request via a standard material transfer agreement.

Cell culture and transfection

HEK 293T cells (ATCC cat# CRL-1126) were maintained in DMEM medium containing 10% fetal bovine serum, 100 units/mL of penicillin G sodium salt and 100 µg/mL of streptomycin sulfate. Transfection of HEK 293T cells by calcium phosphate was conducted as previously described [238, 242-245, 248]. To express fusion precursors, HEK 293T cells were seeded in a 24-well plate the day before transfection to achieve ~30% confluence at the time of transfection. Chloroquine was added to each well to a final concentration of 25 µM. A total of 0.25 µg of plasmid DNA in 32.85 µL H_20 was mixed with 4.65 µL of 2 M CaCl2, followed by the addition of 37.5 µL of 2x HBS (50 mM Hepes, 10 mM KCl, 12 mM Dextrose, 280 mM NaCl, and 1.5 mM Na_2HPO_4, pH 7.04 - 7.05) dropwise. This mixture was then added to the 293T cells. After 7-11 hours of incubation, the culture medium was replaced with chloroquine-free medium, and PR inhibitors were added at the indicated concentrations as needed. Approximately 30 hours after transfection, the culture medium was aspirated, and the cells were in situ lysed in 50 µL of pre-chilled lysis buffer (20 mM Tris-HCl, 150 mM NaCl, 1% sodium deoxycholate, 1% Triton X-100, pH 8.0, with a protease inhibitor cocktail). Under these conditions, the cellular chromosomes formed viscous and filamentous aggregates that were removed with a pipette tip. The remaining post-nuclear lysate was then collected for SDS-PAGE or stored at -20°C.

SDS-PAGE and Western Blotting

Equal volumes (10 µL) of post-nuclear lysates were resolved using 8-16% gradient SDS-PAGE followed by protein transfer to PVDF membranes (MilliporeSigma, cat# IPVH 00010). The membranes were blocked with 2% casein blocking buffer (2% casein (w/v) in PBS, 2 mM NaN_3, 0.04% Tween-20, pH ~7.0) for one hour at room temperature before probing with primary antibodies (rabbit anti-GST (Rockland, cat# 600-401-B86), mouse anti-GAPDH (Millipore, cat# MAB374), mouse anti-HA (Sigma, cat#H9658), mouse anti-flag (Sigma, cat#F1804)) for ~12 hours at 4˚C. Secondary antibodies used were either IR800 fluorescence labeled goat anti-mouse (LI-COR, cat# 926-32210) or IR700 fluorescence labeled goat anti-rabbit (Rockland, cat# 611-130-122), depending on the primary antibody. Visualization was performed with an Odyssey CLx Infrared Imaging System (LI-COR Biotechnology, Lincoln, Nebraska). Individual band intensity was measured using Image Studio Software (LI-COR Biotechnology, Lincoln, Nebraska). HA- and Flag- reactive bands detecting the mature PR were normalized to the GAPDH-reactive band intensity in each respective lane. GST- and Flag- reactive bands detecting either full-length precursors or N-terminal autoprocessing fragments were used to determine precursor autoprocessing efficiency.

Generation of Single-round Infectious Virus Particles

HEK 293T cells were maintained in DMEM medium containing 10% fetal bovine serum, 100 units/mL of penicillin G sodium salt and 100 µg/mL of streptomycin sulfate. Specific PR mutations were introduced into the reporter using standard PCR-mediated mutagenesis. A plasmid encoding vesicular stomatitis virus-glycoprotein (VSV-G) was used for Env pseudo typing. HEK 293T cells were co-transfected with the reporter and VSV-G plasmid using calcium phosphate as previously described [238, 242-245, 248], with specific deviations noted below. Briefly, HEK 293T cells were seeded in 10 cm plates. A total of 6.5 µg of plasmid DNA (5.5 µg of the viral reporter plasmid plus 1 µg of the VSV-G plasmid per plate) in 788.4 µL of H_20 was mixed with 111.6 µL of 2 M CaCl2, followed by dropwise addition of 900 µL of 2x HBS. The solution was then added to the plates with HEK 293T cells. After 7-9 hours of incubation, the culture medium was replaced with 8.5 mL of chloroquine-free medium containing PR inhibitors at the indicated concentrations. Approximately 50 hours after transfection, the culture medium containing viral particles was collected from each 10 cm plate and clarified through 0.45µM PES syringe filters (Cytiva Whatman Uniflo Syringe Filter, 9915-2504). The clarified supernatant was divided into five aliquots: three containing 1.8 mL and two containing 0.45 mL. One 0.45mL aliquot was frozen at -20˚C for p24 ELISA analysis, while the others were pelleted at 20,800 × g for 100 minutes through a 25% (w/v in phosphate-buffered saline (PBS)) sucrose cushion. The pelleted viruses from the other 0.45 mL aliquot were resuspended in 60 µL of 1.5x SDS loading buffer and subjected to SDS-PAGE analysis followed by Western blotting. For infection, one aliquot of pelleted particles from 1.8 mL of culture supernatant was resuspended in 12 µL of DMEM overnight at 4˚C.

Infection and Quantification by Fluorescence Microscopy

U2OS (ATCC HTB-96) cells were cultured in DMEM medium supplemented with 10% fetal bovine serum, 100 units/mL penicillin G sodium salt and 100 µg/mL streptomycin sulfate. Cells were seeded at ~25% confluency for infection. Pelleted virus particles were resuspended by brief vortexing and mixed with 175 µL of U2OS cell suspension before plating. The virus + cell suspension mixtures were subjected to 7-fold serial dilutions (*i.e.*, 25 µL of the virus + cell suspension added to 150 µL of cell suspension), creating a total of six dilutions, covering a 16,800-fold range of viral input for each virus preparation. Equal volumes of mixtures (150 µL) were added to a Greiner 96-well glass-bottom plate (VWR, cat# 82050-792) for plating and infection. About 50 hours post-infection, Hoechst stain (ThermoFisher, cat# H3570) at 0.2 µg/mL was added to each well and incubated for 30 minutes at 37˚C. Live cell imaging was then performed at 37˚C with 5% CO_2 using a Keyence fluorescence microscope (BZ-X710, Keyence Corporation of America, Itasca, Illinois) with a 20x objective, capturing images in both DAPI and RFP channels. An automated 5x3 stitching program ensured that >1000 cells were captured in most samples. The DAPI and RFP images were stitched together using BZ-X Analyzer software before quantification. ImageJ software, with a custom batch analysis macro, was used to count blue nuclei (total cells) and red nuclei (infected cells). In brief, images were converted to 8-bit greyscale, thresholded to differentiate positive signals from noise, and processed with the “Fill Holes” and “Watershed” functions to enhance nucleus masking and separated clustered nuclei. The "Analyze Particles" function, with defined size (300 - 9000 pixel units) and circularity (0.1-

1.0) parameters, was applied. Nuclear counts were verified across different threshold values for accuracy, and manual counting was conducted when variations in fluorescence intensity or cell overcrowding caused significant fluctuations in nuclear counts.

Quantification of Viral Particles by Western Blotting

Viral lysates were resolved by SDS-PAGE and transferred to a PVDF membrane (MilliporeSigma, cat# IPVH 00010). Mouse monoclonal (183-H12-5C) anti-p24 (BEI Resources, cat# ARP-3537) and rabbit polyclonal anti-17 (BEI Resources, cat# ARP-4105) were used as primary antibodies. Secondary antibodies included IR700 fluorescence-labeled goat anti-rabbit (Rockland, cat# 611-132-003) and IR800 goat anti-mouse (Rockland, cat# 610-132-121). Blots were visualized using an Odyssey infrared dual laser scanning unit (LI-COR Biotechnology, Lincoln, Nebraska). The intensity sum of all p24-reactive bands was calculated to determine the total p24 content for each viral sample, using ImageStudio quantification software. We experimentally determined adequate amounts of viral lysates (~ 2-8 μL for each sample) to ensure p24-reactive signals in the linear response range. The total p24 content of untreated wild-type virus was set as 100, and each sample's p24 content was calculated relative to this reference.

Quantification of Viral Particles by p24 ELISA

The ZeptoMetrix RETROtek HIV-1 p24 Antigen ELISA 2.0 kit (catalog #: 0801002) was used to quantify p24 content. Five p24 standards with concentrations ranging from 5 pg/mL to 100 pg/mL were prepared. A total of 200 µL of each standard and 200 µL of serially diluted culture medium (ranging from 20,000- to 2,500,000-fold dilution) were added to the p24-coated microplate and incubated at 37˚C for 90 minutes. After aspiration and washing, 100 µL of p24 detection antibody was added to each well and incubated for one hour at 37˚C. Following another round of wash, 100 µL of HRP substrate was added, and incubated at room temperature for 30 minutes before being stopped with 100 µL Stop Solution. Optical density was measured at 450 nm using a BioTek Synergy H4 Hybrid Microplate reader (Agilent Technologies, Santa Clara, California).

2.3 Results

PI susceptibility analyzed in the context of GST-fused precursor

We previously utilized GST-fused mini-precursors expressed in transiently transfected mammalian cells to examine precursor autoprocessing and its response to PI treatment [238, 242-244]. Here, we investigated whether this assay could also evaluate drug susceptibility or resistance. As illustrated in Figure 2.1A, the fusion precursor consists of the M1-PR precursor (comprising the p6*-PR mini-precursor with a 9-amino-acid truncation at the N-terminus of p6*) with the native cleavage site at the N-terminus of PR (black arrow, Figure 2.1A). The precursor is flanked by GST-Flag at the N-terminus and an HA epitope at the C-terminus. Upon expression, the precursor undergoes autoproteolysis, releasing GST-Flag-M1 and PR-HA. In the absence of any PI, the PR-HA product subsequently self-degrades, consistent with previous observations of recombinant mature PRs purified from *E. coli* [236, 300] and other fusion precursors [238, 242, 244, 301]. This assay allows simultaneous analysis of precursor autoprocessing and mature PR self-degradation in response to PI treatment.

In this context, both the WT and mutant fusion precursors autoprocessed in the absence of PIs (Fig. 2.1B, lanes 1 and 15), as indicated by the detection of GST-Flag-M1 with minimal full-length (FL) unprocessed precursor. PI treatment suppressed autoprocessing, resulting in increased detection of FL precursors in a concentration-dependent manner. By plotting the band intensity of GST-Flag-M1 relative to the total Flag-reactive proteins (GST-Flag-M1 + FL precursor) as a function of PI concentration, we determined the apparent EC_{50} values for

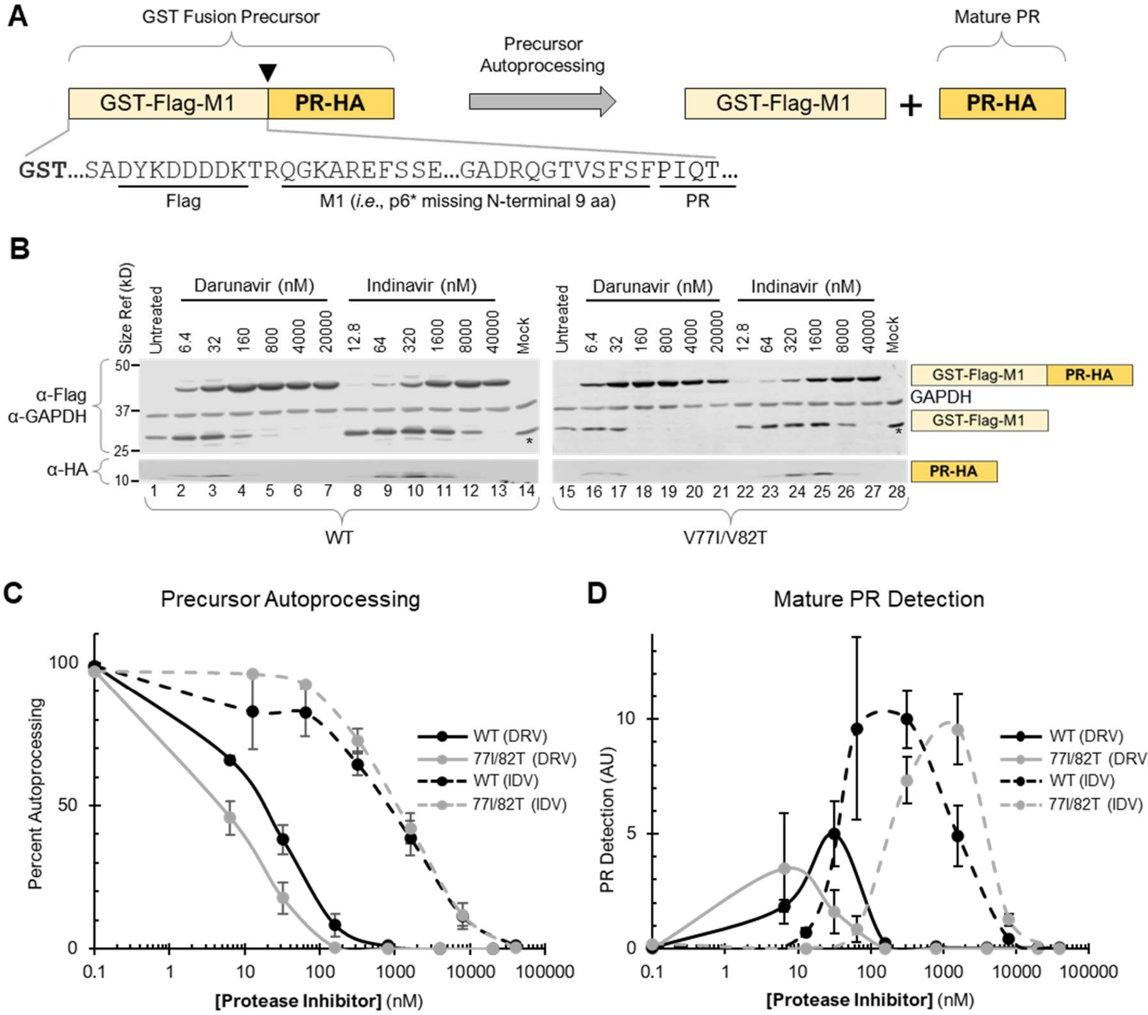

Figure 2.1. Drug susceptibility in the context of GST-fused precursor. **A**. Schematic of the GST-fused M1-PR precursor and its autoprocessing. **B.** Representative Western blotting results. Cell lysates were collected 30 hrs post-transfection, resolved by 8-16% gradient SDS-PAGE, and transferred to a PVDF membrane. The blot was divided into two sections based on size. The upper section (25 kDa to 55 kDa) was probed sequentially with GAPDH and Flag antibodies; the lower section was probed with HA antibody for detection of PR-HA (~ 10 kDa). A trace amount (~ 3% of total DNA) of a GFP-Flag encoding plasmid was included in the mock transfection to monitor transfection efficiency, and GFP expression was detected by Flag antibody (lanes 14 and 28, indicated by an asterisk). **C.** Precursor autoprocessing in response to PI treatment. The ratio of GST-Flag-M1 intensity to the total Flag-reactive fragments (GST-Flag-M1+FL) was determined to represent precursor autoprocessing efficiency. **D.** Detection of the released PR-HA in response to PI treatment. The intensity of the PR-HA band, normalized to the GAPDH signal in the same lane, was plotted against PI concentration. Standard deviation bars represent three technical replicates. The image shown is a representative of six experimental repeats.

precursor autoprocessing (Fig. 2.1C). Our data confirmed that DRV is a more potent inhibitor than IDV, as evidenced by a leftward shift and lower EC_{50} values for DRV (solid lines) compared to IDV (dashed lines). Additionally, the 77I/82T mutation minimally affected IDV susceptibility in precursor autoprocessing compared to the WT (grey vs. black dashed lines), while slightly increasing sensitivity to DRV (grey vs. black solid lines). The liberated mature PR-HA exhibited a bell-shaped detection profile in response to PI treatment (Fig. 2.1D), collectively determined by catalytic kinetics of precursor autoprocessing for mature PR release and subsequent self-degradation of mature PR. Notably, higher PI concentrations were required to suppress precursor autoprocessing than to inhibit mature PR self-degradation, consistent with previous reports [238, 242, 244, 245]. In the absence of PIs, mature PR was undetectable due to self-degradation (Fig. 2.1B, lane 1). At PI concentrations sufficient to suppress self-degradation without significantly inhibiting precursor autoprocessing, PR-HA detection increased (left side of the bell curve, in Fig. 2.1D). Further increases in PI concentration inhibited precursor autoprocessing, reducing PR production and detection (right side of the bell curve, in Fig. 2.1D). Thus, the left side of the bell curve serves as a proxy for estimating the EC_{50} of PR self-degradation. Our data showed that the self-degradation EC_{50} values for the WT and mutant PRs in response to IDV were approximately 40 nM and 200 nM, respectively, indicating a ~ 5-fold increase in resistance conferred by the mutation (grey dashed line for IDV rightward shifted compared to black dashed line for the WT, in Fig. 2.1D). Conversely, the mutant displayed slightly increased sensitivity to DRV treatment (a leftward shift of solid grey line). Collectively, these findings indicate that when examined in the context of GST-fused precursor, the double mutation exhibits diverse effects on different biochemical reactions in a PI-specific manner. While conferring IDV resistance in PR self-degradation, it minimally influences precursor autoprocessing and increases sensitivity to DRV in both reactions. These results support the notion that precursor and mature PRs are enzymatically distinct, and RAMs can differentially modulate these reactions as well.

PI susceptibilities of mature PRs expressed via P2A peptide, bypassing precursor autoprocessing

We next developed a platform to directly study mature PRs, bypassing the prerequisite autoprocessing reaction. As shown in Figure 2.2A, the PR-HA coding sequence was placed downstream of the P2A peptide (derived from porcine teschovirus-1) [252, 302]. This peptide inhibits peptidyl transferase activity in the ribosome, effectively "skipping" the formation of a peptide bond between Gly and Pro, the last two residues of the P2A peptide. Consequently, two separate proteins are produced from a single polycistronic mRNA: the upstream protein ends with the 2A peptide, and the downstream protein begins with the Pro residue, corresponding to the P1' residue of HIV-1 mature PRs. Effective ribosomal skipping was confirmed by the detection of the upstream protein, MBP-Flag-P2A (Fig. 2.2B), although sporadic readthrough translation produced the full-length protein.

Mature PRs generated via P2A-mediated ribosomal skipping also showed a high propensity for self-degradation, rendering them undetectable in the absence of PIs (Fig. 2.2B, lanes 1 and 15). PI treatment induced a concentration-dependent accumulation of PR (Fig. 2.2B, HA blot), allowing for the determination of self-degradation EC_{50} values in this assay context (Fig. 2.2C). The double mutant caused a ~ 5-fold rightward shift in IDV susceptibility, suggesting increased resistance. Interestingly, this IDV resistance in PR self-degradation correlated well with the results observed in the GST-fused precursor assay, despite the higher absolute EC_{50} in the P2A platform. As in the previous assay, the mutation slightly increased sensitivity to DRV when assessed using the P2A platform.

Drug susceptibility analysis in the context of fusion precursors containing a signal peptide at the N-terminus

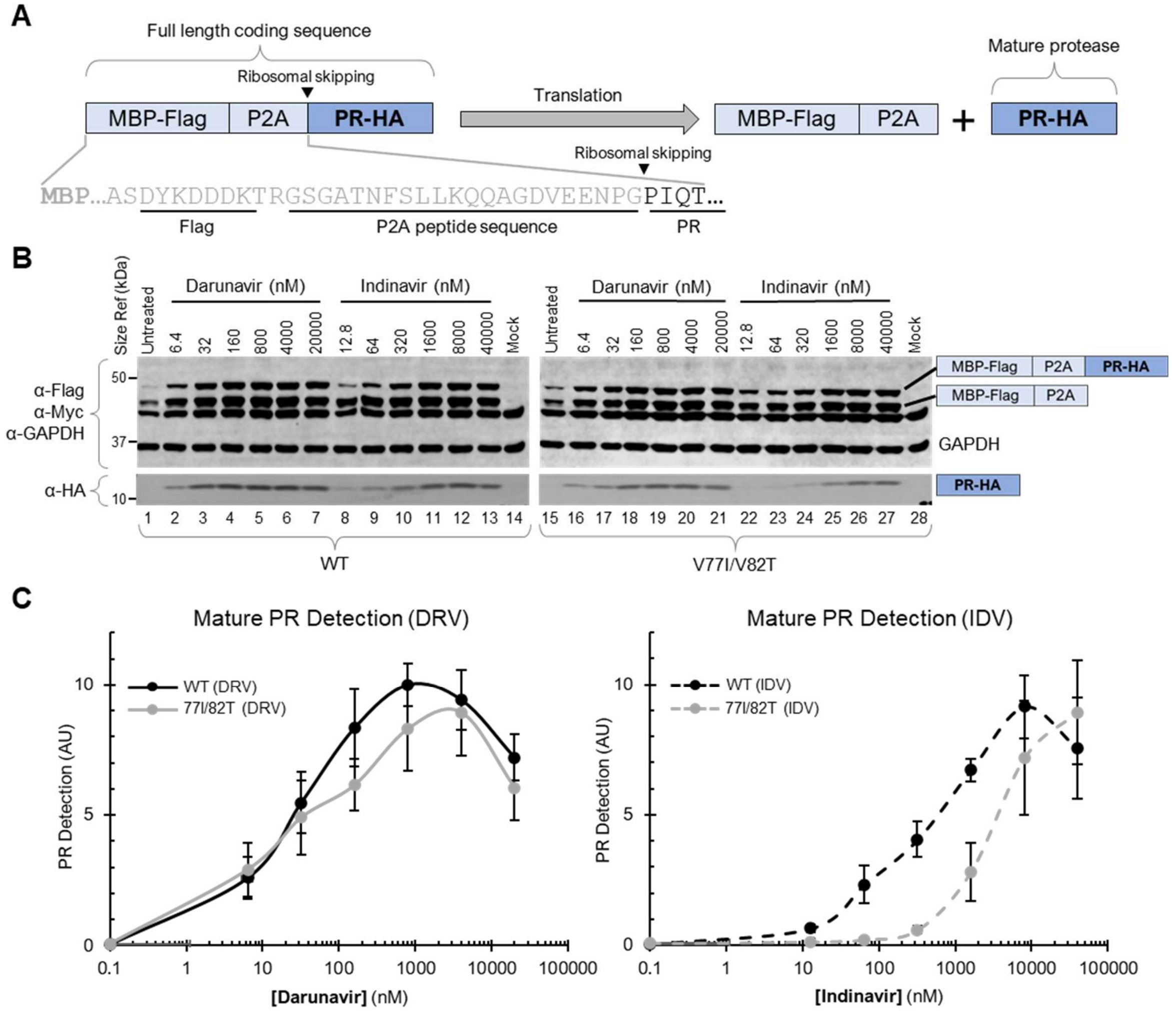

Figure 2.2. Drug susceptibility of mature PRs expressed via the P2A ribosomal skipping peptide. A. Schematic of the P2A construct and the anticipated proteins produced. **B.** Representative Western blot results. Cell lysates collected at 30 hrs post-transfection were resolved by 8-16% gradient SDS-PAGE and transferred onto a PVDF membrane. The blot was divided into two sections based on size. The upper section (25 kDa to 55 kDa) was probed with GAPDH and Flag antibodies, while the lower section was probed with HA antibody. **C.** Quantification of PR-HA detection in response to IDV and DRV treatment. The band intensity of PR-HA normalized to the GAPDH signal was plotted against PI concentration. Standard deviation bars represent three technical replicates, with the image shown as a representative of three experimental repeats.

We previously reported that a 26 aa signal peptide (SigP), derived from the N-terminus of maltose binding protein (MBP), modulates fusion precursor catalysis, enabling the released mature PRs to resist self-degradation [245, 246]. This signal peptide facilitates transmembrane translocation of MBP to the periplasm in *E. coli* [303, 304], but its role in transfected mammalian cells remains incompletely characterized. Our earlier work demonstrated that SigP-containing precursors are targeted to membranous structures in transfected HeLa cells, suggesting that the subcellular environment near membranes may influence precursor catalysis and promote the generation of degradation-resistant mature PRs [245]. Notably, mutation H69D in the PR sequence completely abolished precursor autoprocessing in this context, which was observed exclusively in assays using proviral constructs, while in other assay platforms, it remained partially active [245, 246].

To further investigate PI susceptibility in this unique assay context, we employed an expression vector containing the GST-fused M1-PR precursor with the SigP at the N-terminus (Figure 2.3A, left). The resulting precursors exhibited reduced autoprocessing efficiency, as indicated by the presence of the FL precursor even in the absence of any PI. However, they still autoprocessed to liberate SigP-GST-M1 and PR-Flag products (Fig. 2.3B, lanes 1 & 15). We quantified precursor autoprocessing efficiency by calculating the ratio of SigP-GST-M1 band intensity to the sum of SigP-GST-M1 and FL precursor. Our results showed that the 77I82T mutation conferred IDV resistance (indicated by a right-shift of grey vs. black dashed lines) and increased DRV susceptibility (a left-shift of grey vs. black solid lines) during precursor autoprocessing (Fig. 2.3C). To the best of our knowledge, this is the first experimental data showing altered PI susceptibility for precursor autoprocessing. Notably, the mature PRs released in this context exhibited reduced self-degradation, and their detection profiles mirrored the precursor autoprocessing response (Fig. 2.3D), with no additional resistance observed.

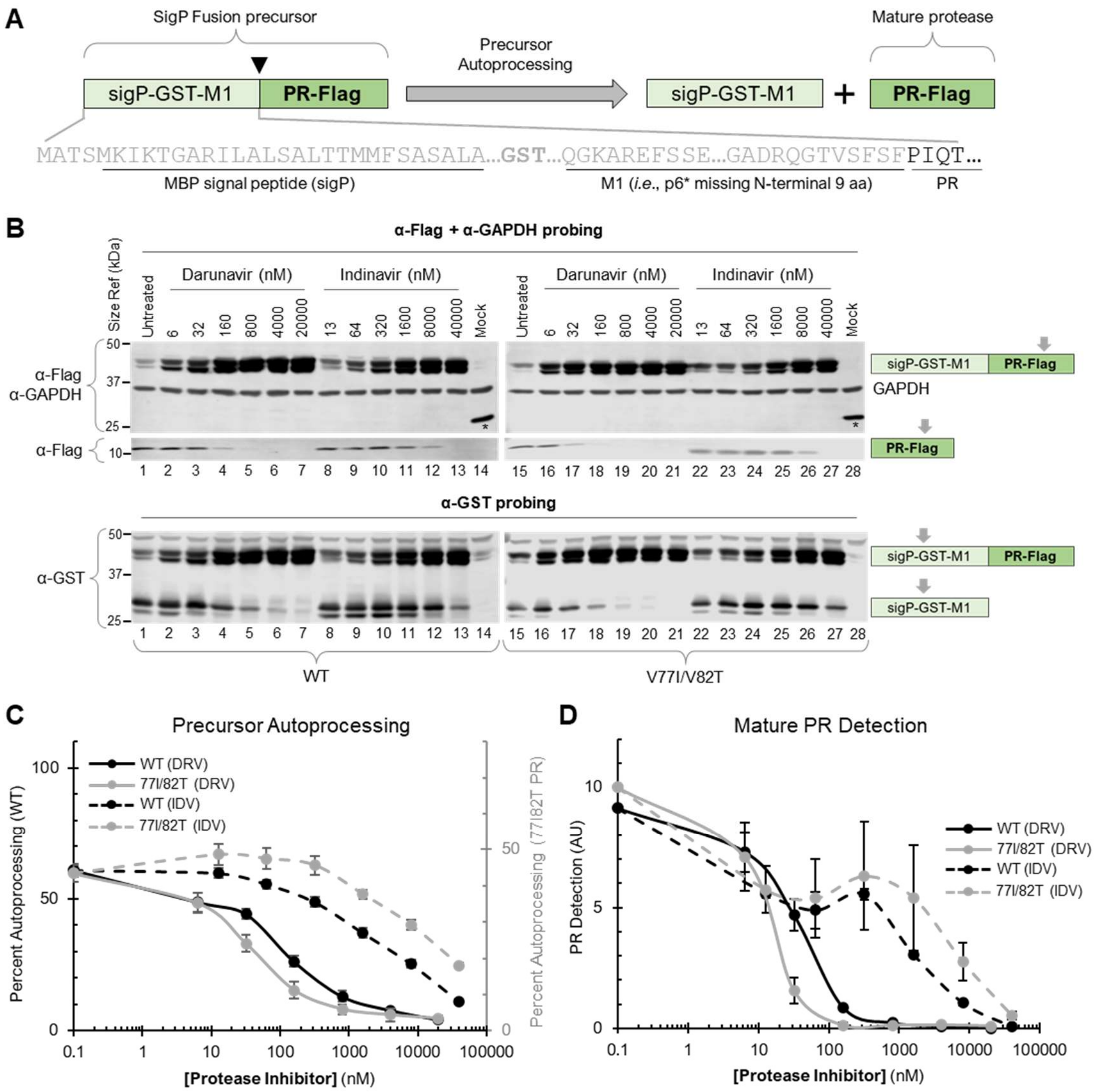

Figure 2.3. Drug susceptibility in the context of precursors carrying a signal peptide at the N-terminus. A. Schematic of the model fusion precursor and the anticipated autoprocessing reaction. **B.** Representative Western blot results. Cell lysates collected 30 hrs post-transfection were resolved by 8-16% gradient SDS-PAGE and transferred to a PVDF membrane. The blot was divided into two sections based on size. The upper section (25 kDa to 55 kDa) was probed with GAPDH, GST, and Flag antibodies. GAPDH and Flag signals were imaged in the 800 nm channel, while GST signals were imaged in the 700 nm channel. The lower section was probed with Flag antibody to detect mature PR (~ 10 kDa). A trace amount (~3% of total DNA) of a GFP-Flag encoding plasmid was included in the mock transfection to monitor transfection efficiency, and GFP expression was detected by Flag antibody (lanes 14 and 28, indicated by an asterisk). **C&D.** Quantification of precursor autoprocessing and mature PR detection in response to PI treatment. Autoprocessing efficiency was calculated by the ratio of GST-Flag-M1 intensity to the total GST-reactive fragments (GST-Flag-M1 + FL). The intensity of PR-Flag normalized to the GAPDH signal in the same lane was plotted against PI concentration. Standard deviation bars represent three technical replicates, with the image shown as a representative of five experimental repeats.

Drug resistance assessment using an infectivity assay with improved sensitivity

Variations in PI susceptibility observed across different model assays, including our own, are not entirely unexpected. Each assay evaluates specific aspects of PR catalysis, such as precursor autoprocessing, mature PR self-degradation, or substrate proteolysis by recombinant PR *in vitro*. [189, 213, 244, 245, 248, 270, 271]. In infected cells, the autoprocessing of the Gag-Pol precursor is subject to intricate temporospatial regulation, and the released mature PRs process at least 10 distinct substrate sequences, each with varying proteolysis kinetics. Given that a single viral particle contains, on average, 1,500 copies of Gag and 80 copies of Gag-Pol, ~8,000 proteolytic reactions are required to produce a single, fully mature, infectious virus particle. Consequently, PI treatment can differentially affect these reactions catalyzed by either precursors or mature PRs, collectively influencing viral infectivity at various levels. Studying only a subset of these reactions may not fully capture the impact of PI treatment on viral infectivity and DR.

To address this limitation, we developed a new infectivity assay, designed to quantify PI susceptibility and resistance development with improved sensitivity. First, we engineered a reporter with Vpu and Env truncated and with a H2B-mRFP coding sequence in-frame inserted right after the third codon of Nef followed by a stop codon upstream of the unique XhoI site in the Nef sequence (Fig. 2.4A). HEK 293T cells were co-transfected with this reporter and the VSV-G plasmid and treated with or without PI as necessary to produce viral particles. These particles were collected by pelleting the culture medium through a 25% sucrose cushion and directly mixed with target U2OS cells. Upon productive infection, the H2B-mRFP reporter is expressed and incorporated into the nucleosomes, enabling the quantification of individual infected cells through the detection of red nuclei using fluorescence microscopy (Fig. 2.4A).

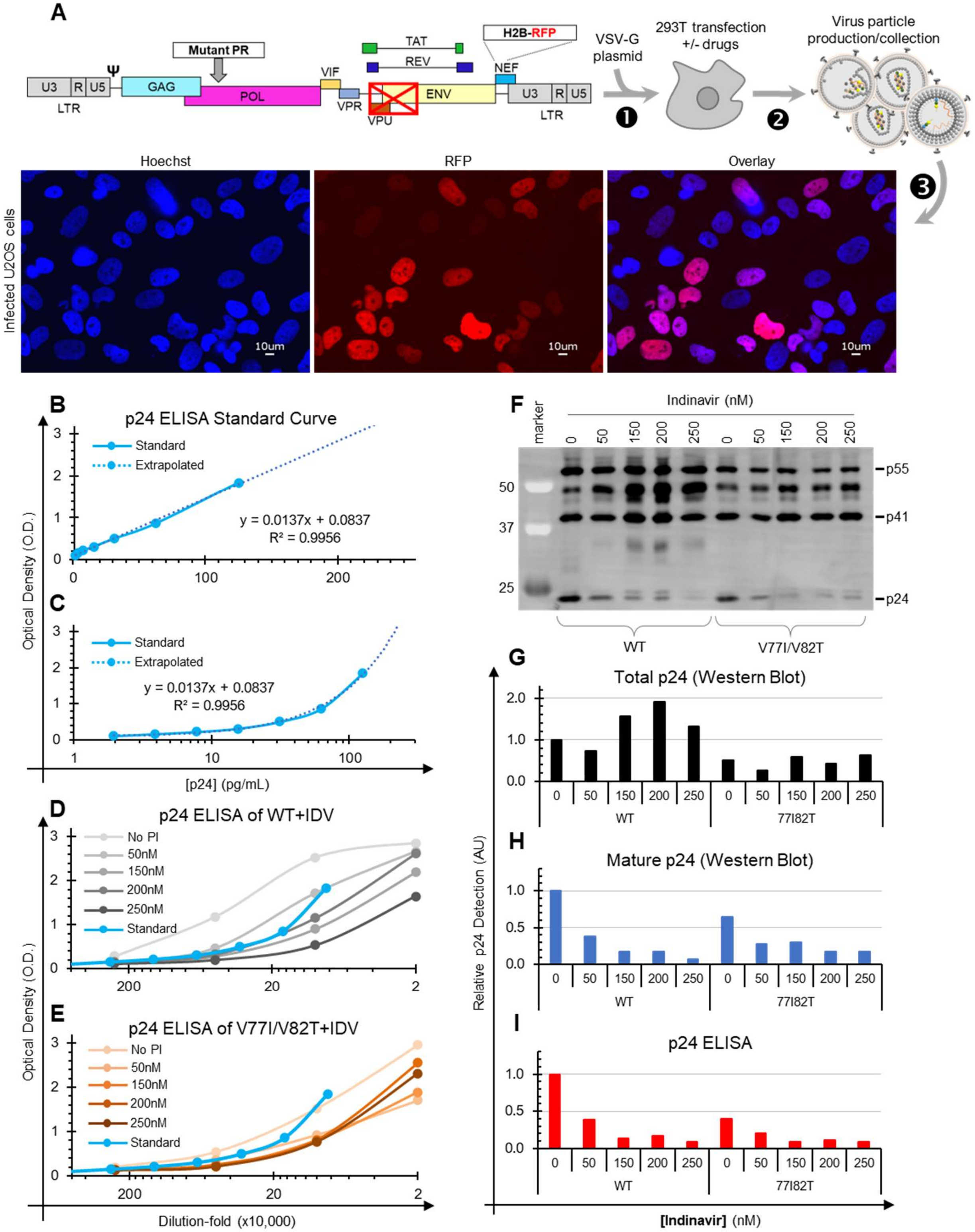

A
U3
R
U5
LTR
Ψ
GAG
Mutant PR
POL
VIF
VPR
VPU
TAT
REV
ENV
H2B-RFP
NEF
U3
R
U5
LTR
VSV-G plasmid
293T transfection +/- drugs
Virus particle production/collection
❶
❷
❸
Hoechst
RFP
Overlay
Infected U2OS cells
10um
10um
10um
B
p24 ELISA Standard Curve
Standard
Extrapolated
y = 0.0137x + 0.0837
R² = 0.9956
3
2
1
0
0
100
200
C
Standard
Extrapolated
y = 0.0137x + 0.0837
R² = 0.9956
3
2
1
0
1
10
100
Optical Density (O.D.)
[p24] (pg/mL)
D
p24 ELISA of WT+IDV
No PI
50nM
150nM
200nM
250nM
Standard
3
2
1
0
200
20
2
E
p24 ELISA of V77I/V82T+IDV
No PI
50nM
150nM
200nM
250nM
Standard
3
2
1
0
200
20
2
Optical Density (O.D.)
Dilution-fold (x10,000)
F
Indinavir (nM)
marker
0
50
150
200
250
0
50
150
200
250
50
37
25
p55
p41
p24
WT
V77I/V82T
G
Total p24 (Western Blot)
2.0
1.0
0.0
0
50
150
200
250
0
50
150
200
250
WT
77I82T
H
Mature p24 (Western Blot)
1.0
0.5
0.0
0
50
150
200
250
0
50
150
200
250
WT
77I82T
I
p24 ELISA
1.0
0.5
0.0
0
50
150
200
250
0
50
150
200
250
WT
77I82T
Relative p24 Detection (AU)
[Indinavir] (nM)

Figure 2.4. Schematic and quantification of viral infectivity. **A.** Schematic of the infectivity assay showing the major steps involved. **B&C.** p24 ELISA standard curves plotted against known amounts of p24 antigen with linear (B) and logarithmic (C) X-axes. **D&E.** p24 ELISA data for the indicated samples at serial dilutions. The solid cyan line is the standard curve, overlaid according to OD values. **F.** Western blot results of the indicated samples. Pelleted viral particles were resolved by 8-16% gradient SDS-PAGE and transferred to a PVDF membrane. The blot was probed with a mouse monoclonal p24 antibody (183-H12-5C) and visualized with an 800 nm goat anti-mouse antibody. **G-I.** Quantification of virus input by intensity sum of all p24-reactive bands (G), band intensity of the fully processed p24 capsid (H), and p24 ELISA data (I). The data presented are representative of two experimental repeats.

We also compared p24 ELISA and Western blotting for quantification and normalization of virus input. The p24 ELISA is known for its high sensitivity, detecting p24 antigen within a linear response range of single digits to a few hundred pg/mL (Figs. 2.4B & 2.4C). To ensure measurement accuracy, we analyzed each sample at four diluted concentrations, covering 20,000- to 2,500,000-fold dilutions, ensuring at least one measurement fell within the linear response range (*i.e.*, OD values between 0.2 and 0.8) (Fig. 2.4I). Notably, the OD values of undiluted culture medium were already outside the linear response range, and the dilution factors required to ensure reliable OD determination varied among samples (Figs. 2.4D & 2.4E). In addition, these samples exhibited differing responses to dilution when the standard curve was superimposed onto the graphs for comparison based on OD values. We speculated that these samples contained varying amounts of p24-containing fragments with diverse reactivities to p24 ELISA, distinct from fully processed p24 antigen. To test this speculation, aliquots of the same samples were analyzed by Western blotting using a monoclonal p24 antibody (Fig. 2.4F). Our data revealed diverse Gag processing patterns in samples produced under different conditions (WT vs. the mutant at various PI concentrations). Notably, even the untreated WT control exhibited detection of the full-length unprocessed Gag polyprotein, further confirming the heterogeneity of viral particles in their Gag processing, as previously reported [220]. Quantification of band intensity showed that Western blot data for fully processed p24 (Fig. 2.4H) were generally consistent with p24 ELISA data (Fig. 2.4I). PI treatment reduced the amount of mature p24 associated with these viral particles to varying degrees, as expected. Thus, p24 ELISA appeared biased toward fully processed p24, which did not accurately reflect the amount of total viral particles produced in each sample (Fig. 2.4G). Consequently, we used Western blotting to detect total p24 content in each viral preparation to represent the number of viral particles used for infection and total p24 content for each sample was normalized to the total p24 content of the untreated WT control (set to 100) to define the relative viral input for subsequent analyses.

Since the exact number of infectious units in each sample is unknown and varies depending on mutations and PI treatment, we infected constant amounts of target U2OS cells with a wide range of virus inputs (spanning ~10,000-fold). Infectivity was defined as the number of H2B-RFP-positive cells per 1,000 target U2OS cells, which followed a sigmoidal profile as a function of virus input (Figs. 2.5A & 2.5B). The plateaued shoulder (right-most portion of the untreated control curves) represents a condition where the number of infectious units exceeds the available target cells, resulting in ~100% infection but an underestimation of infectious units. The tail end (left-most portion of the respective curves) reflects conditions with insufficient infectious units for productive infection. The middle region, optimal for reliable quantification and comparison, exhibited increased infectivity as virus input increased.

Increasing concentrations of IDV reduced viral infectivity (curves shifted to the right) and displayed a nonlinear response to PI treatment. Hence, we compared the infectivity profiles of WT and double mutant viruses across a range of IDV concentrations (Figs. 2.5C-F). Without PI treatment, both the mutant and WT control showed no significant differences across the tested viral inputs (Fig. 2.5C). At 20 nM IDV, the mutant was slightly less infectious than the WT control (Fig. 2.5D). At 200 nM IDV, the mutant was more infectious than the WT control particularly at high viral inputs (Fig. 2.5E). At 2,000 nM IDV, both were effectively suppressed (Fig. 2.5F). Collectively, our data showed that 77I82T-mediated IDV resistance is intricately influenced by both drug concentration and virus input. The difference in IDV susceptibility between the mutant and WT control peaked at ~200 nM IDV and tapered at both ends of the concentration spectrum. Note that this concentration aligns with estimated IDV levels in the bloodstream of patients undergoing IDV-containing cART [257, 305-309]. When virus input was low *(e.g.*, <1), 200 nM IDV was sufficient at suppressing both WT and mutant viruses (Fig. 2.5E, left box). At high inputs (*e.g.*, >10), the mutant contained more infectious units than the WT, and 200 nM IDV was insufficient for suppression (Fig. 2.5E, right box). Therefore, the highest IDV resistance was

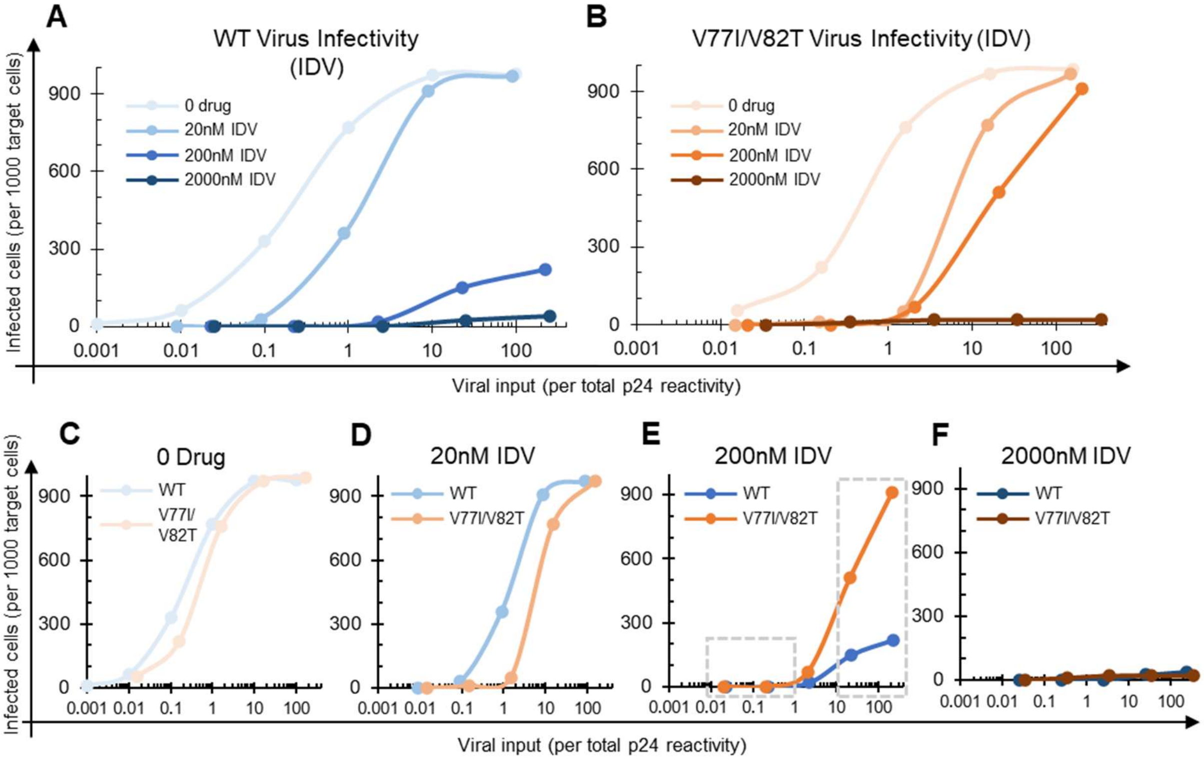

Figure 2.5. Infectivity analysis of the WT and 77I82T viruses. A&B. Infectivity profiles of the WT (A) and 77I82T (B) viruses at various IDV concentrations. **C-F.** Infectivity comparisons between the WT and 77I82T viruses at the indicated IDV concentrations. The results are representative of three experimental repeats.

detected at 200 nM IDV with high virus inputs. To our knowledge, this assay is the first to experimentally recapitulate IDV resistance caused by the 77I82T mutant at clinically relevant concentrations. Taken together, our infectivity analysis illustrated that both virus input and PI concentration cooperatively determine DR manifestation, highlighting the importance of assessing DR over a range of virus inputs, rather than a single arbitrary input, for more accurate DR assessment and mechanistic study.

Mutation contributions to drug resistance defined

Building on the confirmation of 77I82T-mediated indinavir (IDV) resistance using our infectivity assay, we next explored whether this assay could sensitively delineate the roles of individual mutations in the development of DR. PR residue 82, directly involved in substrate/inhibitor binding, is a well-documented driver of DR through mutations such as V82A and V82T [295, 297, 310]. In contrast, mutation 77I, located far from the catalytic site based on the mature PR structure, is typically classified as compensatory or polymorphic. To investigate further, we assessed the WT, single mutants (V77I and V82T), and double mutants (V77I/V82T) across physiologically relevant IDV concentrations.

In the absence of any PI, all four viruses exhibited similar infectivity profiles (Fig. 2.6A), with mutants harboring 82T exhibiting slightly reduced infectivity compared to the WT and 77I, suggesting a potential fitness cost associated with this mutation. At 50 nM IDV, the double mutant showed modest resistance relative to the other three viruses but remained comparable overall (Fig. 2.6B). At 150 nM IDV, the WT control was more strongly suppressed than the mutants, especially at higher virus inputs. As IDV concentrations increased to 200 nM and 250 nM, the 82T single mutant and the 77I82T double mutant consistently demonstrated higher infectivity than the WT and 77I mutants. These findings highlight the precision of our infectivity assay in defining mutation-specific contributions to IDV resistance: 1) mutation 82T plays a

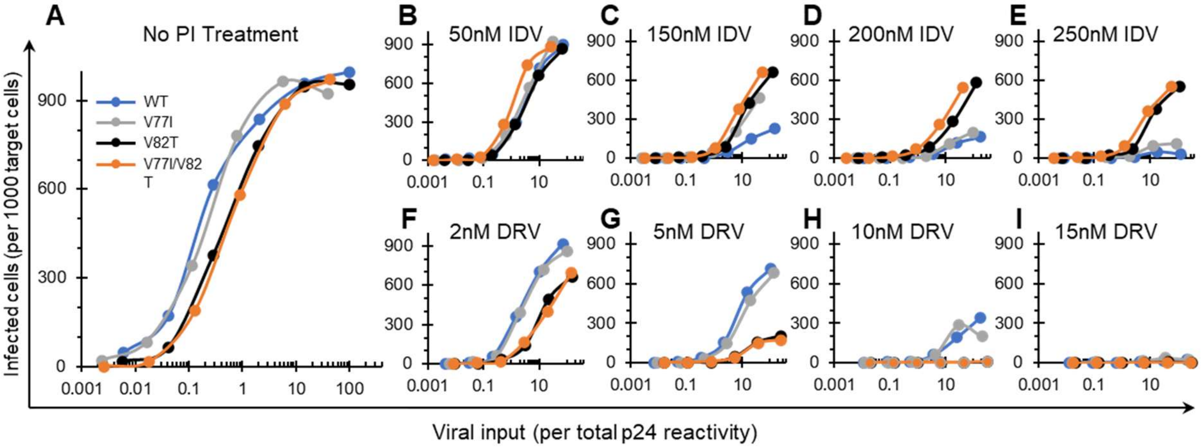

Figure 2.6. Mutation contributions to PI susceptibility as defined by the infectivity analysis. A. Infectivity profiles of the WT and mutants without PI treatment. **B-E.** Comparisons among the four constructs at the indicated IDV concentrations. **F-I.** Comparisons among the four constructs at the indicated DRV concentrations. The results are representative of three experimental repeats.

primary role in driving IDV resistance; 2) mutation 77I alone exhibited minor resistance at 150nM IDV but reverted to WT-like susceptibility at 200 and 250 nM IDV (Fig. 2.6C-E); 3) there was a slight additive cooperativity between mutation 77I and 82T mutations in conferring IDV resistance.

We next evaluated the impact of these mutations on DRV susceptibility, given previous evidence suggesting that the double mutation may increase sensitivity to DRV (Figs. 2.1C&D, 2.2C, and 2.3C). Interestingly, 82T-containing mutants (single or double) were consistently more sensitive to DRV suppression than the WT and 77I mutant, particularly at 2, 5, and 10 nM DRV concentrations. The maximal difference was observed at 5 nM DRV (Figs. 2.6F-H). Treatment with 15 nM DRV abolished infectivity across all tested viruses (Fig. 2.6I). These results underscore the multifaceted effects of the V82T mutation. While driving IDV resistance, it simultaneously increases sensitivity to DRV-mediated inhibition. Conversely, mutation 77I had no discernible impact on DRV susceptibility.

2.4 Discussion

HIV-1 DR remains a significant challenge in achieving sustained suppression of viral replication in people living with HIV-1 undergoing cART. Among the myriad factors contributing to DR, a key obstacle is the disconnect between genotype- or phenotype-based predictions and treatment outcomes: genotypic profiles often fail to predict clinical prognosis precisely and reliably. To bridge this gap, we investigated PI susceptibility and resistance using the 77I82T double mutant as a model across several cell-based assays. Our findings revealed significant variations in DR assessment depending on the assay employed and led to the development of a sensitive assay platform for infectivity quantification, significantly improving DR assessment accuracy.

Variations in PI susceptibility and context-dependent catalysis flexibility of HIV PR

Within infected cells, HIV PR is initially synthesized as part of the Gag-Pol polyprotein precursor, which undergoes regulated autoprocessing to release the mature PR. Previous studies, including those from our group, have shown that precursor and mature PRs differ enzymatically, with precursors often being more resistant to PI suppression than mature PRs [238, 242, 244, 245]. Furthermore, precursors exhibit catalytic flexibility influenced by factors, such as fusion contexts and mutations, within or beyond the PR coding region. For example, different fusion contexts can produce mature PRs with identical sequences but distinct catalytic properties: self-degradation prone *vs.* resistant [244, 245, 270, 271]. This enzymatic flexibility implies that precursor and mature PRs can adopt discrete conformations with varying activities, adding another layer of complexity to DR assessment and mechanistic characterization. Our study showed that PI susceptibility varies by assay context, underscoring this catalytic flexibility. For example, assays producing mature PRs prone to self-degradation detected 77I82T-mediated IDV resistance by proxy of self-degradation (Figs. 2.1D and 2.2C). However, the same mutation showed no significant effect on precursor autoprocessing (Fig. 2.1C). In contexts utilizing fusion precursors with an MBP-derived signal peptide (SigP) at the N-terminus–producing mature PRs resistant to self-degradation [245, 248]–77I82T-mediated IDV resistance was observed at the precursor autoprocessing step (Fig. 2.3C), but not in the released mature PR (Fig. 2.3D). As it remains unclear how many distinct forms of precursor and mature PRs are required for productive virion maturation, existing assay models may not provide a holistic DR assessment. This limitation prompted the development of a new infectivity assay platform.

Modifications to improve infectivity quantification sensitivity

To improve infectivity quantification sensitivity and DR assessment accuracy, we modified the conventional PhenoSense® assays at several key steps. We employed H2B-mRFP as a reporter, enabling the identification of infected cells at single-cell resolution, which also improves the quantification of individual infectious units. In contrast, PhenoSense® assays use a luciferase reporter, which relies on enzymatic amplification and varies significantly between cells, reducing accuracy in quantification of individual infectious units.

We normalized virus input using total p24-reactive signals measured by Western blot analysis. In contrast, PhenoSense® assays rely on p24 ELISA, which can be biased toward fully processed p24 and may not accurately reflect total viral particles in each sample (Fig. 2.4). Notably, viral particles produced by transfected 293T cells are heterogeneous in morphology, containing varying amounts of full-length Gag polyprotein [220] and PI treatment can further alter the proportion of fully processed p24 in different samples. Such biases can result in unequal amounts of total viral particles used for infection, undermining the accuracy of conventional assays. Our WB analysis provided detailed information on both total viral input and processing patterns to better correlate infectious units in each sample. Our results revealed that infectivity follows sigmoidal response profiles as virus input increases (Figs. 2.5 & 2.6). These complex responses can be overlooked if viral samples are tested at a single arbitrary input, leading to inconsistent or misleading conclusions. For instance, examining a virus input of “1” in Fig. 2.5D shows that the 77I82T mutant is less infectious than the WT control in the presence of 20 nM IDV, suggesting slightly low fitness. However, a virus input of “100” in Fig. 2.5E shows that the mutant 77I82T was more infectious than the WT control at 200 nM IDV, indicating resistance to IDV. Such contrasting results highlight the necessity of testing across a wide range of virus inputs to accurately assess DR. By employing this approach, our platform avoids misleading conclusions that might arise from testing at a single arbitrary virus input, providing a robust framework for precise DR assessment.

Involvement of multiple factors in the clinical manifestation of DR

Our infectivity analysis revealed that, in addition to RAMs identified through genotyping, both PI concentration and the viral input also influence infectivity profiles in a non-linear manner (Figs. 2.5 & 2.6). By using PI concentration as a proxy for plasma drug levels in patients and viral input as a proxy for circulating viral loads, we provided experimental evidence elucidating how these factors collectively determine clinical manifestation of DR. Furthermore, our analysis resolved a long-standing question of why 77I82T-mediated IDV resistance manifests in some patients but not in others.

It is well-established that most antiretroviral drugs bind serum proteins to varying degrees, with only the unbound (free) drugs exerting antiviral activity [311]. Free drug concentrations in plasma are influenced by the pharmacokinetic properties of inhibitors and the variability in serum protein composition [312]. For example, IDV concentration fluctuates over time and across patients, with a minimum trough concentration (C_{min}) of ~ 150 nM [257, 305-309]. In our experiments, IDV stock solutions were added directly to the culture medium to approximate free IDV concentrations. Our data showed that the 77I82T mutant virus is more infectious than the WT when IDV concentrations are in the low hundred nM range–close to the physiological trough IDV concentrations. Interestingly, this replication advantage was not observed at IDV concentrations that were either too low or too high (clinically unachievable). This finding supports the hypothesis that the mutant virus can outcompete the WT virus under prolonged suboptimal IDV concentrations, leading to clinical manifestation of DR [313].

Additionally, our results underscore the importance of maintaining both sufficient PI concentrations and low viral loads for effective cART. For patients harboring 77I82T mutation, if viral load is kept low, IDV at 200 nM is still effective (Fig. 2.5E, the left box region). However, if viral load is not adequately suppressed, the mutant virus replicates more efficiently than the WT virus at suboptimal IDV levels (Fig. 2.5E, the right box region), increasing the risk of treatment failure. By simultaneously examining PI concentration and viral load, our assay reconciled the variability in treatment outcomes observed among patients with the 77I82T mutation. Additional research is required to validate this assay platform further by investigating other RAMs, thereby enhancing its reliability and accuracy for DR assessment and cART prognosis evaluation.

Our assay demonstrated much improved sensitivity in delineating the contributions of individual mutations to DR development. Specifically, we found that the V82T mutation plays a primary role in mediating IDV resistance, while V77I contributes only marginally but synergizes with V82T to enhance IDV resistance. Additionally, V82T increases sensitivity to DRV inhibition, a finding previously speculated based on genetic and statistical analyses [257, 298, 314, 315]. These results suggest that mutations conferring resistance to one inhibitor may concurrently increase sensitivity to another. This insight provides valuable information for personalized medicine, particularly in guiding regimen selection for patients experiencing DR. Consequently, our assay holds promise for clinical application by leveraging patient-derived sequences to tailor personalized treatment strategies.

CHAPTER 3:

DIVERSE AND DISTINCT DRUG RESISTANCE PROFILES MANIFESTED BY A PANEL OF MULTI-PROTEASE-INHIBTOR-RESISTANT STRAINS OF HIV-1

3.1 Introduction

In the HIV infected cell, Gag and GagPol polyproteins are translated from the unprocessed viral genomic RNA and subsequently assemble, along with two copies of the genomic RNA and several other viral and host factors, at the host cell membrane in preparation for particle budding [316-321]. The Gag polyprotein contains the matrix (MA), capsid (CA), nucleocapsid (NC), and p6 proteins, while GagPol (in addition to matrix, capsid, and nucleocapsid), encodes the protease (PR), the reverse transcriptase (RT), and the integrase (IN) [143]. Upon or shortly after immature virus particles bud from the host cell, protease autoprocessing is initiated by the PR from within GagPol wherein the protease processes cleavage sites at its own N- and C-terminus to liberate the mature PR, which subsequently cleaves 10 distinct cleavage sites in both Gag and GagPol to liberate each of the respective mature viral proteins [265, 322]. Cleavage of Gag and GagPol by the mature PR is proceeded by a corresponding rearrangement of the inner viral particle landscape that marks the transition from immature, non-infectious viral particles to mature, infectious virus particles. Mature, infectious virus particles are characterized by the formation of a conical capsid core, composed of over 1500 mature CA proteins, which encloses the condensed viral RNA-nucleocapsid complex in preparation for infection of a new target cell and subsequent translocation of the genomic information through the cytoplasm to the host cell nucleus [323-325]. Mature CA (referred to as mature p24 herein) production and subsequent capsid core formation is a product of Gag/GagPol processing by the viral PR, and is thus used as a proxy to reflect viral particle maturation and as an indirect inference of particle infectivity [326].

The PR has been a target for inhibition since the late 1980's due to its indispensable role in facilitating viral particle maturation and subsequent infectivity; the first protease inhibitor (PI) was approved by the FDA in the 1990's, and nine have been approved for HIV treatment since. All 10 currently available PIs are substrate analogs designed via structure-guided drug design to bind the active site of the mature PR with high affinity [194-196]. Unfortunately, it is common that treatment with PIs results in spontaneous accumulation of mutations in the PR gene that reduce PI affinity and are therefore associated with drug resistance development [257, 294]. These so-called resistance-associated mutations (RAMs) are loosely categorized as either primary RAMs or secondary RAMs [327]. Primary mutations are often acquired early in the course of PI treatment and are usually located in or near the substrate-binding cleft of the PR where they alter the conformation of the PR active site such that PI affinity is reduced. Primary mutations often only mildly contribute to the drug resistance phenotype but are associated with resistance development to multiple PIs and often reduce PR activity. Secondary mutations arise later during continuous PI treatment and contribute to high-level drug resistance; secondary mutations often amplify the effect of primary mutations on the drug resistance phenotype while simultaneously compensating for the deleterious effects on PR activity caused by primary mutations [327, 328].

Although the effects of many individual RAMs on PI response have been thoroughly characterized, PI resistance quickly becomes unpredictable as mutations accumulate in the PR gene and beyond. Both genotypic and phenotypic approaches exist to predict and investigate PI resistance. Genotypic approaches, wherein patient-derived strains are isolated and sequenced to identify mutations associated with resistance, are advantageous to detect RAMs present at levels below the detection limit of phenotypic tests and also to detect mutations that do not cause resistance themselves but are associated with the acquirement of additional RAMs [261]. However, the accuracy of genotypic analysis is inherently limited by both the number and specific combination of RAMs present in the PR gene due to the increasingly complex effect of RAMs as they accumulate. Phenotypic investigation is therefore often superior to genotypic analysis in that phenotypic testing investigates PI response of specific strains and therefore is not limited by the number or combination of RAMs present in a given strain. Thus, phenotypic testing is a preferred method for drug resistance prediction and detection. However, many commonly employed phenotypic tests are commercialized and therefore lack transparency, reproducibility, and applicability to both patient-specific drug selection and drug resistance research. Here, we expand upon our previously established phenotypic infectivity assay to establish its direct applicability in both patient-specific treatment selection and drug resistance investigation. We provide a detailed comparison to previously established phenotypic data derived from a common group of multi-PI resistant mutants [255] that highlights the increased sensitivity of our assay and offers a comprehensive phenotypic readout compared to the limited results obtained via current methods.

3.2 Materials and Methods

DNA mutagenesis

All the plasmids used in this experiment were constructed using standard PCR-mediated mutagenesis and cloning procedures as previously described [238, 242-245, 248]. The H2B reporter proviral construct was engineered from a pNL4-3 reporter expressing human placental alkaline phosphatase (a kind gift from Dr. Ned R Landau) [299]. Briefly, the H2B-mRFP coding sequence was inserted in-frame immediately after the third codon of nef, followed by a stop codon upstream of the unique XhoI site in the nef sequence. As a result, H2B-mRFP is expressed upon productive integration of proviral DNA following infection, while nef expression is not anticipated. Additionally, the PciI-to-PciI fragment (1.4 kb) spanning the entire vpu and N-terminal half of the env coding sequence was deleted and replaced with an 8-nt linker carrying a

BssHII site, ensuing that neither Vpu nor functional Env is produced in this construct. Each construct was verified by sequencing analysis and is available upon request through a standard material transfer agreement.

Generation of Single-rounded Infectious Virus Particles

HEK 293T cells were maintained in DMEM medium containing 10% fetal bovine serum, 100 units/mL of penicillin G sodium salt and 100 µg/mL of streptomycin sulfate. HEK 293T cells were co-transfected with the H2B-mRFP reporter and a plasmid encoding vesicular stomatitis virus-glycoprotein (VSV-G) using calcium phosphate as previously described [238, 242-245, 248] with specific deviations noted below. Briefly, HEK 293T cells were seeded in 12-well plates at ~20% confluency. ~16 hours after cell seeding, cells were treated with chloroquine at 25 µM working concentration immediately prior to transfection. For transfection, a total of 1 µg of plasmid DNA (0.8 µg of the viral reporter plasmid plus 0.2 µg of the VSV-G plasmid per well) in 65.7 µl of H_20 was mixed with 9.3 µl of 2 M CaCl2, followed by the dropwise addition of 75 µl of 2x HBS. The respective solutions were then added to the respective plates with HEK 293T cells. After 7-9 hours of incubation, the culture medium was replaced with 1 mL chloroquine-free medium containing PR inhibitors at indicated concentrations. Approximately 50 hours after transfection, the culture medium containing viral particles was collected from each transfected sample and clarified via 96-well 0.45 µm filter plates (VWR, cat# 97052-126). The filtered culture supernatant from each well was divided into two aliquots, one containing 650 µL and the other containing 150 µL, which were both pelleted at 20,800 × g for 105 minutes through a 25% (w/v in phosphate-buffered saline (PBS)) sucrose cushion. Infection was done in 384-well glass bottom plates. The aliquot of pelleted particles from 650 µL of culture supernatant was resuspended in 5 µL of DMEM overnight at 4˚C. The pelleted viruses from the other 150 µL aliquot were resuspended in 30 µL of 1.5x SDS loading buffer and subjected to SDS-PAGE analysis followed by Western blotting.

Infection and Quantification by Fluorescence Microscopy

U2OS (ATCC HTB-96) cells were cultured in DMEM medium with 10% fetal bovine serum, 100 units/mL penicillin G sodium salt and 100 µg/mL streptomycin sulfate. The cells were plated at ~25% confluency in a Cellvis 384-well glass bottom plate (Cellvis, cat# P384-1.5H-N) at the time of infection. The pelleted virus particles were resuspended by brief vertexing and mixed with equal volumes of U2OS cell suspension (35 µL) before plating. Virus + cell suspension mixtures were then subject to 8-fold serial dilutions (*i.e.*, 5 µL of the virus + cell suspension added to 35 µL of cell suspension for 8-fold dilution in 384-well plates), with a total of 5 dilutions (covering up to a 16,800-fold range of viral input) per virus prep. Approximately 50 hours after infection, Hoechst stain (ThermoFisher, cat# H3570) at a working concentration of 0.2 µg/mL was added to each well and incubated at 37˚C for 30 minutes prior to live cell imaging at 37˚C/5% CO_2. Imaging was performed using a Keyence fluorescence microscope (BZ-X710, Keyence Corporation of America, Itasca, Illinois) with a 20x objective in both DAPI and RFP channels. An automated 5x3 stitching program ensured capturing >1000 cells in most samples. The DAPI and RFP images were stitched using BZ-X Analyzer software prior to quantification. For quantification, ImageJ software was used with a custom batch analysis macro to count the blue nuclei (total cells) and red nuclei (infected cells). Images were converted to 8-bit greyscale and thresholded to distinguish positive signals from noise. The “Fill Holes” and “Watershed” operations enhanced nucleus masking and separated clustered nuclei. The "Analyze Particles" function was used with defined sizes (300 - 9000 pixel units) and circularity (0.1-1.0). Nuclear counts were verified over a range of threshold values for accuracy. Cell counts were also validated in parallel via CellPose segmentation software [329, 330] using a custom nuclei segmentation model trained via the human-in-the-loop training function. Some samples exhibited large fluctuations in segmented nuclei due to variations in fluorescence intensity or cell crowding, requiring validation via manual counting where necessary. Raw infectivity profiles were generated by plotting viral input (see below) versus infected cells per 1000 counted cells.

Area-under-curve calculations were performed in excel using a four-parameter sigmoidal fitting software (MyCurveFit version R2) to generate fitted curves for infectivity profiles; the resulting fit curves were integrated from 0.01 to 100 using a standard trapezoid method. To construct EC_{50} plots, the resulting integrated infectivity values for each infectivity profile were plotted against drug concentration. These plots were again subject to curve fitting using a four-parameter sigmoidal fitting software (MyCurveFit, version R2). The resulting sigmoidal parameters were used to calculate precise EC_{50} values and relative fold-change values (i.e., EC_{50} of mutant/EC_{50} of WT reference) for each mutant.

Quantification of Viral Particles by Western Blotting

Equal volumes of viral lysates were resolved by SDS-PAGE and transferred to a PVDF membrane (MilliporeSigma, cat# IPVH 00010). The primary antibodies used were mouse monoclonal (183-H12-5C) anti-p24 (BEI Resources, cat# ARP-3537) and rabbit polyclonal anti-17 (BEI Resources, cat# ARP-4105). Secondary antibodies included IR700 fluorescence-labeled goat anti-rabbit (Rockland, cat# 611-132-003) and IR800 goat anti-mouse (Rockland, cat# 610-132-121). Blots were visualized with an Odyssey infrared dual laser scanning unit (LI-COR Biotechnology, Lincoln, Nebraska). The intensity sum of all p24-reactive bands was calculated to determine total p24 content for each viral sample using ImageStudio quantification software. Total p24 content for untreated wild-type virus was set as 100, with each sample's total p24 content calculated relative to this reference. Total p24 content for each virus prep was used for normalization to reflect viral input for each sample.

Evaluation of mature PR activity in mammalian cells

For expression of fusion precursors, HEK 293T cells were seeded in a 24-well plate the day before transfection to achieve ~30% confluence at the time of transfection. Chloroquine was added into each well to a final concentration of 25 µM. A total of 0.5 µg of plasmid DNA in 65.7

µl H_20 was first mixed with 9.3 µl of 2 M CaCl2. Then 75 µl of 2 x HBS (50 mM Hepes, 10 mM KCl, 12 mM Dextrose, 280 mM NaCl, and 1.5 mM Na_2HPO_4, pH 7.04~7.05) was added dropwise to the mixture. This mixture was added directly to the 293T cells. After 7-11 hours incubation, the culture medium was replaced with chloroquine-free medium. PR inhibitors were added at indicated concentrations at this step as needed. At about 30 hours post-transfection, the culture medium was aspired out and the cells were lysed *in situ* in 50 µl of pre-chilled lysis buffer (20 mM Tris-HCl, 150mM NaCl, 1% sodium deoxycholate, 1% Triton X-100, pH 8.0, with protease inhibitor cocktail). Under these conditions, the cellular chromosomes formed viscous and filamentous aggregates that could be easily removed with a pipette tip. The remaining post-nuclear lysate was then collected for SDS-PAGE or stored at -20°C.

Equal volumes (10 µl) of post-nuclear lysates were resolved by 8-16% gradient SDS-PAGE followed by protein transfer to PVDF membranes (MilliporeSigma, cat# IPVH 00010). Membranes were probed sequentially by the indicated combinations of primary antibodies (rabbit anti-GST (Rockland, cat# 600-401-B86), mouse anti-GAPDH (Millipore, cat# MAB374), mouse anti-HA (Sigma, cat#H9658), mouse anti-flag (Sigma, cat#F1804)) for ~12 hours at 4˚C. Either IR800 fluorescence labeled goat anti-mouse (LI-COR, cat# 926-32210) or IR700 fluorescence labeled goat anti-rabbit (Rockland, cat# 611-130-122) was used depending on the corresponding primary antibody. Visualization occurred on an Odyssey CLx Infrared Imaging System (LI-COR Biotechnology, Lincoln, Nebraska). Individual band intensity was measured using Image Studio Software (LI-COR Biotechnology, Lincoln, Nebraska). HA- and Flag-reactive bands that detected the mature PR were normalized to the GAPDH-reactive band intensity in each respective lane. GST- and Flag- reactive bands detecting either full-length precursor or the N-terminal fragments were used to determine expression efficiency of the mature PR via the P2A peptide.

3.3 Results

Multi-PI resistant mutants displayed various infectivity profiles

We first sought to determine whether and how various mutations impact infectivity in the absence of PI using our recently established infectivity assay. The 13 mutants were randomly split into two groups for infectivity assessment throughout this study: group 1 includes mutants B, G, H, K, M, N, and X, and group 2 includes mutants A, C, J, L, O, and P (Figure 3.1 and Supplemental Table 3.1). WT controls were included within each experiment throughout the study for side-by-side comparison and to control for slight variations among experiments. Generally, all mutants were infectious in the absence of PI (Figure 3.2A & B) and showed typical sigmoidal infectivity profiles wherein the magnitude of infectivity is proportional to viral input with non-linear coordination. Meanwhile, mutant viruses harboring either the inactivating D25N mutation in the PR catalytic site or the H69D mutation which suppresses PR autoprocessing contain only unprocessed p55 (Figure 3.2 F) and are therefore non-infectious as expected (Figure 3.2C).

Based on infectivity profiles, these mutants could be roughly divided into two classes. Mutants B, K, O, and X showed infectivity profiles nearly identical to that of WT, suggesting minimal impact of their collective mutations on infectivity. Similarly, mutants G, H, M, and N showed a very slight decrease in infectivity relative to WT, as evidenced by the minor right-shift of each respective profile. In contrast, mutants C, J, L, and P (Figure 3.2B) showed a moderate decrease in infectivity while mutant A was the least infectious despite similar amounts of viral particles produced (lane 9 & 10 in Fig 3.2E). These results suggest that, while the collective mutations in some mutants had minimal influence on overall viral infectivity as in mutant B, G, H, K, M, N, O, and X, some mutants as in A, C, J, L, and P showed reduced viral infectivity to various extents. We also observed minor variations in total virus production among these

Figure 3.1. p6*-PR sequences of 13 clinically isolated multi-PI resistant mutant strains. Numbers and letters (left) indicate initial identification code and our corresponding nomenclature, respectively. NL4-3 (top) reflects WT p6*-PR sequence. Mutants are split into Group 1 and Group 2 (left) for experiments throughout.

Supplemental Table 3.1. Comprehensive multi-PI resistant mutant data adapted from (cite Varghese here). RC (%) = replication competency as assessed via PhenoSense®.

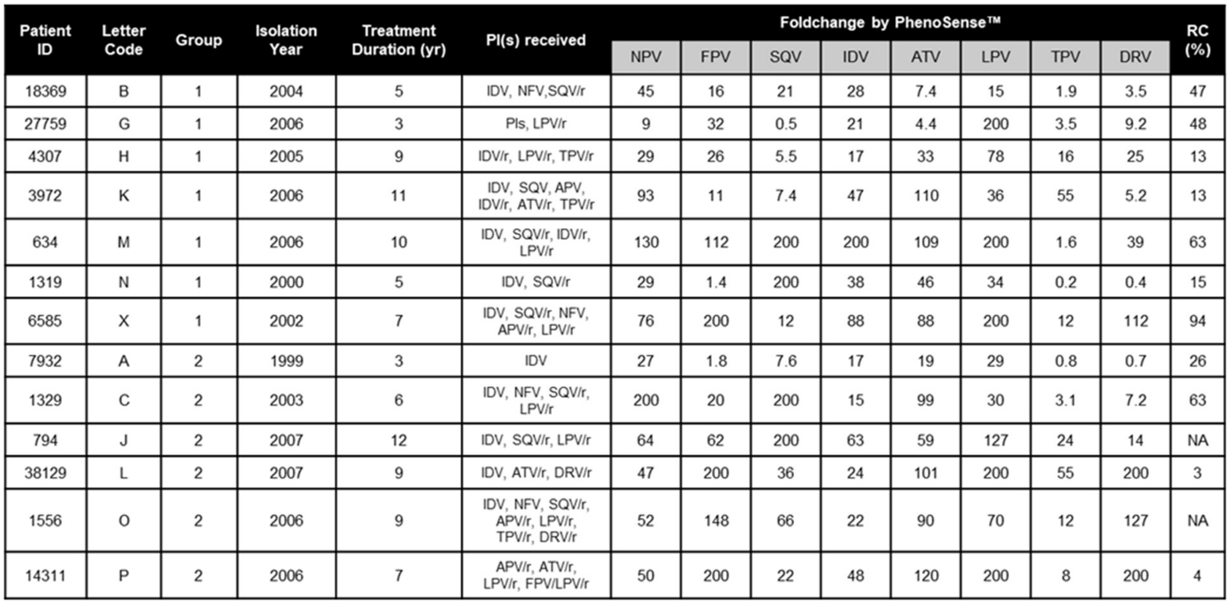

Patient ID	Letter Code	Group	Isolation Year	Treatment Duration (yr)	PI(s) received	Foldchange by PhenoSense™								RC (%)
						NPV	FPV	SQV	IDV	ATV	LPV	TPV	DRV	
18369	B	1	2004	5	IDV, NFV,SQV/r	45	16	21	28	7.4	15	1.9	3.5	47
27759	G	1	2006	3	PIs, LPV/r	9	32	0.5	21	4.4	200	3.5	9.2	48
4307	H	1	2005	9	IDV/r, LPV/r, TPV/r	29	26	5.5	17	33	78	16	25	13
3972	K	1	2006	11	IDV, SQV, APV, IDV/r, ATV/r, TPV/r	93	11	7.4	47	110	36	55	5.2	13
634	M	1	2006	10	IDV, SQV/r, IDV/r, LPV/r	130	112	200	200	109	200	1.6	39	63
1319	N	1	2000	5	IDV, SQV/r	29	1.4	200	38	46	34	0.2	0.4	15
6585	X	1	2002	7	IDV, SQV/r, NFV, APV/r, LPV/r	76	200	12	88	88	200	12	112	94
7932	A	2	1999	3	IDV	27	1.8	7.6	17	19	29	0.8	0.7	26
1329	C	2	2003	6	IDV, NFV, SQV/r, LPV/r	200	20	200	15	99	30	3.1	7.2	63
794	J	2	2007	12	IDV, SQV/r, LPV/r	64	62	200	63	59	127	24	14	NA
38129	L	2	2007	9	IDV, ATV/r, DRV/r	47	200	36	24	101	200	55	200	3
1556	O	2	2006	9	IDV, NFV, SQV/r, APV/r, LPV/r, TPV/r, DRV/r	52	148	66	22	90	70	12	127	NA
14311	P	2	2006	7	APV/r, ATV/r, LPV/r, FPV/LPV/r	50	200	22	48	120	200	8	200	4

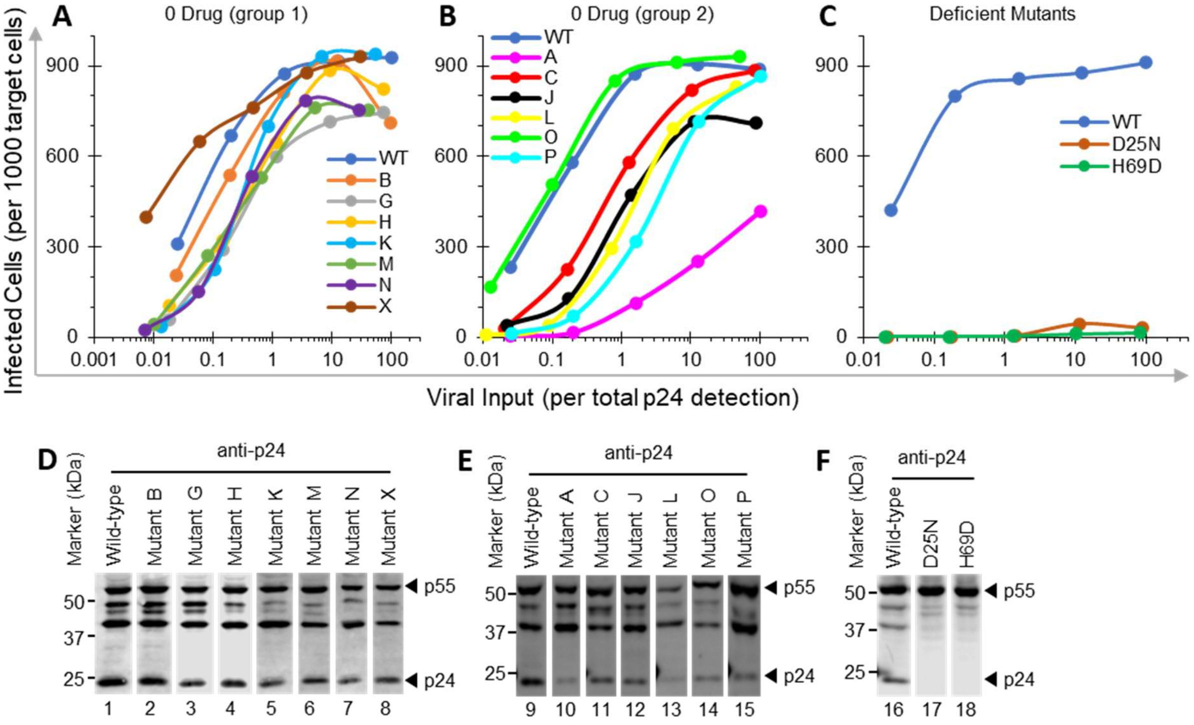

Figure 3.2. Infectivity in the absence of PI to assess baseline infectivity. Infectivity profiles were generated in the absence of PI for each mutant in Group 1 (panel A) and Group 2 (panel B). Both groups include a separate WT control as indicated. Infectivity of viruses harboring mutations to either abolish PR activity (D25N) or autoprocessing (H69D) were measured to serve as negative controls (panel C). Total p24 content of virus preps was detected via Western blot to evaluate viral production and normalize respective infectivity profiles for viral input (panels D-F).

mutants (slight right- or left-shift of virus inputs), suggesting that these mutations may also mildly impact particle production, which needs to be further investigated. Additionally, the reduced infectivity generally aligned with a reduced ratio of the fully processed p24 to total p24-reactive bands, suggesting possible alterations in Gag processing in these mutants. Taken together, our data confirmed that most of these mutants are comparable to WT in virus infectivity with a few showing reduced infectivity in our assay, suggesting different RAM combinations have different impact on virus infectivity.

Multi-PI resistant mutants show diverse responses to darunavir (DRV) treatment

Darunavir (DRV) is one of the three most prescribed PIs for its extremely high binding affinity and unique design. Also, DRV is the most recently FDA-approved PI and is often used in salvage regiments to combat drug resistance due to its preferential binding to main-chain atoms in the PR backbone [275, 331, 332]. Thus, we sought to evaluate how these mutants respond to DRV treatment. We treated each mutant with DRV at concentrations ranging from ~60 nM to 1000 nM, which are comparable to plasma concentrations in patients under cART, and the WT controls ranged from 1.25 nM to 20 nM which is sufficient for suppression of WT viral infectivity. Dose-response infectivity profiles of individual constructs are shown in Figure 3.3 (panel A-H for mutant B, G, H, K, M, N, and X along with the corresponding WT control, and panel I-O for mutant A, C, J, L, O, and P along with the corresponding WT control). The WT controls in both group 1 and group 2 showed similar dose-dependent response to DRV as expected (Figure 3.3A & I). Treatment as low as 1.25 or 2.5 nM DRV was sufficient to moderately reduce WT infectivity, and treatment with 10 nM DRV completely abolished infectivity of the WT viruses in both experiments. All the tested mutants were less sensitive to DRV inhibition than the WT control, exhibiting various response profiles. We calculated the area under the curve (AUC) to represent integrated infectivity and plotted the integrated infectivity over DRV concentration for assessment of apparent EC_{50} values of these mutants (Figure 3.4).

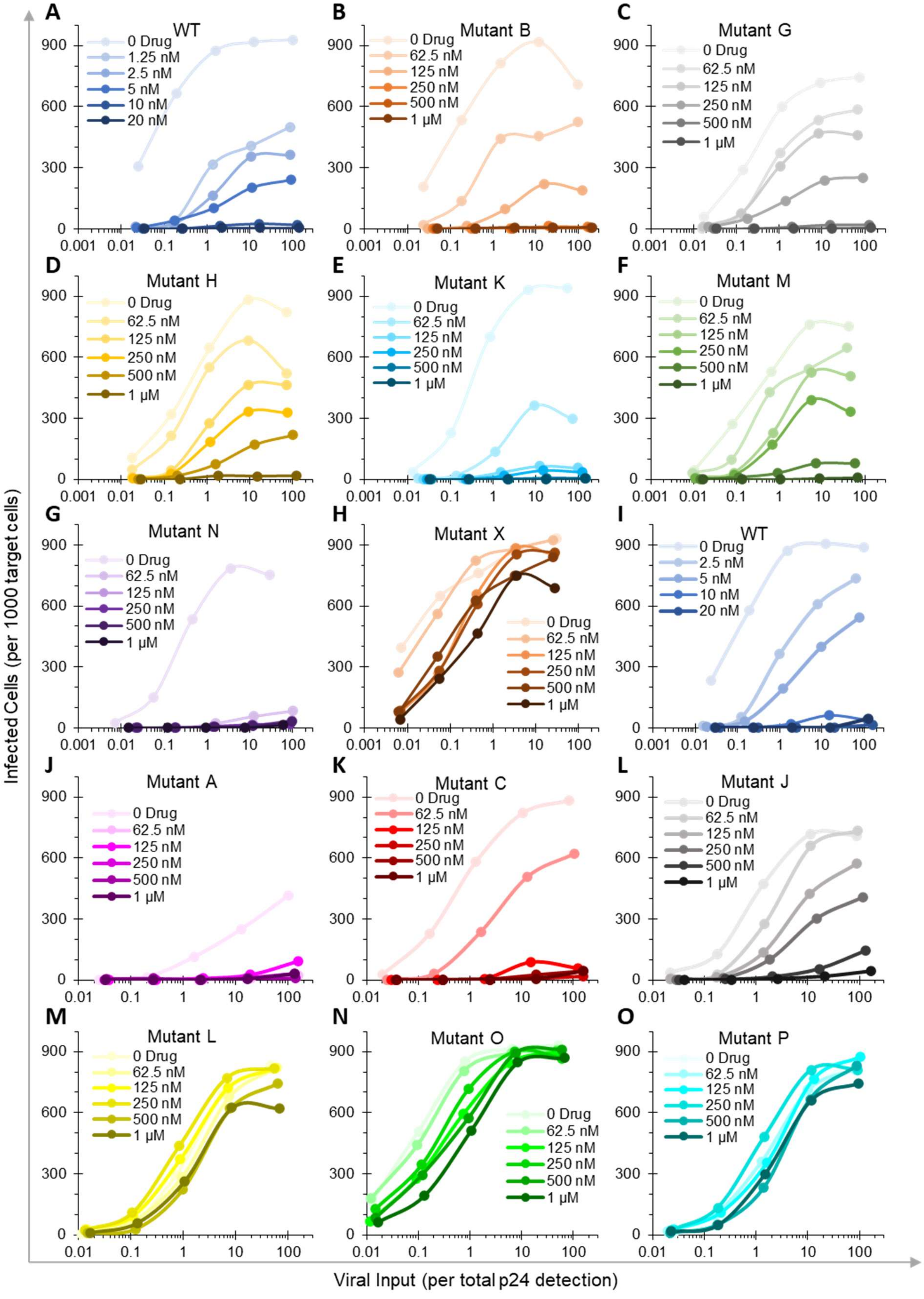
A
WT
0 Drug
1.25 nM
2.5 nM
5 nM
10 nM
20 nM
B
Mutant B
0 Drug
62.5 nM
125 nM
250 nM
500 nM
1 µM
C
Mutant G
0 Drug
62.5 nM
125 nM
250 nM
500 nM
1 µM
D
Mutant H
0 Drug
62.5 nM
125 nM
250 nM
500 nM
1 µM
E
Mutant K
0 Drug
62.5 nM
125 nM
250 nM
500 nM
1 µM
F
Mutant M
0 Drug
62.5 nM
125 nM
250 nM
500 nM
1 µM
G
Mutant N
0 Drug
62.5 nM
125 nM
250 nM
500 nM
1 µM
H
Mutant X
0 Drug
62.5 nM
125 nM
250 nM
500 nM
1 µM
I
WT
0 Drug
2.5 nM
5 nM
10 nM
20 nM
J
Mutant A
0 Drug
62.5 nM
125 nM
250 nM
500 nM
1 µM
K
Mutant C
0 Drug
62.5 nM
125 nM
250 nM
500 nM
1 µM
L
Mutant J
0 Drug
62.5 nM
125 nM
250 nM
500 nM
1 µM
M
Mutant L
0 Drug
62.5 nM
125 nM
250 nM
500 nM
1 µM
N
Mutant O
0 Drug
62.5 nM
125 nM
250 nM
500 nM
1 µM
O
Mutant P
0 Drug
62.5 nM
125 nM
250 nM
500 nM
1 µM
0
300
600
900
0.001
0.01
0.1
1
10
100
Infected Cells (per 1000 target cells)
Viral Input (per total p24 detection)

Figure 3.3. Raw infectivity profiles of each multi-PI resistant mutant treated with darunavir (DRV) ranging from 62.5 nM to 1 μM. Group 1 mutants (panels B-H) and Group 2 mutants (panels J-O) were evaluated in two separate experiments which included individual WT controls for Group 1 (panel A) and Group 2 (panel I).

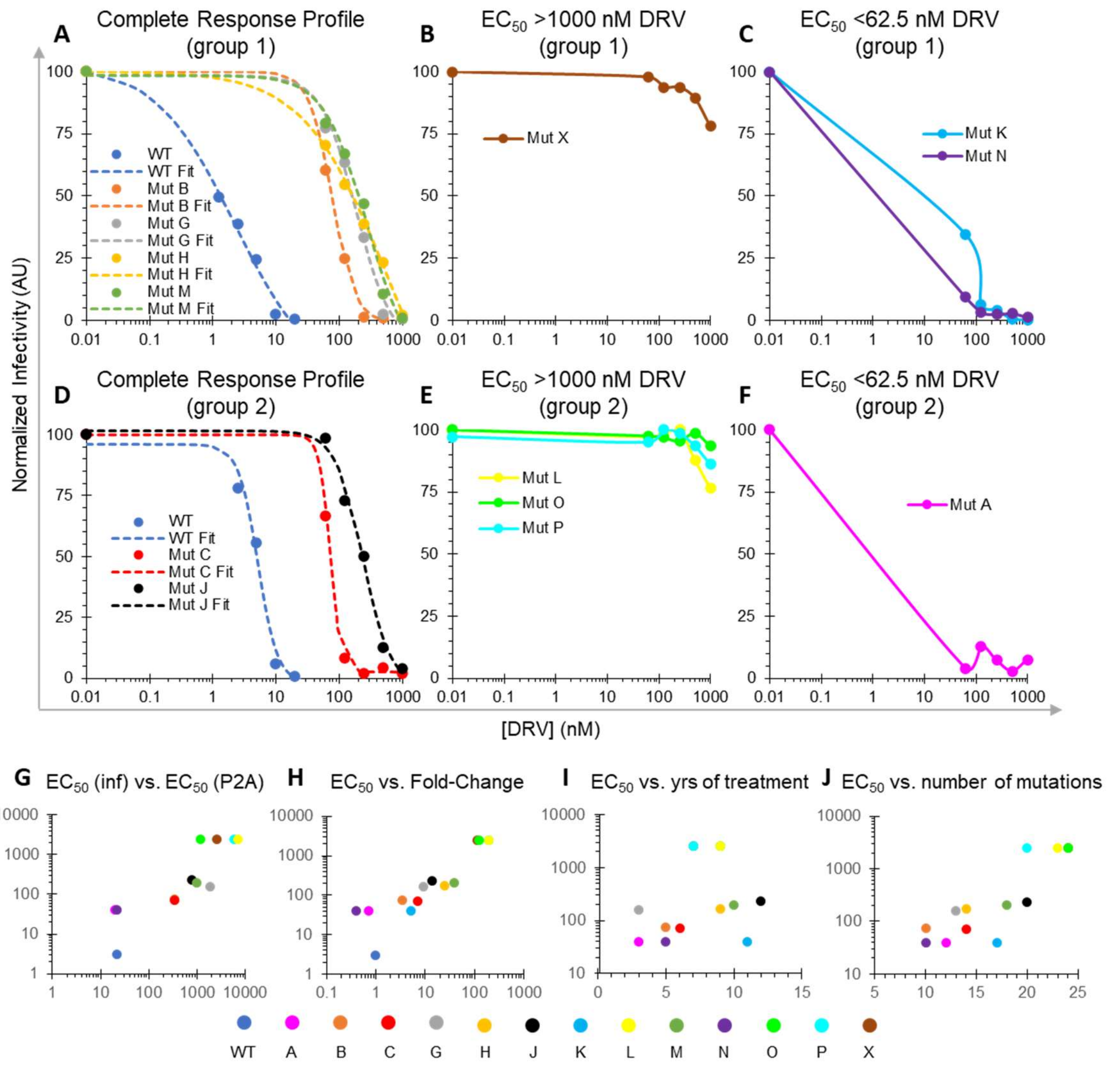

Figure 3.4. Area-Under-Curve calculations for EC50 estimation in response to DRV. The integrated infectivity profiles of mutants that showed complete response profiles were plotted and fitted using a four-parameter sigmoidal model to calculate estimated EC50 values (panels A & D). The integrated infectivity profiles of mutants with EC50 values above 1 µM (panels B & E) or below 62.5 nM (panels C & F) were plotted but did not undergo curve-fitting due to insufficient infectivity coverage over the PI concentration range tested. Our calculated EC50 values for each mutant were plotted against the EC50 values calculated in the P2A context (panel G), the previously reported fold-change values measured via PhenoSense® (panel H), the duration (in years) in which each patient received PI therapy (panel I), and the number of mutations in each mutant p6*-PR sequence (panel J). Arbitrary EC50 values for mutants with working EC50 values above 1 µM DRV as measured by our assay (mutants X, L, O, and P) were set at 2.5 µM for comparison in panels G-J. Likewise, arbitrary EC50 values for mutants with working EC50 values below 62.5 nM DRV as measured by our assay (mutants K, N, and A) were set at 40 nM for comparison in panels G-J.

Accordingly, these mutants clustered into three classes. First, many mutants, including mutants B, G, H, M, C, and J were moderately responsive to DRV showing EC_{50} values ranging from 75 to 300 nM (Figure 3.4A & D). Thus, compared to the WT controls with EC_{50} values in the single-digit nM range, these mutants were 30- to 100-folder higher in their apparent EC_{50} values, suggesting some resistance to DRV treatment [333]. Another class contained mutant X, L, O, and P, which remained fully infectious even when treated with up to 1 μM DRV, indicating high levels of resistance (Figure 3.4B & E). Additionally, mutant K, N and A form the third class, which were efficiently suppressed by 62.5 nM DRV, the lowest concentration tested, rendering it infeasible for accurate EC_{50} determination (Figure 3.4C & F). Therefore, re-evaluation of these mutants at a lower DRV concentration range, such as 0.5 to 100 nM range, would be necessary for accurate estimation of their EC_{50} values. Nonetheless, these three mutants (A, K, N) are expected to respond well, *i.e.,* sensitive, to DRV treatment. In summary, we detected wide deviations in overall DRV sensitivity by our infectivity assay, suggesting the existence of multiple RAM combinations mediating various levels of drug resistance.

To establish feasibility of our assay for reliable drug resistance assessment, we further compared our results to previously reported PhenoSense® data [255]. Note that the conventional PhenoSense® assays report drug resistance as a “fold-change” – a ratio of the drug concentration needed to inhibit the patient’s virus relative to that of a wild-type reference strain, while we determine apparent EC_{50} values through integrated infectivity for direct assessment of PI susceptibility. The scatter plot of our EC_{50} values in nM vs. the reported fold-changes demonstrated a satisfactory correlation of these two readouts (Figure 3.4H), suggesting our assay generally matches results reported by the conventional PhenoSense® assay. Additionally, our assay provided more detailed information, facilitating better correlation analysis of treatment outcome with plasma drug concentrations in patients. For example, according to the clinical threshold for resistance cut-off in PhenoSense® assays, DRV fold-changes greater than 90-fold are considered resistant. Under these criteria, mutant X, L, O, and P would be reported resistant, while the remaining mutants would be reported responsive. However, our results indicated that mutants G, H, M, and J, with EC_{50} values in a few hundred nM range (Table 3.1), might not respond well to DRV treatment if the DRV plasma concentration is not sufficiently maintained in patients under cART. PhenoSense® results indicated that mutants A & N, with fold-changes <1.0, would become more responsive to DRV treatment, whereas our data suggested low levels of resistance compared to the WT (Figure 3.3, Table 3.1).

Additionally, we noticed that increasing drug resistance, as indicated by increasing EC_{50} values, was positively correlated with number of mutations in PR (Figure 3.4J), but not directly correlated with cART duration (Figure 3.4I). Another intriguing observation is that each mutant exhibited various resistance to DRV although only mutant O and L were reported to be exposed to DRV-containing regimen. In particular, mutant P and X developed high levels of DRV resistance in the absence of DRV treatment. Consequently, it appears that certain drug resistant mutations might evolve in the absence of selection pressure, warranting sensitive and reliable drug resistance assessment to guide regimen selections optimized for individual patients.
We previously examined an IDV-resistant PR double mutant with several cell-based assays aiming to establish a simple and reliable platform for drug resistance assessment (see Chapter 2).

In addition to the infectivity assay mentioned above, we also developed a mammalian expression plasmid that produces mature PR from a bicistronic mRNA through P2A peptide-mediated ribosomal skipping. Briefly, the mature PR sequence of each mutant was inserted in-frame directly downstream of the P2A peptide (derived from porcine teschovirus-1) [334]. During translation, the ribosome skips forward at the C-terminus of the P2A sequence and fails to

Table 3.1. Infectivity comparison to previously reported fold-change (FC) values measured via PhenoSense®. Mutants are ordered from top (smallest) to bottom (largest) according to PhenoSense® FC values in response to the indicated PI. EC$_{50}$ values calculated via our assay for each mutant in response to DRV (Figure 4.4) and SQV (Figure 4.7) are shown. (a) indicates arbitrary EC$_{50}$ values set at 40 nM for mutants showing nearly complete infectivity inhibition at 62.5 nM DRV (mutants N, A, K). (b) indicates arbitrary EC$_{50}$ values set at 2500 nM for mutants showing minimal infectivity inhibition up to 1000 nM DRV (mutants X, O, P, L).

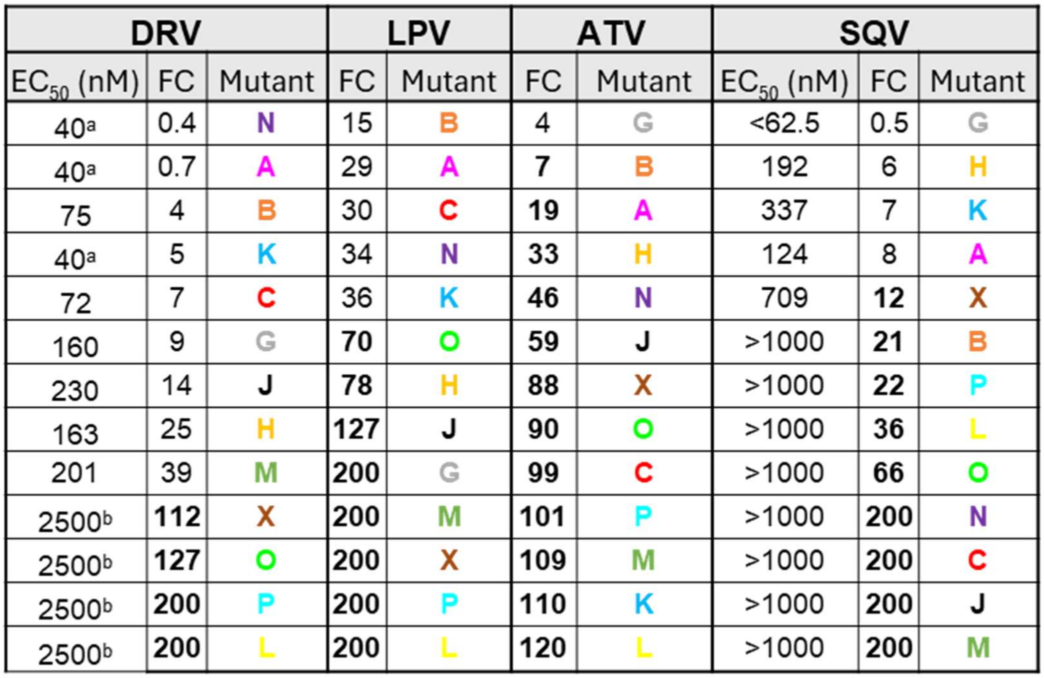

DRV			LPV		ATV		SQV		
EC$_{50}$ (nM)	FC	Mutant	FC	Mutant	FC	Mutant	EC$_{50}$ (nM)	FC	Mutant
40[a]	0.4	N	15	B	4	G	<62.5	0.5	G
40[a]	0.7	A	29	A	**7**	B	192	6	H
75	4	B	30	C	**19**	A	337	7	K
40[a]	5	K	34	N	**33**	H	124	8	A
72	7	C	36	K	**46**	N	709	**12**	X
160	9	G	**70**	O	**59**	J	>1000	**21**	B
230	14	J	**78**	H	**88**	X	>1000	**22**	P
163	25	H	**127**	J	**90**	O	>1000	**36**	L
201	39	M	**200**	G	**99**	C	>1000	**66**	O
2500[b]	**112**	X	**200**	M	**101**	P	>1000	**200**	N
2500[b]	**127**	O	**200**	X	**109**	M	>1000	**200**	C
2500[b]	**200**	P	**200**	P	**110**	K	>1000	**200**	J
2500[b]	**200**	L	**200**	L	**120**	L	>1000	**200**	M

synthesize a peptide bond, thus releasing the nascent polypeptide while continuing translation to produce two separate protein products (Supplemental Figure 3.1 A). We treated transfected cells with varying concentrations of PI, and PR response to PI was measured by mature PR detection in cell lysates that reflects inhibition of spontaneous PR self-degradation in the presence of PI. In this P2A-context, mutants A, N, and the WT control all showed indistinguishable responses to DRV treatment, as evidenced by the near overlap of mature PR detection curves with approximate EC_{50} values between 10 and 50 nM DRV (Supplemental Figure 3.1 C & F). Mutants B, C, J, and M formed a cluster, showing less responsiveness to DRV treatment, with approximate EC_{50} values between 200-1000 nM DRV. Mutants G, H, L, O, P, and X were the least responsive to DRV treatment, with approximate EC_{50} values exceeding 1000 nM DRV (Supplemental Figure 3.1 E, Figure 3.4 G). Mutant H showed no detection of mature PR at any DRV concentration tested. Meanwhile, the N-terminal fragment (MBP-Flag) was nearly undetectable as well (Supplemental Figure 3.1 B, lanes 22-28). Whole-plasmid sequencing analysis of this construct verified the corresponding sequences, discounting possible errors in the expression vector that would prevent expression. We speculate that mutant H, when expressed in mammalian cells via the P2A peptide, might be highly active at degrading itself and its upstream fragment (MBP-flag) as in the case of mutant L (Supplemental Figure 3.1 B, lanes 8-14), however further examination is needed to validate this hypothesis. Mutant K also showed a detection profile consistent with G, H, L, O, P, and X in the P2A context although the data is not shown here.

We noticed that the absolute EC_{50} values differed significantly between these two assays likely because of different readouts used to proxy drug susceptibility: the infectivity assay analyzes mutant effects on overall infectivity, whereas the P2A assay focuses on the self-degradation property of the mature PR. Nonetheless, the rank order of these mutants, by EC_{50} values for mature PR detection (Supplemental Figure 3.1) was generally in good agreement with

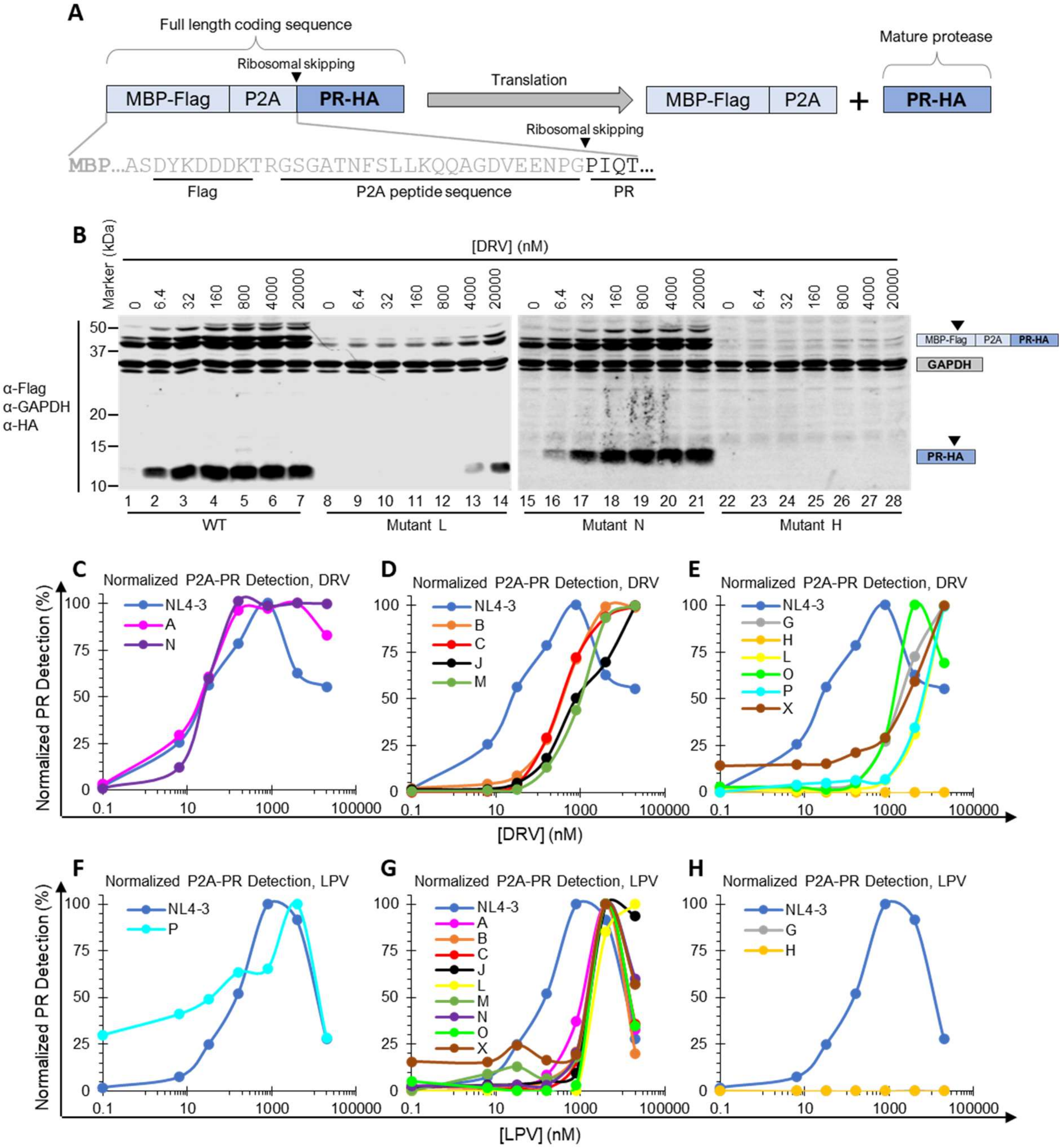
A
Full length coding sequence
Ribosomal skipping
MBP-Flag
P2A
PR-HA
Translation
Mature protease
MBP-Flag
P2A
+
PR-HA
Ribosomal skipping
MBP...ASDYKDDDKTRGSGATNFSLLKQAGDVEENPGPIQT...
Flag
P2A peptide sequence
PR
B
Marker (kDa)
[DRV] (nM)
0
6.4
32
160
800
4000
20000
50
37
20
15
10
α-Flag
α-GAPDH
α-HA
MBP-Flag P2A PR-HA
GAPDH
PR-HA
1 2 3 4 5 6 7 8 9 10 11 12 13 14 15 16 17 18 19 20 21 22 23 24 25 26 27 28
WT
Mutant L
Mutant N
Mutant H
C
Normalized P2A-PR Detection, DRV
NL4-3
A
N
D
Normalized P2A-PR Detection, DRV
NL4-3
B
C
J
M
E
Normalized P2A-PR Detection, DRV
NL4-3
G
H
L
O
P
X
Normalized PR Detection (%)
0
25
50
75
100
0.1
10
1000
100000
[DRV] (nM)
F
Normalized P2A-PR Detection, LPV
NL4-3
P
G
Normalized P2A-PR Detection, LPV
NL4-3
A
B
C
J
L
M
N
O
X
H
Normalized P2A-PR Detection, LPV
NL4-3
G
H
[LPV] (nM)

Supplemental Figure 3.1. Evaluating multi-PI resistant mutant mature PR response to DRV and LPV in mammalian cells. Each mutant PR sequence was cloned into a mammalian expression vector immediately downstream of the P2A peptide for bicistronic expression of MBP-Flag and PR-HA (panel A). Inhibition of mature PR self-degradation in response to PI was quantified via Western blot detection of HA-containing fragments and normalized to GAPDH (panel B). Samples are plotted based on estimated EC50 values of PR self-degradation inhibition in response to PI. Several mutant responses overlapped that of WT PR in response to DRV (panel C). EC50 values for four mutants were nearly 1000 nM DRV (panel D), while the remaining mutants displayed estimated EC50 values above 1000 nM DRV (panel E). The self-degradation inhibition profile of one mutant overlapped that of WT in response to LPV (panel F), while most mutants displayed EC50 values for self-degradation inhibition above 1000 nM LPV (panel G). Several mutants were nearly undetectable in the presence of LPV (panel H).

resistance rank order determined by EC_{50} values for integrated infectivity (Figure 3.4G). For example, response to DRV treatment of mutants A & N were similar to WT in both assays. Mutants B, C, J, and M were clustered together as moderately resistant to DRV in the P2A assay (Supplemental Figure 3.1D) while showing slightly different variations when assessed with the infectivity assay (Figure 3.4A & D). With P2A analysis, mutant G and H were grouped into the highly resistant class along with mutant L, O, P, X (Supplemental Figure 3.1E) but were more sensitive to DRV than L, O, P, and X in the infectivity analysis (Figure 3.4A). Consequently, our findings revealed that while results of both assays are in general agreement, our infectivity analysis provides more comprehensive information assessing DRV resistance with the P2A assay offering similar assessment but with reduced sensitivity and resolution.

Multi-PI resistant mutants show high levels of resistance to lopinavir (LPV)

Lopinavir (LPV) is also one of the three most prescribed PIs, especially in Africa, for its cost-effectiveness [335], wide availability in resource-limited settings [336], and relative stability [337]. We next determined response profiles of these mutant viruses to LPV ranging from 62.5 to 1000 nM with the WT control treated with up to 50 nM LPV. Our results revealed that LPV is less potent than DRV at suppressing the WT control as only about 50% inhibition was detected at 25 & 50 nM LPV (Figure 3.5 A & I), which is consistent with a previous report showing an *in vitro* EC_{50} of around 25 nM for LPV [338]. Also, the 13 mutants tested were mostly resistant to LPV treatment, as each mutant remained at least mildly infectious up to 1000 nM LPV (Figure 3.5). Mutants B, H, K, N, A, and C showed limited inhibition at high LPV concentrations, whereas mutants G, M, X, J, L, O, and P were completely irresponsive up to 1000 nM LPV treatment (Figure 3.5). These results caution the use of LPV as a salvage inhibitor since LPV appears to lack potency in the multi-PI resistant strains tested here, which indicates that resistance to LPV may require fewer RAMs compared to other PIs. Once again, compared to previously reported PhenoSense® results, which suggested mutant B, A, C, N, and K remain

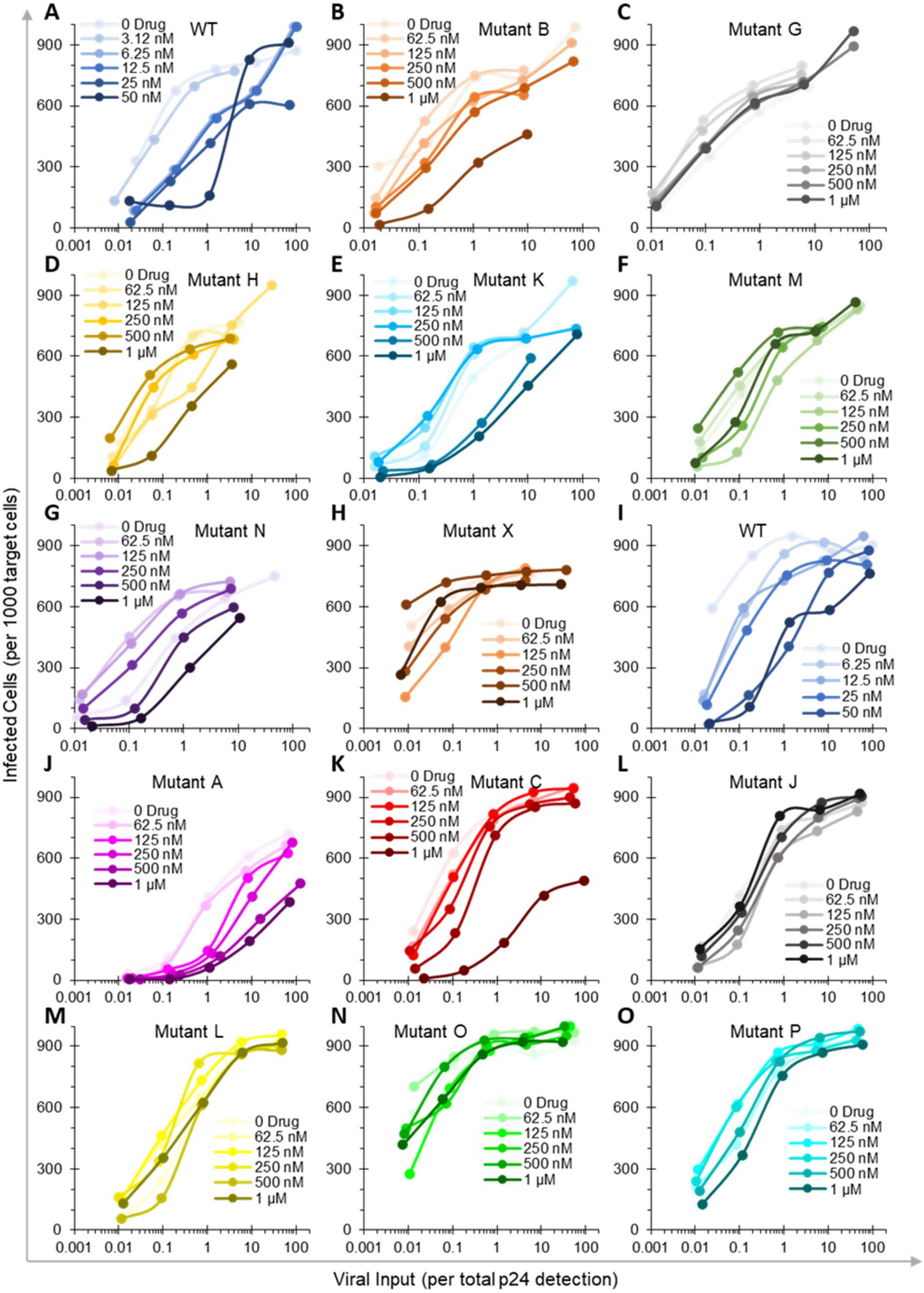
A
WT
0 Drug
3.12 nM
6.25 nM
12.5 nM
25 nM
50 nM
B
Mutant B
0 Drug
62.5 nM
125 nM
250 nM
500 nM
1 µM
C
Mutant G
0 Drug
62.5 nM
125 nM
250 nM
500 nM
1 µM
D
Mutant H
0 Drug
62.5 nM
125 nM
250 nM
500 nM
1 µM
E
Mutant K
0 Drug
62.5 nM
125 nM
250 nM
500 nM
1 µM
F
Mutant M
0 Drug
62.5 nM
125 nM
250 nM
500 nM
1 µM
G
Mutant N
0 Drug
62.5 nM
125 nM
250 nM
500 nM
1 µM
H
Mutant X
0 Drug
62.5 nM
125 nM
250 nM
500 nM
1 µM
I
WT
0 Drug
6.25 nM
12.5 nM
25 nM
50 nM
J
Mutant A
0 Drug
62.5 nM
125 nM
250 nM
500 nM
1 µM
K
Mutant C
0 Drug
62.5 nM
125 nM
250 nM
500 nM
1 µM
L
Mutant J
0 Drug
62.5 nM
125 nM
250 nM
500 nM
1 µM
M
Mutant L
0 Drug
62.5 nM
125 nM
250 nM
500 nM
1 µM
N
Mutant O
0 Drug
62.5 nM
125 nM
250 nM
500 nM
1 µM
O
Mutant P
0 Drug
62.5 nM
125 nM
250 nM
500 nM
1 µM
0
300
600
900
0.001
0.01
0.1
1
10
100
Infected Cells (per 1000 target cells)
Viral Input (per total p24 detection)

Figure 3.5. Raw infectivity profiles of each multi-PI resistant mutant treated with lopinavir (LPV) ranging from 62.5 nM to 1 μM. Group 1 mutants (panels B-H) and Group 2 mutants (panels J-O) were evaluated in two separate experiments which included individual WT controls for Group 1 (panel A) and Group 2 (panel I).

responsive to LPV based on clinical cut-off threshold of fold-changes (Table 3.1), our infectivity assay provides more information on LPV susceptibility by considering physiologically relevant drug concentrations.

We also measured mature PR detection profiles in response to LPV treatment in the P2A system (Supplemental Figure 3.1) to further compare and assess the reliability of different assays. Most mutants clustered together to display EC_{50} values greater than 1000 nM LPV (Supplemental Figure 3.1 G), which is in agreement with our infectivity results. Interestingly, mutant P showed high sensitivity to LPV treatment in the P2A context, as the detection profile of the mutant P mature PR nearly overlapped that of the WT control (Supplemental Figure 3.1 F). We interpreted this discrepancy to suggest that while self-degradation kinetics of mature PR could be used as an alternative proxy for drug response assessment, cautions are warranted because this assay only focuses on a specific aspect of PR activity. Additionally, both mutant G and H were nearly undetectable in the P2A context at any LPV concentration (Supplemental Figure 3.1 H), indicating that mutant G and H self-degradation was not sufficiently inhibited to cause mature PR accumulation and subsequent detection. Note that mutants G and H responded to LPV treatment similarly to mutants B, J, and N in the infectivity assay, once again suggesting some differences in drug resistance assessment between these two assays. We acknowledge that the mature PR made by P2A-mediated ribosomal skipping might fold differently compared to the mature PR released from precursor autoprocessing even with the same sequence, thus possessing distinct catalytic kinetics as previously reported [245]. Taken together, results of these analyses validated our infectivity assay for sensitive and informative drug resistance assessment.

Multi-PI resistant mutants show high levels of resistant to atazanavir (ATV)

We also determined response profiles to atazanavir (ATV) as it is one of the three currently recommended PIs for second-line regimens in people failing first-round ART [339]. Our data confirmed that ATV suppressed the WT control with EC_{50} values around 10 nM (Supplemental Figure 3.2A & I), which is consistent with previous reports [340]. Similar to LPV responses, most mutants were highly resistant to ATV at concentrations tested (~30-500 nM) (Supplemental Figure 3.2). The reported PhenoSense® results suggested that only mutant G would remain responsive to ATV treatment, whereas our data demonstrated that mutant A, B, and G moderately responded to ATV treatment, as evidenced by the progressive flattening of the infectivity profiles as ATV concentration was increased (Supplemental Figure 3.2). Once again, our results were in general agreement with PhenoSense® reports with a few exceptions. For example, PhenoSense® reports suggested that mutant G would be more responsive than mutant B followed by mutant A (Table 3.1). However, our infectivity assay indicated that mutant A was more responsive than both mutant G and B (Supplemental Figure 3.2). Taken together, despite wide use of both LPV and ATV in salvage ART regimens, they are relatively less effective against the multi-PI resistant mutants tested in the present study.

Saquinavir (SQV) as an interesting alternative to either LPV or ATV

Saquinavir (SQV) was the first FDA-approved PI used in early cART, however its clinical utilization has decreased in favor of newer, more potent PIs. We wondered if development of resistance towards newer PIs (DRV, LPV, and ATV) would result in similar resistance to SQV and thus determined SQV infectivity profiles (Figure 3.6). Our assay confirmed that SQV treatment inhibited the WT control with the EC_{50} values at ~ 25 nM (Figure 3.7 A & D), similar to LPV. Notably, mutants A, G, H, K, and X, which were largely resistant to LPV and ATV, showed moderate levels of response to SQV treatment (Figure 3.7). Particularly, mutant G was highly responsive to SQV treatment, as 62.5 nM SQV was sufficient to completely abolish infectivity (Figure 3.7 C). Mutants H, K, and X showed calculated EC_{50} values of 192 nM, 337 nM, and 709

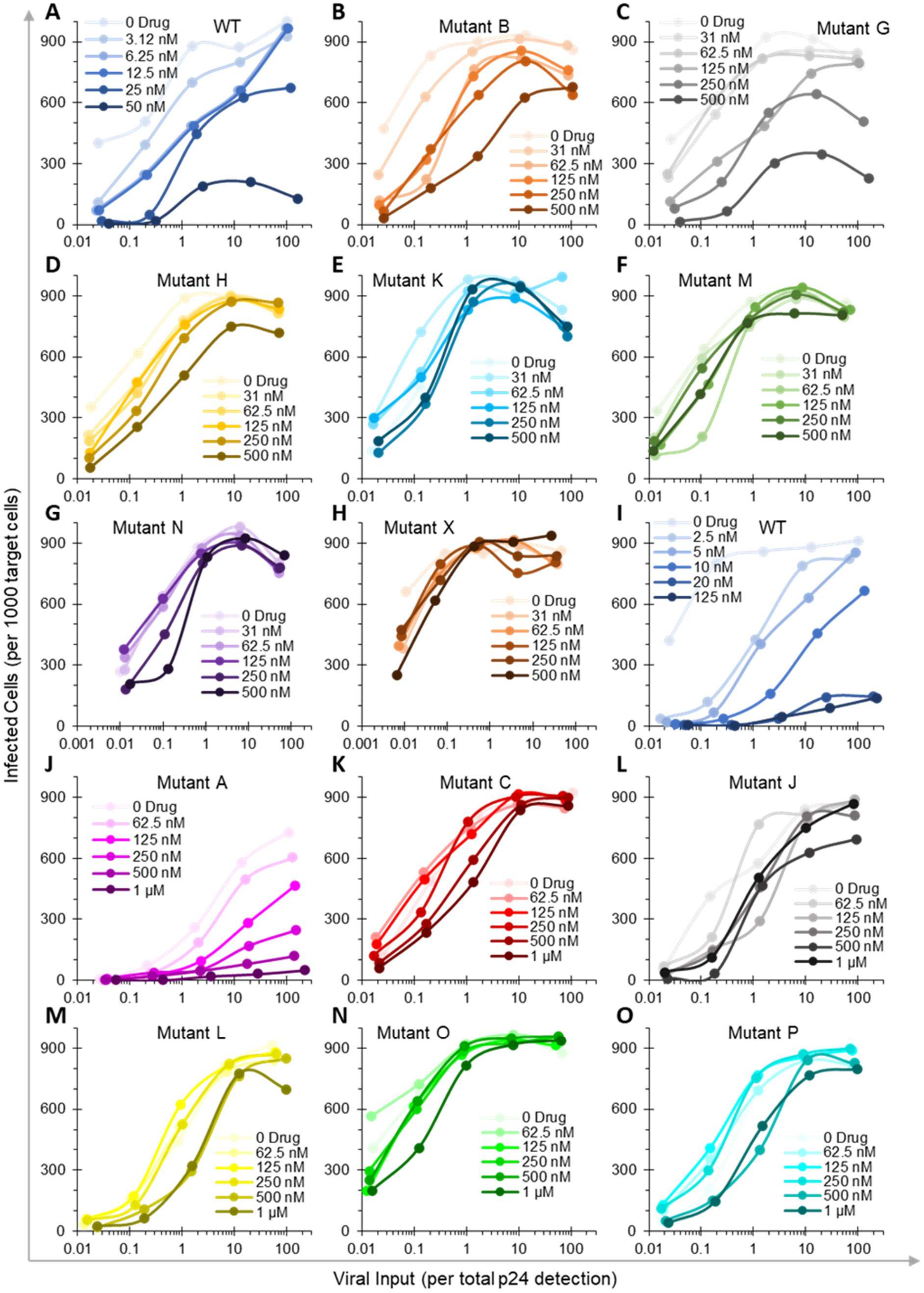
Infected Cells (per 1000 target cells)
Viral Input (per total p24 detection)
A
WT
0 Drug
3.12 nM
6.25 nM
12.5 nM
25 nM
50 nM
B
Mutant B
0 Drug
31 nM
62.5 nM
125 nM
250 nM
500 nM
C
Mutant G
0 Drug
31 nM
62.5 nM
125 nM
250 nM
500 nM
D
Mutant H
0 Drug
31 nM
62.5 nM
125 nM
250 nM
500 nM
E
Mutant K
0 Drug
31 nM
62.5 nM
125 nM
250 nM
500 nM
F
Mutant M
0 Drug
31 nM
62.5 nM
125 nM
250 nM
500 nM
G
Mutant N
0 Drug
31 nM
62.5 nM
125 nM
250 nM
500 nM
H
Mutant X
0 Drug
31 nM
62.5 nM
125 nM
250 nM
500 nM
I
WT
0 Drug
2.5 nM
5 nM
10 nM
20 nM
125 nM
J
Mutant A
0 Drug
62.5 nM
125 nM
250 nM
500 nM
1 μM
K
Mutant C
0 Drug
62.5 nM
125 nM
250 nM
500 nM
1 μM
L
Mutant J
0 Drug
62.5 nM
125 nM
250 nM
500 nM
1 μM
M
Mutant L
0 Drug
62.5 nM
125 nM
250 nM
500 nM
1 μM
N
Mutant O
0 Drug
62.5 nM
125 nM
250 nM
500 nM
1 μM
O
Mutant P
0 Drug
62.5 nM
125 nM
250 nM
500 nM
1 μM
0
300
600
900
0.001
0.01
0.1
1
10
100

Supplemental Figure 3.2. Raw infectivity profiles of each multi-PI resistant mutant treated with atazanavir (ATV) ranging from 31 nM-500 nM for Group 1 or 62.5 nM-1 µM for Group 2. Group 1 mutants (panels B-H) and Group 2 mutants (panels J-O) were evaluated in two separate experiments which included individual WT controls for Group 1 (panel A) and Group 2 (panel I).

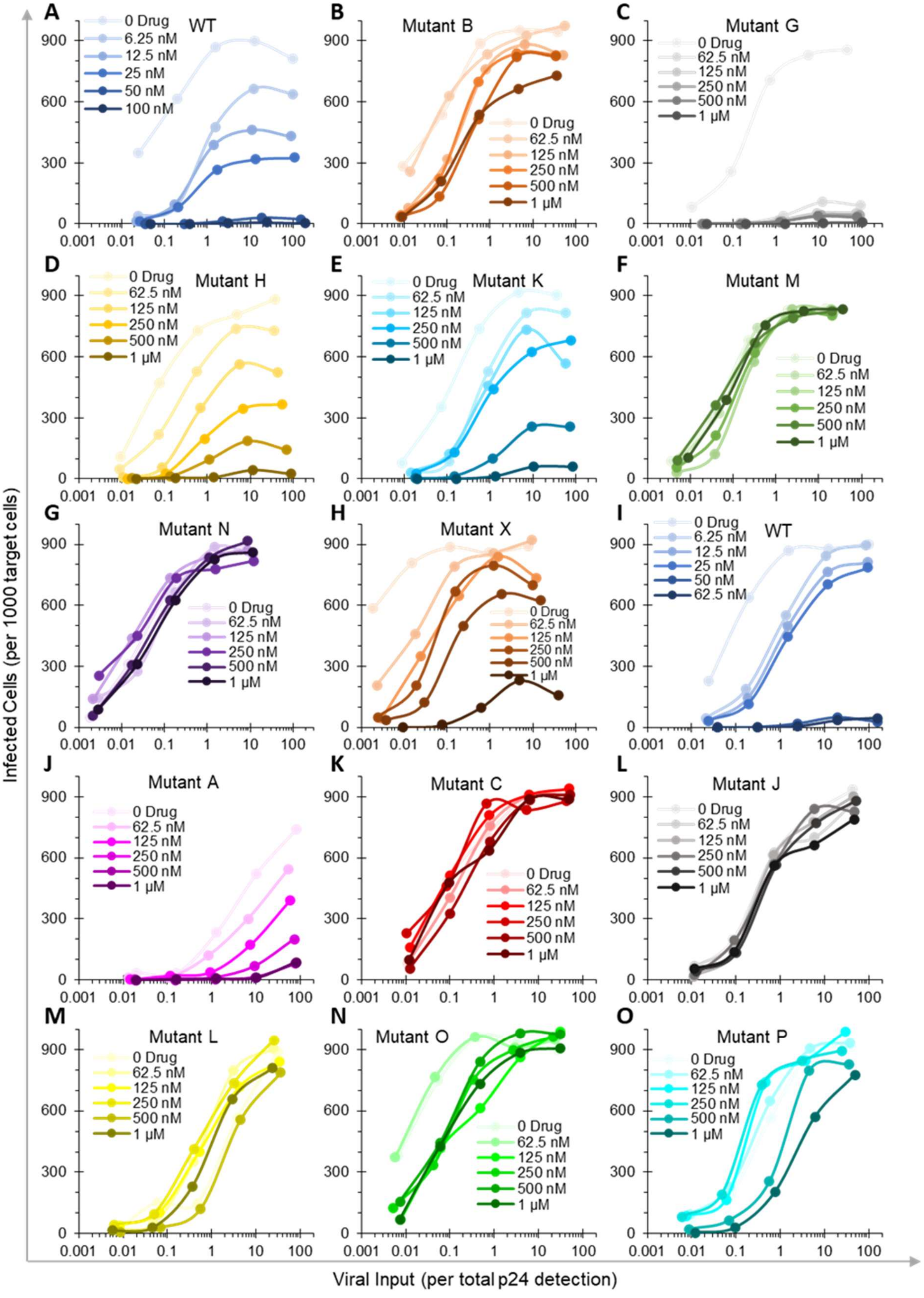
Infected Cells (per 1000 target cells)
Viral Input (per total p24 detection)
A
WT
0 Drug
6.25 nM
12.5 nM
25 nM
50 nM
100 nM
B
Mutant B
0 Drug
62.5 nM
125 nM
250 nM
500 nM
1 μM
C
Mutant G
0 Drug
62.5 nM
125 nM
250 nM
500 nM
1 μM
D
Mutant H
0 Drug
62.5 nM
125 nM
250 nM
500 nM
1 μM
E
Mutant K
0 Drug
62.5 nM
125 nM
250 nM
500 nM
1 μM
F
Mutant M
0 Drug
62.5 nM
125 nM
250 nM
500 nM
1 μM
G
Mutant N
0 Drug
62.5 nM
125 nM
250 nM
500 nM
1 μM
H
Mutant X
0 Drug
62.5 nM
125 nM
250 nM
500 nM
1 μM
I
WT
0 Drug
6.25 nM
12.5 nM
25 nM
50 nM
62.5 nM
J
Mutant A
0 Drug
62.5 nM
125 nM
250 nM
500 nM
1 μM
K
Mutant C
0 Drug
62.5 nM
125 nM
250 nM
500 nM
1 μM
L
Mutant J
0 Drug
62.5 nM
125 nM
250 nM
500 nM
1 μM
M
Mutant L
0 Drug
62.5 nM
125 nM
250 nM
500 nM
1 μM
N
Mutant O
0 Drug
62.5 nM
125 nM
250 nM
500 nM
1 μM
O
Mutant P
0 Drug
62.5 nM
125 nM
250 nM
500 nM
1 μM
0
300
600
900
0.001
0.01
0.1
1
10
100

Figure 3.6. Raw infectivity profiles of each multi-PI resistant mutant treated with saquinavir (SQV) ranging from 62.5 nM to 1 μM. Group 1 mutants (panels B-H) and Group 2 mutants (panels J-O) were evaluated in two separate experiments which included individual WT controls for Group 1 (panel A) and Group 2 (panel I).

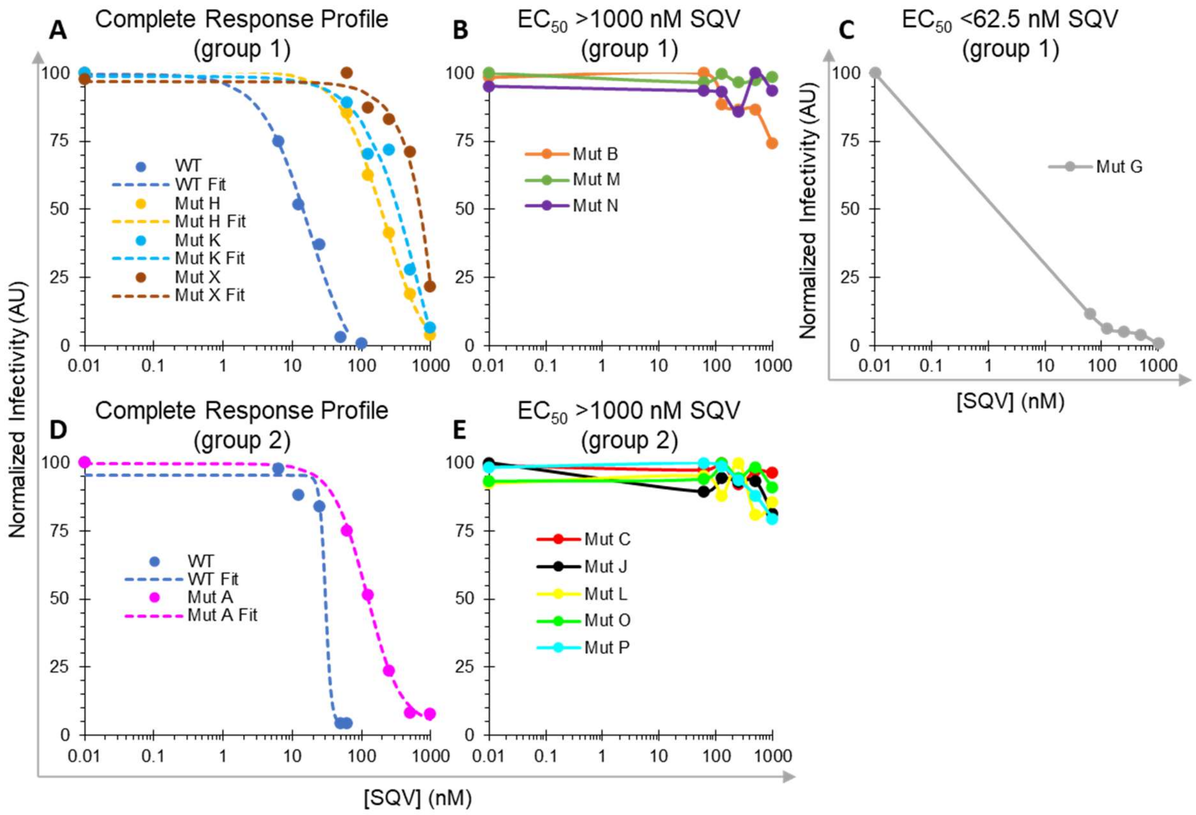

Figure 3.7. Area-Under-Curve calculations for EC50 estimation in response to SQV. The integrated infectivity profiles of mutants that showed complete response profiles were plotted and fitted using a four-parameter sigmoidal model to calculate estimated EC50 values (panels A & D). The integrated infectivity profiles of mutants with EC50 values above 1 μM (panels B & E) or below 62.5 nM (panel C) were plotted but did not undergo curve-fitting due to insufficient infectivity coverage over the PI concentration range tested.

nM, respectively (Table 3.1), whereas only minimal impact on infectivity was observed for these mutants in response to either 1000 nM LPV or 500 nM ATV (Figure 3.5, Supplemental Figure 3.2, respectively). Mutant A, which was most responsive to DRV, moderately responsive to ATV, and unresponsive to LPV, showed an EC_{50} value of 124 nM SQV (Table 3.1), indicating better overall responsiveness to SQV compared to either LPV or ATV. In summary, our data provided ample evidence confirming general agreement of our infectivity assay with PhenoSense® results with more detailed information and improved resolution. It is also interesting to note that SQV treatment was more efficient than either LPV or ATV at suppressing some resistant mutants.

3.4 Discussion

It is widely accepted that the emergence of HIV-1 drug resistance is an accumulative and dynamic process, driven by the virus's continuous evolution driven by the introduction of mutations during replication and subsequent selection of mutations that confer resistance while preserving essential functions for productive replication. We recently developed an infectivity assay for sensitive assessment of how different compounds influence viral infectivity using a reporter that expresses H2B-mRFP upon productive infection. H2B is a histone variant, and incorporation of H2B-mRFP into the chromatin highlights the nucleus of the infected cell red for quantification of individual infected cells as a proxy of virus infectivity. With this assay platform, we investigated the contribution of each mutation in a double mutant (77I82T) known to confer resistance to IDV for their contribution to drug resistance development (see Chapter 2). The present work sought to further evaluate the utility of our infectivity assay on drug resistance assessment. Towards this goal, we examined a panel of prototypical multi-PI-resistant mutants, which were previously analyzed using conventional PhenoSense® assays, and compared our results with the reported data. These comparative analyses validated our infectivity assay for its performance comparable to the conventional PhenoSense® assay on drug resistant assessment. Furthermore, results of our analyses suggest that different RAM combinations result in different response profiles to different PIs, which may aid in personalized PI selection for individuals experiencing drug resistance.

RAMs have diverse and separate effects on viral infectivity, replication competency and drug resistance

When random mutations are accumulated via spontaneous errors during replication, many mutations do not automatically offer advantage to evade drug treatment, but rather more likely have a net neutral or even a slightly negative impact on viral replication and infectivity. Subsequently, the buildup of mutations over time impacts both the infectious potential of the virus as well as the viral response to drug treatment. The conventional PhenoSense® assays assess this particular aspect by replication competency, defined as the 50% tissue culture infectious dose ($TCID_{50}$), which ranged from 300 to 36,000 infectious units after 1 week of culture with a median of 3,000 infectious units. This panel of 13 mutants was reported to vary in RC ranging from 3% to 94% [255]. On the other hand, our assay data showed that all mutants were infectious with a few showing slightly reduced infectivity in single-round infection. We speculated that this discrepancy likely resulted from differences in experimental set-up and final readout. Note that we determine viral infectivity in a single-round infection in correlation with virus input normalized to total p24 detection via Western blot, while PhenoSense® assays determine infectious units per p24 ELISA.

Nevertheless, the overall results of these two assays are in reasonable agreement showing various mutations have diverse impacts on replication competency and/or viral infectivity. For example, mutant P and L were reported with only 3-4% RC, whereas our data confirmed that both mutants were mildly less infectious compared to the WT in the absence of PI (Figure 3.2B).

However, we acknowledge that neither replication competency (as measured by PhenoSense®) nor single-round infectivity (as measured by our assay) are reliable predicters for drug resistance. In other words, highly resistant mutants might be as infectious (*i.e.,* high in RC) as the WT control or less infectious (*i.e.,* low in RC), and vice versa. For example, mutants L and P (Figure 3.2B) were among the mutants with the high levels of resistance to each PI tested but also displayed reduced infectivity in the absence of drug treatment. On the other hand, mutant O, which was also highly resistant to each PI tested, displayed baseline infectivity nearly identical to the WT control in the absence of drug treatment. Mutant A, which was the least infectious of the panel in the absence of drug treatment and significantly less infectious than the WT control (Figure 3.2B), was more resistant to SQV treatment than mutant G and was nearly as resistant as mutant H (Table 3.1, Figure 3.7). Collectively, these observations suggest that the impact of mutations on viral fitness does not necessarily correlate with the level of drug resistance, implicating diverse and distinct influences of each mutation on virus fitness and resistance development.

Our assay offers more information for drug resistance assessment in correlation with PI concentrations

Another difference between our infectivity assay and the conventional PhenoSense® assays lies in quantification of infectivity: we count individual infected cells highlighted by H2B-mRFP while PhenoSense® assays use the total fluorescence intensity as a proxy. Accordingly, our assay, in theory, can determine a single infectious unit in viral particle samples, which significantly improves detection sensitivity. We noticed that the exact EC_{50} values of the WT control (Figure 3.4) were calculated to be 1.3 nM DRV (for group 1 WT control) and 5 nM DRV (for group 2 WT control). Although these values themselves are very similar and are well within the limits of experimental variation, the resulting fold-change values calculated for mutant viruses will vary highly depending on which WT EC_{50} value is used for division. Subsequently, we used EC_{50} values for direct comparison of drug susceptibility (Figure 3.4) in correlation with drug concentrations. This information is critical for meaningful prognosis assessment because plasma drug concentrations vary significantly among different inhibitors and patients with diverse genetic and metabolic backgrounds [306, 341, 342].

Additionally, our fold-change values directly reflect drug susceptibility in correlation with drug concentrations, whereas the clinical cut-off threshold of fold-changes with PhenoSense® assay vary significantly for different PIs to define resistant or responsive. We contribute the wider separations in fold-change values in our assay platform to single-cell resolution capable of detecting one infected cell out of thousands of targets, thus providing more quantitative assessment. For example, PhenoSense® results predicted that 9 of 13 tested mutants should be responsive to DRV treatment as their fold-change values were under the upper clinical cutoff of 90 (Table 3.1). However, our infectivity analysis revealed that mutant G, J, H, and M displayed EC_{50} values in the few hundred nanomolar range with predicted EC_{90} values around 0.5 μM, which might be challenging to fully suppress these mutants in practice. Similarly, mutant H, K, X, and A were predicted to be responsive to SQV according to the fold-changes (Table 3.1) but their EC_{50} values were all greater than 100 nM SQV with a few estimated EC_{90} values over 0.3 μM. Consequently, our results would caution the use of DRV or SQV for these patients carrying these mutant strains unless their free drug concentrations (unbound with serum protein, available to enter cells) in plasma are verified to be around 1 μM. Despite these differences, scatter plot analysis of our calculated EC_{50} values vs the reported PhenoSense® fold-changes in response to DRV showed a linear correlation (Figure 3.4H), confirming our assay as another useful tool for drug resistance assessment, which also offers additional information for salvage inhibitor selection.

Parallel comparison between our infectivity assay and PR detection profile in the P2A platform revealed that RAMs manifest multiple effects on diverse aspects of PR activities. Mutant G, for instance, was moderately resistant to DRV in our infectivity assay with an EC_{50} value around 150 nM DRV (Table 3.1). In the P2A context, however, mutant G self-degradation was far less sensitive and grouped with mutants L, O, P, and X, which were the least responsive in both the P2A and viral contexts (Table 3.1, Figure 3.4, Supplemental Figure 3.1). Mutant G was also the least sensitive to LPV treatment in the P2A context, whereas the response was indistinguishable from other mutants in live virus treated with LPV (Figure 3.5, Supplemental Figure 3.1). Mutant P on the other hand was highly susceptible to LPV treatment in the P2A context, as self-degradation of the mature PR was inhibited at similar concentrations as the WT control (Supplemental Figure 3.1 F). However, mutant P was highly resistant to LPV in the viral context (Figure 3.5) and was equally resistant to DRV treatment in both viral and P2A contexts (Figure 3.4 and Supplemental Figure 3.1, respectively). This highlights the flexibility and context dependence of drug resistance, as PR response to PI may differ drastically between contexts. Thus, assays that cover these diverse aspects as much as possible, such as our infectivity assay and PhenoSense® assays, are expected to provide more comprehensive information for drug resistance assessment.

Multiple and diverse manifestations of PI-resistance

As mentioned above, PI resistance development is a balancing act wherein the random mutations acquired during HIV replication could alter not only PI susceptibility but also PR activity towards its natural substrates. Mutations simultaneously conferring drug resistance and maintaining essential activities are expected to survive and evolve into resistant strains. Our results demonstrated that these 13 mutants are distinct from one another in their PI-resistance, *i.e.*, each mutant displays its own unique response profiles to the tested PIs. HIV-1 PR recognizes and processes at least ten specific substrate sequences in Gag and Gag-Pol, which share low sequence homology. This built-in substrate flexibility implies an inherent accommodation of various mutations throughout the PR coding sequence, which might account for the evolution of multiple RAM combinations that confer different levels of drug resistance to various PIs.

Different PIs also vary in their potency and propensity for the development of resistance

Our data indicates that, across the panel of representative, multi-PI resistant mutants, DRV showed the most potency against these mutants. DRV binds the mature PR with a picomolar K_d *in vitro* and is also considered the most effective PI in combating drug resistance because it was designed to bind main chain atoms in the PR backbone. Thus, it is not surprising to find that DRV shows the highest potency among the available PIs against multi-PI resistant mutants. Also, more point mutations seem to be required for the development of DRV resistance; the most resistant strains (X, O, P, L) among our tested panel carry more than 20-point mutations, ranging from 20 to 24 in the PR coding region alone (Figure 3.4J, Supplemental Table 3.1). It is worth noting that only mutants L and O were isolated from patients who received DRV at some point during their treatment history [255] (Supplemental Table 3.1), however this panel of mutants displayed various levels of resistance to DRV. Therefore, we speculated that some RAMs might confer resistance to multiple PIs whereas others might confer resistance to specific PIs regardless of prior exposure, and different combinations of these RAMs collectively determine response profiles unique to each mutant. For example, mutant L and P are highly resistant to the four PIs we tested in this study, likely due to the accumulation of multiple RAMs.

Interestingly, mutant G showed moderate resistance to DRV, LPV, and ATV but was sensitive to SQV inhibition. Our lab has recently shown similar results in a V77I/V82T PR double mutant, wherein the V82T single mutation is responsible for driving resistance to indinavir (IDV) while simultaneously increasing the sensitivity of the mutant to DRV treatment (manuscript submitted). Notably, PhenoSense® analysis reported a fold-change value of 0.5 for mutant G in response to SQV, which was also indicative of higher SQV susceptibility. Likewise, our infectivity assay showed an EC_{50} value of ~62.5 nM, similar to that of the WT. Additionally, eight of the 13 patients from whom the mutants were isolated received SQV therapy at some point in their treatment history (Supplemental Table 3.1). Mutant A, G, H, P, and L were isolated from patients who were never prescribed SQV; however, our data indicates that these mutants are highly diverse in their susceptibility to SQV treatment (Figure 3.7, Table 3.1). Also, mutant A, which was at least somewhat responsive to the other PIs tested, showed little response to LPV treatment (Figure 3.5). Taken together, this data implicates the complexity of the drug resistance phenotype that is not predictable simply based on treatment history and highlights the fact that response to a given PI cannot necessarily be predicted based on response to other PIs. Some mutants that are highly resistant to DRV show lower EC_{50} values in response to SQV (mutants G and X), some show an increase in EC_{50} against SQV versus DRV (mutants B, H, K, M, N, A, C, and J), while others that are highly resistant to DRV are also highly resistant to SQV (mutants L, O, and P).

Similarly, resistance to ATV and LPV did not necessarily correlate to treatment history in the patients from which the mutants were isolated. Only three of the 13 patients received ATV at some point during their treatment history [255]; mutants K, L, and P were isolated from these respective patients. However, all but mutant G demonstrated various levels of ATV resistance (Supplemental Figure 3.2). Likewise, eight of the 13 patients received LPV therapy at some point during their clinical history [255] yet all mutants were resistant to LPV suppression to various extents. Results of our analyses showed that high levels of resistance to LPV and ATV are prevalent in the mutant panel we tested, indicating RAMs conferring resistance to these two PIs emerge easily and are selected efficiently. Despite that PhenoSense® analysis reported a few mutants with fold-changes less than the clinical cut-off thresholds (Table 3.1), our results demonstrated that none of these mutants could be completely suppressed by LPV or ATV at 500 nM (Figure 3.5 and Supplemental Figure 3.2, respectively). Our findings therefore argue that these two PIs might not serve patients well in fighting drug resistance despite being among the most prescribed drugs. Together, our data highlights the necessity for sensitive and comprehensive drug resistance assessment for informed PI selection to combat drug resistance. Additionally, we highlight the versatility of our infectivity assay in providing a comprehensive picture of the resistance phenotype which reveals the relationship between viral load, physiological PI availability, infectivity, and drug resistance.

CHAPTER 4:

HIGH-THROUGHPUT SCREENING AND CHARACTERIZATION OF NOVEL INHIBITORS TARGETING HIV-1 PROTEASE PRECURSOR AUTOPROCESSING

4.1 Introduction

The HIV-1 protease (PR) is one of three virally encoded enzymes essential for productive HIV replication. It is initially translated as part of the Gag-Pol polyprotein, which, along with Gag, is synthesized from unspliced viral genomic RNA [84, 343]. Gag-Pol is produced through a regulated -1 ribosomal frameshift near the end of the nucleocapsid coding sequence [128, 130, 344-346]. The embedded PR is flanked N-terminally by the p6* peptide, which overlaps with the p6 reading frame in Gag, and C-terminally by reverse transcriptase (RT). Within infected cells, Gag, Gag-Pol, and viral genomic RNA co-assemble at the plasma membrane and hijack cellular ESCRT machinery to facilitate viral particle budding [170, 347, 348]. Gag-Pol autoprocessing occurs during or shortly after budding, with the still-embedded PR cleaving its own N- and C-terminal sites to release mature PR. The free mature PR then recognizes and processes at least 10 distinct cleavage sites within Gag and Gag-Pol [212, 213, 239, 270-272].

Concerted proteolytic processing of Gag and Gag-Pol by mature PR is critical for generating infectious viral particles [133, 198, 214, 215, 232, 349, 350]. Given its essential role in viral infectivity, extensive efforts have focused on targeting mature PR for antiretroviral drug development, leading to the FDA approval of ten protease inhibitors (PIs). These non-cleavable substrate analog PIs suppress proteolytic activity by binding to the catalytic site of mature PR with high affinity [219, 236, 351]. Combinational antiretroviral therapy (cART), which employs inhibitors targeting multiple viral components vital for HIV replication, effectively suppresses viral spread and has significantly improved the quality of life and lifespan of people living with HIV.

However, the emergence of drug-resistant strains in some individuals remains a major challenge, reducing overall cART efficacy and therefore warranting the need for novel therapeutic strategies.

Gag-Pol autoprocessing is a complex process in which Gag-Pol serves as both the enzyme and the substrate. While the precise enzymatic kinetics and regulatory mechanisms remain to be fully elucidated, it is well established that mature PR production requires precursor autoproteolysis at both its N- and C-termini. Mutagenesis studies blocking cleavage between PR and RT show no significant impact on PR activity and only a moderate reduction in infectivity [234], suggesting that C-terminal fusions have a limited impact on mature PR function. In contrast, blocking cleavage between p6* and PR nearly abolishes infectivity [232, 233, 273], underscoring the crucial role of N-terminal cleavage in liberating mature PR and defining p6*-PR as a miniprecursor. *In vitro* studies further confirm a dramatic increase in proteolytic activity coupled with the removal of p6* from the p6*-PR miniprecursor [200, 236, 292]. We previously established a cell-based assay to study p6*-PR precursor autoprocessing in transfected mammalian cells [187, 242, 244, 245]. Using this system, we showed that catalytic site PIs are significantly less effective at suppressing precursor-mediated autoprocessing, suggesting that mature PR and its precursors differ both enzymatically and conformational [187, 238, 242-248, 293]. Findings from other studies also support this notion [200, 232, 241, 249, 250, 270, 271]. Consequently, we proposed targeting protease precursors for the discovery of novel inhibitors with mechanisms of action distinct from those of known catalytic site PIs.

Structure-based rational design of autoprocessing inhibitors is impractical due to the lack of detailed atomic information on the p6*-PR precursor [201]. To overcome this limitation, we adapted our cell-based autoprocessing assay for high-throughput screening (HTS) using an amplified luminescent proximity homogeneous assay ELISA (AlphaLISA) to quantify autoprocessing efficiency [248]. This platform faithfully recapitulated all phenotypes observed with proviral constructs, suggesting a similar underlying autoproteolysis mechanism [243-248], and was previously validated in a screen of ~23,000 diverse small-molecule compounds [248]. In this study, we expanded our screening efforts to a library of ~320,000 small molecules to identify chemical scaffolds that inhibit p6*-PR precursor autoprocessing. Positive hit compounds were further validated using a newly developed infectivity assay capable of detecting a single infectious unit across a broad range of viral inputs. Several chemical scaffolds demonstrating infectivity inhibition were identified, and their structure-activity relationships (SAR) were explored through an analog-by-catalog approach. Finally, the top hit compound C7 was assessed for its efficacy against a panel of multi-PI-resistant strains isolated from patients. Collectively, our results provide proof of concept for novel drug discovery targeting HIV protease precursors.

4.2 Materials and Methods

DNA Mutagenesis

All plasmids used in this study were constructed using standard PCR-mediated mutagenesis and cloning techniques as previously described [238, 242-245, 248]. The H2B reporter proviral construct was engineered from a pNL4-3 reporter plasmid expressing human placental alkaline phosphatase (a kind gift from Dr. Ned R. Landau) [299]. In brief, the H2B-mRFP coding sequence was inserted in-frame immediately after the third codon of nef, followed by a stop codon upstream of the unique XhoI site in the nef sequence. As a result, H2B-mRFP is expressed upon productive integration of proviral DNA following infection, while nef expression is not anticipated. Additionally, the PciI-to-PciI fragment (1.4 kb) spanning the entire vpu and N-terminal half of the env coding sequence was deleted and replaced with an 8-nt linker carrying a BssHII site, ensuing that neither Vpu nor functional Env is produced in this construct. Each construct was verified by sequencing analysis and is available upon request through a standard material transfer agreement.

Cell Culture and Transfection for AlphaLISA HTS

HEK 293T cells were purchased from ATCC (Manassas, VA) and maintained in DMEM medium supplemented with 10% fetal bovine serum, 100 units/mL of penicillin G sodium salt, and 100 µg/mL of streptomycin sulfate. Transfection of HEK 293T cells using calcium phosphate in multiwell plates was performed as previously described [242, 243, 247, 248]. For AlphaLISA analysis of bulk transfected cells in 384-well plates, HEK 293T cells were seeded at ~20% confluency in either 10 cm or 15 cm dishes and allowed to attach and grow for ~12 hr prior to transfection. Chloroquine was added to a final concentration of 25 µM before transfection. A DNA-calcium mixture was prepared by combining 6 µg plasmid DNA in 788.4 µL H_2O, followed by the addition of 111.6 µL of 2 M $CaCl_2$. Then, 900 µL of 2× HBS buffer (50 mM Hepes, 10 mM KCl, 12 mM dextrose, 280 mM NaCl, and 1.5 mM Na_2HPO_4, pH 7.04-7.05) was added dropwise to the DNA-calcium mixture with gentle vortexing. The resulting mixture was added dropwise to each dish. At 9–12 hr post-transfection, bulk transfected cells were detached using trypsin/EDTA and then pooled in DMEM before seeding 30 µL per well in a 384-well plate at ~25% calculated confluency. PIs or test compounds (Dissolve in 20 µL DMEM) were then added to each well. Negative controls consisted of transfected cells treated with up to 1.25% DMSO alone, as most PIs and small molecule compounds were dissolved in DMSO stock solutions.

After ~24 hr of incubation, the culture medium was removed by a gentle swing, and cells were lysed *in situ* with 20 µL assay solution containing 1× AlphaLISA Immunoassay buffer (PerkinElmer AL000F), protease inhibitor cocktail, 15 µg/mL anti-Flag acceptor beads (PerkinElmer AL112R), and 11.25 µg/mL glutathione donor beads (PerkinElmer 6765301). As a positive control, purified GST-Flag-p6* protein, serially diluted in 1× AlphaLISA Immunoassay buffer (5-fold dilutions, 8 points total), was spiked into wells containing only DMSO. Following at least another additional 2 hr incubation at 37 °C, fluorescence signals were recorded first when needed, followed by AlphaLISA signal detection using either an EnSpire or an EnVision 2104 Microplate Reader (PerkinElmer).

For HTS in a 1536-well format, HEK293T cells were bulk-transfected using JetPRIME (Polyplus, New York) following the manufacturer's recommendations. At 16 hours post-transfection, cells were collected, cryogenically snap-frozen into aliquots to ensure consistent performance across screens, and seeded into 1536-well plates pre-spotted with test compounds at 40-50% cell confluency in 5 µL. After ~24 hr of incubation, AlphaLISA detection reagents were directly added to the wells and AlphaLISA signals were measured following another 2 hr incubation at 37°C.

Generation of Single-round Infectious Virus Particles

HEK 293T cells were co-transfected with the H2B-mRFP reporter and a VSV-G encoding plasmid for Env pseudotyping using calcium phosphate as previously described [238, 242-245, 248]. Briefly, HEK 293T cells were seeded in 12-well plates. A total of 1 µg of plasmid DNA (0.8 µg of the viral reporter plasmid plus 0.2 µg of the VSV-G plasmid per well) was mixed with 65.7 µL of H_20 and 9.3 µL of 2 M CaCl2, followed by the dropwise addition of 75 µL of 2× HBS. The transfection solution was then added dropwise to the wells. After 7-9 hours of incubation, the culture medium was replaced with 1 mL of chloroquine-free medium containing PR inhibitors or HTS hits at the indicated concentrations. Approximately 50 hr post-transfection, culture supernatants containing viral particles were collected and clarified using 96-well 0.45 µm filter plates (VWR, cat# 97052-126). The filtered supernatant was divided into 650 µL and 150 µL aliquots. All samples were pelleted at 20,800 × g for at least 100 minutes through a 25% (w/v) sucrose cushion in PBS. The pelleted virus from the 650 µL aliquot was resuspended in 5 µL of

DMEM and incubated overnight at 4˚C for infection. The 150 µL aliquot was resuspended in 30 µL of 1.5× SDS loading buffer and subjected to SDS-PAGE analysis followed by Western blotting.

Quantification of Viral Particles by Western Blotting

Equal volumes of viral lysates were resolved by SDS-PAGE, transferred to a PVDF membrane (MilliporeSigma, cat# IPVH 00010), and probed with primary antibodies: mouse monoclonal anti-p24 (183-H12-5C, BEI Resources, cat# ARP-3537) and rabbit polyclonal anti-17 (BEI Resources, cat# ARP-4105). Secondary antibodies included IR700 fluorescence-labeled goat anti-rabbit (Rockland, cat# 611-132-003) and IR800 goat anti-mouse (Rockland, cat# 610-132-121). Blots were visualized using an Odyssey infrared dual-laser scanning unit (LI-COR Biotechnology, Lincoln, NE). The total p24 content for each viral sample was determined using ImageStudio software by summing the intensity of all p24-reactive bands. The total p24 content of untreated wild-type virus was arbitrarily set to 100 (AU), with all other samples calculated relative to this reference.

Infection and Quantification of Infectivity

U2OS cells (ATCC HTB-96) cells were cultured in DMEM supplemented with 10% fetal bovine serum, 100 units/mL penicillin G sodium salt, and 100 µg/mL streptomycin sulfate. For infection, U2OS cells were detached and resuspended to achieve ~25% confluency in a 384-well glass-bottom plate (Cellvis, cat# P384-1.5H-N). Pelleted viral particles resuspended in PBS were mixed with 40 µL of U2OS cell suspension, followed by an 8-fold serial dilution (5 µL of the virus-cell suspension added to 35 µL of fresh cell suspension), resulting in a total of 5-6 input values per virus prep. An equal volume (35 µL) of the virus-cell suspension was then seeded for infection. Approximately 50 hours post-infection, Hoechst stain (ThermoFisher, cat# H3570) was added to each well at a working concentration of 0.2 µg/mL and incubated at 37˚C for 30 minutes before live-cell imaging under 37˚C/5% CO_2 conditions. Imaging was performed using a Keyence fluorescence microscope (BZ-X710, Keyence Corporation of America, Itasca, IL) with a 20x objective in both DAPI and RFP channels. A 5x3 automated stitching program was applied to capture >1000 cells per sample.

For quantification, ImageJ software was used with a custom batch analysis macro to count blue nuclei (total cells) and red nuclei (infected cells). In brief, stitched images were converted to 8-bit grayscale and thresholded to distinguish signals from background noise. The “Fill Holes” and “Watershed” operations were applied to enhance nucleus masking and separate clustered nuclei. The "Analyze Particles" function was used with pre-defined sizes (300–9000 pixel units) and circularity (0.1–1.0) parameters. Nuclear counts were validated across a range of threshold values for accuracy. Some samples exhibiting extreme fluctuations in nuclear counts due to variations in fluorescence intensity or cell overcrowding required manual verification. For C6 SAR analysis and the multi-PI resistant mutant panel (Figures 4.5 and 4.6, respectively), infected cells were quantified using CellPose segmentation software [329, 330] with a custom nuclei segmentation model trained via the human-in-the-loop training function. Samples with significant variations in segmented nuclei due to fluorescence intensity fluctuations or cell crowding were cross validated using ImageJ or manual counting as needed. For integrated infectivity analysis, the area under the curve (AUC) was calculated using sigmoidal equations best fit to the corresponding infectivity curves, with viral input value ranging from 0.01 to 100.

4.3 Results

HTS of a small molecule library and hit compound selection

We previously engineered expression plasmids with the p6*-PR miniprecursor sandwiched between various fusion tags to study HIV precursor autoprocessing in transfected mammalian cells [242-247]. Domain organization of a typical fusion precursor is illustrated in Figure 4.1A. The NL4-3 derived p6*-PR contains two natural autoproteolysis sites: the proximal (P) site, located between p6* and PR, which is essential for the liberation of mature PR, and the distal (D) site at the N-terminal region of p6*. Autoprocessing at these two sites appears to be independent of each other [242, 244]. To specifically examine autoprocessing at the proximal site, we engineered the M1-PR precursor. Also, we previously reported that precursor autoprocessing at the proximal site is context-dependent, with the maltose binding protein signal peptide at the N-terminus leading to autoprocessing outcomes similar to those observed with viral particles produced by proviral constructs [245]. Therefore, the fusion precursors used for HTS also contained this signal peptide (Fig. 4.1A).

This assay was previously optimized for high-throughput screening (HTS) of autoprocessing inhibitors using an amplified luminescent proximity homogeneous assay (AlphaLISA) in a 384-well format [248]. AlphaLISA is a label-free, wash-free assay that utilizes latex-based donor and acceptor beads that are small enough to remain suspended in solution [352-355]. These beads can be conjugated with a variety of chemicals and/or antibodies to facilitate specific target binding. We employed glutathione-coated donor beads and anti-FLAG coated acceptor beads to quantify full-length fusion precursors in crude cell lysates (Fig. 4.1B). The donor beads are embedded with phthalocyanine, a photosensitizer, which, upon excitation at 680 nm, converts ambient oxygen into short-lived singlet oxygen ($t_{1/2} = 4$ µsec). Due to its high reactivity, singlet oxygen diffuses only ~200 nm in solution. The acceptor beads contain europium, which emits chemiluminescence peaking at 615 nm when it reacts with singlet oxygen. Consequently, the chemiluminescent signal is proportional to the amount of FL precursor under optimized conditions. Effective autoprocessing cleaves the precursor, resulting in an average distance greater than 200 nm between donor and acceptor beads, so only background chemiluminescent signal is produced.

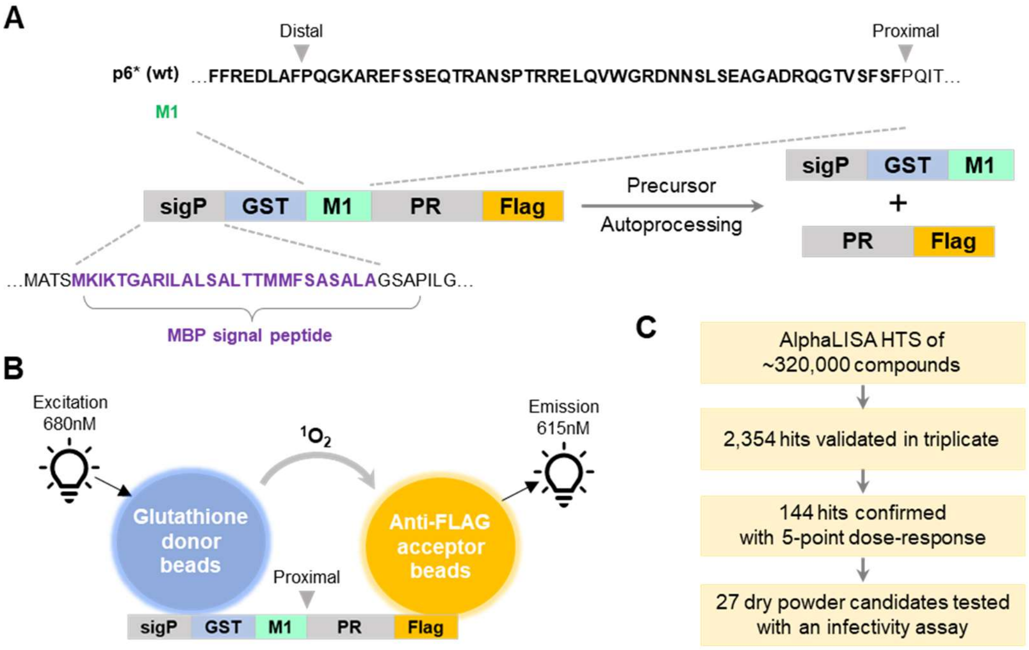

Figure 4.1. Schematic of fusion precursor construct (Panel A) and AlphaLISA (Panel B), and flow chart of an HTS campaign carried out at Sanford Burnham Prebys Discovery center (Panel C).

To further enhance throughput capacity, we miniaturized the assay to a 1536-well format and conducted a pilot screen of ~ 20,000 small-molecule compounds at a single dose (10 μM). The resulting scatterplot demonstrated that while negative (-) controls followed a tight Gaussian distribution around 0% inhibition, positive (+) controls displayed considerable variation across all plates (Supp Fig. 4.1). Despite this variability, plate-to-plate performance remained robust with strong signal-to-background (S/B) ratios, acceptable standard deviations, and Z' scores ≥0.5 after removing outlier wells (Supp Table 4.1). Given the low hit rate observed in our previous screen of ~25,000 small-molecule compounds [248], we evaluated apparent hit rates using two criteria: (1) a % inhibition threshold (with the positive control set at 100% inhibition) and (2) a Z-score (measured in standard deviation units). These analyses suggested that applying a ≥10% inhibition threshold or a Z-score > 4 would yield an overall hit rate of ~ 1% to capture weak hits (Supp Table 4.2). The full HTS campaign was subsequently completed following the same approach as the pilot screen (Supp Table 4.3). Using a Z-score ≥4, we identified 2,354 initial hits, corresponding to a 0.74% hit rate. These initial hits were cherry-picked and re-tested in triplicate using the primary AlphaLISA assay, confirming 144 hits. The confirmed hits then underwent an abbreviated 5-point dose-response analysis in triplicate (100, 50, 25, 12.5, and 6.25 μM; 2-fold dilutions), revealing 90 compounds with some degree of dose-dependent response, though many were weak. Of these, 27 commercially available compounds were selected for further confirmation and characterization.

Using the primary AlphaLISA assay, we evaluated these compounds at a single dose of 40 μM in quadruplicate, comparing their activity to darunavir (DRV), the most potent HIV protease inhibitor available in clinical use (Fig. 4.2A). Precursor autoprocessing was partially inhibited at 10 nM DRV (lightest blue data points) and completely suppressed at concentrations above 100 nM (darker blue data points). These compounds exhibited varying degrees of inhibitory activity: some showing partial inhibition like 10 nM DRV, while others demonstrated minimal effects,

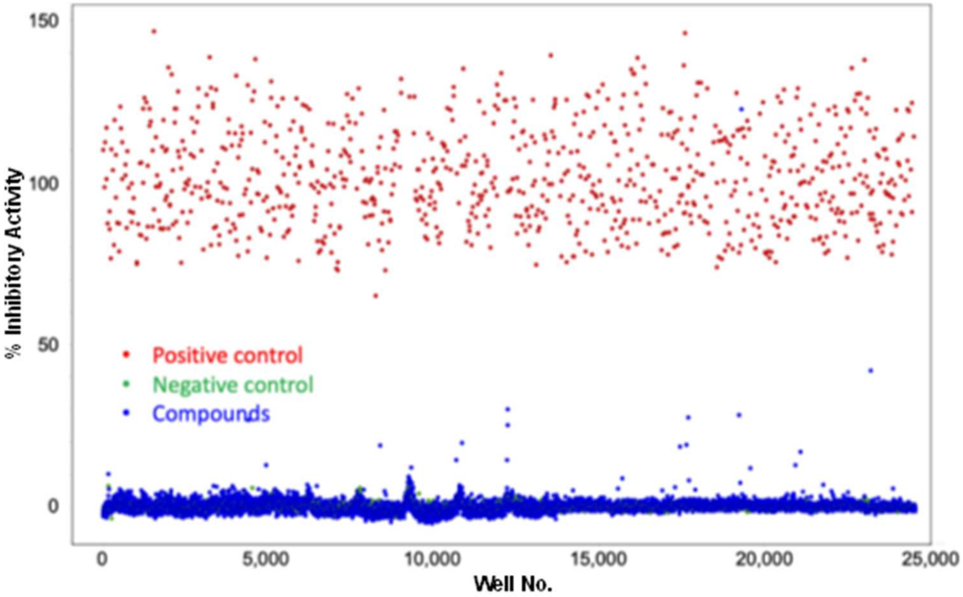

Supplemental Figure 4.1. Scatterplot of a pilot screen from sixteen 1536-well plates, with outlier data points excluded.

Supplemental Table 4.1. Performance of the pilot sixteen 1536-well plates.
3SD (%) is calculated as ((3 x SD of Negative Control)/Mean of Positive Control) x 100%
3SD (%) can be minimal hit selection criteria when using Positive control as reference

				Negative Control				**Positive Control**		
Plate ID	Date	Invalidate Wells (Positive control)	S/B	Mean	SD	SD (%)	**3SD (%)**	Mean	SD	Z' Factor
PN-021963.D04	exp 2	13	13	148	43	2.3	**6.8**	1882	255	0.52
PN-021964.D04	exp 2	7	12	130	36	2.3	**7.0**	1541	208	0.52
PN-021965.D04	exp 2	10	13	132	42	2.6	**7.6**	1662	244	0.48
PN-021966.D04	exp 2	9	13	122	29	1.8	**5.4**	1594	210	0.54
PN-021968.D04	exp 3	12	14	123	43	2.6	**7.9**	1632	225	0.51
PN-021969.D04	exp 3	16	11	133	60	4.0	**11.9**	1508	198	0.51
PN-021970.D04	exp 3	15	11	151	56	3.6	**10.8**	1543	177	0.56
PN-021971.D04	exp 3	15	12	142	50	3.2	**9.6**	1578	209	0.52
PN-021972.D04	exp 3	10	12	148	51	3.0	**9.0**	1701	217	0.54
PN-021956.D04	exp 1	10	19	120	33	1.4	**4.3**	2296	340	0.51
PN-021957.D04	exp 1	10	17	125	36	1.6	**4.9**	2223	334	0.5
PN-021958.D04	exp 1	6	20	120	29	1.2	**3.6**	2383	359	0.5
PN-021959.D04	exp 1	16	21	114	28	1.2	**3.5**	2369	346	0.52
PN-021960.D04	exp 1	9	20	120	30	1.2	**3.7**	2415	339	0.54
PN-021961.D04	exp 1	3	21	120	26	1.0	**3.1**	2546	362	0.54
PN-021962.D04	exp 1	5	21	138	52	1.8	**5.5**	2796	351	0.58
Average		10	16	130	40	2.2	**6.5**	1979	273	0.52
SD		4	4	12	11	0.9	**2.7**	438	70	0.02

Supplemental Table 4.2. Hit rates vs different selection criteria

By % inhibition (+) control = 100%			By Z-score (units of s.d.)	
Selection	Hits		Selection	Hits
≥ 10%	19 (0.09%		≥ 3	431 (2.10%)
≥ 15%	12 (0.06%)		≥ 5	86 (0.42%)
≥ 20%	7 (0.03%)		≥ 8	28 (0.14%)
≥ 30%	2 (0.01%)		≥ 10	22 (0.11%)
≥ 40%	2 (0.01%)		≥ 15	14 (0.07%)
≥ 50%	1 (0.005%)		≥ 20	10 (0.05%)

Supplemental Table 4.3. Small molecule screening data

Category	Parameter	Description
Assay	Type of assay	A cell-based function assay
	Target	HIV-1 fusion precursor with the p6*-PR miniprecursor sandwiched between GST and Flag
	Primary measurement	quantification of the unprocessed fusion precursor in cells treated with compounds
	Key reagents	AlphaLISA glutathione-coated donor beads and anti-Flag coated acceptor beads
	Assay protocol	doi: 10.1038/s41598-018-36730-4
	Additional comments	
Library	Library size	320,000
	Library composition	Drug-like small-molecule compounds
	Source	Sanford Burnham Prebys Medical Discovery Institute, a collection of ~350,000 small molecules
	Additional comments	
Screen	Format	1536-well
	Concentration(s) tested	10 µM
	Plate controls	DMSO at a final concentration of 0.5% as the negative control; darunavir (0.5 µM), a known HIV protease inhibitor, as the positive control.
	Reagent/ compound dispensing system	Labcyte Echo 555 acoustic dispensers
	Detection instrument and software	An EnSpire or EnVision 2104 microplate reader (PerkinElmer).
	Assay validation/QC	S/B ≥16, z’ ≥0.5 (Supplementary table 1)
	Correction factors	
	Normalization	The mean of positive controls of each plate is normalized to 100%
	Additional comments	
Post-HTS analysis	Hit criteria	≥10% inhibition or Z-score >4
	Hit rate	0.74%
	Additional assay(s)	Orthogonal infectivity assay
	Confirmation of hit purity and structure	Re-purchased dry powder of the 27 validated hits
	Additional comments	

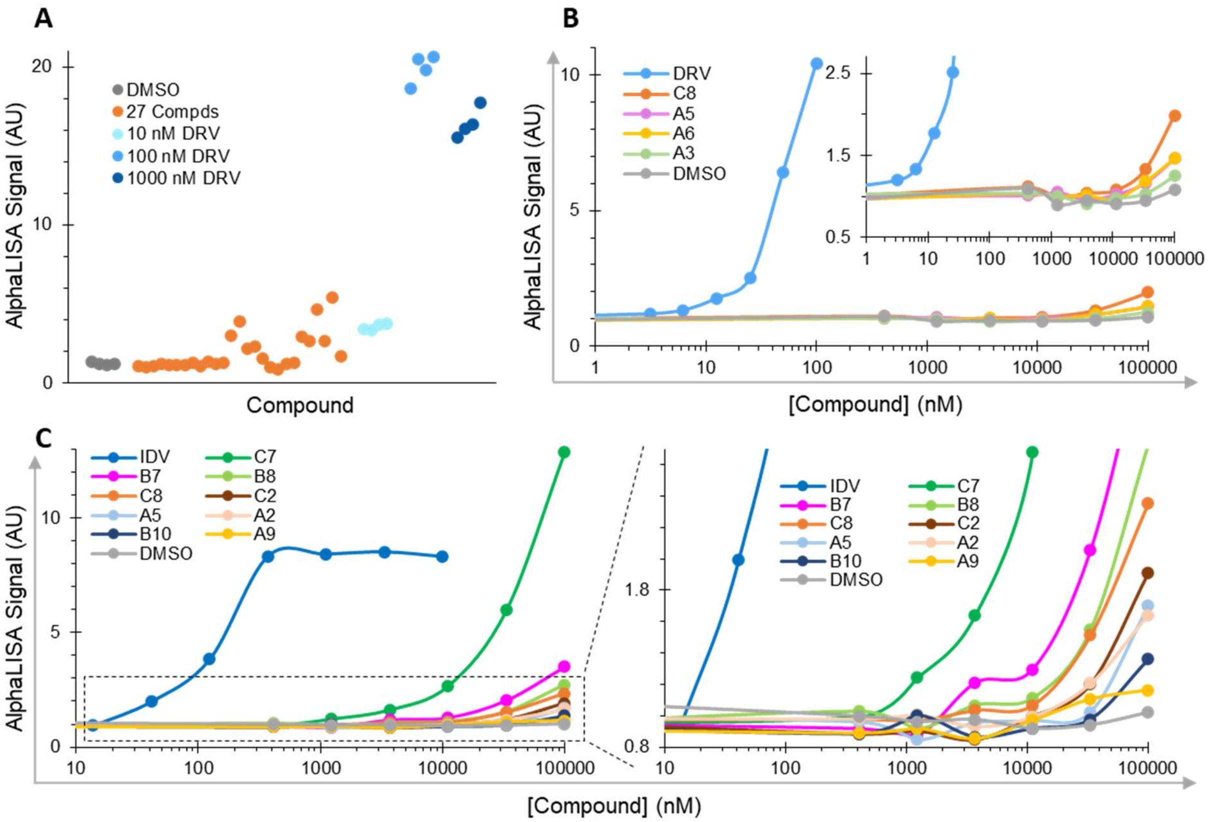

Figure 4.2. Confirmation of the 27 candidates using the primary AlphaLISA screening assay. Darunavir (DRV) or indinavir (IDV) was analyzed in parallel as a positive control. Each data point represents the average of duplicate or quadruplicate samples. The graphs are representative of two independent experiments.

comparable to the DMSO control. Similarly, in a 7-point, 3-fold serial dilution analysis, with the highest concentration tested at 100 μM (Figs. 4.2B & C), most compounds displayed marginal activity at high micromolar concentrations. Notably, compound C7 stood out with a strong AlphaLISA signal, suggesting potential inhibition of precursor autoprocessing. Additionally, a few other compounds demonstrated activity above the DMSO control. Although these compounds were less potent than known PI controls in suppressing precursor autoprocessing, the confirmation of several hits showing partial inhibitory activity is encouraging. These findings underscore the potential of our HTS campaign in discovering novel inhibitory compounds.

Orthogonal analysis of the 27 hit compounds

To further evaluate these hit compounds, we employed our newly established infectivity assay, designed to identify and quantify individual infectious units in viral samples. The conversion of an immature, non-infectious particle into a fully infectious virus requires a series of highly coordinated proteolytic reactions catalyzed by HIV PR. Each HIV particle typically contains ~1,500 copies of Gag and 80 copies of Gag-Pol, collectively involving approximately 8,000 proteolytic reactions at 10 distinct substrate sites, each exhibiting unique proteolysis kinetics. These maturation reactions respond differently to PI treatment, leading to heterogeneity in viral morphology and infectivity. This variability is particularly evident in viral particles generated via transient transfection, which exhibit a spectrum of maturation states [220]. Since productive infection depends on successful integration of reverse-transcribed proviral DNA and subsequent expression of early genes such as tat, rev, and nef, we engineered a reporter encoding H2B-mRFP within the nef coding region to facilitate the identification of individual infectious units. Incorporation of expressed H2B-mRFP into nucleosomes highlights the nucleus in red, allowing for the quantification of infected cells via fluorescence microscopy.

Since viral input and the exact number of infectious units in each sample vary significantly depending on expected experimental variation (Fig. 4.3A & B), we infect a constant number of target U2OS cells with a broad range of viral inputs (spanning ~10,000-fold) based on total p24-reactive signals. Infectivity is then determined by quantifying the number of H2B-RFP-positive cells per 1,000 target U2OS cells, which follows a characteristic sigmoidal curve as a function of viral input (Figs. 4.3C-H). The plateau phase of the curve reflects conditions where the number of infectious units exceeds the available target cells, resulting in nearly 100% infection which is likely an underestimate of the actual number of infectious units. Conversely, the tail end of the curve corresponds to conditions where viral input is too low to mediate productive infection. The middle region, where infectivity increases proportionally with viral input, provides the optimal range for reliable quantification and comparison. Notably, there is no one-size-fits-all viral input that guarantees infectivity within this middle region for meaningful side-by-side comparison. Consequently, we performed infectivity analysis over a broad range of viral inputs.

The 27 hit compounds were randomly divided into two groups and tested at a single dose of 40 μM for initial assessment. To account for potential experimental variations, each experiment included the following controls: untreated (no drug) samples and samples treated with 1 nM and 4 nM DRV, a known PI with EC_{50} values in the single-digit nM range. At 40 μM, many compounds demonstrated minimal inhibitory activity, as their infectivity response curves closely resembled those of the untreated WT controls (Figs. 4.3C & D). Consequently, this group was classified as "minimally responsive," consistent with the AlphaLISA validation results (Fig. 4.2). Encouragingly, a subset of compounds exhibited marginal inhibitory effects, with infectivity response curves overlapping or nearly overlapping with the 1 nM DRV-treated condition (Figs. 4.3E & F). Additionally, compounds B7, C5, C6, C7, and C8 displayed infectivity profiles comparable to the 4 nM DRV-treated condition (Figs. 4.3G & H), suggesting a promising inhibitory effect. Notably, many "inhibitory" candidates also showed reduced viral

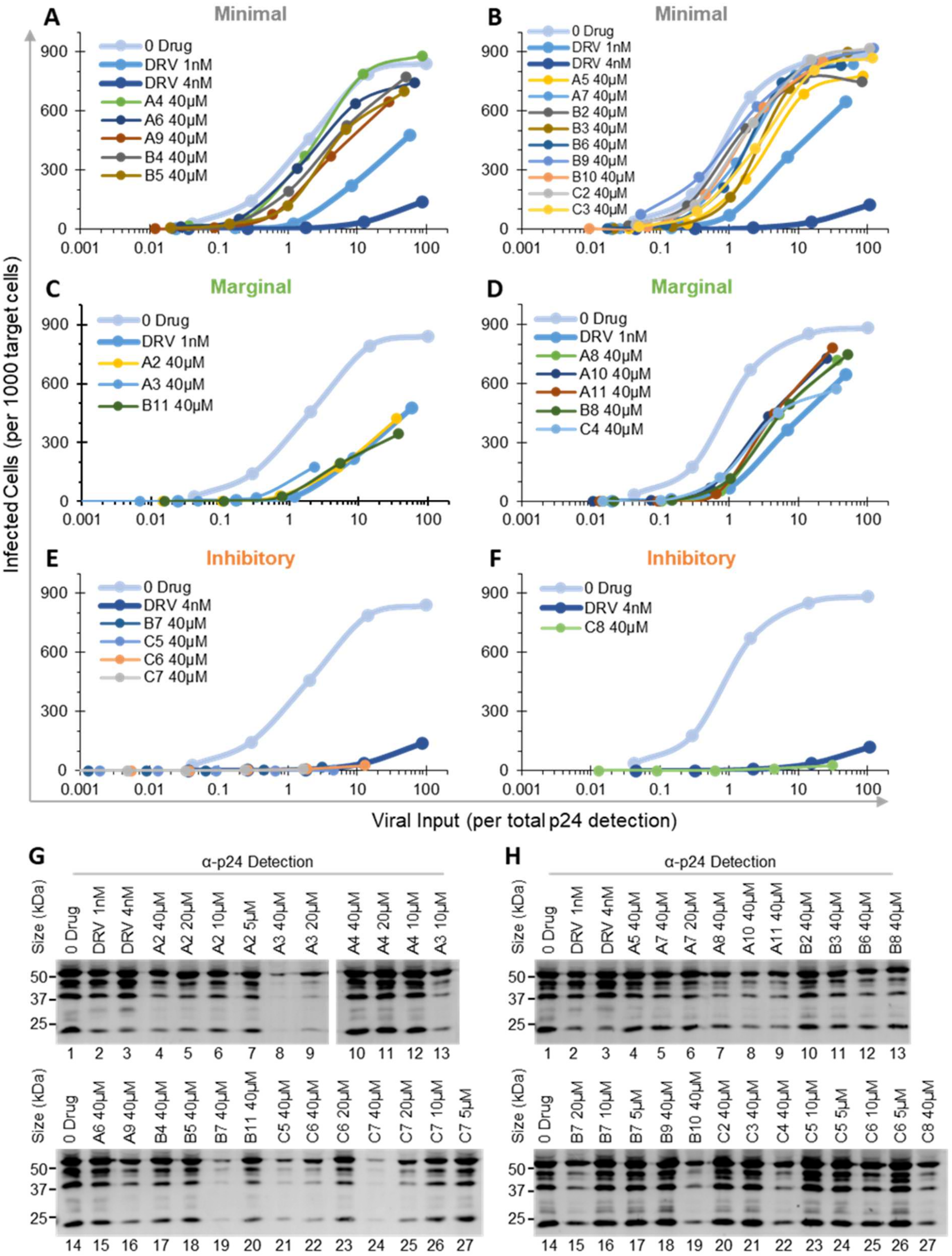
A
Minimal
0 Drug
DRV 1nM
DRV 4nM
A4 40μM
A6 40μM
A9 40μM
B4 40μM
B5 40μM
B
Minimal
0 Drug
DRV 1nM
DRV 4nM
A5 40μM
A7 40μM
B2 40μM
B3 40μM
B6 40μM
B9 40μM
B10 40μM
C2 40μM
C3 40μM
C
Marginal
0 Drug
DRV 1nM
A2 40μM
A3 40μM
B11 40μM
D
Marginal
0 Drug
DRV 1nM
A8 40μM
A10 40μM
A11 40μM
B8 40μM
C4 40μM
E
Inhibitory
0 Drug
DRV 4nM
B7 40μM
C5 40μM
C6 40μM
C7 40μM
F
Inhibitory
0 Drug
DRV 4nM
C8 40μM
0
300
600
900
0.001
0.01
0.1
1
10
100
Infected Cells (per 1000 target cells)
Viral Input (per total p24 detection)
G
α-p24 Detection
Size (kDa)
0 Drug
DRV 1nM
DRV 4nM
A2 40μM
A2 20μM
A2 10μM
A2 5μM
A3 40μM
A3 20μM
A4 40μM
A4 20μM
A4 10μM
A3 10μM
50
37
25
1 2 3 4 5 6 7 8 9 10 11 12 13
Size (kDa)
0 Drug
A6 40μM
A9 40μM
B4 40μM
B5 40μM
B7 40μM
B11 40μM
C5 40μM
C6 40μM
C6 20μM
C7 40μM
C7 20μM
C7 10μM
C7 5μM
50
37
25
14 15 16 17 18 19 20 21 22 23 24 25 26 27
H
α-p24 Detection
Size (kDa)
0 Drug
DRV 1nM
DRV 4nM
A5 40μM
A7 40μM
A7 20μM
A8 40μM
A10 40μM
A11 40μM
B2 40μM
B3 40μM
B6 40μM
B8 40μM
50
37
25
1 2 3 4 5 6 7 8 9 10 11 12 13
Size (kDa)
0 Drug
B7 20μM
B7 10μM
B7 5μM
B9 40μM
B10 40μM
C2 40μM
C3 40μM
C4 40μM
C5 10μM
C5 5μM
C6 10μM
C6 5μM
C8 40μM
50
37
25
14 15 16 17 18 19 20 21 22 23 24 25 26 27

Figure 4.3. Assessment of 27 candidates using a newly established HIV infectivity assay. Viral particles, produced by transfected HEK 293T cells and treated with hit compounds or darunavir (DRV), were divided into two aliquots: ~3/4 were pelleted to infect U2OS cells (Panel A-F), and the remaining ~1/4 were analyzed by WB to quantify virus input based on total p24-reactive signals (Panel G-H). Constant numbers of U2OS target cells were infected with a wide range of virus inputs (over ~10,000-fold) based on total p24-reactive signals. Infectivity is defined as the number of H2B-RFP positive cells per 1,000 target cells, exhibiting a typical sigmoidal profile as a function of virus input. The total p24-reactive signals from the wild-type control without PI treatment were arbitrarily set to 100, and the p24 signals of other samples were expressed relative to the wild-type control to represent viral input (Panel G-H). The plots are representative of two independent experiments.

input, particularly at higher concentrations, as indicated by decreased total p24-reactive signals (Figs. 4.3A & B). This reduction in viral input resulted in a leftward shift in the infectivity profile when plotted against virus input normalized to total p24-reactive signals, relative to the untreated WT control. We speculate that this phenomenon may arise from one or more factors, either independently or in combination: (1) the compounds may be cytotoxic at high micromolar concentrations, leading to reduced viral particle production from transfected cells, or (2) they may directly suppress viral production through a yet-to-be-defined dose-dependent mechanism. Further investigation is necessary to delineate the underlying causes and inform subsequent pharmacological development.

Structure-Activity Relationship (SAR) Analyses via Analog-by-Catalog

Among these inhibitory candidates, we focused on compounds C7 and C6 for their similar molecular structures (Fig. 4.4A) and consistent inhibitory activity in both AlphaLISA and infectivity assays. Both share a common core scaffold with a bromide extension at moiety #1, differing only at moiety #2–C7 contains a piperidine ring, whereas C6 features a morpholine ring. To evaluate the impact of these structural differences, we examined vial infectivity following treatment with C7 or C6 at concentrations ranging from 1.25 μM to 40 μM in 2-fold serial dilutions. For comparison, viral samples treated with DRV were included in the same experiment (Fig. 4.4B). Both C7 and C6 exhibited clear dose-dependent inhibition of viral infection (Figs. 4.4C & D). We also observed reduction of viral input particularly in samples treated with ≥20 μM of either compound (Fig. 4.4E). WB analysis revealed that while the proportion of fully processed p24 among total p24-reactive bands remained similar, the total amount of pelleted viral particles decreased at high concentrations of C7 and C6. In contrast, DRV treatment did not reduce viral production but instead lowered the ratio of fully processed p24, a well-documented effect of known PIs. These differences in viral production and Gag processing hint that C7 and C6 inhibit infectivity through mechanisms distinct from DRV.

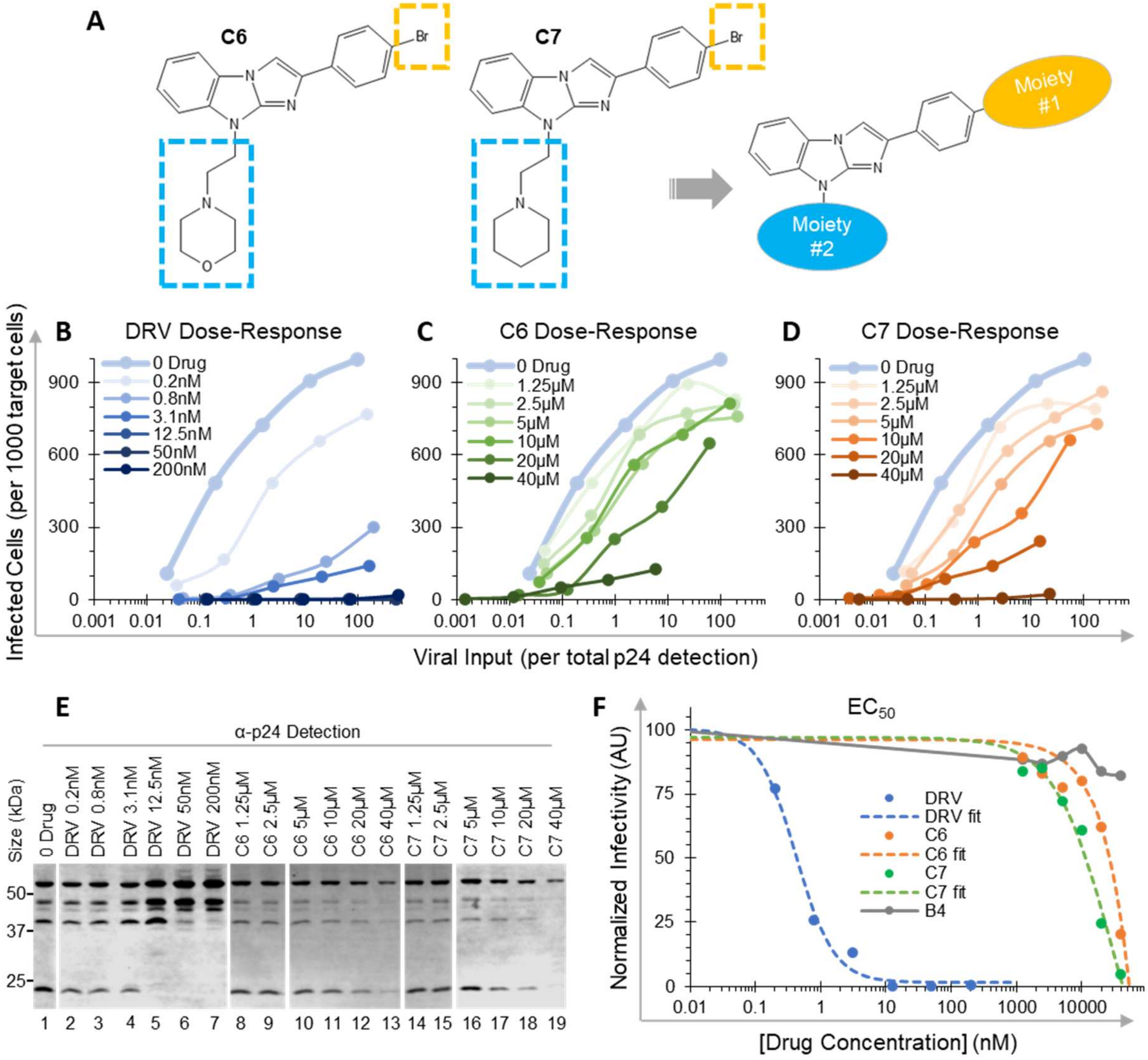

Figure 4.4. Comparative analysis of C7 vs. C6 to assess the effects of different moieties on anti-HIV infectivity. Compounds C7 and C6 share the same core structure and bromide extension at moiety #1, with slight differences at moiety #2 (Panel A). Both were tested with 2-fold serial dilutions, with 40 μM as the highest concentration, in parallel with DRV at concentrations surrounding its known EC_{50} value (Panels B-D). Western blot detection of total p4 content was used to normalize infectivity profiles, with the total p24 signal from untreated WT set to 100 (Panel E). The area under each infectivity curve was calculated to represent integrated infectivity and plotted against drug concentration, allowing estimation of EC_{50} values of each compound (Panel F). The plots are representative of three independent experiments.

To further compare potency, we calculated the area under the curve (AUC) to correlate integrated infectivity with drug concentration for estimation of apparent EC_{50} values (Fig. 4.4F). DRV demonstrated potent inhibition with an EC_{50} < 1 nM, whereas C7 and C6 exhibited EC_{50} values of ~10 µM and ~25 µM, respectively. In contrast, compound B4, another candidate from the 27 hits, showed no detectable inhibition at concentrations up to 40 µM (Fig. 4.4F, gray dots). Although C7 and C6 were significantly less potent than DRV, they provide proof of concept for developing novel inhibitors targeting HIV protease precursor autoprocessing. Interestingly, C7 consistently outperformed C6, albeit by a small but reproducible margin, suggesting that structural modifications at moiety #2 may influence activity, offering valuable insights for further pharmacological development.

To assess the impact of modifications at moiety #1, we analyzed a panel of commercially available C6 analogs (Fig. 4.5A). The WT control, treated with or without DRV at concentrations ranging from 0.31 nM to 10 nM (Fig. 4.5B), was compared to C6 and its analogs (Figs. 4.5C–G). Among these, compound D4, which carries a phenyl group at moiety #1, exhibited slightly greater inhibition than the bromide group in C6, particularly at concentrations above 20 µM. In contrast, substitutions with a methyl group (D5), hydrogen (D6), or fluorine (D7) resulted in reduced inhibitory potency (Figs. 4.5E–G). Western blot analysis consistently detected reduced viral input in C6- and D4-treated samples at concentrations ≥20 µM, while the ratio of fully processed p24 remined similar (Fig. 4.5H), consistent with a mechanism of action distinct from known PIs. AUC analysis of integrated infectivity further confirmed the relative contributions of these chemical groups, ranking phenyl ≥ bromine > methyl/hydrogen/fluorine (Fig. 4.5I). These SAR findings highlight the utility of our infectivity assay in sensitively assessing the effects of diverse chemical modifications, providing valuable insights into structural features that influence compound activity.

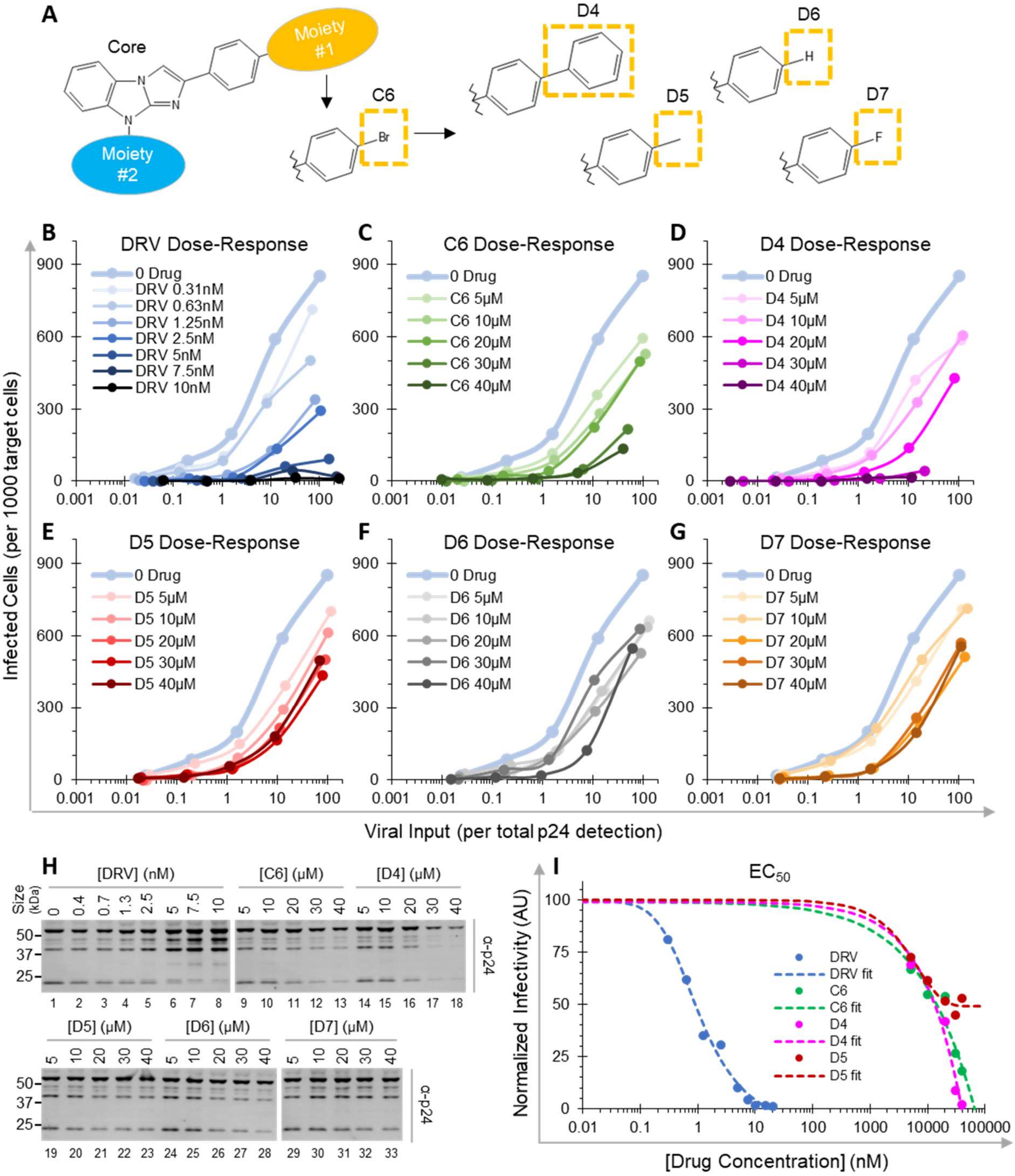

Figure 4.5. Schematic of a panel of C6 analogs carrying various chemical groups at moiety #1 (Panel A). Dose-response curves to DRV (Panel B) and each compound (Panels C-G) along with total p24 detection (Panel H) were used to estimate EC_{50} values of indicated compounds (Panel I). The area under each curve represents integrated infectivity. The plots are representative of three independent experiments.

Compound C7 inhibits WT and several PI-resistant mutants with similar potency

To further investigate the mechanism of action of these hit compounds, we examined whether and how compound C7 affects other viruses with p6*-PR sequences different from the NL4-3-derived sequence, the target of this HTS campaign. Three previously reported PI-resistant p6*-PR sequences [255] were selected, and are referred to by the respective letter codes (mutant H, M, or X) (Fig. 4.6A). Infectivity analysis confirmed their varying resistance to DRV with EC_{50} values ranged from ~200 nM (for mutant H and M) to > 1 μM (for mutant X), while EC_{50} for WT control is ~ 1 nM (Figs. 4.6B-G). Encouragingly, C7 treatment resulted in a similar dose-response inhibition for all tested mutants as well as the NL4-3 control (Figures 4.6H−K). At low micromolar concentrations (< 20 μM), the infectivity profiles overlapped, indicating low antiviral potency, which is consistent with these initial hits being partially active. However, treatment with C7 at ≥20 μM reduced the infectivity of all three tested resistant mutants and the NL4-3 control to comparable levels, along with a reduction of virus input (Fig. 4.6L). Integrated infectivity analysis demonstrated similar EC_{50} values less than 50 μM (Fig. 4.6M), despite the varying levels of DRV resistance (Fig. 4.6G). These findings suggest that compound C7 functions through a distinct mechanism from DRV, highlighting its potential as a pan-inhibitor targeting yet-to-be-identified, more conserved functional groups or motifs involved in HIV protease precursor autoprocessing.

4.4 Discussion

Proof of concept for an innovative drug discovery approach

Growing evidence suggests that HIV-1 protease precursors differ enzymatically—and likely conformationally—from mature PRs [187, 238, 242, 244, 249]. For example, current PIs, designed to target the catalytic site of mature PRs, are less effective at suppressing precursor autoprocessing, a phenomenon observed in both HIV-1 protease and SARS-CoV-2 main

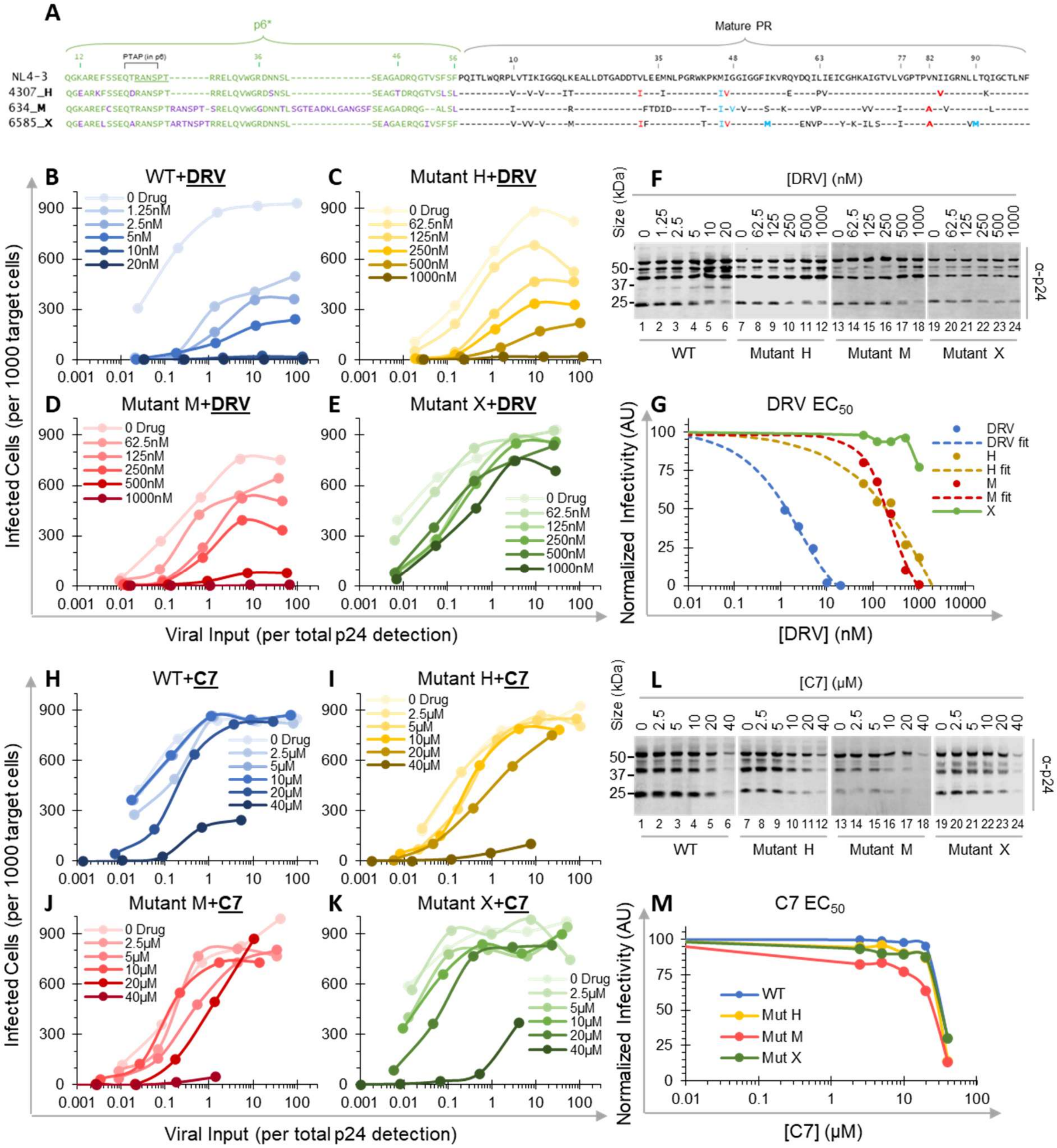

Figure 4.6. The p6*-PR sequences of three mutants derived from patients with PI resistance are shown in comparison to the NL4-3 strain (Panel A). Dose-response curves to DRV (Panels B-F) or C7 (Panels H-L) were used to estimate EC_{50} values of each sequence in response to DRV (Panel G) or C7 (Panel M). The area under each curve represents integrated infectivity. The plots are representative of three independent experiments.

protease precursors [242, 244, 248, 249, 356]. This suggests that novel inhibitors targeting precursor autoprocessing through distinct mechanisms could offer a new strategy to combat drug resistance and enhance cART efficacy. However, rational drug design remains unfeasible due to the lack of atomic-resolution structures of HIV-1 protease precursors and their inherent catalytic flexibility [187, 244, 245]. To overcome these obstacles, we developed a cell-based assay for functional screening of autoprocessing inhibitors in transfected HEK 293T cells expressing a fusion precursor [248]. This assay was validated using known PIs, and a previous screen of ~20,000 compounds (Life Chemicals diversity set) identified ~20 potential hits with slight activity above DMSO controls, though none were confirmed by the primary assay [248]. In the current HTS of ~320,000 small molecules, we identified 2,354 positive hits, but only a handful were validated with partial activity. The low hit and confirmation rates are expected by design for high selectivity. Additionally, since precursor autoprocessing is believed to be an intramolecular proteolysis event [241], it is inherently difficult to suppress. This underscores the necessity of large-scale HTS campaigns to uncover chemical scaffolds or fragments as starting points for innovative drug development. The successful identification of C7 and its analogs provides proof of concept for this approach in novel drug discovery.

Selected hits exhibited novel mechanisms of action

Although the confirmed hit compounds only partially suppressed precursor autoprocessing in the primary AlphaLISA assay (Fig. 4.3), they nonetheless inhibited viral infectivity with low micromolar potency in a highly sensitive assay capable of detecting single infectious units (Figs. 4.4F & 4.5I). These findings suggest that even a mild disruption of p6*-PR processing can have a profound impact on viral infectivity, consistent with previous reports [131, 135, 180, 239, 357-360]. Notably, the top hit, compound C7, demonstrated similar potency in inhibiting viral infectivity of both WT and multiple PI-resistant mutants (Fig. 4.6M), suggesting a distinct mechanism of action from known PIs. We acknowledge that inhibitory effects were observed only at high micromolar concentrations (*e.g.*, >20 µM), at which point reduced viral production was also evident. This raises the possibility that the observed inhibition of infectivity could be due to a decrease in viral input caused by hit treatment at high micromolar concentrations. Nonetheless, it is noteworthy that compounds selected to interfere with autoprocessing also led to reduced viral production—an effect not observed with known PIs, which suppress viral infectivity without impacting viral production. Our findings provide compelling evidence that these selected hits operate through mechanisms distinct from known PIs. Further hit-to-lead optimization of these candidates holds promise for identifying more potent inhibitors to combat drug resistance and improve cART efficacy.

Precise SAR analysis enabled by sensitive infectivity assay

The 27 validated hits comprise of diverse chemical scaffolds with minimal resemblance to known PIs. We focused on C7 and C6 as they share a common core scaffold. Our initial SAR analysis, conducted via analogy-by-catalog, centered on C6 simply because of commercial availability, whereas many C7 analogs were not readily accessible. However, using our sensitive infectivity assay, we were able to discern subtle differences in the contribution of moiety #1 substitutions to inhibitory activity (Fig. 4.5I). While this initial SAR analysis did not yield compounds with significantly improved potency, it demonstrated the feasibility of this approach for optimizing hit compounds into promising lead candidates.

In summary, this report presents a HTS campaign of small-molecule compounds targeting HIV-1 protease precursor autoprocessing, followed by hit characterization. Several validated hit compounds that partially suppressed precursor autoprocessing also inhibited viral infectivity in a highly sensitive infectivity assay. Notably, the top hit, compound C7, exhibited comparable potency against both WT and multiple PI-resistant mutants, suggesting a distinct mechanism of action from currently available PIs. However, further investigation and lead optimization are necessary, as the EC_{50} values of C7 and its analogs remain in the low micromolar range.

CHAPTER 5:

HIGH-THROUGHPUT SCREENING AND CHARACTERIZATION OF NATURAL PRODUCT EXTRACTS AND SUBFRACTIONS TARGETING HIV-1 PROTEASE PRECURSOR AUTOPROCESSING

5.1 Introduction

The HIV-1 protease (PR) is an essential viral protein encoded within the GagPol polyprotein. The viral PR is responsible for proteolytic processing of both Gag and GagPol polyproteins to liberate matrix (MA), capsid (CA), nucleocapsid (NC), reverse transcriptase (RT), and integrase (IN), all of which play essential roles in the viral lifecycle [190]. For complete Gag and GagPol processing, the protease must first undergo autoprocessing, in which the protease, embedded within GagPol, processes the cleavage sites at its own N- and C-termini to liberate the mature PR [143, 187]. Autoprocessing initiates within immature viral particles, which are largely composed of Gag, GagPol, and the viral genomic RNA; completion of autoprocessing and subsequent cleavage of Gag and GagPol by the mature PR facilitates virion maturation, or the transition from immature, non-infectious viral particles to mature, infectious viral particles [361, 362].

Autoprocessing is initiated via transient dimerization of two GagPol polyproteins to form a proteolytically active GagPol precursor which first processes the SP1/NC and TFR/p6* sites via an intramolecular mechanism [239-241]. Additionally, blockage of processing at the p6*/PR cleavage site via mutagenesis drastically reduces Gag/GagPol processing and nearly abolishes infectivity in live virus [232, 233], and various *in vitro* studies indicate that the PR gains mature-like activity only after removal of the N-terminal p6* peptide [200, 212, 231]. Thus, the p6*-PR has been identified as a mini-precursor for autoprocessing study, as processing of the p6*/PR cleavage site is required for Gag/GagPol processing and particle infectivity. Due to its indispensable role in the viral lifecycle, the PR has long been a subject of intense study. To date, nine protease inhibitors (PIs) have been developed and approved for use by the FDA. All nine PIs are non-cleavable substrate analogs which bind to the mature PR active site with nanomolar affinities [275-277, 351, 363]. Unfortunately, the emergence of drug-resistant HIV strains in patients treated with these PIs is a recurrent problem [259, 280, 364, 365] warranting novel inhibitors with different mechanisms of action (MOAs) to improve the overall success of cocktail therapies.

Despite the potency and efficacy of the current PIs against the mature PR, PIs are much less effective against the p6*-PR mini-precursor. Various studies, including data from our lab, show that p6*-PR processing *in vitro*, in *E. coli*, and in mammalian cells is up to 1000-fold less sensitive to PI treatment compared to the mature PR [242, 244, 245, 248-251]. Likewise, inhibition of the initial cleavage at SP1/NC by GagPol dimers also requires PI concentrations far exceeding that required for mature PR inhibition [241, 251]. This data together suggests that the mature PR and its precursors are enzymatically different. However, structure-based design of autoprocessing inhibitors is infeasible as precursor structures are unavailable [201]. Here, we used a previously established cell-based AlphaLISA platform [243-245, 247, 248, 356] for functional screening of 2030 natural product extracts (NPEs) to identify candidates showing inhibitory activities against the p6*-PR autoprocessing reaction. We employed a newly developed infectivity assay to validate the top two screening hits in live virus particles, which both show dose-dependent inhibition of infectivity. Fractionation and sub-fractionation of the crude NPEs proved successful for separation of inhibitory compounds from non-inhibitory compounds. Thus, our work offers proof-of-concept for the use of NPEs in drug screening and identified several compounds that set the foundation for autoprocessing inhibitor development. This anti-HIV strategy of targeting different functional stages (precursor and mature PR) at different regions (catalytic and non-catalytic site) of the protease will hopefully offer new promise in combating the HIV epidemic.

5.2 Materials and Methods

DNA Mutagenesis

All plasmids used in this study were constructed using standard PCR-mediated mutagenesis and cloning techniques as previously described [238, 242-245, 248]. The H2B reporter proviral 287 construct was engineered from a pNL4-3 reporter plasmid expressing human placental alkaline phosphatase (a kind gift from Dr. Ned R. Landau) [135]. In brief, the H2B-mRFP coding sequence was 289 inserted in-frame immediately after the third codon of nef, followed by a stop codon upstream of the unique XhoI site in the nef sequence. As a result, H2B-mRFP is expressed upon productive integration of proviral DNA following infection, while nef expression is not anticipated. Additionally, the PciI-to-PciI fragment (1.4 kb) spanning the entire vpu and N-terminal half of the env coding sequence was deleted and replaced with an 8-nt linker carrying a BssHII site, ensuing that neither Vpu nor functional Env is produced in this construct. Each construct was verified by sequencing analysis and is available upon request through a standard material transfer agreement.

Cell Culture and Transfection for AlphaLISA HTS

HEK 293T cells were purchased from ATCC (Manassas, VA) and maintained in DMEM medium supplemented with 10% fetal bovine serum, 100 units/mL of penicillin G sodium salt, and 100 µg/mL of streptomycin sulfate. Transfection of HEK 293T cells using calcium phosphate in multiwell plates was performed as previously described [242, 243, 247, 248]. For AlphaLISA analysis of bulk transfected cells in 384-well plates, HEK 293T cells were seeded at ~20% confluency in either 10 cm or 15 cm dishes and allowed to attach and grow for ~12 hr prior to transfection. Chloroquine was added to a final concentration of 25 µM before transfection. A DNA-calcium mixture was prepared by combining 6 µg plasmid DNA in 788.4 µL H2O, followed by the addition of 111.6 µL of 2 M CaCl2. Then, 900 µL of 2× HBS buffer (50 mM Hepes, 10 mM KCl, 12 mM dextrose, 280 mM NaCl, and 1.5 mM Na2HPO4, pH 7.04-7.05) was added dropwise to the DNA-calcium mixture with gentle vortexing. The resulting mixture was added dropwise to each dish. At 9–12 hr post-transfection, bulk transfected cells were detached using trypsin/EDTA and then pooled in DMEM before seeding 30 µL per well in a 384-well plate at ~25% calculated confluency. PIs or test compounds (Dissolve in 20 µL DMEM) were then added to each well. Negative controls consisted of transfected cells treated with up to 1.25% DMSO alone, as most PIs and small molecule compounds were dissolved in DMSO stock solutions. After ~24 hr of incubation, the culture medium was removed by a gentle swing, and cells were lysed in situ with 20 µL assay solution containing 1× AlphaLISA Immunoassay buffer (PerkinElmer AL000F), protease inhibitor cocktail, 15 µg/mL anti-Flag acceptor beads (PerkinElmer AL112R), and 11.25 µg/mL glutathione donor beads (PerkinElmer 6765301). As a positive control, purified GST-Flag-p6* protein, serially diluted in 1× AlphaLISA Immunoassay buffer (5-fold dilutions, 8 points total), was spiked into wells containing only DMSO. Following at least another additional 2 hr incubation at 37 °C, fluorescence signals were recorded first when needed, followed by AlphaLISA signal detection using either an EnSpire or an EnVision 2104 Microplate Reader (PerkinElmer). For HTS in a 1536-well format, HEK293T cells were bulk-transfected using JetPRIME (Polyplus, New York) following the manufacturer’s recommendations. At 16 hours post-transfection, cells were collected, cryogenically snap-frozen into aliquots to ensure consistent performance across screens, and seeded into 1536-well plates pre-spotted with test compounds at 40-50% cell confluency in 5 µL. After ~24 hr of incubation, AlphaLISA detection reagents were directly added to the wells and AlphaLISA signals were measured following another 2 hr incubation at 37°C.

Generation of Single-round Infectious Virus Particles

HEK 293T cells were co-transfected with the H2B-mRFP reporter and a VSV-G encoding plasmid for Env pseudotyping using calcium phosphate as previously described [238, 242-245, 248]. Briefly, HEK 293T cells were seeded in 12-well plates. A total of 1 µg of plasmid DNA (0.8 µg of the viral reporter plasmid plus 0.2 µg of the VSV-G plasmid per well) was mixed with 65.7 µL of H20 and 9.3 µL of 2 M CaCl2, followed by the dropwise addition of 75 µL of 2× HBS. The transfection solution was then added dropwise to the wells. After 7-9 hours of incubation, the culture medium was replaced with 1 mL of chloroquine-free medium containing PR inhibitors or HTS hits at the indicated concentrations. Approximately 50 hr post-transfection, culture supernatants containing viral particles were collected and clarified using 96-well 0.45 µm filter plates (VWR, cat# 97052-126). The filtered supernatant was divided into 650 µL and 150 µL aliquots. All samples were pelleted at 20,800 × g for at least 100 minutes through a 25% (w/v) sucrose cushion in PBS. The pelleted virus from the 650 µL aliquot was resuspended in 5 µL of DMEM and incubated overnight at 4˚C for infection. The 150 µL aliquot was resuspended in 30 µL of 1.5× SDS loading buffer and subjected to SDS-PAGE analysis followed by Western blotting.

Quantification of Viral Particles by Western Blotting

Equal volumes of viral lysates were resolved by SDS-PAGE, transferred to a PVDF membrane (MilliporeSigma, cat# IPVH 00010), and probed with primary antibodies: mouse monoclonal anti-p24 (183-H12-5C, BEI Resources, cat# ARP-3537) and rabbit polyclonal anti-17 (BEI Resources, cat# ARP-4105). Secondary antibodies included IR700 fluorescence labeled goat anti-rabbit (Rockland, cat# 611-132-003) and IR800 goat anti-mouse (Rockland, cat# 610-132-121). Blots were visualized using an Odyssey infrared dual-laser scanning unit (LI-COR Biotechnology, Lincoln, NE). The total p24 content for each viral sample was determined using ImageStudio software by summing the intensity of all p24-reactive bands. The total p24 content of untreated wild-type virus was arbitrarily set to 100 (AU), with all other samples calculated relative to this reference.

Infection and Quantification of Infectivity

U2OS cells (ATCC HTB-96) cells were cultured in DMEM supplemented with 10% fetal bovine serum, 100 units/mL penicillin G sodium salt, and 100 µg/mL streptomycin sulfate. For infection, U2OS cells were detached and resuspended to achieve ~25% confluency in a 384-well glass-bottom plate (Cellvis, cat# P384-1.5H-N). Pelleted viral particles resuspended in PBS were mixed with 40 µL of U2OS cell suspension, followed by an 8-fold serial dilution (5 µL of the virus-cell suspension added to 35 µL of fresh cell suspension), resulting in a total of 5-6 input values per virus prep. An equal volume (35 µL) of the virus-cell suspension was then seeded for infection. Approximately 50 hours post-infection, Hoechst stain (ThermoFisher, cat# H3570) was added to each well at a working concentration of 0.2 µg/mL and incubated at 37˚C for 30 minutes before live-cell imaging under 37˚C/5% CO2 conditions. Imaging was performed using a Keyence fluorescence microscope (BZ-X710, Keyence Corporation of America, Itasca, IL) with a 20x objective in both DAPI and RFP channels. A 5x3 automated stitching program was applied to capture >1000 cells per sample. For quantification, ImageJ software was used with a custom batch analysis macro to count blue nuclei (total cells) and red nuclei (infected cells). In brief, stitched images were converted to 8-bit grayscale and thresholded to distinguish signals from background noise. The “Fill Holes” and “Watershed” operations were applied to enhance nucleus masking and separate clustered nuclei. The "Analyze Particles" function was used with pre-defined sizes (300–9000 pixel units) and circularity (0.1–1.0) parameters. Nuclear counts were validated across a range of threshold values for accuracy. Some samples exhibiting extreme fluctuations in nuclear counts due to variations in fluorescence intensity or cell overcrowding required manual verification. Cells were also quantified using CellPose segmentation software [329, 330] with a custom nuclei segmentation model trained via the human-in-the-loop training function. Samples with significant variations in segmented nuclei due to fluorescence intensity fluctuations or cell crowding were cross validated using ImageJ or manual counting as needed. For integrated infectivity analysis, the area under the curve (AUC) was calculated using sigmoidal equations best fit to the corresponding infectivity curves, with viral input value ranging from 0.01 to 100.

5.3 Results

High throughput screening (HTS) of natural product extracts (NPEs) with primary AlphaLISA assay

To cast a wide net for the identification of novel HIV-1 protease precursor autoprocessing inhibitors, we proposed to screen a collection of NPEs derived from a variety of microbes (~35K extracts, 5-25 compounds per extract, totaling ~0.6 million chemicals). These NPEs are stored in 384-well plates and our primary AlphaLISA assay was already optimized in 384-well format as previously described [248]. We also validated the feasibility of using frozen aliquots of bulk transfected cells to streamline the screening process. Given that each extract has multiple compounds, the exact concentration of each compound is unknown. So, we screened each extract at 200-fold dilution, which diluted DMSO to 0.5% final concentration, the highest concentration tolerable with the AlphaLISA assay. This HTS campaign identified ~700 NPEs, all of which showed low activities with signals marginally above the DMSO controls. Unfortunately, none passed the confirmation step when re-tested in triplicate. This is not a complete surprise because our AlphaLISA assay is designed to be highly selective with low hit rates. Additionally, these NPEs are known to vary significantly in concentration of individual compounds within the mixture, which in part accounted for the observed low activities.

To increase compound concentration for screening, we lyophilized crude NPEs to remove DMSO and used cell culture medium to directly resuspend various compounds. This approach allowed us to screen with concentrations at least 5-fold higher than the previous NPE screen, which identified more NPEs showing signals above the DMSO controls (Figure 5.1). Out of these initial hits from 2080 concentrated NPEs we screened, we confirmed ~20 hits with partial activities after re-testing at duplicate. Through our HTS campaigns, including these two NPE screens and several other small molecule screens, it has been relatively consistent that our primary AlphaLISA assay only identified positive hits with partial activities because the assay is highly selective, and positive hits must simultaneously lack significant cytotoxic effects, permeate the cell membrane, and suppress precursor autoprocessing.

Characterization of hit NPEs and the corresponding subfractions using our recently established infectivity assay

To further examine biological effects of partially active hits on HIV precursor autoprocessing, we measured the infectivity of viruses treated with hit NPEs using our recently established infectivity assay capable of discerning a single infected cell among thousands of target cells. Any disturbance to HIV-1 protease activity, either in precursor or mature form, is expected to influence virus infectivity to various extents. As described in the previous chapters, this assay has proven highly sensitive for hit validation and drug resistance assessment. Thus, we used this assay as an orthogonal assay for additional evaluation of hit NPEs and the respective subfractions. NPE Hit A was the most active NPE according to the initial AlphaLISA screen and subsequent validation. It was initially grown and fractionated via size-exclusion chromatography into nine fractions (namely, fractions 3-11). Each of the nine fractions were tested at two initial doses: 133 µg/mL or 400 µg/mL NPE dissolved in DMEM culture medium (Figure 5.2). Viral particles were collected from the culture medium of transfected HEK 293T cells for infectivity analysis. Treatment with Fractions 3-8 resulted in no significant impact on viral infectivity even at

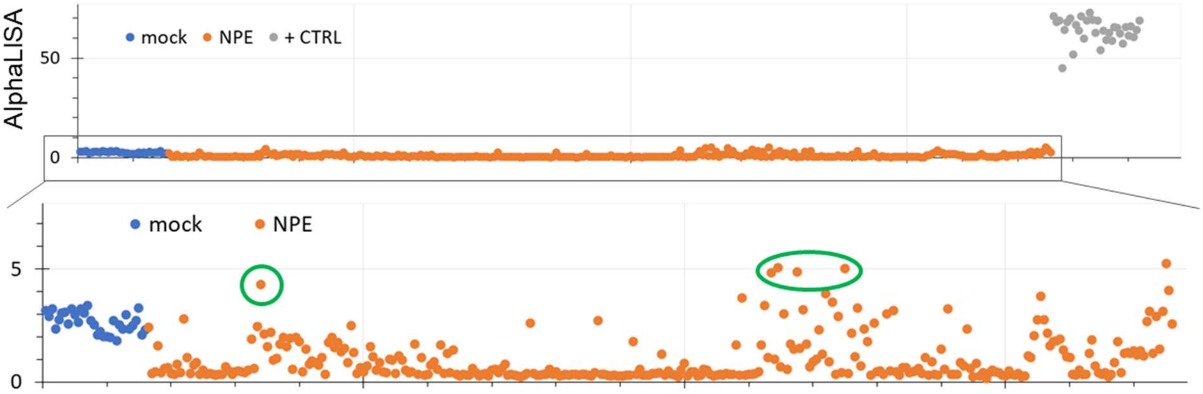

Figure 5.1. Representative AlphaLISA screening data using concentrated crude and subfraction NPEs. Green circles highlight confirmed NPEs.

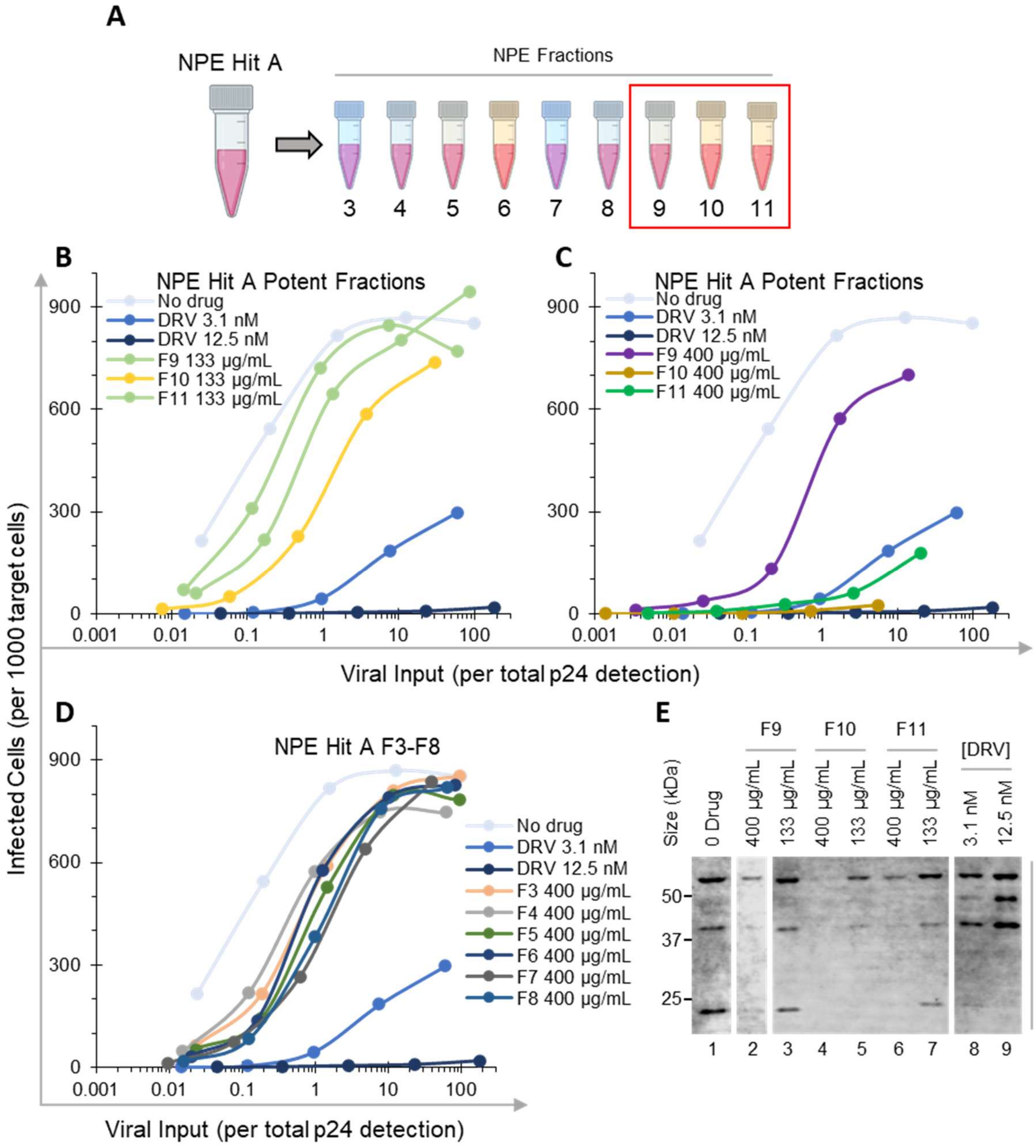

Figure 5.2. Fractionation and characterization of NPE Hit A efficacy in live virus. NPE Hit A was initially fractionated into 8 crude fractions, labeled F3-F11; the red box indicates fractions that displayed inhibitory properties (panel A). Fractions 9, 10, and 11 showed a mild inhibitory effect at 133 µg/mL (panel B) and varying degrees of infectivity inhibition at 400 µg/mL (panel C). Fractions 3-8 did not significantly impact infectivity at 400 µg/mL (panel D). Total p24 content for virus preps treated with F9-F11 was measured via Western blot (panel E).

400 μg/mL compared to an untreated control (Figure 5.2 D), suggesting the lack of inhibitory activity. Fractions 9, 10, and 11 each showed mild infectivity inhibition at 133 μg/mL, although treatment with 3.1 nM DRV was far superior (Figure 5.2 B). Fractions 10 and 11 showed significant infectivity inhibition at 400 μg/mL; the infectivity profile of Fraction 10 nearly overlapped with the 12.5 nM DRV control, and Fraction 11 was slightly more potent than 3.1 nM DRV but slightly less potent than Fraction 10 (Figure 5.2 C). Fraction 9 at 400 μg/mL was markedly less potent than either Fraction 10 or 11.

In parallel, we examined whether and how NPE treatment affects viral production using total p24 detection intensity measured by Western blot (Figure 5.2 E). Our data revealed significantly lower levels of viral particles, nearing the detection limit, in samples treated with 400 μg/mL NPE versus 133 μg/mL NPE (Figure 5.2 E). One might argue that the observed reduction in infectivity is solely attributed to reduced viral production, however we have consistently observed varying infectivity in samples containing equal amounts of total p24-reative contents. For example, F9, F10, and F11 all had severe reduction in viral particle production with 400 μg/mL treatment (Figure 5.2E). However, F9 was much more infectious than F11 despite less viral production compared to F11 (Figure 5.2C). Therefore, we speculate that different compounds in these subfractions might affect viral production and infectivity separately through distinct mechanisms, or a compound may simultaneously affect both. It’s premature to attribute the reduced infectivity exclusively to general cytotoxicity; further purification and analysis of individual compounds in these subfractions would be critical to define underlying causes.

Encouraged by the observed decrease in infectivity of virus treated with Fractions 9-11, we combined fractions 9-11 and further sub-fractioned the mixture into 16 sub-fractions for additional characterization. Unfortunately, due to limitations in starting material, *i.e.*, Fractions 9-11, the highest treatment concentration achievable for each Hit A sub-fraction was 30 μg/mL

(Supplemental Figure 5.1). Encouragingly, combined Fractions 9-11 (the starting material for sub-fractioning) reproduced a dose-dependent decrease in infectivity similar to treatment with individual Fractions 9, 10, and 11 (Supplemental Figure 5.1 B). However, none of the 16 sub-fractions showed a detectable impact on viral infectivity at 30 µg/mL relative to an untreated control (Supplemental Figure 5.1 C & D). Results of mass spectroscopic analysis of these subfractions indicated degradation of the associated chemical components during sub-fractionation. Thus, a modified fractionation protocol was employed to reduce the likelihood of acid-mediated chemical breakdown. Using the modified method, NPE Hit A was initially fractionated into four Fractions for infectivity testing. However, none of the fractions produced via the amended fractionation protocol showed an effect on viral infectivity (Supplemental Figure 5.2).

NPE Hit B displays dose-dependent inhibition of infectivity

We next examined the second positive NPE hit identified via AlphaLISA screening. NPE Hit B was fractionated into four fractions (Fraction 1-4) for an initial assessment. Fraction 4 of NPE Hit B showed promising dose-dependent inhibition of viral infectivity, with the 20 µg/mL treated samples consistently showing potency comparable to treatment with 15 nM DRV across three separate replicates (Figure 5.3 B, C, & D). Viral production was reduced in samples treated with both concentrations of NPE Hit B (Figure 5.3 E) however the reduction was not obviously dependent on dose as was the case for NPE Hit A fractions 9-11. However, this is likely due to the large disparity between treatment concentrations; 400 ug/mL for NPE Hit A experiments (Figure 5.2) versus 20 ug/mL for Hit B (Figure 5.3). In contrast, Hit B Fractions 1-3 did not show any reduction in infectivity compared to the untreated control, suggesting lack of active compounds in these fractions. We further fractioned Hit B Fraction 4 into 16 sub-fractions (sub-fractions 4.1-4.16) hoping to separate active from inactive molecules in the mixture.

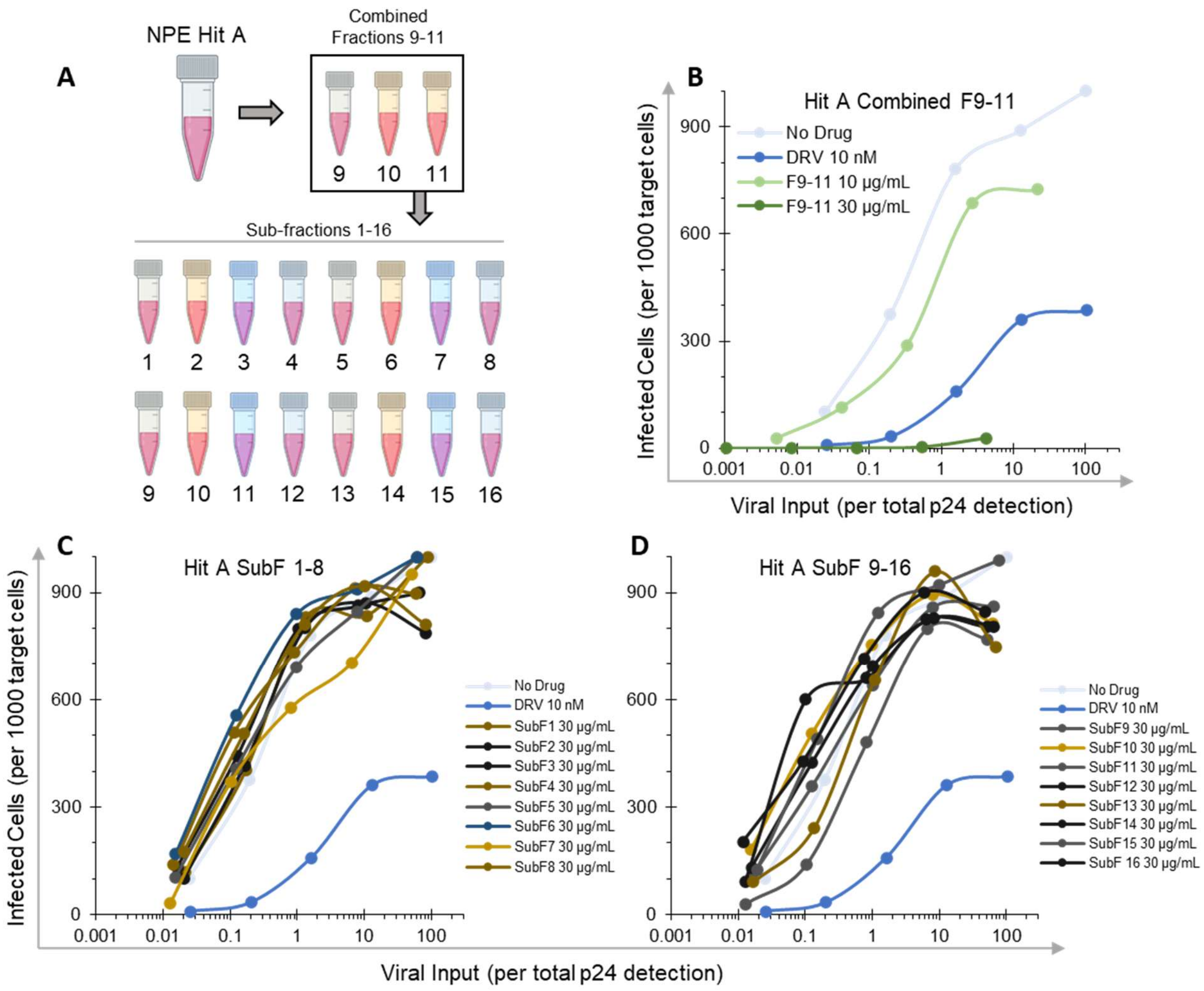

Supplemental Figure 5.1. Sub-fractionation and characterization of NPE Hit A efficacy in live virus. NPE Hit A Fractions 9-11 were combined and used as starting material for sub-fractionation to produce 16 sub-fractions (panel A). Treatment with combined Fractions 9-11, *i.e.,* the starting material for sub-fractionation, showed dose-dependent inhibition of infectivity (panel B). Sub-fractions 1-8 (panel C) or sub-fractions 9-16 (panel D) did not display inhibitory properties at the highest tested concentration.

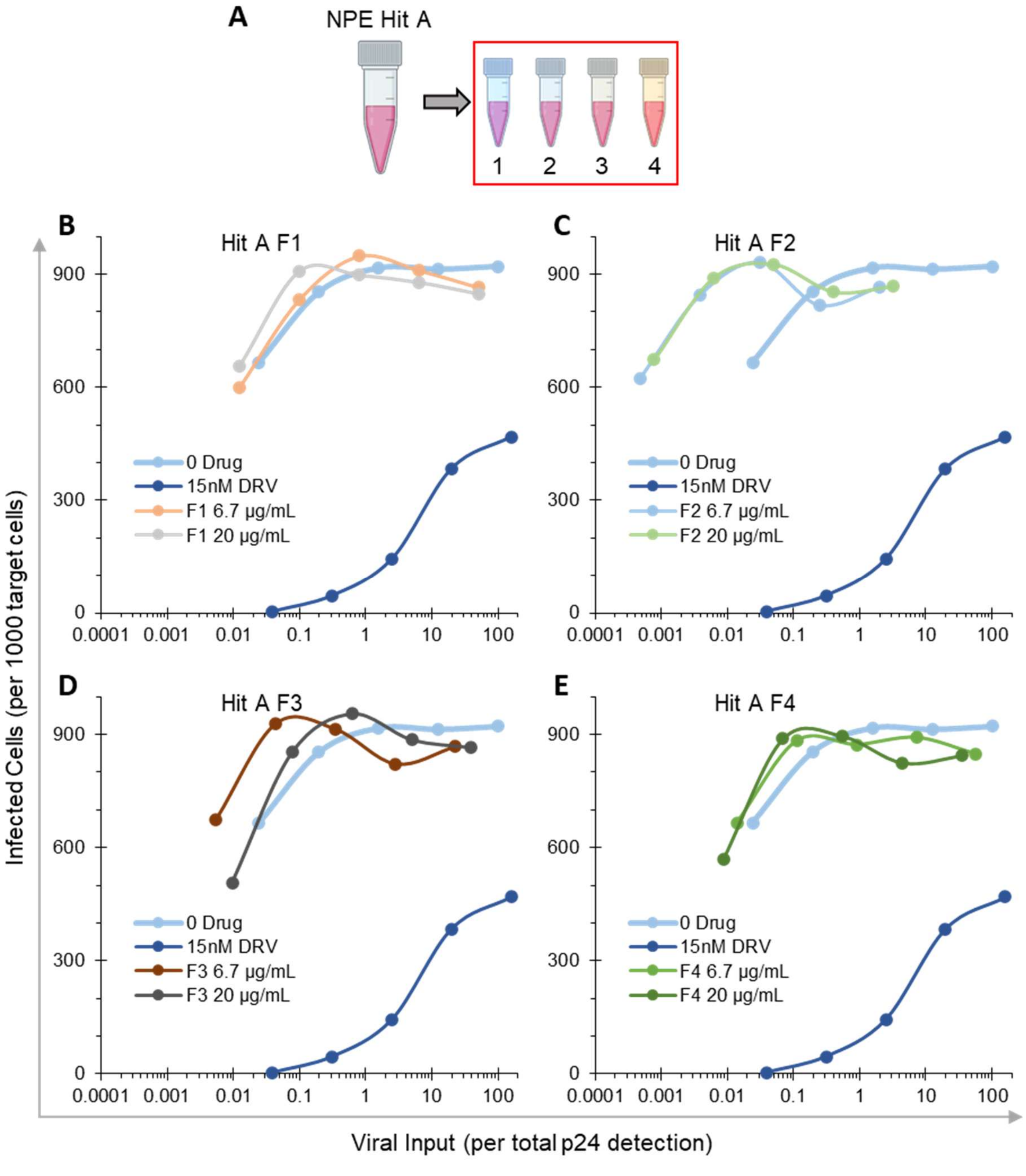

Supplemental Figure 5.2. Re-fractionation and characterization of NPE Hit A efficacy in live virus. The crude NPE Hit A was re-fractioned into four fractions using an alternative fractionation protocol (panel A). None of the four fractions displayed detectable infectivity inhibition up to 20 µg/mL (panels B-E).

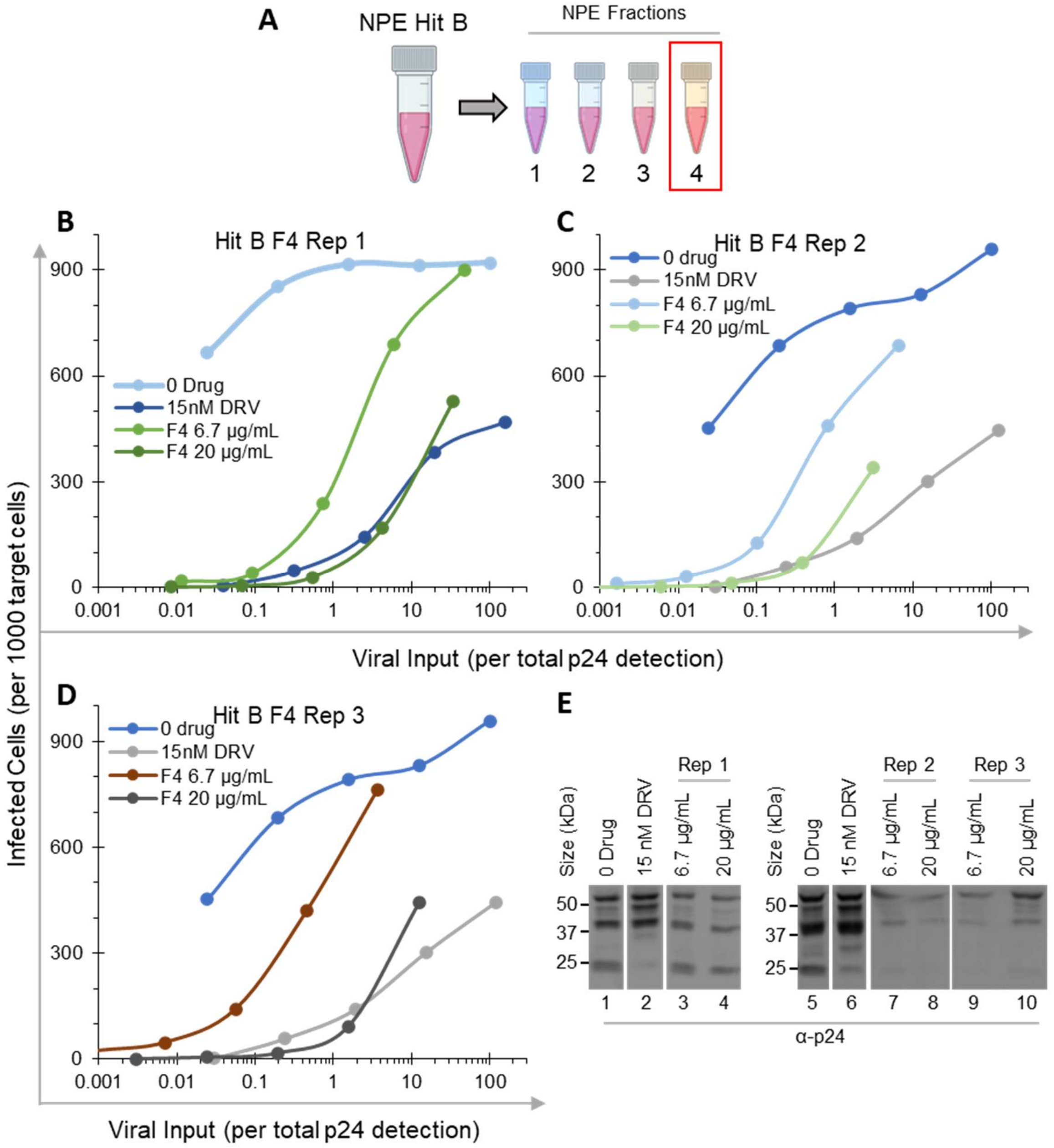

Figure 5.3. Fractionation and characterization of NPE Hit B efficacy in live virus. NPE Hit B was initially fractionated into four fractions for testing in virus (panel A). NPE Hit B Fraction 4 (F4) showed dose-dependent infectivity inhibition up to 20 µg/mL in three separate experimental replicates (panels B-D). NPE Hit B treatment showed a marked decrease in viral production across replicates as measured by Western blot detection of p24-containing bands (panel E).

Encouragingly, four of the 16 sub-fractions (4.11, 4.12, 4.13, 4.14) displayed dose-dependent infectivity inhibition (Figure 5.4B-E). Treatment with 20 µg/mL also resulted in a consistent ~90% reduction in viral input (Figure 5.4 F). The remaining 12 sub-fractions showed no inhibitory activity at 20 µg/mL, as each infectivity profile overlapped with the untreated control (Figure 5.4 G). Results of mass spectroscopic analysis revealed multiple and diverse compounds in these four sub-fractions indicating that they might collectively contribute to the observed phenomenon. Furthermore, because the positive sub-fractions were clustered together, we speculated that the potentially active molecules may share a common chemical scaffold with minor differences in structure and thus are eluted at similar rates via size-exclusion chromatography. This hypothesis was supported by HPLC data that showed a cluster of similar chemical signatures from eluted molecules in sub-fractions 11-14 (data not shown).

Second-round fractionation of NPE Hit B reveals several fractions with inhibitory properties

Second-round sub-fractioning of NPE Hit B Fraction 4 produced 15 sub-fractions (Figure 5.5 A). Of the 15 sub-fractions, sub-fraction 8 showed a chemical signature highly similar to the chemical signature observed in the first-round sub-fractions 11-14. Thus, sub-fraction 8 was further sub-fractioned into four fractions (Figure 5.5 A). However, none of these sub-fractions (labeled 4.8.1-4.8.4, respectively) showed a significant reduction in viral infectivity (Supplemental Figure 5.3). Instead, four other second-round sub-fractions, sub-fractions 3, 4, 9, and 10, showed promising dose-dependent inhibition of viral infectivity (Figure 5.5 B-E). For example, treatment with 15 µg/mL of either sub-fraction 4.3 or 4.4 (Figure 5.5 B & C) reduced the infectivity of the resulting virus to levels below that of 5 nM DRV treatment. Likewise, treatment with 15 µg/mL of either sub-fraction 4.9 or 4.10 also caused a significant reduction in viral infectivity, although 4.9 and 4.10 were not as potent as the 5 nM DRV control (Figure 5.5 D & E).

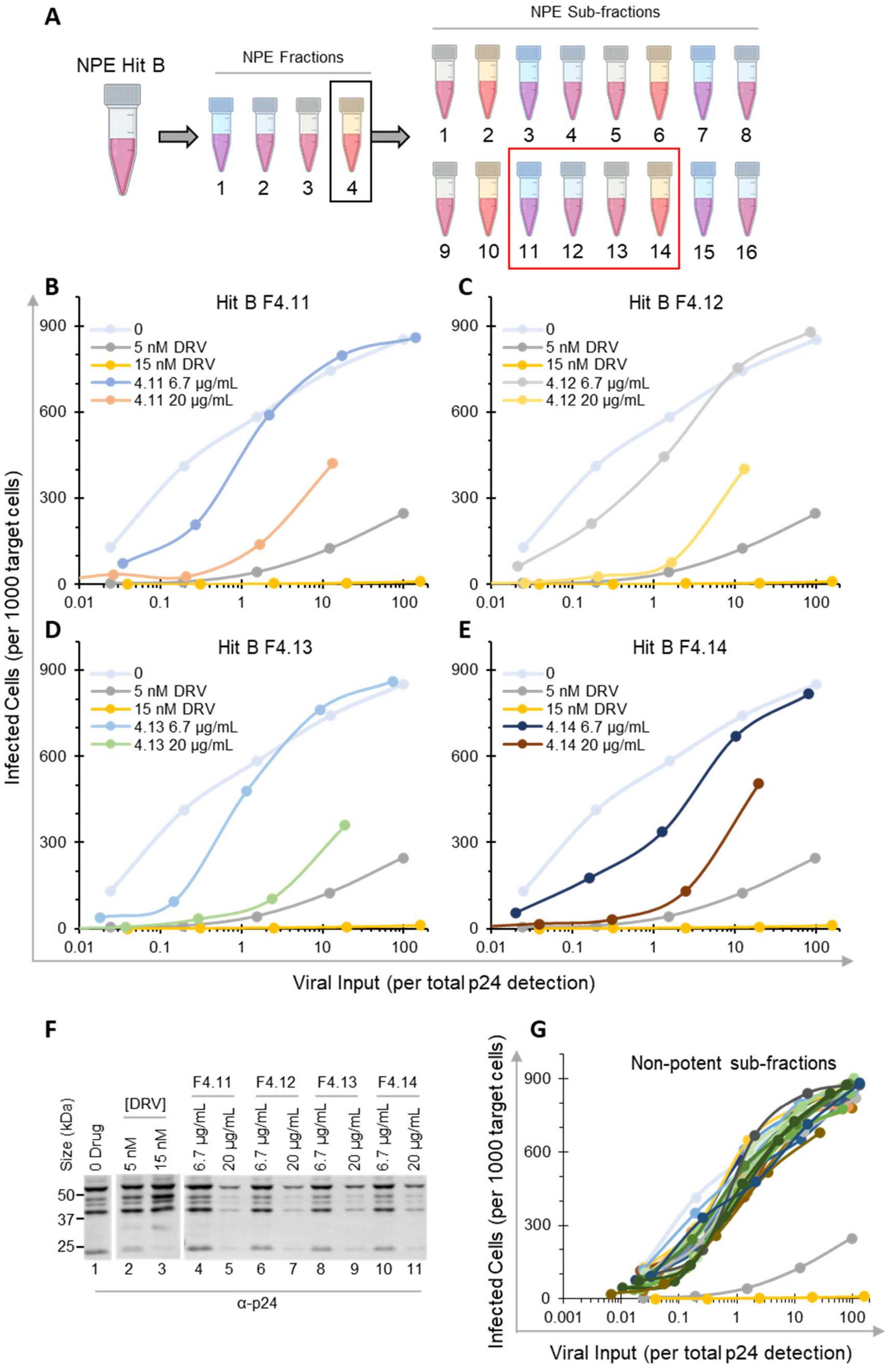
A
NPE Hit B
NPE Fractions
1 2 3 4
NPE Sub-fractions
1 2 3 4 5 6 7 8
9 10 11 12 13 14 15 16
B
Hit B F4.11
0
5 nM DRV
15 nM DRV
4.11 6.7 µg/mL
4.11 20 µg/mL
C
Hit B F4.12
0
5 nM DRV
15 nM DRV
4.12 6.7 µg/mL
4.12 20 µg/mL
D
Hit B F4.13
0
5 nM DRV
15 nM DRV
4.13 6.7 µg/mL
4.13 20 µg/mL
E
Hit B F4.14
0
5 nM DRV
15 nM DRV
4.14 6.7 µg/mL
4.14 20 µg/mL
Infected Cells (per 1000 target cells)
0 300 600 900
0.01 0.1 1 10 100
Viral Input (per total p24 detection)
F
Size (kDa)
0 Drug
[DRV]
5 nM
15 nM
F4.11
F4.12
F4.13
F4.14
6.7 µg/mL
20 µg/mL
50
37
25
1 2 3 4 5 6 7 8 9 10 11
α-p24
G
Non-potent sub-fractions
Infected Cells (per 1000 target cells)
0 300 600 900
0.001 0.01 0.1 1 10 100
Viral Input (per total p24 detection)

Figure 5.4. Sub-fractionation and characterization of NPE Hit B efficacy in live virus. NPE Hit B Fraction 4 was sub-fractioned into 16 sub-fractions (F4.1-F4.16, respectively) for testing in virus (panel A). Sub-fractions 11-14 (F4.11-F4.14, respectively) showed dose-dependent inhibition of infectivity with 20 μg/mL treatment approaching that of 5 nM DRV (panels B-E). F4.11-F4.14 showed a dose-dependent reduction in viral production measured via Western blot detection of p24-containing bands (panel F). The remaining Hit B Fraction 4 sub-fractions did not display inhibitory properties in live virus (panel G).

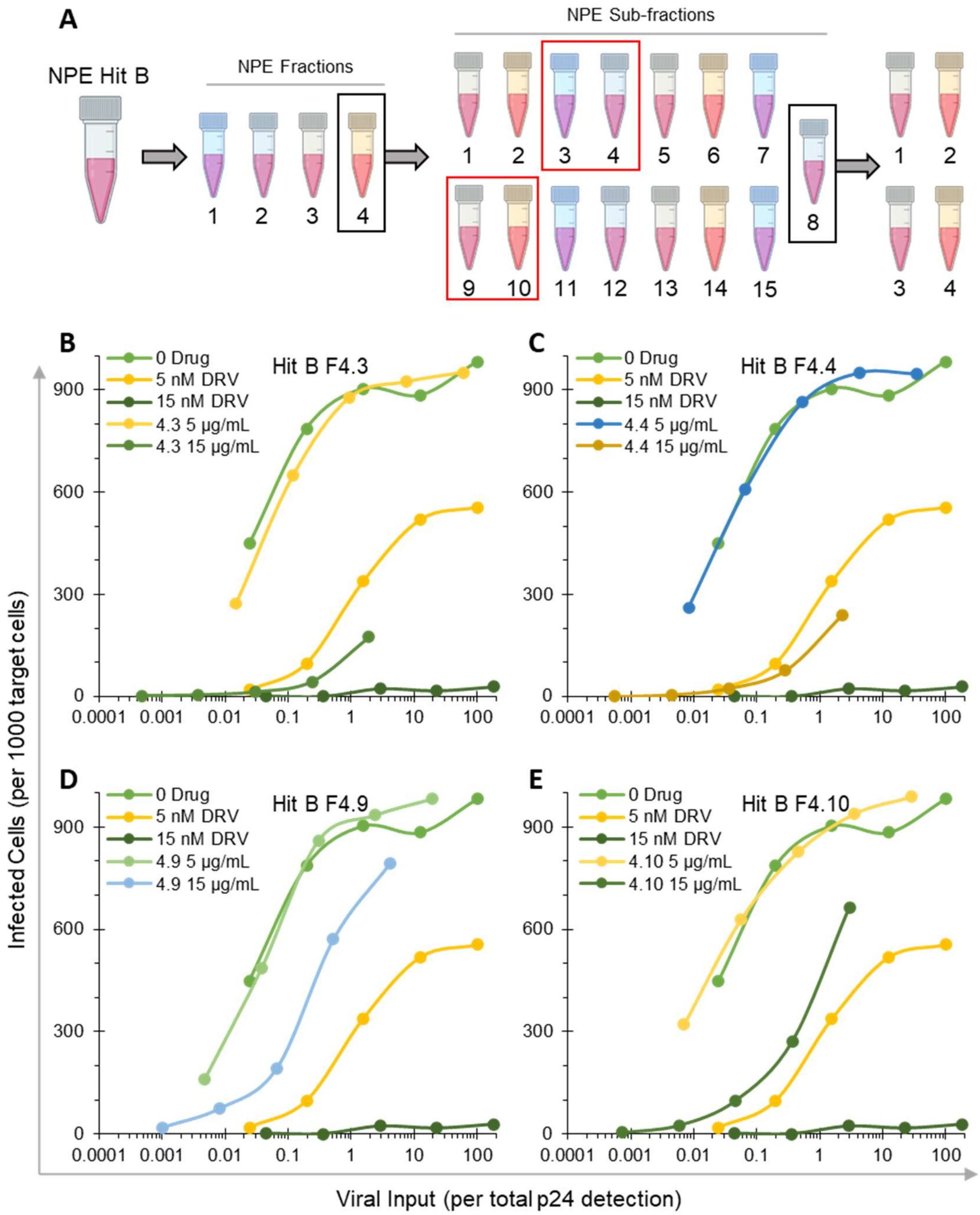

Figure 5.5. Second round sub-fractionation and characterization of NPE Hit B efficacy in live virus. NPE Hit B Fraction 4 underwent a second round of sub-fractioning into 15 sub-fractions (F4.1-F4.15, respectively) for testing in virus (panel A). Sub-fraction 8 (F4.8) was subject to additional sub-fractioning into four fractions (F4.8.1-F4.8.4, respectively) based on chromatographic signatures identifying potentially potent molecules (panel A). F4.3 (panel B) and F4.4 (panel C) displayed dose-dependent inhibitory activity as treatment with 15 µg/mL of both sub-fractions was more effective than 5 nM DRV. F4.9 (panel D) and F4.10 (panel E) also displayed dose-dependent inhibitory activity, although 15 µg/mL had less impact on infectivity than 5 nM DRV in both cases.

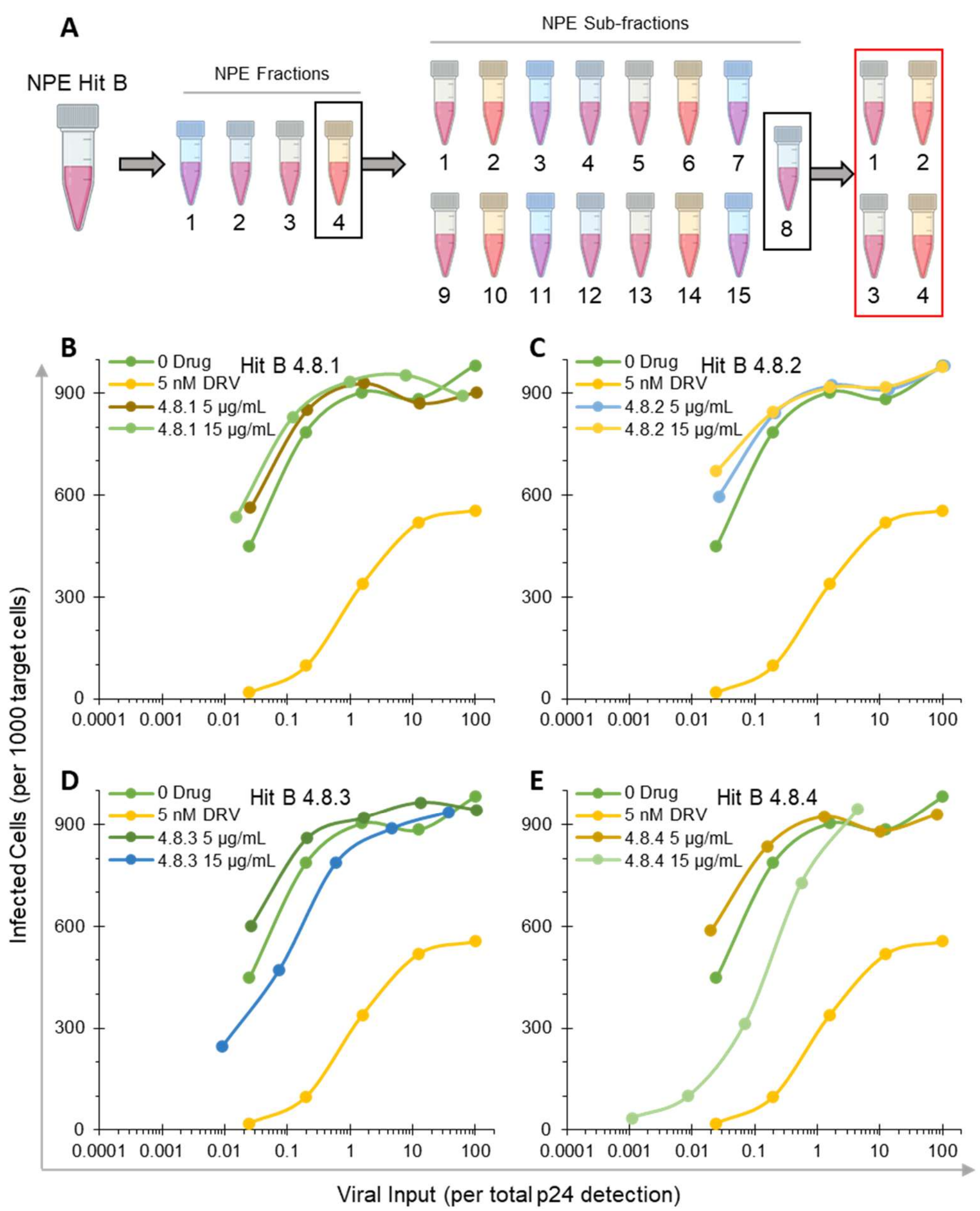

Supplemental Figure 5.3. Second round sub-fractionation and characterization of NPE Hit B efficacy in live virus. NPE Hit B Fraction 4 underwent a second round of sub-fractioning into 15 sub-fractions (F4.1-F4.15, respectively) for testing in virus (panel A). Sub-fraction 8 (F4.8) was subject to additional sub-fractioning into four fractions (F4.8.1-F4.8.4, respectively) based on chromatographic signatures identifying potentially potent molecules (panel A). F4.8.1-F4.8.3 did not show promising inhibitory activity in live virus (panels B-D). F4.8.4 displayed partial inhibitory activity at 15 µg/mL but was not as effective at 5 nM DRV treatment (panel E).

To improve the analysis of our comparative analysis data, we calculated the area-under-curve (AUC) of the respective infectivity profiles using a simple trapezoid method from x=0.03 to x=3 with interpolation of data points to represent integrated infectivity. This range of x values was chosen to maximize the area captured for NPE-treated infectivity profiles, as the viral production was drastically reduced in most samples treated with 15 µg/mL NPE and as such the relative viral input from most samples was roughly 90% less than the untreated control (Figure 5.6 B). The resulting “integrated infectivity” value offers a direct metric by which the relative efficacy of each individual NPE sub-fraction can be evaluated against the untreated control as well as respective DRV-treated controls. As shown in Figure 5.6 A, sub-fractions 4.3 and 4.4 were more potent than 5 nM DRV treatment, and sub-fractions 4.2, 4.9, and 4.10 showed greater than 25% reduction in infectivity compared to the untreated control (Figure 5.6 A). Based on the observed pattern of reduced infectivity as a result of NPE treatment, there may be two “clusters” of potentially active molecules in NPE Hit B Fraction 4, one of which elutes between sub-fraction 4.2 and 4.5 and the other of which elutes between sub-fraction 4.8 and 4.10. Current work is focusing on further sub-fractioning of sub-fractions 4.3 and 4.4 to identify single molecules responsible for the observed activity.

5.4 Discussion

Natural product extract screening reveals several promising candidates that show infectivity inhibition in live virus

Fraction 4 of the crude NPE Hit B showed dose-dependent infectivity inhibition (Figure 5.3 B-D) and only a moderate impact on viral production in the producer cells compared to the untreated control (Figure 5.3 E). Sub-fractioning of Hit B Fraction 4 proved successful, as four of the 16 sub-fractions showed dose-dependent infectivity inhibition at 6.7 and 20 µg/mL, respectively (Figure 5.4 B-E). Each of the four sub-fractions (4.11-4.14) impacted viral production at 20

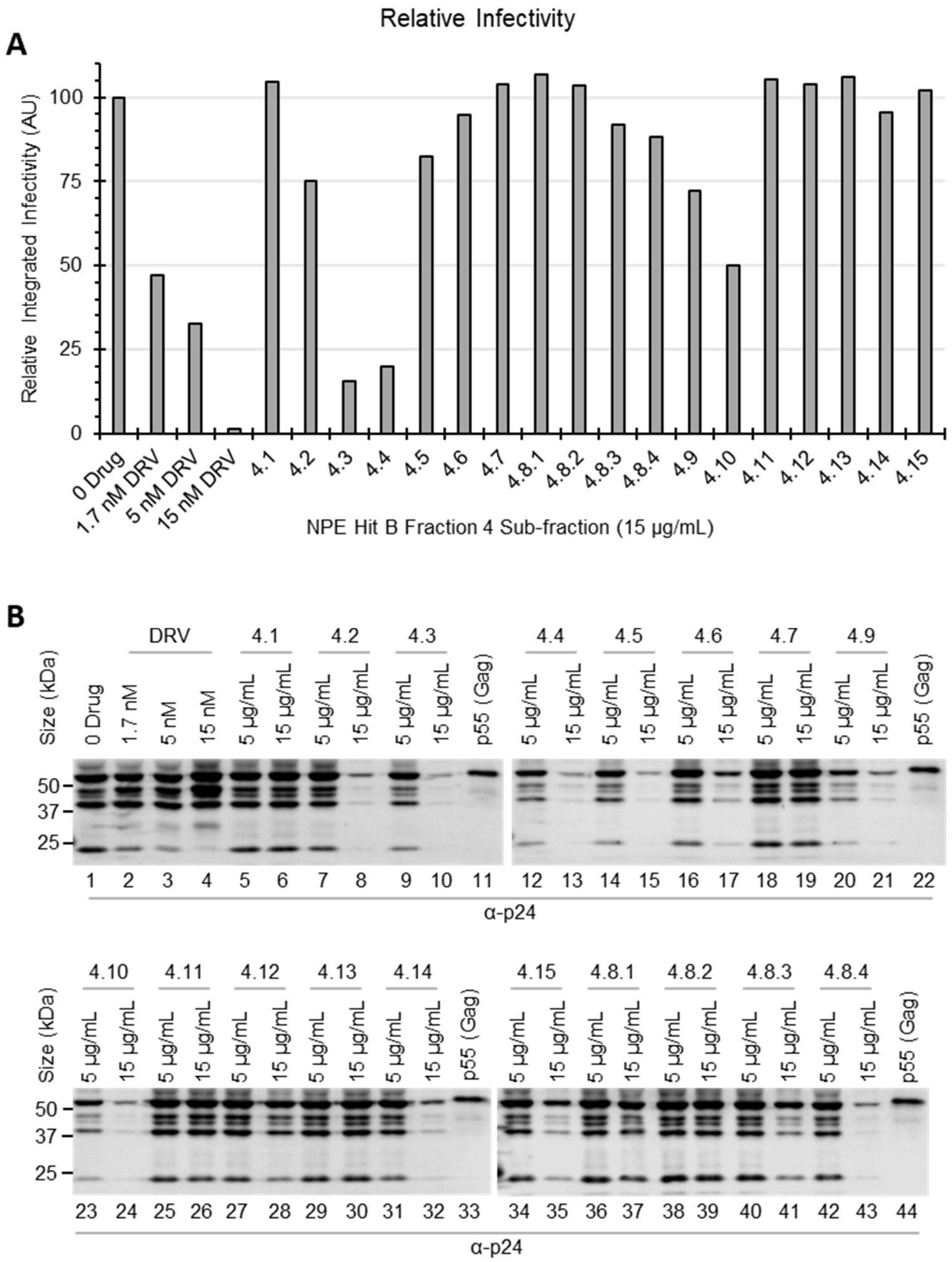

Figure 5.6. Integrated infectivity profiles for comparison of inhibitory properties among NPE Hit B second round sub-fractions. The infectivity profiles generated in the presence of NPE Hit B sub-fractions F4.1-F4.7, F4.8.1-F4.8.4, and F4.9-F4.15 were integrated using a standard trapezoid method from x=0.03 to x=3 and normalized to the WT integrated infectivity in the same bounds. The relative integrated infectivity for each sub-fraction is plotted in panel A. Various impacts on viral production were observed as a result of NPE treatment at increasing concentrations, as measured via Western blot detection of total p24-containing bands (panel B).

μg/mL (Figure 5.4 F) but nonetheless showed potencies similar to Fraction 4. Based on chromatography data, several unique chemical signatures were present in the molecules eluted in the later sub-fractions of Hit B Fraction 4, which thus prompted re-fractionation/sub-fractionation to further separate molecules present in fractions 4.11 to 4.14.

During second-round sub-fractioning of NPE Hit B Fraction 4, sub-fraction 8 displayed similar chemical signatures initially observed in sub-fractions 4.11-4.14 of round-one sub-fractioning; thus, sub-fraction 8 was further sub-fractioned into four additional fractions (4.8.1-4.8.4; Supplemental Figure 5.3). Due to the consistent chemical signatures in round-one sub-fractions 4.11-4.14 and round-two sub-fractions 4.8, we expected to see similar effects on viral infectivity in both rounds. However, none of the second-round sub-fraction 8 fractions showed any detectable potency (Supplemental Figure 5.3 B-E) despite testing at similar concentrations compared with sub-fractions 4.11-4.14 (Figure 5.4 B-E). Additionally, sub-fractions 4.8.1-4.8.4 only mildly impacted viral production; sub-fraction 4.8.4 caused a significant reduction in total p24 signal in collected viral samples but did not impact infectivity, providing evidence that cytotoxic effects of NPE treatment is not necessarily correlated with decreased infectivity (Figure 5.6 B). Sub-fractions 4.11-4.14 all showed a similar impact on viral production (Figure 5.4 F) but also showed significant reduction in viral infectivity, unlike any of the other sub-fractions. Several second-round sub-fractions did show promising infectivity inhibition, including sub-fraction 4.3, 4.4, 4.9, and 4.10 (Figure 5.5 B-E & Figure 5.6 A). Sub-fractions 4.3 and 4.4 were the most effective at suppressing viral infectivity, as both were more potent than 5 nM DRV treatment (Figure 5.6 A). Sub-fractions 4.9 and 4.10 inhibited infectivity to a lesser extent but still showed >25% reduction in infectivity compared to the untreated control (Figure 5.6 A). Thus, as was the case with NPE Hit A, sub-fractioning of NPE Hit B proved to be unpredictable, however NPE Hit B sub-fractioning continually produced potent sub-fractions showing promising inhibition of viral infectivity.

It is also important to note that, although viral production was impacted to varying degrees depending on NPE treatment conditions, a reduction in viral production did not necessarily correlate with a reduction in infectivity. Treatment with second-round sub-fractions 4.5, 4.8.4, and 4.14 greatly reduced viral production compared to the untreated control, as evidenced by the large decrease in total p24 detection intensity measured via Western blot (Figure 5.6 B, lanes 15, 32, and 43 compared to lane 1), but did not show a decrease in infectivity of equal magnitude (Figure 5.6 A). However, sub-fraction treatment that led to a reduction in infectivity was also accompanied by a reduction in viral production for each potent fraction. First-round Hit B sub-fractions 4.11-4.14 (Figure 5.4) and second-round Hit B sub-fractions 4.3, 4.4, 4.9, and 4.10 (Figure 5.6) all caused a significant reduction in viral infectivity and a corresponding decrease in viral production. Although not experimentally validated, qualitative measures of NPE-treated producer cells revealed signs of cytotoxicity, namely a change in cellular morphology and a reduction in attached cells (data not shown) that correlated with a decrease in total p24 Western blot signal. Cellular morphology and viral production in the DRV-treated controls was also comparable to the untreated control throughout the study, highlighting that PI treatment does not impact viral production (Figure 5.2 E, lanes 1, 8, 9; Figure 5.3 E, lanes 1& 2; Figure 5.4 F, lanes 1-3; Figure 5.6 B, lanes 1-4). Thus, without ruling out the possibility that NPE treatment directly influences viral production, it is likely that the observed reduction in p24 detection intensity is due to cytotoxicity. It is therefore an important observation that cytotoxicity (i.e., a reduction in viral production) does not necessarily predict a corresponding reduction in infectivity, which eliminates the possibility that infectivity is reduced in select NPE-treated samples due to cytotoxic effects on viral production instead of interaction with proteolytically active precursor(s).

Infectivity analysis offers sensitive, precise drug resistance quantification for confident HTS validation

High-throughput screening (HTS) was successful in the identification of several NPE compounds capable of inhibiting proteolytic processing of a fusion p6*-PR precursor in mammalian cells. Subsequent infectivity analysis of the NPEs identified via HTS revealed a range of potencies with respect to infectivity inhibition despite similar levels of precursor autoprocessing inhibition in the primary screening assay. Assuming that the effect of NPE treatment on p6*-PR processing is similar in both p6*-PR fusion precursors and in live virus particles, the wide range of efficacies with respect to infectivity compared to the generally mild, consistent effect on fusion p6*-PR precursor processing in live cells suggests that even a minor perturbation of the p6*-PR processing reaction in viral particles has a large overall effect on particle maturation and the subsequent infectivity of virus particles. This observation highlights the importance and utility of our infectivity assay in HTS hit validation, as inhibition of the p6*-PR precursor in a fusion-precursor context is not necessarily indicative of the magnitude of inhibition observed in live virus particles. Future work will aim to further optimize NPE fractionation protocols to reliably separate potent molecules from crude NPE mixtures, which is also paramount for the separation of potentially potent molecules from potentially toxic molecules. Overall, our data highlights the utility of our novel infectivity assay in HIV-1 inhibitor discovery and has laid the foundation for future work aiming to develop a first-in-class HIV-1 autoprocessing inhibitor.

CHAPTER 6:

SUMMARY AND FUTURE DIRECTIONS

6.1 Summary

My dissertation explored the context-dependent relationship between the protease, protease autoprocessing, and drug resistance (Chapter 2); how the unique mutational landscape of the p6*-PR gene influences drug resistance manifestation (Chapter 3); and autoprocessing as a novel target for inhibitor development using high-throughput screening (HTS) and subsequent characterization in live viruses (Chapters 4 & 5).

Using our recently developed infectivity assay, we successfully recapitulated the clinically observed indinavir (IDV) resistance of a PR double mutant V77I/V82T in a laboratory setting and identified the V82T mutation as the main driver of the IDV resistance phenotype; we also established that viruses harboring V82T are more sensitive to darunavir (DRV) inhibition than WT virus, highlighting that resistance to one PI may increase sensitivity to others. We validated our infectivity assay and established its applicability in sensitive drug resistance assessment by thorough examination of a panel of multi-PI resistant mutants. We showed that resistance reflected as a fold-change value may not be the most informative for selection of antiretroviral (ART) therapies, as fold-change values do not relate drug resistance to PI concentration. EC_{50} determination is likely a better alternative for PI selection because it can be used in combination with protease inhibitor pharmacodynamics to determine whether available PI concentrations in plasma are sufficient to suppress viral replication.

We identified several novel chemical scaffolds and crude natural product extracts (NPEs) through HTS campaigns that show inhibitory activity in live virus particles which sets the foundation for novel autoprocessing inhibitor development. Of note, small molecule C7 showed similar EC_{50} values toward WT and several multi-PI resistant strains, providing evidence that C7 inhibits viral activity with a novel mechanism of action (MOA). A handful of the inhibitory small molecules/NPEs cause a significant reduction in viral production, however low viral production is not necessarily correlated with low infectivity. Overall, this thesis shows the utility of our novel infectivity assay with applications in drug discovery, drug resistance, and mechanistic study.

6.2 Structure activity relationship (SAR) assessment of small molecule C7 for increased potency

As shown in Chapter 4, C7 showed the highest inhibitory activity against both WT and multi-PI resistant viruses. C6 and C7 share a core chemical scaffold which we used as a foundation for initial SAR shown in Chapter 4; work is currently underway in the lab to expand on the initial SAR experiments using an analog-by-catalog approach to characterize diverse small molecules which share a similar core chemical scaffold. In addition to modifications at chemical moiety #1, as shown in Chapter 4, we expanded our search to include molecules that share the core chemical scaffold but also differ at moiety #2 and moiety #3 (Figure 6.1). ~150 such molecules were identified and purchased for characterization in our infectivity assay. Examples of such molecules with unique moieties at positions 1, 2, and 3 are shown in Figure 6.1 B-D.

Initial analog-by-catalog experiments to improve the inhibitory activity of C6 (*i.e.*, molecules D4-D7, Chapter 4) suggested that a bulky molecule at moiety #1 may be preferred, as the molecule with the highest observed inhibitory activity (D4) contains a phenyl group. Second-round SAR will further investigate this hypothesis using a large variety of molecules with different chemical groups at moiety #1 to provide further insight into the preliminary D-group SAR results. The current analog-by-catalog experiments also seek to validate the inhibitory activity of the

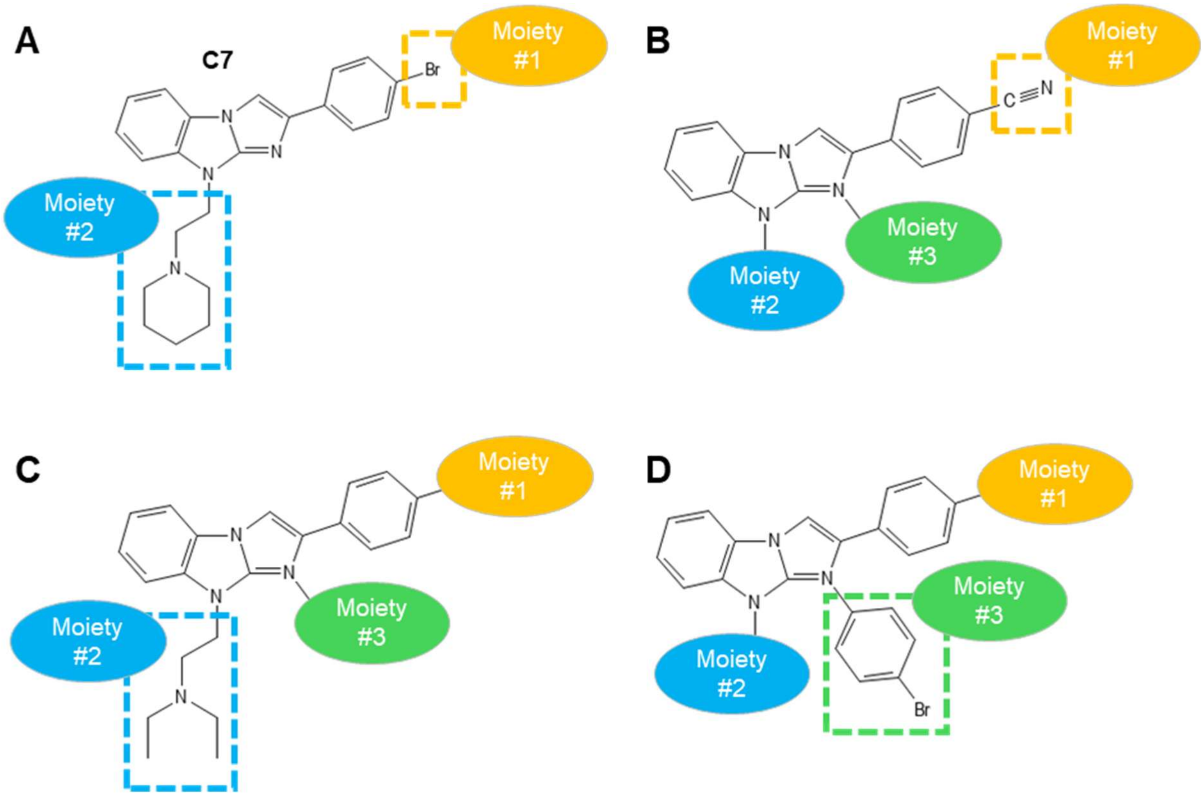

Figure 6.1. Expanded C7 SAR analysis using analog-by-catalog. The structure of C7 is shown in panel A. Example substitutions at moiety #1, #2, and #3 of second round compounds shown in panels B-D. Complete molecular structures of analogs are intentionally withheld.

proposed core chemical scaffold and improve potency by expanding the molecule at each of the three chemical moieties. We anticipate many rounds of analog-by-catalog SAR experiments followed by thorough characterization in live virus particles to sequentially improve upon the potency of top candidate molecules. We acknowledge that the analog-by-catalog approach is limited in the availability and existence of compounds with scaffolds similar to that of C7 and thus hope to explore medicinal chemical synthesis through collaboration in the future.

6.3 Engineering and characterization of tagged Gag/Gag-Pol constructs for HIV-1 translation imaging

In the infected cell, Gag and Gag-Pol are translated from the full-length viral mRNA. Gag-Pol is produced via a regulated -1 ribosomal frameshift near the end of the Gag coding region, which results in the production of Gag-Pol at a 1:20 Gag-Pol:Gag ratio. The mechanisms that govern this conserved ratio remain to be fully understood. It is possible that ~5% of mRNAs continually translate the -1 frame while all others translate Gag (0 frame), or that the -1 frame of each mRNA is translated roughly 5% of the time. It is also possible that the conserved 20:1 Gag:Gag-Pol ratio maintenance is stochastic, wherein frameshifting is regulated via subcellular localization or yet-to-be defined mechanisms that selectively induce frameshifting.

We are in current collaboration with Dr. Tim Stasevich and Ph.D. candidate Sam Klink to further investigate the regulatory mechanisms that govern translational frameshifting of HIV-1 mRNA. The Stasevich lab uses a variety of fluorescently labeled antibody fragments (Fabs), nanobodies, and single-chain variable fragments (scFvs) that bind protein tags, epitopes, and RNA secondary structures which allows for real-time tracking and measurement of translation dynamics in live cells. Prior work from the Stasevich lab investigating HIV-1 frameshifting dynamics used constructs with the HIV-1 slippery sequence and stem loop structure inserted upstream of separate reading frames encoding either tandem Flag epitopes or tandem SunTAG epitopes (derived from GCN4 transcription factor). Translation of the 0 frame produces Flag-containing polypeptides that are bound by fluorescently labeled anti-Flag Fabs, and translation of the -1 frame produces SunTAG-containing polypeptides that are bound by fluorescently labeled anti-SunTAG scFvs; the relative Fab and scFV signals are measured via fluorescence microscopy. This work revealed that frameshifting mRNAs seem to localize in “frameshifting factories” and may frameshift with a bursty mechanism [136, 366-368]. However, this remains to be validated in infected cells expressing Gag and Gag-Pol from the integrated provirus. To image viral polyprotein translation in infected cells, the first goal is to engineer viral reporter constructs with protein/epitope tags inserted in both the 0 and -1 frames that retain the capacity to infect target cells. Upon transcription and translation of the integrated provirus, nanobody/tag interactions can be measured via fluorescence microscopy to measure translation in real time.

The major challenge with this approach is identifying a combination of protein tags that are “tolerated” by the virus such that viral particles remain infectious despite the presence of tagged polyproteins in the immature viral particles. Prior work in our lab indicates that many tags are not inherently tolerated by the virus likely due to the disruption of particle assembly or maturation. This challenge is partially overcome by generating viral particles using various ratios of constructs that express untagged Gag and Gag-Pol in combination with the tagged viral reporter construct for viral particle production. The constructs expressing untagged polyprotein lack the necessary 5’ motifs for RNA dimerization and incorporation into viral particles, which allows us to generate virus particles composed largely of untagged polyproteins which enhances maturation and infectivity. The viral reporter construct, which encodes the tagged polyproteins, retains the necessary 5’ elements for incorporation into viral particles and thus all infected cells in this approach express tagged polyproteins from the provirus. However, viral infectivity sufficient for translation imaging is highly dependent on the ratio of untagged

Gag/Gag-Pol used for viral production, the size of each epitope/protein tag, and the number of total epitope/protein tags.

Current experiments seek to define the impact on infectivity of a variety of tags in different locations in both the 0 and -1 frame. Data included here investigated tags attached to the C-terminus of MA, the N-terminus of CA, and the N-terminus of RT (Figure 6.2 A). Infectivity of all viruses harboring tagged polyproteins were markedly less infectious than WT (Figure 6.2 B-D), however these viruses were made using a 50:50 ratio of untagged polyprotein to tagged polyprotein indicating potential for additional experiments using alternate ratios to enhance overall infectivity. In general, viruses harboring a tag at the C-terminus of MA (Figure 6.2 B) were more infectious than viruses harboring tags at the N-terminus of CA (Figure 6.2 C) or viruses with tags in both frames (Figure 6.2 D). There appears to be a size constraint for tags at the C-terminus of MA, as viruses encoding GFP or 6 tandem HA tags were more infectious than the 21 tandem SunTAG. Tags at the N-terminus of CA were not tolerated regardless of size. This is likely explained by the intricate regulation of viral assembly, immature lattice formation, and capsid core formation that depend on both the N- and C-terminus of CA. Thus, relatively small tags at the C-terminus of MA may be the best option for translation imaging in live cells. The infectivity of viruses encoding tags in both frames (Figure 6.2 D) was also largely reduced compared to WT, however infection was detected in both samples. 0-frame tags in these experiments did not include 6xHA or GFP, which may be better tolerated in the dual-tagged constructs based on tolerability in single tagged constructs (Figure 6.2 B).

Many combinations of tags in both the 0 and -1 frame along with a variety of DNA ratios to optimize virus production have been investigated. Overall, preliminary work is promising, as either a GFP tag or 6 tandem HA tags seem to be generally tolerated when inserted in the C-

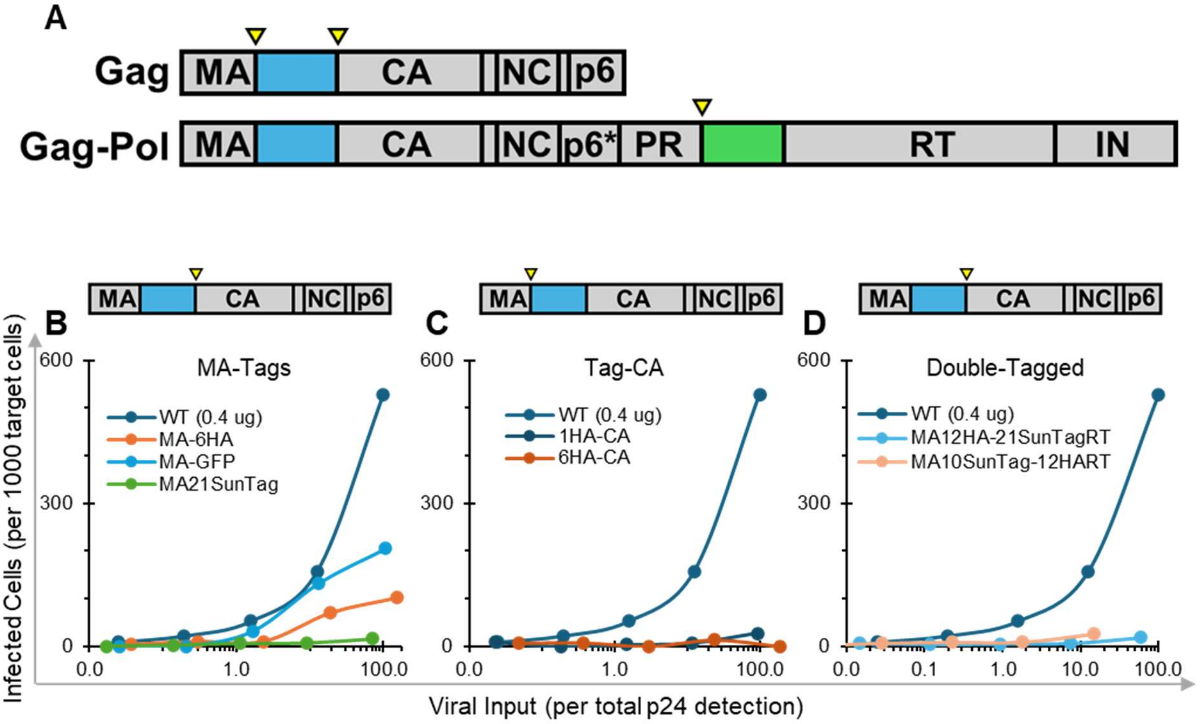

Figure 6.2. Infectivity of tagged virus. Locations of 0 frame (blue) and -1 frame (green) tags are shown in panel A. Yellow arrows indicate protease cleavage sites that are deleted or conserved depending on the construct. Infectivity of tagged viruses with tags at the C-terminus of MA (panel B), the N-terminus of CA (panel C), or at the C-terminus of MA plus the N-terminus of RT (panel D) are indicated. Note that the conserved proteolytic cleavage site for the construct tagged in the -1 frame (panel D) is indicated by the yellow arrow in panel A. All viruses were produced using a 50:50 ratio of untagged Gag/Gag-Pol to tagged reporter construct.

terminus of MA. Constructs tagged in both the 0 and -1 frame show detectable infectivity, although infectivity is dramatically lower in these constructs compared to WT. Future engineering will combine tolerated 0 frame tags with various -1 frame tags and will additionally investigate the effects of single tags in the -1 frame on viral infectivity. Of note, the magnitude of infectivity measured by our assay is dependent on both the amount of virus produced and on the number of target cells for infection. We produce virus in 12-well plates and infect ~3000 U2OS target cells. Thus, although infectivity may be low in our assay, scaling viral production would likely increase infectivity and will be useful for generating sufficient virus for infection and subsequent imaging. An additional consideration to optimize imaging protocols is the relative size of the tags used in the 0 frame versus the -1 frame. Because Gag (0 frame) is ~20 times more abundant than Gag-Pol in the infected cell, the signal from bound nanobodies in the -1 frame needs to be sufficient to detect Gag-Pol despite its low abundance relative to Gag. Thus, the goal of future experiments is to insert as many tag repeats as possible in the -1 frame to enhance Gag-Pol signal in the infected cell without disturbing assembly, particle maturation, or infectivity.

REFERENCES

1. Passos, D.O., et al., *Retroviral integrase: Structure, mechanism, and inhibition*. 2021, Elsevier. p. 249-300.
2. Hemelaar, J., *The origin and diversity of the HIV-1 pandemic.* Trends in Molecular Medicine, 2012. **18**(3): p. 182-192.
3. Sharp, P.M. and B.H. Hahn, *Origins of HIV and the AIDS Pandemic.* Cold Spring Harbor Perspectives in Medicine, 2011. **1**(1): p. a006841-a006841.
4. Keele, B.F., et al., *Chimpanzee Reservoirs of Pandemic and Nonpandemic HIV-1.* Science, 2006. **313**(5786): p. 523-526.
5. Nyamweya, S., et al., *Comparing HIV-1 and HIV-2 infection: Lessons for viral immunopathogenesis.* Reviews in Medical Virology, 2013. **23**(4): p. 221-240.
6. Naif, H.M., *Pathogenesis of HIV infection.* Infectious Disease Reports, 2013. **5**(11): p. e6.
7. Watts, J.M., et al., *Architecture and secondary structure of an entire HIV-1 RNA genome.* Nature, 2009. **460**(7256): p. 711-716.
8. Mallery, D.L., et al., *IP6 is an HIV pocket factor that prevents capsid collapse and promotes DNA synthesis.* eLife, 2018. **7**.
9. Ganser-Pornillos, B.K., A. Cheng, and M. Yeager, *Structure of full-length HIV-1 CA: a model for the mature capsid lattice.* Cell, 2007. **131**(1): p. 70-9.
10. Wang, H., et al., *Cryo-EM structure of a CD4-bound open HIV-1 envelope trimer reveals structural rearrangements of the gp120 V1V2 loop.* Proceedings of the National Academy of Sciences, 2016. **113**(46): p. E7151-E7158.
11. Chen, B., *Molecular Mechanism of HIV-1 Entry.* Trends in Microbiology, 2019. **27**(10): p. 878-891.
12. Shaik, M.M., et al., *Structural basis of coreceptor recognition by HIV-1 envelope spike.* Nature, 2019. **565**(7739): p. 318-323.
13. Zheng, Y., et al., *Structure of CC Chemokine Receptor 5 with a Potent Chemokine Antagonist Reveals Mechanisms of Chemokine Recognition and Molecular Mimicry by HIV.* Immunity, 2017. **46**(6): p. 1005-1017.e5.
14. Wang, Q., A. Finzi, and J. Sodroski, *The Conformational States of the HIV-1 Envelope Glycoproteins.* Trends in Microbiology, 2020. **28**(8): p. 655-667.
15. Lukas, J. Lee, and B. Liang, *Capturing Glimpses of an Elusive HIV Gp41 Prehairpin Fusion Intermediate.* Structure, 2014. **22**(9): p. 1225-1226.
16. Weissenhorn, W., et al., *Atomic structure of the ectodomain from HIV-1 gp41.* Nature, 1997. **387**(6631): p. 426-430.
17. Chan, D.C., et al., *Core Structure of gp41 from the HIV Envelope Glycoprotein.* Cell, 1997. **89**(2): p. 263-273.
18. Zhao, M., et al., *Insertion and Anchoring of HIV-1 Fusion Peptide into Complex Membrane Mimicking Human T-cell*. 2024, Cold Spring Harbor Laboratory.

19. Santos Da Silva, E., et al., *<scp>HIV</scp> -1 capsids mimic a microtubule regulator to coordinate early stages of infection.* The EMBO Journal, 2020. **39**(20): p. e104870.
20. Dharan, A., et al., *KIF5B and Nup358 Cooperatively Mediate the Nuclear Import of HIV-1 during Infection.* PLOS Pathogens, 2016. **12**(6): p. e1005700.
21. Dharan, A., et al., *Bicaudal D2 facilitates the cytoplasmic trafficking and nuclear import of HIV-1 genomes during infection.* Proceedings of the National Academy of Sciences, 2017. **114**(50): p. E10707-E10716.
22. Christensen, D.E., et al., *Reconstitution and visualization of HIV-1 capsid-dependent replication and integration in vitro.* Science, 2020. **370**(6513): p. eabc8420.
23. Francis, A.C. and G.B. Melikyan, *Single HIV-1 Imaging Reveals Progression of Infection through CA-Dependent Steps of Docking at the Nuclear Pore, Uncoating, and Nuclear Transport.* Cell Host & Microbe, 2018. **23**(4): p. 536-548.e6.
24. Rasaiyaah, J., et al., *HIV-1 evades innate immune recognition through specific cofactor recruitment.* Nature, 2013. **503**(7476): p. 402-405.
25. Yoh, S.M., et al., *Recognition of HIV-1 capsid by PQBP1 licenses an innate immune sensing of nascent HIV-1 DNA.* Molecular Cell, 2022. **82**(15): p. 2871-2884.e6.
26. Sumner, R.P., et al., *Disrupting <scp>HIV</scp> -1 capsid formation causes <scp>cGAS</scp> sensing of viral DNA.* The EMBO Journal, 2020. **39**(20).
27. Beilhartz, G.L. and M. Götte, *HIV-1 Ribonuclease H: Structure, Catalytic Mechanism and Inhibitors.* Viruses, 2010. **2**(4): p. 900-926.
28. Müller, B., et al., *Co-expression of the Subunits of the Heterodimer of HIV-1 Reverse Transcriptase in Escherichia coli.* Journal of Biological Chemistry, 1989. **264**(24): p. 13975-13978.
29. Schatz, O., et al., *Point mutations in conserved amino acid residues within the C-terminal domain of HIV-1 reverse transcriptase specifically repress RNase H function.* FEBS Letters, 1989. **257**(2): p. 311-314.
30. Kohlstaedt, L.A., et al., *Crystal Structure at 3.5 Å Resolution of HIV-1 Reverse Transcriptase Complexed with an Inhibitor.* Science, 1992. **256**(5065): p. 1783-1790.
31. Jacobo-Molina, A., et al., *Crystal structure of human immunodeficiency virus type 1 reverse transcriptase complexed with double-stranded DNA at 3.0 A resolution shows bent DNA.* Proceedings of the National Academy of Sciences, 1993. **90**(13): p. 6320-6324.
32. Sarafianos, S.G., et al., *Structure and Function of HIV-1 Reverse Transcriptase: Molecular Mechanisms of Polymerization and Inhibition.* Journal of Molecular Biology, 2009. **385**(3): p. 693-713.
33. Barraud, P., et al., *New insights into the formation of HIV-1 reverse transcription initiation complex.* Biochimie, 2007. **89**(10): p. 1204-1210.
34. Tisné, C., B.P. Roques, and F. Dardel, *The Annealing Mechanism of HIV-1 Reverse Transcription Primer onto the Viral Genome.* Journal of Biological Chemistry, 2004. **279**(5): p. 3588-3595.
35. Hu, W.S. and S.H. Hughes, *HIV-1 Reverse Transcription.* Cold Spring Harbor Perspectives in Medicine, 2012. **2**(10): p. a006882-a006882.

36. You, J.C. and C.S. McHenry, *Human immunodeficiency virus nucleocapsid protein accelerates strand transfer of the terminally redundant sequences involved in reverse transcription.* Journal of Biological Chemistry, 1994. **269**(50): p. 31491-31495.
37. Azoulay, J., et al., *Destabilization of the HIV-1 Complementary Sequence of TAR by the Nucleocapsid Protein Through Activation of Conformational Fluctuations.* Journal of Molecular Biology, 2003. **326**(3): p. 691-700.
38. Butovskaya, E., et al., *HIV-1 Nucleocapsid Protein Unfolds Stable RNA G-Quadruplexes in the Viral Genome and Is Inhibited by G-Quadruplex Ligands.* ACS Infectious Diseases, 2019. **5**(12): p. 2127-2135.
39. Götte, M., et al., *Temporal Coordination between Initiation of HIV (+)-Strand DNA Synthesis and Primer Removal.* Journal of Biological Chemistry, 1999. **274**(16): p. 11159-11169.
40. Zila, V., et al., *Cone-shaped HIV-1 capsids are transported through intact nuclear pores.* Cell, 2021. **184**(4): p. 1032-1046.e18.
41. Burdick, R.C., et al., *HIV-1 uncoats in the nucleus near sites of integration.* Proceedings of the National Academy of Sciences, 2020. **117**(10): p. 5486-5493.
42. Li, C., et al., *HIV-1 cores retain their integrity until minutes before uncoating in the nucleus.* Proceedings of the National Academy of Sciences, 2021. **118**(10): p. e2019467118.
43. Burdick, R.C., et al., *HIV-1 uncoating requires long double-stranded reverse transcription products.* Science Advances, 2024. **10**(17).
44. De Iaco, A. and J. Luban, *Cyclophilin A promotes HIV-1 reverse transcription but its effect on transduction correlates best with its effect on nuclear entry of viral cDNA.* Retrovirology, 2014. **11**(1): p. 11.
45. Buffone, C., et al., *Nup153 Unlocks the Nuclear Pore Complex for HIV-1 Nuclear Translocation in Nondividing Cells.* Journal of Virology, 2018. **92**(19).
46. Price, A.J., et al., *Host Cofactors and Pharmacologic Ligands Share an Essential Interface in HIV-1 Capsid That Is Lost upon Disassembly.* PLoS Pathogens, 2014. **10**(10): p. e1004459.
47. Bejarano, D.A., et al., *HIV-1 nuclear import in macrophages is regulated by CPSF6-capsid interactions at the nuclear pore complex.* eLife, 2019. **8**.
48. Goldgur, Y., et al., *Structure of the HIV-1 integrase catalytic domain complexed with an inhibitor: A platform for antiviral drug design.* Proceedings of the National Academy of Sciences, 1999. **96**(23): p. 13040-13043.
49. A, *HIV-1 integrase crosslinked oligomers are active in vitro.* Nucleic Acids Research, 2005. **33**(3): p. 977-986.
50. Li, M., et al., *HIV-1 Integrase Assembles Multiple Species of Stable Synaptic Complex Intasomes That Are Active for Concerted DNA Integration In vitro.* Journal of Molecular Biology, 2024. **436**(10): p. 168557.
51. Woerner, A.M., et al., *Localization of DNA Binding Activity of HIV-1 Integrase to the C-Terminal Half of the Protein.* AIDS Research and Human Retroviruses, 1992. **8**(2): p. 297-304.

52. Schauer, M. and A. Billich, *The N-terminal region of HIV-1 integrase is required for integration activity, but not for DNA-binding.* Biochemical and Biophysical Research Communications, 1992. **185**(3): p. 874-880.
53. Schröder, A.R.W., et al., *HIV-1 Integration in the Human Genome Favors Active Genes and Local Hotspots.* Cell, 2002. **110**(4): p. 521-529.
54. Cherepanov, P., et al., *HIV-1 Integrase Forms Stable Tetramers and Associates with LEDGF/p75 Protein in Human Cells.* Journal of Biological Chemistry, 2003. **278**(1): p. 372-381.
55. Lee, K., et al., *Flexible Use of Nuclear Import Pathways by HIV-1.* Cell Host & Microbe, 2010. **7**(3): p. 221-233.
56. Sowd, G.A., et al., *A critical role for alternative polyadenylation factor CPSF6 in targeting HIV-1 integration to transcriptionally active chromatin.* Proceedings of the National Academy of Sciences, 2016. **113**(8): p. E1054-E1063.
57. Rasheedi, S., et al., *The Cleavage and Polyadenylation Specificity Factor 6 (CPSF6) Subunit of the Capsid-recruited Pre-messenger RNA Cleavage Factor I (CFIm) Complex Mediates HIV-1 Integration into Genes.* Journal of Biological Chemistry, 2016. **291**(22): p. 11809-11819.
58. Engelman, A.N. and P.K. Singh, *Cellular and molecular mechanisms of HIV-1 integration targeting.* Cellular and Molecular Life Sciences, 2018. **75**(14): p. 2491-2507.
59. Cherepanov, P., et al., *Identification of an Evolutionarily Conserved Domain in Human Lens Epithelium-derived Growth Factor/Transcriptional Co-activator p75 (LEDGF/p75) That Binds HIV-1 Integrase.* Journal of Biological Chemistry, 2004. **279**(47): p. 48883-48892.
60. Shun, M.-C., et al., *LEDGF/p75 functions downstream from preintegration complex formation to effect gene-specific HIV-1 integration.* Genes & Development, 2007. **21**(14): p. 1767-1778.
61. Schaller, T., et al., *HIV-1 Capsid-Cyclophilin Interactions Determine Nuclear Import Pathway, Integration Targeting and Replication Efficiency.* PLoS Pathogens, 2011. **7**(12): p. e1002439.
62. Di Nunzio, F., et al., *Nup153 and Nup98 bind the HIV-1 core and contribute to the early steps of HIV-1 replication.* Virology, 2013. **440**(1): p. 8-18.
63. Ocwieja, K.E., et al., *HIV Integration Targeting: A Pathway Involving Transportin-3 and the Nuclear Pore Protein RanBP2.* PLoS Pathogens, 2011. **7**(3): p. e1001313.
64. Koh, Y., et al., *Differential Effects of Human Immunodeficiency Virus Type 1 Capsid and Cellular Factors Nucleoporin 153 and LEDGF/p75 on the Efficiency and Specificity of Viral DNA Integration.* Journal of Virology, 2013. **87**(1): p. 648-658.
65. Burdick, R.C., et al., *Intranuclear Positions of HIV-1 Proviruses Are Dynamic and Do Not Correlate with Transcriptional Activity.* mBio, 2022. **13**(1).
66. Francis, A.C., et al., *HIV-1 replication complexes accumulate in nuclear speckles and integrate into speckle-associated genomic domains.* Nature Communications, 2020. **11**(1).
67. Marini, B., et al., *Nuclear architecture dictates HIV-1 integration site selection.* Nature, 2015. **521**(7551): p. 227-231.

68. Albanese, A., et al., *HIV-1 Pre-Integration Complexes Selectively Target Decondensed Chromatin in the Nuclear Periphery.* PLoS ONE, 2008. **3**(6): p. e2413.
69. Müller, H.P. and H.E. Varmus, *DNA bending creates favored sites for retroviral integration: an explanation for preferred insertion sites in nucleosomes.* The EMBO Journal, 1994. **13**(19): p. 4704-4714.
70. Pryciak, P.M. and H.E. Varmus, *Nucleosomes, DNA-binding proteins, and DNA sequence modulate retroviral integration target site selection.* Cell, 1992. **69**(5): p. 769-780.
71. Bushman, F.D. and R. Craigie, *Activities of human immunodeficiency virus (HIV) integration protein in vitro: specific cleavage and integration of HIV DNA.* Proceedings of the National Academy of Sciences, 1991. **88**(4): p. 1339-1343.
72. Sherman, P.A. and J.A. Fyfe, *Human immunodeficiency virus integration protein expressed in Escherichia coli possesses selective DNA cleaving activity.* Proceedings of the National Academy of Sciences, 1990. **87**(13): p. 5119-5123.
73. Lesbats, P., A.N. Engelman, and P. Cherepanov, *Retroviral DNA Integration.* Chemical Reviews, 2016. **116**(20): p. 12730-12757.
74. Lusic, M. and R.F. Siliciano, *Nuclear landscape of HIV-1 infection and integration.* Nature Reviews Microbiology, 2017. **15**(2): p. 69-82.
75. Vink, C., et al., *Analysis of the junctions between human immunodeficiency virus type 1 proviral DNA and human DNA.* Journal of Virology, 1990. **64**(11): p. 5626-5627.
76. Mulder, L.C.F. and M.A. Muesing, *Degradation of HIV-1 Integrase by the N-end Rule Pathway.* Journal of Biological Chemistry, 2000. **275**(38): p. 29749-29753.
77. Mulder, L.C.F., L.A. Chakrabarti, and M.A. Muesing, *Interaction of HIV-1 Integrase with DNA Repair Protein hRad18.* Journal of Biological Chemistry, 2002. **277**(30): p. 27489-27493.
78. Mousnier, A., et al., *von Hippel–Lindau binding protein 1-mediated degradation of integrase affects HIV-1 gene expression at a postintegration step.* Proceedings of the National Academy of Sciences, 2007. **104**(34): p. 13615-13620.
79. Yoder, K.E. and F.D. Bushman, *Repair of Gaps in Retroviral DNA Integration Intermediates.* Journal of Virology, 2000. **74**(23): p. 11191-11200.
80. Rumbaugh, J.A., G.M. Fuentes, and R.A. Bambara, *Processing of an HIV Replication Intermediate by the Human DNA Replication Enzyme FEN1.* Journal of Biological Chemistry, 1998. **273**(44): p. 28740-28745.
81. Espeseth, A.S., et al., *siRNA Screening of a Targeted Library of DNA Repair Factors in HIV Infection Reveals a Role for Base Excision Repair in HIV Integration.* PLoS ONE, 2011. **6**(3): p. e17612.
82. Yoder, K.E., et al., *The Base Excision Repair Pathway Is Required for Efficient Lentivirus Integration.* PLoS ONE, 2011. **6**(3): p. e17862.
83. D'Orso, I., *The HIV-1 Transcriptional Program: From Initiation to Elongation Control.* Journal of Molecular Biology, 2024: p. 168690.
84. Emery, A. and R. Swanstrom, *HIV-1: To Splice or Not to Splice, That Is the Question.* Viruses, 2021. **13**(2): p. 181.

85. Verdin, E., *DNase I-hypersensitive sites are associated with both long terminal repeats and with the intragenic enhancer of integrated human immunodeficiency virus type 1*. Journal of Virology, 1991. **65**(12): p. 6790-6799.
86. Widlak, P., R.B. Gaynor, and W.T. Garrard, *In Vitro Chromatin Assembly of the HIV-1 Promoter.* Journal of Biological Chemistry, 1997. **272**(28): p. 17654-17661.
87. Brahma, S. and S. Henikoff, *The BAF chromatin remodeler synergizes with RNA polymerase II and transcription factors to evict nucleosomes.* Nature Genetics, 2024. **56**(1): p. 100-111.
88. Rafati, H., et al., *Repressive LTR Nucleosome Positioning by the BAF Complex Is Required for HIV Latency.* PLoS Biology, 2011. **9**(11): p. e1001206.
89. Kato, H., M. Horikoshi, and R.G. Roeder, *Repression of HIV-1 Transcription by a Cellular Protein.* Science, 1991. **251**(5000): p. 1476-1479.
90. Williams, S.A., et al., *NF-κB p50 promotes HIV latency through HDAC recruitment and repression of transcriptional initiation.* The EMBO Journal, 2006. **25**(1): p. 139-149.
91. Pendergrast, P.S., et al., *Mutations in the carboxy-terminal domain of TBP affect the synthesis of human immunodeficiency virus type 1 full-length and short transcripts similarly.* Journal of Virology, 1996. **70**(8): p. 5025-5034.
92. Buratowski, S., et al., *Five intermediate complexes in transcription initiation by RNA polymerase II.* Cell, 1989. **56**(4): p. 549-561.
93. Harlen, K.M. and L.S. Churchman, *The code and beyond: transcription regulation by the RNA polymerase II carboxy-terminal domain.* Nature Reviews Molecular Cell Biology, 2017. **18**(4): p. 263-273.
94. Ruiz, A., et al., *Characterization of the Influence of Mediator Complex in HIV-1 Transcription.* Journal of Biological Chemistry, 2014. **289**(40): p. 27665-27676.
95. Richter, W.F., et al., *The Mediator complex as a master regulator of transcription by RNA polymerase II.* Nature Reviews Molecular Cell Biology, 2022. **23**(11): p. 732-749.
96. Akhtar, M.S., et al., *TFIIH Kinase Places Bivalent Marks on the Carboxy-Terminal Domain of RNA Polymerase II.* Molecular Cell, 2009. **34**(3): p. 387-393.
97. Glover-Cutter, K., et al., *TFIIH-Associated Cdk7 Kinase Functions in Phosphorylation of C-Terminal Domain Ser7 Residues, Promoter-Proximal Pausing, and Termination by RNA Polymerase II.* Molecular and Cellular Biology, 2009. **29**(20): p. 5455-5464.
98. Sheridan, P.L., et al., *Histone acetyltransferases regulate HIV-1 enhancer activity in vitro.* Genes & Development, 1997. **11**(24): p. 3327-3340.
99. Van Lint, C., et al., *Transcriptional activation and chromatin remodeling of the HIV-1 promoter in response to histone acetylation.* The EMBO Journal, 1996. **15**(5): p. 1112-1120.
100. Gilchrist, D.A., et al., *Pausing of RNA Polymerase II Disrupts DNA-Specified Nucleosome Organization to Enable Precise Gene Regulation.* Cell, 2010. **143**(4): p. 540-551.
101. Zhang, Z., et al., *Negative Elongation Factor NELF Represses Human Immunodeficiency Virus Transcription by Pausing the RNA Polymerase II Complex.* Journal of Biological Chemistry, 2007. **282**(23): p. 16981-16988.

102. Marshall, N.F. and D.H. Price, *Purification of P-TEFb, a Transcription Factor Required for the Transition into Productive Elongation.* Journal of Biological Chemistry, 1995. **270**(21): p. 12335-12338.
103. Guntaka, R.V., *Transcription termination and polyadenylation in retroviruses.* Microbiological Reviews, 1993. **57**(3): p. 511-521.
104. Garcia, J.A., et al., *Functional domains required for tat-induced transcriptional activation of the HIV-1 long terminal repeat.* The EMBO Journal, 1988. **7**(10): p. 3143-3147.
105. Rice, A.P. and M.B. Mathews, *Transcriptional but not translational regulation of HIV-1 by the tat gene product.* Nature, 1988. **332**(6164): p. 551-553.
106. Jakobovits, A., et al., *A Discrete Element 3' of Human Immunodeficiency Virus 1 (HIV-1) and HIV-2 mRNA Initiation Sites Mediates Transcriptional Activation by an HIV <i>trans</i> Activator.* Molecular and Cellular Biology, 1988. **8**(6): p. 2555-2561.
107. Taylor, J.P., et al., *TAR-independent transactivation by Tat in cells derived from the CNS: a novel mechanism of HIV-1 gene regulation.* The EMBO Journal, 1992. **11**(9): p. 3395-3403.
108. Malim, M.H., et al., *Immunodeficiency virus rev trans-activator modulates the expression of the viral regulatory genes.* Nature, 1988. **335**(6186): p. 181-183.
109. Felber, B.K., et al., *rev protein of human immunodeficiency virus type 1 affects the stability and transport of the viral mRNA.* Proceedings of the National Academy of Sciences, 1989. **86**(5): p. 1495-1499.
110. Malim, M.H., et al., *The HIV-1 rev trans-activator acts through a structured target sequence to activate nuclear export of unspliced viral mRNA.* Nature, 1989. **338**(6212): p. 254-257.
111. Staudt, R.P., et al., *Structure, function, and inhibitor targeting of HIV-1 Nef-effector kinase complexes.* Journal of Biological Chemistry, 2020. **295**(44): p. 15158-15171.
112. Garcia, J.V. and A.D. Miller, *Serine phosphorylation-independent downregulation of cell-surface CD4 by nef.* Nature, 1991. **350**(6318): p. 508-511.
113. Garcia, J.V., J. Alfano, and A.D. Miller, *The negative effect of human immunodeficiency virus type 1 Nef on cell surface CD4 expression is not species specific and requires the cytoplasmic domain of CD4.* Journal of Virology, 1993. **67**(3): p. 1511-1516.
114. Anderson, S., et al., *Nef from primary isolates of human immunodeficiency virus type 1 suppresses surface CD4 expression in human and mouse T cells.* Journal of Virology, 1993. **67**(8): p. 4923-4931.
115. Vanlandschoot, P., et al., *Nanobodies®: New ammunition to battle viruses.* Antiviral Research, 2011. **92**(3): p. 389-407.
116. Marin, M., et al., *HIV-1 Vif protein binds the editing enzyme APOBEC3G and induces its degradation.* Nature Medicine, 2003. **9**(11): p. 1398-1403.
117. Sheehy, A.M., N.C. Gaddis, and M.H. Malim, *The antiretroviral enzyme APOBEC3G is degraded by the proteasome in response to HIV-1 Vif.* Nature Medicine, 2003. **9**(11): p. 1404-1407.
118. Lecossier, D., et al., *Hypermutation of HIV-1 DNA in the Absence of the Vif Protein.* Science, 2003. **300**(5622): p. 1112-1112.

119. Izumi, T., et al., *HIV-1 viral infectivity factor interacts with TP53 to induce G2 cell cycle arrest and positively regulate viral replication.* Proceedings of the National Academy of Sciences, 2010. **107**(48): p. 20798-20803.
120. Salamango, D.J. and R.S. Harris, *Dual Functionality of HIV-1 Vif in APOBEC3 Counteraction and Cell Cycle Arrest.* Frontiers in Microbiology, 2021. **11**.
121. Belzile, J.-P., et al., *HIV-1 Vpr-Mediated G2 Arrest Involves the DDB1-CUL4AVPRBP E3 Ubiquitin Ligase.* PLoS Pathogens, 2007. **3**(7): p. e85.
122. Ahn, J., et al., *HIV-1 Vpr Loads Uracil DNA Glycosylase-2 onto DCAF1, a Substrate Recognition Subunit of a Cullin 4A-RING E3 Ubiquitin Ligase for Proteasome-dependent Degradation.* Journal of Biological Chemistry, 2010. **285**(48): p. 37333-37341.
123. Eldin, P., et al., *Vpr expression abolishes the capacity of HIV-1 infected cells to repair uracilated DNA.* Nucleic Acids Research, 2014. **42**(3): p. 1698-1710.
124. Wu, Y., et al., *The DDB1–DCAF1–Vpr–UNG2 crystal structure reveals how HIV-1 Vpr steers human UNG2 toward destruction.* Nature Structural & Molecular Biology, 2016. **23**(10): p. 933-940.
125. Fernandes, J., B. Jayaraman, and A. Frankel, *The HIV-1 Rev response element.* RNA Biology, 2012. **9**(1): p. 6-11.
126. Emery, A., et al., *Characterizing HIV-1 Splicing by Using Next-Generation Sequencing.* Journal of Virology, 2017. **91**(6): p. JVI.02515-16.
127. Ocwieja, K.E., et al., *Dynamic regulation of HIV-1 mRNA populations analyzed by single-molecule enrichment and long-read sequencing.* Nucleic Acids Research, 2012. **40**(20): p. 10345-10355.
128. Jacks, T., et al., *Characterization of ribosomal frameshifting in HIV-1 gag-pol expression.* Nature, 1988. **331**(6153): p. 280-3.
129. Moosmayer, D., et al., *Expression and frameshifting but extremely inefficient proteolytic processing of the HIV-1 gag and pol gene products in stably transfected rodent cell lines.* Virology, 1991. **183**(1): p. 215-224.
130. Shehu-Xhilaga, M., S.M. Crowe, and J. Mak, *Maintenance of the Gag/Gag-Pol Ratio Is Important for Human Immunodeficiency Virus Type 1 RNA Dimerization and Viral Infectivity.* Journal of Virology, 2001. **75**(4): p. 1834-1841.
131. Chen, C. and R.C. Montelaro, *Characterization of RNA elements that regulate gag-pol ribosomal frameshifting in equine infectious anemia virus.* J Virol, 2003. **77**(19): p. 10280-7.
132. Wang, X., et al., *Regulation of HIV-1 Gag-Pol Expression by Shiftless, an Inhibitor of Programmed -1 Ribosomal Frameshifting.* Cell, 2019. **176**(3): p. 625-635.e14.
133. Karacostas, V., et al., *Overexpression of the HIV-1 gag-pol polyprotein results in intracellular activation of HIV-1 protease and inhibition of assembly and budding of virus-like particles.* Virology, 1993. **193**(2): p. 661-71.
134. Park, J. and C.D. Morrow, *Overexpression of the gag-pol precursor from human immunodeficiency virus type 1 proviral genomes results in efficient proteolytic processing in the absence of virion production.* Journal of Virology, 1991. **65**(9): p. 5111-5117.

135. Dulude, D., et al., *Decreasing the frameshift efficiency translates into an equivalent reduction of the replication of the human immunodeficiency virus type 1*. Virology, 2006. **345**(1): p. 127-36.
136. Lyon, K., et al., *Live-Cell Single RNA Imaging Reveals Bursts of Translational Frameshifting*. Mol Cell, 2019. **75**(1): p. 172-183 e9.
137. Anokhin, B. and P. Spearman, *Viral and Host Factors Regulating HIV-1 Envelope Protein Trafficking and Particle Incorporation*. Viruses, 2022. **14**(8): p. 1729.
138. Wyatt, R. and J. Sodroski, *The HIV-1 Envelope Glycoproteins: Fusogens, Antigens, and Immunogens*. Science, 1998. **280**(5371): p. 1884-1888.
139. Pancera, M., et al., *Structure of HIV-1 gp120 with gp41-interactive region reveals layered envelope architecture and basis of conformational mobility*. Proceedings of the National Academy of Sciences, 2010. **107**(3): p. 1166-1171.
140. Decroly, E., et al., *The convertases furin and PC1 can both cleave the human immunodeficiency virus (HIV)-1 envelope glycoprotein gp160 into gp120 (HIV-1 SU) and gp41 (HIV-I TM)*. Journal of Biological Chemistry, 1994. **269**(16): p. 12240-12247.
141. Hallenberger, S., et al., *Inhibition of furin-mediated cleavage activation of HIV-1 glycoprotein gpl60*. Nature, 1992. **360**(6402): p. 358-361.
142. Kirschman, J., et al., *HIV-1 Envelope Glycoprotein Trafficking through the Endosomal Recycling Compartment Is Required for Particle Incorporation*. Journal of Virology, 2018. **92**(5).
143. Sundquist, W.I. and H.G. Krausslich, *HIV-1 assembly, budding, and maturation*. Cold Spring Harb Perspect Med, 2012. **2**(7): p. a006924.
144. Yu, X., et al., *The matrix protein of human immunodeficiency virus type 1 is required for incorporation of viral envelope protein into mature virions*. Journal of Virology, 1992. **66**(8): p. 4966-4971.
145. Fäcke, M., et al., *A large deletion in the matrix domain of the human immunodeficiency virus gag gene redirects virus particle assembly from the plasma membrane to the endoplasmic reticulum*. Journal of Virology, 1993. **67**(8): p. 4972-4980.
146. Yuan, X., et al., *Mutations in the N-terminal region of human immunodeficiency virus type 1 matrix protein block intracellular transport of the Gag precursor*. J Virol, 1993. **67**(11): p. 6387-94.
147. Dorfman, T., et al., *Role of the matrix protein in the virion association of the human immunodeficiency virus type 1 envelope glycoprotein*. Journal of Virology, 1994. **68**(3): p. 1689-1696.
148. Tedbury, P.R., et al., *HIV-1 Matrix Trimerization-Impaired Mutants Are Rescued by Matrix Substitutions That Enhance Envelope Glycoprotein Incorporation*. Journal of Virology, 2019. **94**(1).
149. Banerjee, P., V. Monje-Galvan, and G.A. Voth, *Cooperative Membrane Binding of HIV-1 Matrix Proteins*. 2023, Cold Spring Harbor Laboratory.
150. Saad, J.S., et al., *Structural basis for targeting HIV-1 Gag proteins to the plasma membrane for virus assembly*. Proc Natl Acad Sci U S A, 2006. **103**(30): p. 11364-9.
151. Saad, J.S., et al., *Point mutations in the HIV-1 matrix protein turn off the myristyl switch*. J Mol Biol, 2007. **366**(2): p. 574-85.

152. Liao, Z., et al., *Lipid Rafts and HIV Pathogenesis: Host Membrane Cholesterol Is Required for Infection by HIV Type 1.* AIDS Research and Human Retroviruses, 2001. **17**(11): p. 1009-1019.
153. Chan, R., et al., *Retroviruses Human Immunodeficiency Virus and Murine Leukemia Virus Are Enriched in Phosphoinositides.* Journal of Virology, 2008. **82**(22): p. 11228-11238.
154. Schur, F.K., et al., *An atomic model of HIV-1 capsid-SP1 reveals structures regulating assembly and maturation.* Science, 2016. **353**(6298): p. 506-8.
155. Pak, A.J., et al., *Immature HIV-1 lattice assembly dynamics are regulated by scaffolding from nucleic acid and the plasma membrane.* Proceedings of the National Academy of Sciences, 2017. **114**(47): p. E10056-E10065.
156. Mallery, D.L., et al., *Cellular IP6 Levels Limit HIV Production while Viruses that Cannot Efficiently Package IP6 Are Attenuated for Infection and Replication.* Cell Reports, 2019. **29**(12): p. 3983-3996.e4.
157. Dick, R.A., et al., *IP6 Regulation of HIV Capsid Assembly, Stability, and Uncoating.* Viruses, 2018. **10**(11): p. 640.
158. Dick, R.A., et al., *Inositol phosphates are assembly co-factors for HIV-1.* Nature, 2018. **560**(7719): p. 509-512.
159. Morellet, N., et al., *Determination of the structure of the nucleocapsid protein NCp7 from the human immunodeficiency virus type 1 by 1H NMR.* The EMBO Journal, 1992. **11**(8): p. 3059-3065.
160. De Rocquigny, H., et al., *Viral RNA annealing activities of human immunodeficiency virus type 1 nucleocapsid protein require only peptide domains outside the zinc fingers.* Proceedings of the National Academy of Sciences, 1992. **89**(14): p. 6472-6476.
161. Gien, H., et al., *Cationic Residues of the HIV-1 Nucleocapsid Protein Enable DNA Condensation to Maintain Viral Core Particle Stability during Reverse Transcription.* Viruses, 2024. **16**(6): p. 872.
162. Clever, J., C. Sassetti, and T.G. Parslow, *RNA secondary structure and binding sites for gag gene products in the 5' packaging signal of human immunodeficiency virus type 1.* Journal of Virology, 1995. **69**(4): p. 2101-2109.
163. Aldovini, A. and R.A. Young, *Mutations of RNA and protein sequences involved in human immunodeficiency virus type 1 packaging result in production of noninfectious virus.* Journal of Virology, 1990. **64**(5): p. 1920-1926.
164. D'Souza, V. and M.F. Summers, *How retroviruses select their genomes.* Nature Reviews Microbiology, 2005. **3**(8): p. 643-655.
165. Saadatmand, J. and L. Kleiman, *Aspects of HIV-1 assembly that promote primer tRNALys3 annealing to viral RNA.* Virus Research, 2012. **169**(2): p. 340-348.
166. Barat, C., et al., *Analysis of the Interactions of HIV1 Replication Primer tRNALys,3 with Nucleocapsid Protein and Reverse Transcriptase.* Journal of Molecular Biology, 1993. **231**(2): p. 185-190.
167. Olson, E.D. and K. Musier-Forsyth, *Retroviral Gag protein–RNA interactions: Implications for specific genomic RNA packaging and virion assembly.* Seminars in Cell & Developmental Biology, 2019. **86**: p. 129-139.

168. Yang, Y., et al., *Roles of Gag-RNA interactions in HIV-1 virus assembly deciphered by single-molecule localization microscopy.* Proceedings of the National Academy of Sciences, 2018. **115**(26): p. 6721-6726.
169. Paxton, W., R.I. Connor, and N.R. Landau, *Incorporation of Vpr into human immunodeficiency virus type 1 virions: requirement for the p6 region of gag and mutational analysis.* Journal of Virology, 1993. **67**(12): p. 7229-7237.
170. Strack, B., et al., *AIP1/ALIX is a binding partner for HIV-1 p6 and EIAV p9 functioning in virus budding.* Cell, 2003. **114**(6): p. 689-99.
171. Stuchell, M.D., et al., *The Human Endosomal Sorting Complex Required for Transport (ESCRT-I) and Its Role in HIV-1 Budding.* Journal of Biological Chemistry, 2004. **279**(34): p. 36059-36071.
172. Demirov, D.G., J.M. Orenstein, and E.O. Freed, *The Late Domain of Human Immunodeficiency Virus Type 1 p6 Promotes Virus Release in a Cell Type-Dependent Manner.* J.Virol., 2002. **76**(1): p. 105-117.
173. Kondo, E. and H.G. Göttlinger, *A conserved LXXLF sequence is the major determinant in p6gag required for the incorporation of human immunodeficiency virus type 1 Vpr.* Journal of Virology, 1996. **70**(1): p. 159-164.
174. Jenkins, Y., et al., *Biochemical Analyses of the Interactions between Human Immunodeficiency Virus Type 1 Vpr and p6Gag.* J.Virol., 2001. **75**(21): p. 10537-10542.
175. Bachand, F., et al., *Incorporation of Vpr into human immunodeficiency virus type 1 requires a direct interaction with the p6 domain of the p55 gag precursor.* J.Biol.Chem., 1999. **274**: p. 9083-9091.
176. Neil, S.J., T. Zang, and P.D. Bieniasz, *Tetherin inhibits retrovirus release and is antagonized by HIV-1 Vpu.* Nature, 2008. **451**(7177): p. 425-30.
177. Van Damme, N., et al., *The interferon-induced protein BST-2 restricts HIV-1 release and is downregulated from the cell surface by the viral Vpu protein.* Cell Host Microbe, 2008. **3**(4): p. 245-52.
178. Douglas, J.L., et al., *Vpu Directs the Degradation of the Human Immunodeficiency Virus Restriction Factor BST-2/Tetherin via a βTrCP-Dependent Mechanism.* Journal of Virology, 2009. **83**(16): p. 7931-7947.
179. Kuhl, B.D., et al., *Tetherin and Its Viral Antagonists.* Journal of Neuroimmune Pharmacology, 2011. **6**(2): p. 188-201.
180. Telenti, A., et al., *Analysis of natural variants of the human immunodeficiency virus type 1 gag-pol frameshift stem-loop structure.* 2002. **76**(15): p. 7868-7873.
181. Darke, P.L., et al., *HIV-1 protease specificity of peptide cleavage is sufficient for processing of gag and pol polyproteins.* Biochemical and Biophysical Research Communications, 1988. **156**(1): p. 297-303.
182. Meek, T.D., et al., *Human immunodeficiency virus 1 protease expressed in Escherichia coli behaves as a dimeric aspartic protease.* Proceedings of the National Academy of Sciences, 1989. **86**(6): p. 1841-1845.
183. Erickson-Viitanen, S., et al., *Cleavage of HIV-1 gag polyprotein synthesized in vitro: sequential cleavage by the viral protease.* AIDS Res Hum Retroviruses, 1989. **5**(6): p. 577-91.

184. Dreyer, G.B., et al., *Inhibition of human immunodeficiency virus 1 protease in vitro: rational design of substrate analogue inhibitors.* Proceedings of the National Academy of Sciences, 1989. **86**(24): p. 9752-9756.
185. Strickler, J.E., et al., *Characterization and autoprocessing of precursor and mature forms of human immunodeficiency virus type 1 (HIV 1) protease purified from <i>Escherichia coli</i>.* Proteins: Structure, Function, and Bioinformatics, 1989. **6**(2): p. 139-154.
186. Louis, J.M., et al., *Autoprocessing of the HIV-1 protease using purified wild-type and mutated fusion proteins expressed at high levels in Escherichia coli.* Eur J Biochem, 1991. **199**(2): p. 361-9.
187. Huang, L. and C. Chen, *Understanding HIV-1 protease autoprocessing for novel therapeutic development.* Future Med Chem, 2013. **5**(11): p. 1215-29.
188. Pettit, S.C., et al., *The p2 domain of human immunodeficiency virus type 1 Gag regulates sequential proteolytic processing and is required to produce fully infectious virions.* J Virol, 1994. **68**(12): p. 8017-27.
189. Pettit, S.C., et al., *Replacement of the P1 amino acid of human immunodeficiency virus type 1 Gag processing sites can inhibit or enhance the rate of cleavage by the viral protease.* J Virol, 2002. **76**(20): p. 10226-33.
190. Tabler, C.O. and J.C. Tilton, *Mechanism and Kinetics of HIV-1 Protease Activation.* Viruses, 2024. **16**(12): p. 1826.
191. Le Grice, S.F., J. Mills, and J. Mous, *Active site mutagenesis of the AIDS virus protease and its alleviation by trans complementation.* The EMBO Journal, 1988. **7**(8): p. 2547-2553.
192. Erickson, J., et al., *Design, Activity, and 2.8 Å Crystal Structure of a <i>C</i> ₂ Symmetric Inhibitor Complexed to HIV-1 Protease.* Science, 1990. **249**(4968): p. 527-533.
193. DesJarlais, R.L., et al., *Structure-based design of nonpeptide inhibitors specific for the human immunodeficiency virus 1 protease.* Proc Natl Acad Sci U S A, 1990. **87**(17): p. 6644-8.
194. Huff, J.R., *HIV protease: a novel chemotherapeutic target for AIDS.* Journal of Medicinal Chemistry, 1991. **34**(8): p. 2305-2314.
195. Wlodawer, A. and J. Vondrasek, *Inhibitors of HIV-1 protease: a major success of structure-assisted drug design.* Annu Rev Biophys Biomol Struct, 1998. **27**: p. 249-84.
196. Roberts, N.A., et al., *Rational Design of Peptide-Based HIV Proteinase Inhibitors.* Science, 1990. **248**(4953): p. 358-361.
197. Arrigo, S.J. and K. Huffman, *Potent inhibition of human immunodeficiency virus type 1 (HIV-1) replication by inducible expression of HIV-1 PR multimers.* Journal of Virology, 1995. **69**(10): p. 5988-5994.
198. Krausslich, H.G., *Human immunodeficiency virus proteinase dimer as component of the viral polyprotein prevents particle assembly and viral infectivity.* Proc Natl Acad Sci USA, 1991. **88**(8): p. 3213-7.
199. Tang, C., et al., *Visualizing transient events in amino-terminal autoprocessing of HIV-1 protease.* Nature, 2008. **455**(7213): p. 693-6.

200. Louis, J.M., G.M. Clore, and A.M. Gronenborn, *Autoprocessing of HIV-1 protease is tightly coupled to protein folding.* Nat.Struct.Biol., 1999. **6**: p. 868.
201. Agniswamy, J., et al., *Terminal interface conformations modulate dimer stability prior to amino terminal autoprocessing of HIV-1 protease.* Biochemistry, 2012. **51**(5): p. 1041-50.
202. Louis, J.M., et al., *Revisiting monomeric HIV-1 protease. Characterization and redesign for improved properties.* J Biol Chem, 2003. **278**(8): p. 6085-92.
203. Ishima, R., et al., *Folded monomer of HIV-1 protease.* J Biol Chem, 2001. **276**(52): p. 49110-6.
204. Chagas, B.C.A., et al., *Interplay between protease and reverse transcriptase dimerization in a model HIV-1 polyprotein.* Protein Science, 2024. **33**(7).
205. Wang, Q., et al., *CARD8 is an inflammasome sensor for HIV-1 protease activity.* Science, 2021. **371**(6535): p. eabe1707.
206. Wang, Q., et al., *The CARD8 inflammasome dictates HIV/SIV pathogenesis and disease progression.* Cell, 2024. **187**(5): p. 1223-1237.e16.
207. Kulsuptrakul, J., et al., *A human-specific motif facilitates CARD8 inflammasome activation after HIV-1 infection.* eLife, 2023. **12**.
208. Kim, J.G. and L. Shan, *Beyond Inhibition: A Novel Strategy of Targeting HIV-1 Protease to Eliminate Viral Reservoirs.* Viruses, 2022. **14**(6): p. 1179.
209. Tabler, C.O., et al., *The HIV-1 Viral Protease Is Activated during Assembly and Budding Prior to Particle Release.* Journal of Virology, 2022. **96**(9).
210. Bendjennat, M. and S. Saffarian, *The Race against Protease Activation Defines the Role of ESCRTs in HIV Budding.* PLoS Pathog, 2016. **12**(6): p. e1005657.
211. Lee, Y.-M., C.-J. Tian, and X.-F. Yu, *A Bipartite Membrane-Binding Signal in the Human Immunodeficiency Virus Type 1 Matrix Protein Is Required for the Proteolytic Processing of Gag Precursors in a Cell Type-Dependent Manner.* Journal of Virology, 1998. **72**(11): p. 9061-9068.
212. Louis, J.M., et al., *Kinetics and mechanism of autoprocessing of human immunodeficiency virus type 1 protease from an analog of the Gag-Pol polyprotein.* Proc Natl Acad Sci USA, 1994. **91**(17): p. 7970-4.
213. Pettit, S.C., et al., *Processing sites in the human immunodeficiency virus type 1 (HIV-1) Gag-Pro-Pol precursor are cleaved by the viral protease at different rates.* Retrovirology, 2005. **2**: p. 66.
214. Kaplan, A.H., et al., *Partial inhibition of the human immunodeficiency virus type 1 protease results in aberrant virus assembly and the formation of noninfectious particles.* J Virol, 1993. **67**(7): p. 4050-5.
215. Wiegers, K., et al., *Sequential steps in human immunodeficiency virus particle maturation revealed by alterations of individual Gag polyprotein cleavage sites.* J Virol, 1998. **72**(4): p. 2846-54.
216. Li, F., et al., *PA-457: A potent HIV inhibitor that disrupts core condensation by targeting a late step in Gag processing.* Proc.Natl.Acad.Sci.U.S.A, 2003. **100**(23): p. 13555-13560.

217. Koh, Y., et al., *Potent Inhibition of HIV-1 Replication by Novel Non-peptidyl Small Molecule Inhibitors of Protease Dimerization.* J Biol Chem, 2007. **282**(39): p. 28709-20.
218. Lee, S.K., J. Harris, and R. Swanstrom, *A strongly transdominant mutation in the human immunodeficiency virus type 1 gag gene defines an Achilles heel in the virus life cycle.* J Virol, 2009. **83**(17): p. 8536-43.
219. Potempa, M., et al., *The triple threat of HIV-1 protease inhibitors.* Curr Top Microbiol Immunol, 2015. **389**: p. 203-41.
220. Anderson-Daniels, J., et al., *Dominant Negative MA-CA Fusion Protein Is Incorporated into HIV-1 Cores and Inhibits Nuclear Entry of Viral Preintegration Complexes.* J Virol, 2019. **93**(21).
221. Hayashi, H., et al., *Dimerization of HIV-1 protease occurs through two steps relating to the mechanism of protease dimerization inhibition by darunavir.* Proceedings of the National Academy of Sciences, 2014. **111**(33): p. 12234-12239.
222. Weber, I.T., *Comparison of the crystal structures and intersubunit interactions of human immunodeficiency and Rous sarcoma virus proteases.* Journal of Biological Chemistry, 1990. **265**(18): p. 10492-10496.
223. Todd, M.J., N. Semo, and E. Freire, *The structural stability of the HIV-1 protease.* J Mol Biol, 1998. **283**(2): p. 475-88.
224. Brik, A. and C.-H. Wong, *HIV-1 protease: mechanism and drug discovery.* Organic & Biomolecular Chemistry, 2003. **1**(1): p. 5-14.
225. Hornak, V., et al., *HIV-1 protease flaps spontaneously open and reclose in molecular dynamics simulations.* Proceedings of the National Academy of Sciences, 2006. **103**(4): p. 915-920.
226. Deshmukh, L., et al., *Binding kinetics and substrate selectivity in HIV-1 protease−Gag interactions probed at atomic resolution by chemical exchange NMR.* Proceedings of the National Academy of Sciences, 2017. **114**(46): p. E9855-E9862.
227. Impens, F., et al., *A catalogue of putative HIV-1 protease host cell substrates.* bchm, 2012. **393**(9): p. 915-931.
228. Chaudhury, S. and J.J. Gray, *Identification of Structural Mechanisms of HIV-1 Protease Specificity Using Computational Peptide Docking: Implications for Drug Resistance.* Structure, 2009. **17**(12): p. 1636-1648.
229. Prabu-Jeyabalan, M., E. Nalivaika, and C.A. Schiffer, *How does a symmetric dimer recognize an asymmetric substrate? a substrate complex of HIV-1 protease.* Journal of Molecular Biology, 2000. **301**(5): p. 1207-1220.
230. Prabu-Jeyabalan, M., E. Nalivaika, and C.A. Schiffer, *Substrate Shape Determines Specificity of Recognition for HIV-1 Protease.* Structure, 2002. **10**(3): p. 369-381.
231. Louis, J.M., et al., *Proteolytic processing of HIV-1 protease precursor, kinetics and mechanism.* J Biol Chem, 1999. **274**(33): p. 23437-42.
232. Ludwig, C., A. Leiherer, and R. Wagner, *Importance of protease cleavage sites within and flanking human immunodeficiency virus type 1 transframe protein p6* for spatiotemporal regulation of protease activation.* J Virol, 2008. **82**(9): p. 4573-84.

233. Tessmer, U. and H.G. Krausslich, *Cleavage of human immunodeficiency virus type 1 proteinase from the N-terminally adjacent p6* protein is essential for efficient Gag polyprotein processing and viral infectivity.* J Virol, 1998. **72**(4): p. 3459-63.
234. Cherry, E., et al., *Characterization of human immunodeficiency virus type-1 (HIV-1) particles that express protease-reverse transcriptase fusion proteins.* J Mol Biol, 1998. **284**(1): p. 43-56.
235. Louis, J.M., et al., *HIV-1 protease: maturation, enzyme specificity, and drug resistance.* Adv Pharmacol, 2000. **49**: p. 111-46.
236. Louis, J.M., et al., *HIV-1 protease: structure, dynamics, and inhibition.* Adv Pharmacol, 2007. **55**: p. 261-98.
237. Davis, D.A., et al., *Inhibition of HIV-1 replication by a peptide dimerization inhibitor of HIV-1 protease.* Antiviral Res, 2006. **72**(2): p. 89-99.
238. Huang, L., et al., *Modulation of human immunodeficiency virus type 1 protease autoprocessing by charge properties of surface residue 69.* J Virol, 2009. **83**(15): p. 7789-93.
239. Pettit, S.C., et al., *Ordered processing of the human immunodeficiency virus type 1 GagPol precursor is influenced by the context of the embedded viral protease.* J Virol, 2005. **79**(16): p. 10601-7.
240. Pettit, S.C., et al., *The dimer interfaces of protease and extra-protease domains influence the activation of protease and the specificity of GagPol cleavage.* J Virol, 2003. **77**(1): p. 366-74.
241. Pettit, S.C., et al., *Initial cleavage of the human immunodeficiency virus type 1 GagPol precursor by its activated protease occurs by an intramolecular mechanism.* J Virol, 2004. **78**(16): p. 8477.
242. Huang, L. and C. Chen, *Autoprocessing of human immunodeficiency virus type 1 protease miniprecursor fusions in mammalian cells.* AIDS Res Ther, 2010. **7**(1): p. 27.
243. Huang, L., A. Hall, and C. Chen, *Cysteine 95 and other residues influence the regulatory effects of Histidine 69 mutations on Human Immunodeficiency Virus Type 1 protease autoprocessing.* Retrovirology, 2010. **7**: p. 24.
244. Huang, L., Y. Li, and C. Chen, *Flexible catalytic site conformations implicated in modulation of HIV-1 protease autoprocessing reactions.* Retrovirology, 2011. **8**(1): p. 79.
245. Tien, C., et al., *Context-dependent autoprocessing of human immunodeficiency virus type 1 protease precursors.* PLoS One, 2018. **13**(1): p. e0191372.
246. Watanabe, S.M., et al., *The HIV-1 late domain-2 S40A polymorphism in antiretroviral (or ART)-exposed individuals influences protease inhibitor susceptibility.* Retrovirology, 2016. **13**(1): p. 64.
247. Counts, C.J., et al., *A Functional Interplay between Human Immunodeficiency Virus Type 1 Protease Residues 77 and 93 Involved in Differential Regulation of Precursor Autoprocessing and Mature Protease Activity.* PLoS One, 2015. **10**(4): p. e0123561.
248. Huang, L., et al., *Targeting HIV-1 Protease Autoprocessing for High-throughput Drug Discovery and Drug Resistance Assessment.* Sci Rep, 2019.

249. Louis, J.M., et al., *Inhibition of autoprocessing of natural variants and multidrug resistant mutant precursors of HIV-1 protease by clinical inhibitors.* Proc Natl Acad Sci USA, 2011. **108**(22): p. 9072-7.
250. Humpolickova, J., et al., *Inhibition of the precursor and mature forms of HIV-1 protease as a tool for drug evaluation.* Sci Rep, 2018. **8**(1): p. 10438.
251. Davis, D.A., et al., *Activity of human immunodeficiency virus type 1 protease inhibitors against the initial autocleavage in Gag-Pol polyprotein processing.* Antimicrob Agents Chemother, 2012. **56**(7): p. 3620-8.
252. Kim, J.H., et al., *High cleavage efficiency of a 2A peptide derived from porcine teschovirus-1 in human cell lines, zebrafish and mice.* PLoS One, 2011. **6**(4): p. e18556.
253. Waugh, D.S., *Crystal structures of MBP fusion proteins.* Protein Sci, 2016. **25**(3): p. 559-71.
254. Reuten, R., et al., *Maltose-Binding Protein (MBP), a Secretion-Enhancing Tag for Mammalian Protein Expression Systems.* PLoS One, 2016. **11**(3): p. e0152386.
255. Varghese, V., et al., *Prototypical Recombinant Multi-Protease-Inhibitor-Resistant Infectious Molecular Clones of Human Immunodeficiency Virus Type 1.* Antimicrob Agents Chemother, 2013. **57**(9): p. 4290-4299.
256. Kozal, M.J., et al., *Extensive polymorphisms observed in HIV–1 clade B protease gene using high–density oligonucleotide arrays.* Nature Medicine, 1996. **2**(7): p. 753-759.
257. Rhee, S.Y., et al., *HIV-1 protease mutations and protease inhibitor cross-resistance.* Antimicrob Agents Chemother, 2010. **54**(10): p. 4253-61.
258. Mitsuya, H., et al., *Development of Protease Inhibitors and the Fight with Drug-Resistant HIV-1 Variants*. 2008, Elsevier. p. 169-197.
259. Wensing, A.M., N.M. van Maarseveen, and M. Nijhuis, *Fifteen years of HIV Protease Inhibitors: raising the barrier to resistance.* Antiviral Res, 2010. **85**(1): p. 59-74.
260. Colman, P.M., *New Antivirals and Drug Resistance.* Annual Review of Biochemistry, 2009. **78**(1): p. 95-118.
261. Shafer, R.W., *Genotypic Testing for Human Immunodeficiency Virus Type 1 Drug Resistance.* Clinical Microbiology Reviews, 2002. **15**(2): p. 247-277.
262. Dautin, N., G. Karimova, and D. Ladant, *Human immunodeficiency virus (HIV) type 1 transframe protein can restore activity to a dimerization-deficient HIV protease variant.* J Virol, 2003. **77**(15): p. 8216-26.
263. Barre-Sinoussi, F., et al., *Isolation of a T-lymphotropic retrovirus from a patient at risk for acquired immune deficiency syndrome (AIDS).* Science, 1983. **220**(4599): p. 868-71.
264. Gallo, R.C., et al., *Frequent detection and isolation of cytopathic retroviruses (HTLV-III) from patients with AIDS and at risk for AIDS.* Science, 1984. **224**(4648): p. 500-3.
265. Oroszlan, S. and R.B. Luftig, *Retroviral proteinases.* Curr Top Microbiol Immunol, 1990. **157**: p. 153-85.
266. Fujii, K., J.H. Hurley, and E.O. Freed, *Beyond Tsg101: the role of Alix in 'ESCRTing' HIV-1.* Nat Rev Microbiol, 2007. **5**(12): p. 912-6.

267. Votteler, J. and W.I. Sundquist, *Virus budding and the ESCRT pathway.* Cell Host Microbe, 2013. **14**(3): p. 232-41.
268. Pearl, L.H. and W.R. Taylor, *A structural model for the retroviral proteases.* Nature, 1987. **329**(6137): p. 351-4.
269. Darke, P.L., et al., *Dissociation and association of the HIV-1 protease dimer subunits: equilibria and rates.* Biochemistry, 1994. **33**(1): p. 98-105.
270. Lee, S.K., et al., *Context surrounding processing sites is crucial in determining cleavage rate of a subset of processing sites in HIV-1 Gag and Gag-Pro-Pol polyprotein precursors by viral protease.* J Biol Chem, 2012. **287**(16): p. 13279-90.
271. Lee, S.K., M. Potempa, and R. Swanstrom, *The choreography of HIV-1 proteolytic processing and virion assembly.* J Biol Chem, 2012. **287**(49): p. 40867-74.
272. Zybarth, G. and C. Carter, *Domains upstream of the protease (PR) in human immunodeficiency virus type 1 Gag-Pol influence PR autoprocessing.* J Virol, 1995. **69**(6): p. 3878.
273. Paulus, C., C. Ludwig, and R. Wagner, *Contribution of the Gag-Pol transframe domain p6* and its coding sequence to morphogenesis and replication of human immunodeficiency virus type 1*. Virology, 2004. **330**(1): p. 271.
274. Ganser-Pornillos, B.K., M. Yeager, and O. Pornillos, *Assembly and architecture of HIV.* Adv Exp Med Biol, 2012. **726**: p. 441-65.
275. Lefebvre, E. and C.A. Schiffer, *Resilience to resistance of HIV-1 protease inhibitors: profile of darunavir.* AIDS Rev, 2008. **10**(3): p. 131-42.
276. McKeage, K., C.M. Perry, and S.J. Keam, *Darunavir: a review of its use in the management of HIV infection in adults.* Drugs, 2009. **69**(4): p. 477-503.
277. la Porte, C.J., *Saquinavir, the pioneer antiretroviral protease inhibitor.* Expert Opin Drug Metab Toxicol, 2009. **5**(10): p. 1313-22.
278. Lockbaum, G.J., et al., *Structural Adaptation of Darunavir Analogues against Primary Mutations in HIV-1 Protease.* ACS Infect Dis, 2019. **5**(2): p. 316-325.
279. Ghosh, A.K., I.T. Weber, and H. Mitsuya, *Beyond darunavir: recent development of next generation HIV-1 protease inhibitors to combat drug resistance.* Chem Commun (Camb), 2022. **58**(84): p. 11762-11782.
280. Velazquez-Campoy, A. and E. Freire, *Incorporating target heterogeneity in drug design.* J Cell Biochem Suppl, 2001. **Suppl 37**: p. 82-8.
281. Velazquez-Campoy, A., et al., *Structural and thermodynamic basis of resistance to HIV-1 protease inhibition: implications for inhibitor design.* Curr Drug Targets Infect Disord, 2003. **3**(4): p. 311-28.
282. Velazquez-Campoy, A., et al., *Protease inhibition in African subtypes of HIV-1.* AIDS Rev, 2003. **5**(3): p. 165-71.
283. Shafer, R.W. and J.M. Schapiro, *Drug resistance and antiretroviral drug development.* J Antimicrob Chemother, 2005. **55**(6): p. 817-20.
284. Shafer, R.W., et al., *HIV-1 protease and reverse transcriptase mutations for drug resistance surveillance.* AIDS, 2007. **21**(2): p. 215-23.
285. Shafer, R.W. and J.M. Schapiro, *HIV-1 drug resistance mutations: an updated framework for the second decade of HAART.* AIDS Rev, 2008. **10**(2): p. 67-84.

286. Wu, T.D., et al., *Mutation patterns and structural correlates in human immunodeficiency virus type 1 protease following different protease inhibitor treatments.* J Virol, 2003. **77**(8): p. 4836-47.
287. Weber, I.T. and R.W. Harrison, *Decoding HIV resistance: from genotype to therapy.* Future Med Chem, 2017. **9**(13): p. 1529-1538.
288. Shah, D., et al., *Evolution of drug resistance in HIV protease.* BMC Bioinformatics, 2020. **21**(Suppl 18): p. 497.
289. Rhee, S.Y., et al., *Distribution of human immunodeficiency virus type 1 protease and reverse transcriptase mutation patterns in 4,183 persons undergoing genotypic resistance testing.* Antimicrob Agents Chemother, 2004. **48**(8): p. 3122-6.
290. Majerova, T. and P. Novotny, *Precursors of Viral Proteases as Distinct Drug Targets.* Viruses, 2021. **13**(10).
291. Hikichi, Y., et al., *Mechanistic Analysis of the Broad Antiretroviral Resistance Conferred by HIV-1 Envelope Glycoprotein Mutations.* mBio, 2021. **12**(1).
292. Partin, K., et al., *Deletion of sequences upstream of the proteinase improves the proteolytic processing of human immunodeficiency virus type 1.* Proc Natl Acad Sci USA, 1991. **88**(11): p. 4776-80.
293. Watanabe, S.M., et al., *The S40 residue in HIV-1 Gag p6 impacts local and distal budding determinants, revealing additional late domain activities.* Retrovirology, 2013. **10**: p. 143.
294. Condra, J.H., et al., *In vivo emergence of HIV-1 variants resistant to multiple protease inhibitors.* Nature, 1995. **374**(6522): p. 569-71.
295. Condra, J.H., et al., *Genetic correlates of in vivo viral resistance to indinavir, a human immunodeficiency virus type 1 protease inhibitor.* J Virol, 1996. **70**(12): p. 8270-6.
296. Dautin, N., et al., *Sensitive genetic screen for protease activity based on a cyclic AMP signaling cascade in Escherichia coli.* J Bacteriol, 2000. **182**(24): p. 7060-6.
297. Naeger, L.K. and K.A. Struble, *Food and Drug Administration analysis of tipranavir clinical resistance in HIV-1-infected treatment-experienced patients.* AIDS, 2007. **21**(2): p. 179-85.
298. Martinez-Picado, J., et al., *Fitness of human immunodeficiency virus type 1 protease inhibitor-selected single mutants.* Virology, 2000. **275**(2): p. 318-22.
299. He, J. and N.R. Landau, *Use of a novel human immunodeficiency virus type 1 reporter virus expressing human placental alkaline phosphatase to detect an alternative viral receptor.* J Virol, 1995. **69**(7): p. 4587-92.
300. Rose, J.R., R. Salto, and C.S. Craik, *Regulation of autoproteolysis of the HIV-1 and HIV-2 proteases with engineered amino acid substitutions.* J Biol Chem, 1993. **268**(16): p. 11939-45.
301. Mildner, A.M., et al., *The HIV-1 protease as enzyme and substrate: mutagenesis of autolysis sites and generation of a stable mutant with retained kinetic properties.* Biochemistry, 1994. **33**(32): p. 9405-13.
302. Daniels, R.W., et al., *Expression of multiple transgenes from a single construct using viral 2A peptides in Drosophila.* PLoS One, 2014. **9**(6): p. e100637.

303. Kajava, A.V., et al., *The net charge of the first 18 residues of the mature sequence affects protein translocation across the cytoplasmic membrane of gram-negative bacteria.* J Bacteriol, 2000. **182**(8): p. 2163-9.
304. Collier, D.N. and P.J. Bassford, Jr., *Mutations that improve export of maltose-binding protein in SecB- cells of Escherichia coli.* J Bacteriol, 1989. **171**(9): p. 4640-7.
305. Justesen, U.S., *Protease inhibitor plasma concentrations in HIV antiretroviral therapy.* Dan Med Bull, 2008. **55**(4): p. 165-85.
306. Durant, J., et al., *Importance of protease inhibitor plasma levels in HIV-infected patients treated with genotypic-guided therapy: pharmacological data from the Viradapt Study.* AIDS, 2000. **14**(10): p. 1333-9.
307. Pieniazek, D., et al., *Protease sequences from HIV-1 group M subtypes A-H reveal distinct amino acid mutation patterns associated with protease resistance in protease inhibitor-naive individuals worldwide. HIV Variant Working Group.* AIDS, 2000. **14**(11): p. 1489-95.
308. Boffito, M., et al., *Protein binding in antiretroviral therapies.* AIDS Res Hum Retroviruses, 2003. **19**(9): p. 825-35.
309. Illamola, S.M., et al., *Challenges regarding analysis of unbound fraction of highly bound protein antiretroviral drugs in several biological matrices: lack of harmonisation and guidelines.* Drug Discov Today, 2015. **20**(4): p. 466-74.
310. Koch, N., et al., *Comparison of human immunodeficiency virus type 1 (HIV-1) protease mutations in HIV-1 genomes detected in plasma and in peripheral blood mononuclear cells from patients receiving combination drug therapy.* J Clin Microbiol, 1999. **37**(5): p. 1595-7.
311. Dasgupta, A., *Usefulness of monitoring free (unbound) concentrations of therapeutic drugs in patient management.* Clin Chim Acta, 2007. **377**(1-2): p. 1-13.
312. Costa, A.P., et al., *Canine orosomucoid (alpha-1 acid glycoprotein) variants and their influence on drug plasma protein binding.* J Vet Pharmacol Ther, 2021. **44**(1): p. 116-125.
313. Rosenbloom, D.I., et al., *Antiretroviral dynamics determines HIV evolution and predicts therapy outcome.* Nat Med, 2012. **18**(9): p. 1378-85.
314. Vermeiren, H., et al., *Prediction of HIV-1 drug susceptibility phenotype from the viral genotype using linear regression modeling.* J Virol Methods, 2007. **145**(1): p. 47-55.
315. Martinez-Picado, J., et al., *Phenotypic hypersusceptibility to multiple protease inhibitors and low replicative capacity in patients who are chronically infected with human immunodeficiency virus type 1.* J Virol, 2005. **79**(10): p. 5907-13.
316. Floderer, C., et al., *Single molecule localisation microscopy reveals how HIV-1 Gag proteins sense membrane virus assembly sites in living host CD4 T cells.* Scientific Reports, 2018. **8**(1).
317. Ono, A. and E.O. Freed, *Plasma membrane rafts play a critical role in HIV-1 assembly and release.* Proc.Natl.Acad.Sci.U.S.A, 2001. **98**(24): p. 13925-13930.
318. Martinez, N.W., et al., *Kinesin KIF4 Regulates Intracellular Trafficking and Stability of the Human Immunodeficiency Virus Type 1 Gag Polyprotein.* Journal of Virology, 2008. **82**(20): p. 9937-9950.

319. Dong, X., et al., *AP-3 directs the intracellular trafficking of HIV-1 Gag and plays a key role in particle assembly.* Cell, 2005. **120**(5): p. 663-74.

320. Jouvenet, N., S.M. Simon, and P.D. Bieniasz, *Imaging the interaction of HIV-1 genomes and Gag during assembly of individual viral particles.* Proceedings of the National Academy of Sciences, 2009. **106**(45): p. 19114-19119.

321. Kleiman, L., C.P. Jones, and K. Musier-Forsyth, *Formation of the tRNA^{Lys} packaging complex in HIV-1.* FEBS Letters, 2010. **584**(2): p. 359-365.

322. Konvalinka, J., H.-G. Kräusslich, and B. Müller, *Retroviral proteases and their roles in virion maturation.* Virology, 2015. **479-480**: p. 403-417.

323. Accola, M.A., A. Ohagen, and H.G. Gottlinger, *Isolation of human immunodeficiency virus type 1 cores: retention of Vpr in the absence of p6(gag).* J.Virol., 2000. **74**: p. 6198-6202.

324. Welker, R., et al., *Biochemical and Structural Analysis of Isolated Mature Cores of Human Immunodeficiency Virus Type 1.* Journal of Virology, 2000. **74**(3): p. 1168-1177.

325. Kotov, A., et al., *Association of Nef with the Human Immunodeficiency Virus Type 1 Core.* Journal of Virology, 1999. **73**(10): p. 8824-8830.

326. McGraw, A., et al., *Exploring HIV-1 Maturation: A New Frontier in Antiviral Development.* Viruses, 2024. **16**(9): p. 1423.

327. Nijhuis, M., et al., *Increased fitness of drug resistant HIV-1 protease as a result of acquisition of compensatory mutations during suboptimal therapy.* AIDS, 1999. **13**(17): p. 2349-2359.

328. Borman, A.M., S. Paulous, and F. Clavel, *Resistance of human immunodeficiency virus type 1 to protease inhibitors: selection of resistance mutations in the presence and absence of the drug.* Journal of General Virology, 1996. **77**(3): p. 419-426.

329. Stringer, C., et al., *Cellpose: a generalist algorithm for cellular segmentation.* Nature Methods, 2021. **18**(1): p. 100-106.

330. Pachitariu, M. and C. Stringer, *Cellpose 2.0: how to train your own model.* Nature Methods, 2022. **19**(12): p. 1634-1641.

331. Dierynck, I., et al., *Binding Kinetics of Darunavir to Human Immunodeficiency Virus Type 1 Protease Explain the Potent Antiviral Activity and High Genetic Barrier.* Journal of Virology, 2007. **81**(24): p. 13845-13851.

332. El Bouzidi, K., et al., *HIV-1 drug resistance mutations emerging on darunavir therapy in PI-naive and -experienced patients in the UK.* J Antimicrob Chemother, 2016. **71**(12): p. 3487-3494.

333. Calza, L., et al., *Plasma trough concentrations of darunavir/ritonavir and raltegravir in older patients with HIV-1 infection.* HIV Med, 2017. **18**(7): p. 474-481.

334. Ryan, M.D., A.M. King, and G.P. Thomas, *Cleavage of foot-and-mouth disease virus polyprotein is mediated by residues located within a 19 amino acid sequence.* J Gen Virol, 1991. **72 (Pt 11)**: p. 2727-32.

335. Boyer, S., et al., *Cost-Effectiveness of Three Alternative Boosted Protease Inhibitor-Based Second-Line Regimens in HIV-Infected Patients in West and Central Africa.* Pharmacoecon Open, 2020. **4**(1): p. 45-60.

336. Akanmu, A.S., et al., *Immunological and Virological Outcomes of Patients Switched from LPV/r to ATV/r-Containing Second- Line Regimens.* Curr HIV Res, 2015. **13**(3): p. 176-83.
337. Pau, A.K., et al., *Instability of lopinavir/ritonavir capsules at ambient temperatures in sub-Saharan Africa: relevance to WHO antiretroviral guidelines.* AIDS, 2005. **19**(11): p. 1233-1234.
338. Carrillo, A., et al., *In Vitro Selection and Characterization of Human Immunodeficiency Virus Type 1 Variants with Increased Resistance to ABT-378, a Novel Protease Inhibitor.* Journal of Virology, 1998. **72**(9): p. 7532-7541.
339. Weber, I.T., Y.-F. Wang, and R.W. Harrison, *HIV Protease: Historical Perspective and Current Research.* Viruses, 2021. **13**(5): p. 839.
340. Robinson, B.S., et al., *BMS-232632, a Highly Potent Human Immunodeficiency Virus Protease Inhibitor That Can Be Used in Combination with Other Available Antiretroviral Agents.* Antimicrobial Agents and Chemotherapy, 2000. **44**(8): p. 2093-2099.
341. Abdalla, S., et al., *Simultaneous pharmacokinetic modeling of unbound and total darunavir with ritonavir in adolescents: a substudy of the SMILE trial.* Antimicrob Agents Chemother, 2024. **68**(2): p. e0100423.
342. Mulato, A., et al., *Preclinical characterization of a non-peptidomimetic HIV protease inhibitor with improved metabolic stability.* Antimicrob Agents Chemother, 2024. **68**(4): p. e0137323.
343. Stoltzfus, C.M. and J.M. Madsen, *Role of viral splicing elements and cellular RNA binding proteins in regulation of HIV-1 alternative RNA splicing.* Curr HIV Res, 2006. **4**(1): p. 43-55.
344. Hung, M., et al., *Importance of ribosomal frameshifting for human immunodeficiency virus type 1 particle assembly and replication.* 1998. **72**(6): p. 4819-4824.
345. Haraguchi, H., et al., *Intracellular localization of human immunodeficiency virus type 1 Gag and GagPol products and virus particle release: relationship with the Gag-to-GagPol ratio.* Microbiology and Immunology, 2010. **54**(12): p. 734-746.
346. Kobayashi, Y., et al., *Identification of a Cellular Factor That Modulates HIV-1 Programmed Ribosomal Frameshifting.* Journal of Biological Chemistry, 2010. **285**(26): p. 19776-19784.
347. Martin-Serrano, J., T. Zang, and P.D. Bieniasz, *Role of ESCRT-I in retroviral budding.* 2003. **77**(8): p. 4794-4804.
348. Hurley, J.H. and A.K. Cada, *Inside job: how the ESCRTs release HIV-1 from infected cells.* Biochemical Society Transactions, 2018. **46**(5): p. 1029-1036.
349. Loeb, D.D., et al., *Complete mutagenesis of the HIV-1 protease.* Nature, 1989. **340**(6232): p. 397-400.
350. Mattei, S., et al., *Induced maturation of human immunodeficiency virus.* J Virol, 2014. **88**(23): p. 13722-31.
351. Ghosh, A.K., H.L. Osswald, and G. Prato, *Recent Progress in the Development of HIV-1 Protease Inhibitors for the Treatment of HIV/AIDS.* J Med Chem, 2016. **59**(11): p. 5172-208.

352. Ullman, E.F., et al., *Luminescent oxygen channeling immunoassay: measurement of particle binding kinetics by chemiluminescence.* Proc Natl Acad Sci U S A, 1994. **91**(12): p. 5426-30.
353. Ullman, E.F., et al., *Luminescent oxygen channeling assay (LOCI): sensitive, broadly applicable homogeneous immunoassay method.* Clin Chem, 1996. **42**(9): p. 1518-26.
354. McGiven, J.A., et al., *A new homogeneous assay for high throughput serological diagnosis of brucellosis in ruminants.* J Immunol Methods, 2008. **337**(1): p. 7-15.
355. Eglen, R.M., et al., *The Use of AlphaScreen Technology in HTS: Current Status.* Curr Chem Genomics, 2008. **1**: p. 2-10.
356. Huang, L., et al., *Assay Development and Validation for Innovative Antiviral Development Targeting the N-Terminal Autoprocessing of SARS-CoV-2 Main Protease Precursors.* Viruses, 2024. **16**(8).
357. Wang, C.T., Y.C. Chou, and C.C. Chiang, *Assembly and processing of human immunodeficiency virus Gag mutants containing a partial replacement of the matrix domain by the viral protease domain.* J Virol, 2000. **74**(7): p. 3418-22.
358. Whitehurst, N., et al., *Polymorphisms in p1-p6/p6* of HIV type 1 can delay protease autoprocessing and increase drug susceptibility.* AIDS Res Hum Retroviruses, 2003. **19**(9): p. 779-84.
359. Yu, F.H., et al., *Gag-Pol Transframe Domain p6* Is Essential for HIV-1 Protease-Mediated Virus Maturation.* PLoS One, 2015. **10**(6): p. e0127974.
360. Yu, F.H. and C.T. Wang, *HIV-1 protease with leucine zipper fused at N-terminus exhibits enhanced linker amino acid-dependent activity.* Retrovirology, 2018. **15**(1): p. 32.
361. Kohl, N.E., et al., *Active human immunodeficiency virus protease is required for viral infectivity.* Proc Natl Acad Sci USA, 1988. **85**(13): p. 4686-90.
362. Peng, C., et al., *Role of human immunodeficiency virus type 1-specific protease in core protein maturation and viral infectivity.* Journal of Virology, 1989. **63**(6): p. 2550-2556.
363. Weber, I.T. and J. Agniswamy, *HIV-1 Protease: Structural Perspectives on Drug Resistance.* Viruses, 2009. **1**(3): p. 1110-1136.
364. King, N.M., et al., *Structural and thermodynamic basis for the binding of TMC114, a next-generation human immunodeficiency virus type 1 protease inhibitor.* J Virol, 2004. **78**(21): p. 12012-21.
365. Steegen, K., et al., *Prevalence of Antiretroviral Drug Resistance in Patients Who Are Not Responding to Protease Inhibitor-Based Treatment: Results From the First National Survey in South Africa.* J Infect Dis, 2016. **214**(12): p. 1826-1830.
366. Lyon, K. and T.J. Stasevich, *Imaging Translational and Post-Translational Gene Regulatory Dynamics in Living Cells with Antibody-Based Probes.* Trends in Genetics, 2017. **33**(5): p. 322-335.
367. Morisaki, T. and T.J. Stasevich, *Quantifying Single mRNA Translation Kinetics in Living Cells.* Cold Spring Harbor Perspectives in Biology, 2018. **10**(11): p. a032078.

368. Lyon, K.R., T. Morisaki, and T.J. Stasevich, *Imaging and Quantifying Ribosomal Frameshifting Dynamics with Single-RNA Precision in Live Cells*. 2025, Springer US. p. 99-110.